Bottom-up construction of the artificial mitochondrion

Dissertation

zur Erlangung des akademischen Grades

doctor rerum naturalium

(Dr. rer. nat.)

von: **M. Sc. Lado Otrin**

geb. am 05.01.1988 in Ljubljana, Slowenien

genehmigt durch die Fakultät für Verfahrens- und Systemtechnik der Otto-von-Guericke-Universität Magdeburg

Promotionskommission: Prof. Dr. rer. nat. Nora Kulak (Vorsitz)

Prof. Dr.-Ing. Tanja Vidaković-Koch (Gutachter)

Prof. Dr. Sébastien Lecommandoux (Gutachter)

Prof. Dr. Christoph von Ballmoos (Gutachter)

eingereicht am: 03.03.2021

Promotionskolloquium am: 25.06.2021

Abstract

Synthetic life, as envisioned by a bottom-up synthetic biology, appears to be, much like it´s natural counterpart, highly energy demanding. Therefore, in this work, a versatile energy regeneration module was constructed via bottom-up hand-tailored reconstitution procedure to enable continuous supply of adenosine triphosphate (ATP) and another important co-factor, NAD^+. This energy regeneration module can be considered as the artificial respiratory chain (ARC), consisting of four functional parts: the ATP synthase, a proton pump, a NADH dehydrogenase and a compartment. Due to the lack of the repair and replacement mechanisms in the current iteration of the artificial cell, to increase the stability and durability of the energy module, substitution of lipid compartments with the polymer or lipid/polymer hybrid ones was explored. The reconstitution procedure was devised, which enabled simultaneous insertion of several enzymes comprising the ARC in the mentioned polymer-based compartments. The enzyme insertion could be controlled by the choice of mediating detergent and the degree of membrane solubilization by the detergent. In this context, the orientation and reconstitution efficiency of the individual respiratory enzymes were determined in different types of compartments, and the final output of the energy module was analysed in the light of these reconstitution parameters. Moreover, the interplay between the respiratory enzymes and the man-made membranes was analysed in greater detail. In hybrid compartments, the analysis revealed the structural rearrangements and changes in membrane permeability following the enzyme insertion. Meanwhile the protective function of the graft copolymer against reactive oxygen species (ROS) was discovered in enzyme-functionalized polymer compartments in which the preserved enzymatic activity as well as structural integrity of the compartments was observed following the ROS treatment.

To increase the efficiency of the ARC, two variants of the respiratory chain were constructed and tested for the activity – one featuring a proton-translocating respiratory complex I and another featuring non-translocating DT-diaphorase. The most active energy module was then coupled with the metabolic module comprising 17 different enzymes to form the minimal artificial organelle – minimal artificial mitochondrion – which was operational for more than an hour. To enable coupling between the two modules, the composition and osmolarity of the ARC were tuned. In order to examine the effects of fluctuating osmolarity on the activity of the ARC, osmotic stress was applied to the energy module and a staggering resistance of the module to hypertonic as well as hypotonic environment was discovered. Furthermore, membrane tightness was imperative for the establishment of proton gradient, used to drive ATP synthesis by the energy module. Therefore, Poloxamer 188 was used to mend the imperfection in lipid bilayers originating from enzyme insertion, and membrane resealing was achieved resulting in significantly increased ATP synthesis. Finally, an auxiliary oxygen supply system was developed to address oxygen depletion by the module. In this role, the oxygen release from the calcium peroxide particles was analysed and the effect of particles on the activity of the ARC was evaluated. With the oxygen supply system, a remarkable reoxygenation of the energy module was accomplished and the

initial ATP synthesis at the highest rate by the module was significantly extended. Based on these findings, the respiratory tissue was proposed, which combines the essentials for continuous, versatile and efficient energy regeneration.

To enable the step-wise assembly of multiprotein artificial respiratory chains with the preserved optimal configuration of each individual enzyme, membrane fusion mediated by fusogenic proteins was explored. The latter were incorporated into polymer and hybrid compartments to form a versatile and widely biocompatible minimal fusion platform. The insertion of fusogenic proteins in polymer and hybrid compartments was analysed in greater detail with respect to the protein orientation and insertion efficiency, as well as membrane architecture. In addition, protein-mediated fusion of polymer and hybrid compartments was inspected via membrane mixing, as well as the functional coupling between two respiratory enzymes. For the first time it was found that synthetic amphiphile membranes also undergo fusion, mediated by the protein machinery for synaptic secretion, and the remarkably high membrane and content mixing was observed. To elucidate the reasons for successful and efficient fusion, the pore opening dynamics were investigated, which revealed the increased stability of the pores in polymer membranes. Finally, key fusion intermediates of protein-mediated polymer and hybrid fusion were observed with cryo electron microscopy and described, offering unprecedented insights of the fusion process in this novel system.

Zusammenfassung

Das künstliche Leben, so wie es von der Synthetischen Biologie mit einem bottom-up Ansatz vergegenwärtigt wird, scheint, wie sein natürliches Pendant energetisch sehr anspruchsvoll zu sein. Zur Gewährleistung einer kontinuierlichen Zufuhr von Adenosintriphosphat (ATP) und Nicotinamidadenindinukleotid (NAD) wurde in dieser Arbeit ein vielfältiges Energieregenerationsmodul durch maßgeschneiderte Rekonstitution entwickelt. Dieses Modul besteht im Wesentlichen aus einer künstlichen Atmungskette (ARC - artificial respiratory chain), die sich aus vier funktionalen Einheiten zusammensetzt: der ATP-Synthase, einer Protonenpumpe, der NADH-Dehydrogenase und einem Kompartiment. Zur Erhöhung der Stabilität und Beständigkeit des Energiemoduls wurden, auf Grund der mangelnden Reparatur- und Austauschmöglichkeiten derzeitiger künstlicher Zellen, der Austausch von Lipid-Kompartimenten durch Polymer- oder Lipid/Polymer-Kompartimenten, sogenannten Hybriden, untersucht. Für die Entstehung der ARC wurde eine Rekonstitutionsmethode entwickelt, welche den simultanen Einbau mehrerer Enzyme in die erwähnten Polymer-basierten Kompartimente ermöglicht. Die Insertion der Enzyme kann zum einen durch die Wahl des Rekonstitutions-vermittelnden Detergens und zum anderen durch den Grad der Membransolubilisierung durch das Detergens bestimmt kontrolliert werden. In diesem Kontext wurden die Orientierung und die Effizienz der Rekonstitution der einzelnen respiratorischen Enzyme in den verschiedenen Kompartimenten bestimmt und die endgültige Leistung des Energiemoduls mit diesen Rekonstitutionsparametern in Beziehung gesetzt. Zudem wurden die Wechselwirkungen zwischen den Enzymen und den künstlich geschaffenen Membranen ausführlich analysiert. Untersuchungen der Hybrid-Kompartimente ergaben, dass es durch den Einbau von Enzymen zu strukturellen Umlagerungen und Veränderungen in der Permeabilität der Membran kommt, während in einem mit Enzymen funktionalisiertem Polymer-Kompartiment eine schützende Funktion des Graft-Co-polymers gegen reaktive Sauerstoffspezies (ROS) festgestellt werden konnte, nachdem diese mit ROS behandelt wurden. Die Enzymaktivität und die strukturelle Integrität der Kompartimente blieb erhalten.

Zur Erhöhung der ARC-Effizienz wurden zwei Varianten der Atmungskette entwickelt und auf deren Aktivität hin überprüft. Eine Variante enthielt den Protonen-translozierenden Komplex I und die andere die nicht-translozierende DT-diaphorase. Das aktivste Energiemodul wurde im Anschluss mit einem aus siebzehn Enzymen bestehenden Stoffwechselmodul gekoppelt, mit dem Ziel, ein minimales künstliches Organell - ein minimales künstliches Mitochondrium - aufzubauen, wobei das entstandene Konstrukt über eine Stunde funktionsfähig war. Um beide

Module zu koppeln, wurden die Zusammensetzung und die Osmolarität der ARC angepasst. Die Auswirkung von wechselnder Osmolarität auf die Aktivität wurde durch osmotischen Stress untersucht und eine erstaunliche Widerstandsfähigkeit sowohl gegen hypertonische als auch gegen hypotonische Umgebungen festgestellt. Zudem war die Dichtheit der Membran eine feste Voraussetzung für die Schaffung eines pH-Gradienten, der wiederum zur Synthese von ATP befähigt. Fehlordnungen in der Lipiddoppelschicht, welche aufgrund der Enzym-Rekonstitutionen entstanden waren, wurden mittels Poloxamer 188 behoben und die erneute Membranversiegelung führte zu einer deutlich höheren ATP-Synthese. Um die Erschöpfung von Sauerstoff durch das Energiemodul zu beseitigen, wurde mittels Calciumperoxid-Partikeln ein zusätzliches Versorgungssystem mit Sauerstoff entwickelt und dessen Effekt auf die Aktivität der ARC untersucht. Die Freisetzung von Sauerstoff von diesen Partikeln führte zu einer erheblichen Sauerstoffanreicherung und verlängerte die höchste Anfangsrate der ATP-Synthese wesentlich. Bezüglich dieser Erkenntnisse ist die Entwicklung respiratorischer Gewebe vorstellbar, welche alle wesentlichen Voraussetzungen für eine kontinuierliche, vielseitige und effiziente Energieregenerierung besitzen.

Zur schrittweisen Assemblierung multienzymatischer ARC, deren individuelle Enzyme bereits optimal konfiguriert worden sind, wurden Membranfusion-vermittelnde Proteine untersucht. Diese wurden in Polymer- und Hybridkompartimente eingebracht, um eine vielfältige und weitgehend biokompatible minimale Fusionsplattform zu errichten. Die Rekonstitution der Fusionsproteine wurde in Bezug auf die Orientierung des Proteins, die Effizienz der Insertion, wie auch auf die Membranarchitektur hin untersucht. Mit Hilfe der Membranvermischung wurde zusätzlich die Protein-vermittelte Fusion von Polymer- und Hybridkompartimenten sowie die funktionale Kopplung zwischen Enzymen der Atmungskette analysiert. Erstmals wurde festgestellt, dass auch synthetische amphiphile Membranen durch synaptische Sekretionsproteine fusionieren und zudem bemerkenswert hohe Membran- und Gehaltsvermischungen beobachtet werden konnten. Zur Ursachenfindung wurde die Porenöffnungsdynamik gemessen, die eine erhöhte Stabilität der Poren in Polymermembranen aufzeigte. Letztendlich wurden durch Kryoelektronenmikroskopie entscheidende Fusionszwischenstufen von Protein-vermittelter Polymer- und Hybridfusion beobachtet und beschrieben, die einen beispiellosen Einblick in die Fusionsprozesse in diesem neuartigen System gewährten.

Table of contents

1 INTRODUCTION

Chapter 1.2.2, paragraphs 2 and 3 were reprinted (adapted) with permission from L. Otrin et al., Toward Artificial Mitochondrion: Mimicking Oxidative Phosphorylation in Polymer and Hybrid Membranes. *Nano Letters* 17, 6816 (2017) (*1*). Copyright 2017, American Chemical Society.

Chapter 1.3, paragraphs 1–9 were reprinted (adapted) with permission from L. Otrin et al., Artificial Organelles for Energy Regeneration. *Advanced Biosystems* 3, 1800323 (2019) (*2*). Copyright 2019, WILEY-VCH Verlag GmbH & Co. KGaA, Weinheim.

1.1 BOTTOM-UP SYNBIO

Throughout history, the undeniable reliance of humankind on different organisms as means of production of the goods and materials essential for our sustainment has led towards intensification of our interactions with these organisms. With respect to this, large efforts were invested into achieving unprecedented control over them, their life-cycles and their response to our inputs. The course of this process is best exemplified by the changes throughout time evidenced in husbandry and, in particular, in animal breeding. First, the organisms, animals, were collected from their natural environment, and the latter was replicated in locations populated by humans. In this context, the merger of the two previously separated habitats enabled more constant and convenient access to the goods, without drastic alterations to the animal life-cycle. In contrast, much different picture can be seen in the modern animal husbandry. Nowadays, the knowledge that we gathered throughout centuries of co-dependency has helped us to reduce the breeding conditions of animals to bare minimum, to essentials only, while the yield is significantly increased. In this respect, animals are immobilized in spaces not much larger than their body dimensions, all the inputs that they are receiving are directed towards achieving the largest desired output (benefitting us), and the life-cycles of animals were rearranged and retimed to support this. By strictly looking at this through a lens of benevolence and by disregarding the immense ethical concerns, a conclusion can be made that this production system can now be predicted, manipulated and controlled with exquisite precision. With that in mind, a parallel can be drawn between husbandry and biotechnology, whereby the synthetic biology (SynBio) is hoping to achieve the same high degree of control over the production microorganisms (or other organisms-derived systems), while basically

repeating the above-described process. In this context, the production microorganisms were first collected, transferred into a controlled habitat and their growth under these new conditions has been optimized. Then, the product harvesting, in particular its isolation and purification was improved. More importantly, in the next step, the number of inputs in the systems was reduced in order to eliminate the natural redundancies that developed to facilitate adaptation of microorganisms to the everchanging environment. In this new, well-defined and relatively closed environment, the versatility of organisms can be seen as the unnecessary energy and material expenditure that must be avoided in order to increase the efficiency of the system. This manipulation approach ushered in the emergence of the top-down synthetic biology, which is seeking to eliminate natural redundancies seen in organisms via the genome editing thus simplifying them, or to introduce another previously absent functionality to the edited organisms.

The development of the top-down SynBio was to a large degree made possible by major advancements in the related enabling technologies (protein purification and analysis, biosensor design, microfluidics, modelling) as well as by the dramatic increase in the genome editing capabilities (DNA, gene and transcription factors synthesis, sequencing). With the top-down approach, a variety of important milestones were accomplished. For instance, the minimal bacterial genome was designed and built by the lab of Craig Venter comprising 473 genes (513 kb) that supported cell growth of *Mycoplasma mycoides* when transplanted into cytoplasm (*3*). Their genome editing efforts were supported by the lab of Christopher Voigt, which designed Cello (www.cellocad.org), a computer aided design system for logical circuits based on electronic design automation (EDA) module. Cello enabled the automated design of the desired gene circuits by assigning the gates, creating a circuit diagram, determining the requirements and constrains to build the DNA and simulating the performance (*4*). Among other most notable achievements are also the construction of the functional single-chromosome yeast as well as yeast with synthetically fused chromosomes by Shao and colleagues (*5*) and Luo and colleagues (*6*), respectively. Finally, worth noting are also several production-oriented top-down-derived applications. Most recently, a complete biosynthesis of cannabinoids and their unnatural analogues (*7*) as well the artemisinic acid (precursor of the antimalarial drug) (*8*) was achieved in yeast by the lab of Jay Keasling. Other new technologies and landmark achievements delivered in recent years by the top-down SynBio can be found reviewed by Fankang Meng and Tom Ellis (*9*). Nevertheless, despite the remarkably high reduction efficiency of the top-down approach, some residual redundancy could not be avoided. The minimal yeast engineered

by Hutchinson and colleagues (*3*), for instance, contained 149 genes of unknown function. Other major challenges yet to be addressed by top-down SynBio to a sufficient degree according to Roberta Kwok (*10*) in her work titled "Five hard truths for synthetic biology" are poorly defined, incompatible parts, unpredictable circuits of rapidly increasing complexity and poor reaction of systems to variability.

All of these shortcomings are in one way or another addressed by another variant of synthetic biology – bottom-up SynBio. With this approach, first, a library of most basic building blocks, functional parts, is created. This encompasses the isolation and purification of said parts (in the case of nature-derived parts) or their synthesis (nature-derived and man-made parts), as well as their in-depth characterization with respect to their structure, stability and function under the desired conditions. With this, the inputs required to achieve their functionality under the specified conditions are defined and can be used to couple functional parts towards the formation of functional modules under the guidance of the assembly standards. Such standardization can be used further to steer the formation of functional systems by combining several compatible functional modules. Systems are then evaluated based on the predefined performance standards and optimized until a satisfactory performance is reached. The bottom-up progression of system construction based on the principles of engineering assures its high compositional purity, compatibility and efficiency. Furthermore, the accumulated knowledge of nature can be data mined to identify the most suitable existing natural parts for accomplishing a desired function under a variety of specified conditions, while the coupling between parts and the output of the modules/systems can be predicted with the ever-increasing accuracy via modelling. However, the aspirations of the bottom-up SynBio are not confined to the biotechnological applications. Functional modules can be intentionally designed with a purpose of mimicking the basic processes of life, such as growth, motility, reproduction, etc. In this context, perhaps the most ambitious endeavour is the coupling between these life-mimicking modules with the hopes of constructing the artificial cell (also referred to as the "minimal cell"). In this respect, it remains unclear and heavily debated which modules/processes and in which combinations should be considered essential to recreate life and the Max Planck Synthetic biology network ("MaxSynBio") was formed to seek the answers to these and other important fundamental questions. In this context, five essential life-mimicking processes were identified by the MaxSynBio and were included in the artificial cell blueprint (*11*):

- o **Signalling and motility**, reproduction of morphogenetic responses of the cell to environmental or intrinsic cues, in order to stimulate cell adhesion, movement, cytoskeletal reorganization or membrane remodelling.
- o **Replication and division**, the dramatical mechanical transformation required for the successful generation of offspring.
- o **Growth**, prerequisite for the establishment of self-replicating system.
- o **Metabolism**, enables the autonomous production of cell constituents as well as other products of interest,
- o **Energy regeneration**, namely ATP and co-factor (for instance $NAD(P)^+$) regeneration, required to drive all other, energy-dependent life processes.

In the absence of the "information" module (i.e., genetic code), the system comprising the modules specified above would not have been truly autonomous. Nevertheless, the mentioned system design enables the potential subsequent expansion of the cell with additional modules, at later times. Moreover, to support the construction of the artificial cell, the essential enabling technologies were identified by the MaxSynBio – compartment creation and protein production. In this context, an immense impact of the microfluidic technology and cell-free protein expression on the development of SynBio can be seen. Considering the importance of the compartmentalization for the sustainment of life, the former could instead be considered as one of the essential life-processes. Regardless, compartments in the context of the MaxSynBio were predominantly used as a functional part facilitating functionality of other parts. Therefore, *de novo* synthesis of compartments was not emphasized in a manner similar to other life-processes and they were considered as technology rather than a biomimetic process. In recent years, numerous breakthroughs in the context of bottom-up SynBio were reported by the MaxSynBio network and others. However, the focus of this work was the construction of the artificial mitochondrion, which combines the coupling between the energy and metabolic module with the compartmentalization. With respect to this, the following discussion is limited to the background and major advancements related to these three aspects.

1.2 COMPARTMENTALIZATION

1.2.1 Formation of the compartments

The autonomy of (artificial) cells and organelles is to a large extent tied to the essential feature of natural as well as synthetic life – compartmentalization. Amphiphilic membranes not only protect the constructs they enclose from the environment, but also enable spatial and

temporal segregation of biochemical reactions (*12*). More importantly, the compartments employed in this work enabled formation of a proton gradient as well as insertion and activation of respiratory enzymes. A variety of methods were developed through the years that facilitate preparation of amphiphile compartments of different composition, size, surface charge, lamellarity and vesicularity. Most notable classical formation methods include, but are not limited to passive amphiphile film swelling (hydration), solvent dispersion, detergent removal, sonication, freeze-thaw, extrusion and phase transfer (*13*). In this work, different types of compartments were formed via a combination of freeze-thaw and extrusion method. Using this method, thin amphiphile films were first rehydrated with a desired solvent and their size and lamellarity was reduced with several cycles of freezing (in liquid nitrogen) and thawing (water bath), thusly forming highly dispersed multilamellar vesicles. Next, these vesicles were extruded through a filter with a defined pore size so that the lamellarity and polydispersity were reduced. The resulting vesicles were mostly unilamellar with membrane architecture and characteristics closely resembling natural membranes, and the vesicle dispersion was relatively monodispersed (PdI ≈ 0.1–0.2).

In recent years, an immense impact of more novel technologies for vesicle preparation on the bottom-up SynBio could be seen, most notably microfluidics. This method enables preparation of micro- (*14, 15*) and nano-sized (*16, 17*) vesicles and allows precise delivery of various components into preformed vesicles via pico-injection (*18, 19*). Apart from the latter, microfluidics was mainly popularized due to the high size uniformity of the produced vesicles, although it appears that this holds true predominantly on the micro-scale. In this context, a slightly higher polydispersity of nano-sized vesicles formed in microfluidics in comparison to the ones attained with the freeze-thaw, extrusion method is reported by Jahn and colleagues (*17, 20*). Furthermore, vesicles produced in microfluidics are often not unilamellar and, more importantly, contain residual amounts of solvents and detergents used to assist vesicles formation, which drastically alter the biophysical properties of the membranes (*21*). This altered membrane composition in combination with slightly increased polydispersity made the microfluidics-derived vesicles unappealing for the purpose of protein insertion and module integration tackled in this work, although their micro-sized counterparts could potentially be used to house the coupled energy/metabolic modules in future works.

1.2.2   Polymersomes as the alternative to liposomes

Historically, compartments (vesicles) were being formed primarily from various lipids or mixtures of thereof, with a most common purpose of substance encapsulation or protein insertion and characterization. With respect to this, for the applications related to the latter it was particularly important that the natural protein environment was being replicated composition-wise to a sufficient extent to promote enzyme insertion and functionality, while the biophysical properties of the compartments themselves were of secondary importance. Meanwhile, the applications related to the cargo encapsulation and targeted delivery draw the attention primarily to compartments, whereby versatile, tunable and easily obtainable amphiphiles were being sought after as the compartment constituents (*22*). Compartments formed of otherwise biocompatible lipids were found suffering from the increased permeability as a consequence of high lateral mobility (*23*), as well as the overall low chemical and mechanical stability (reviewed in detail in (*22*). The former is mainly tied to the unsaturated fatty acid chains being prone to oxidation, while the ester moieties can undergo hydrolysis. Furthermore, lipid compartments on average exhibit relatively low bending rigidity, lysis tension and critical poration potential, resulting in decreased resistance to mechanical stress. Unsurprisingly, this has led to the substitution of lipid compartments (liposomes) with the polymer ones (polymersomes), considering the comparatively higher stability of block co-polymers and consequently polymersomes (*24-26*). Moreover, polymer chemistry can be finely tuned in order to permit the formation of well-defined vesicles that exhibit desired biophysical properties (membrane thickness, viscosity, etc.) and are capable of responding to various stimuli, such as pH, light, magnetic field, ultrasound and others (*26, 27*).

While the robustness of compartments was being emphasized in the first generation of polymersome-based applications, second generation sought to bestow complexity and additional functionality to polymersomes. To this end, polymer compartments were functionalized with various proteins towards the formation of nano/microreactors, advanced therapeutics, sensors and cell/organelle mimics (*27, 28*). Nevertheless, at that point, predominantly very rigid proteopolymersomes formation methods seem to vastly limit the set of MPs suitable for functional reconstitution to the few robust, most stable, simple model MPs, capable of membrane integration through self-assembly, such as ompF, Tsx, AQP0, and AqpZ (*29-32*). A first step toward the integration of more complex MPs into polymersomes was made by Choi and Montemagno by the integration of bacteriorhodopsin in the form of purple membranes along with ATP synthase into polymersomes, using the triblock copolymer PEtOz-

PDMS-PEtOz (*33*). The light-driven synthesis of ATP was successfully demonstrated in this multiprotein polymersome system and it was attributed to the biocompatibility of the tested polymer. However, no evidence presented in this study suggested that the observed functionality of ATP synthase was not instead facilitated by the large amount of lipids introduced to the polymersomes in the form of purple membranes. A recent example that clearly demonstrated how the functionality of the environment-sensitive membrane protein was sacrificed for higher overall stability and durability of the artificial system was the one of cytochrome *bo₃* quinol oxidase (*bo₃* oxidase) reconstituted in diblock copolymer PBd-PEO compartments as well as in more complex hybrid PBd–PEO/POPC containers.(*34*) While the *bo₃* oxidase retained most of its activity in hybrid containers featuring high lipid content (50–75%), a staggering 70% reduction of activity was observed in hybrid containers at low lipid content (25%). Furthermore, *bo₃* oxidase reconstituted in pure polymersomes showed no significant activity, hinting at the poor biocompatibility of the PBd–PEO membranes. Nevertheless, this study revealed the high relevance of hybrid lipid/polymer containers to the emerging field of synthetic biology for which the stability and durability of the artificial systems are as important as the high retained functionality of all membrane-embedded components of the system.

In this work, I attempted to take a step away from the commonly used block copolymer-based nanocompartments and explore the ones based on the graft copolymer poly(dimethyl siloxane)-graft-poly(ethylene oxide) (PDMS-*g*-PEO). In aqueous solutions, this polymer self-assembles into stable vesicular structures (*35*) with a reported membrane core thickness of 5 nm (*36*). Because of the polymer membrane thickness similar to the one of a typical lipid bilayer and its high fluidity of 371 cP, (e.g., viscosity of *E. coli* membrane extract is 320 cP and of *E. coli* cells is 1160 cP at 23 °C (*37*)) PDMS-*g*-PEO is a promising substitute for classical lipid membranes. Furthermore, PDMS-*g*-PEO can be mixed with lipids to form hybrid lipid/polymer membranes with the composition-dependent, predictable homogeneous or heterogeneous (phase-separated) distribution of both components in the membranes (*38*). Conveniently, polymer or hybrid vesicles with controlled mean diameters can easily be obtained by successive extrusion (small and large unilamellar vesicles), while larger vesicles (giant unilamellar vesicles), suitable for vesicle characterization, can be produced using the electroformation procedure.

1.3 ENERGY REGENERATION

Whether it is the inception of a new cellular life via cell growth and division or the maintenance of the existing one through sustaining a variety of cellular functions, being biologically alive bears heavy energy cost and thus requires continuous energy regeneration (*39*). While the inception of a new cellular life requires synthesis of the entirety of physical components comprising a daughter cell, it is a one-time expenditure and is generally less costly than maintenance. On the other hand, cell maintenance is a continuous process and the cost of it is increasing with the increasing cell division time (*39*). The universal energy currency that is used for these purposes and can be found in all forms of life is adenosine triphosphate (ATP). A vast majority of the cellular energy demand is most efficiently covered by either converting a large variety of energy-rich substrates into ATP in a process called oxidative phosphorylation, or by converting light (electromagnetic) energy into ATP in a process called photophosphorylation (or photosynthesis).

During the process of phosphorylation, electrons are passed from an electron donor ("fuel") with a more negative redox potential to an electron acceptor (oxygen or others, please see Fig.1) with a more positive redox potential through a series of membrane proteins and electron shuttles with incrementally more positive redox potentials, comprising the electron transport chain (ETC). As the electrons are being passed from one respiratory enzyme to another, protons are translocated across the membrane by at least one of those enzymes and a proton motive force (PMF) is established. This chemiosmotic gradient is driving the synthesis of ATP from ADP and inorganic phosphate, catalysed by ATP synthase. In eukaryotes, this process takes place in highly specialized cellular organelles – mitochondria, and is highly conserved. Energy-rich substrates are generally first converted to NADH and succinate in the Krebs cycle. Next, with the oxidation of NADH to NAD^+ and succinate to fumarate by the respiratory complexes I and II, respectively, the electrons are passed through the ETC and to a final acceptor, molecular oxygen (oxidative phosphorylation). Phosphorylation in prokaryotes, in contrast, is said to be branched, flexibly inducible and modular. Bacteria and archaea express a variety of respiratory enzymes and produce different respiratory chains, which enable them to process different electron donors and acceptors, depending on the environment (Fig. 1).
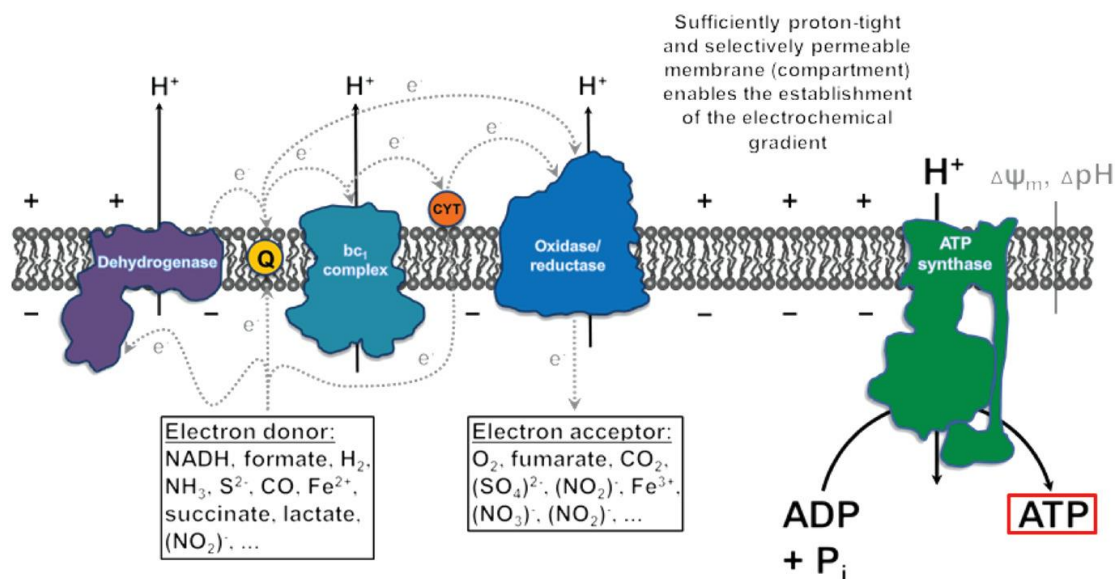
Fig. 1. A schematic representation of phosphorylation in prokaryotes. Electrons are transferred from electron donors to electron acceptors via a series of respiratory enzymes. Electron transfer is coupled with proton translocation across the membrane and the established proton motive force is used to drive ATP synthesis by the ATP synthase. Adapted from (*2*) with permission from Wiley.

These naturally existing energy conversions are valid in the context of bottom-up synthetic biology as well, whereby the proteins and electron shuttles, which constitutes various ETCs can be considered as essential building blocks or functional parts, required to engineer an energy conversion module or organelle. In addition, this machinery should be integrated in a suitable interface (e.g., phospholipid membranes) and should involve some form of compartmentalization to enable the generation of PMF. The explicit questions here are whether and which parts can be omitted and replaced, and what would be the specific process blueprint, tailored with regard to the overall system (e.g., source of energy, coupling with the respective energy sinks, cofactor recycling, closing loops to enable continuous operation, etc.). Additionally, the biological toolbox is already very diverse due to the great heterogeneity of organisms but it can be further extended by introducing fully foreign components, for example of purely chemical origin. This might lead to the optimization of the system functionality and even to the creation of completely new functionalities.

By applying the concept of reductionism to the most efficient natural energy regeneration systems – the ones based on phosphorylation, the essential building blocks necessary for the construction of biomimetic energy regeneration modules can be identified. These are: a proton pump or a PMF generator, ATP synthase and a compartment. Furthermore, the former can be driven by the light or by chemical energy, and on this basis, the energy

modules that they comprise can be divided into light- and chemically-driven. The use of light as a source to produce ATP confers this system several advantages. The harnessing of sunlight essentially taps on a free and unlimited energy source, drawing parallels with photosynthesis and solar cells. Moreover, the light-driven modules can for the most part be considered autonomous and do not require communication with other modules comprising the artificial cell. Because of these factors, they experienced a surge in popularity in recent years and a variety of examples of light-driven energy regeneration constructs were reported on. Most notably, Lee and colleagues (*40*) constructed an elegant photosynthetic organelle comprising two antagonistic light-driven proton pumps, which allow for the dynamic control over ATP synthesis. Berhanu and colleagues (*41*) made additional progress very recently towards autonomous energy regeneration by synthesising the proton pump cell-free. Newly synthesised enzyme was then self-inserted into compartments where it boosted the ATP synthesis and further protein expression. Meanwhile, other alternatives to proton pumping enzymes were explored for the role of PMF generation, such as the employment of photoacids, photobases and others (reviewed in (*2*)).

Meanwhile, chemically-driven regeneration of ATP has been of considerable interest for enzymatic biotechnology and is an integral part of the well-established as well as emerging applications, ranging from synthesis of various high value products to cell-free protein expression. In such applications, ATP is often regenerated from ADP, AMP, adenosine, and polyphosphates, with different kinases, polyphosphate kinases, or crude cell extracts (extensively reviewed in (*42*), see also (*43*)). While these "in bulk" systems may have relevance to bottom-up synthetic biology as well, the main focus of this work are chemically-driven energy regeneration strategies that mimic in nature, the most efficient way of regenerating ATP – oxidative phosphorylation, and involve interfaces and compartmentalization. Such systems not only enable the production of ATP, but also hold a potential for regeneration of important cofactors, such as $NAD(P)^+$, as well as for spatial and temporal separation of otherwise incompatible reaction. Chemically-driven energy modules are generally less autonomous than their light-driven counterparts, since they require constant reducing power driving proton pumps. Nevertheless, this very fact enables coupling of such energy modules with other biomimetic modules, such as synthetic metabolic pathways, via common reducing equivalent in the form of NADH or others.

In the context of oxidative phosphorylation-based chemical-to-ATP conversion, the initial efforts were focused on the reconstitution of minimal electron transport chain. Based on

decades-long research activities of several groups (*44-47*) to characterize building blocks of the ETC (i.e., respiratory enzymes, electron shuttles, such as quinones and cytochromes, as well as cofactors), several minimal energy regeneration devices were constructed by coreconstitution of various proton pumps along with the ATP synthase.

One of the earliest examples of a proton pump combined with the ATP synthase was the cytochrome Qbc (*48*). This protein complex found in thylakoid membranes of chloroplasts and in cyanobacteria catalyses electron cycling around photosystem I as well as linear electron transport between photosystems. In liposomes, successfully coreconstituted complex Qbc stimulated either ATP synthesis or hydrolysis by the generated proton motive force. Furthermore, mutual enzyme stimulation after coreconstitution hinted at potential functional association of these two enzymes.

The pioneering work in bottom-up synthetic biology in the field of energy regeneration, aiming at reconstitution of the entire mitochondrial respiratory chain from purified enzymes, was done by the group of Christoph von Ballmoos at the University of Bern (for a summary of their research, please see (*49*)). In a recent study they investigated functional interplay between the coreconstituted proton pump cytochrome c oxidase or *bo₃* quinol oxidase and the ATP synthase in lipid vesicles (*44*). Such chemiosmotic coupling enabled characterization of the ATP synthesis under steady-state conditions. Remarkable ATP synthesis rates of such bottom-up constructed minimal respiratory chain of 90 ATP s^{-1} ATP synthase^{-1} were achieved. Furthermore, the established module enabled an investigation of a phenomenon known as "mild uncoupling," in which a proton permeability of an inner mitochondrial membrane is being regulated by uncoupling agents. Their work was further expanded by the investigation of lipid composition influence on a functional coupling between a proton pump and the ATP synthase (*50*). The results suggest that a distance between both enzymes in the membrane is influenced by its lipid composition. Enzyme proximity when in high enough densities increased generation of ATP, which further suggests that the proton flow is established along the membrane. This study showcased the importance of interplay between building blocks and its effect on the overall activity of the device.

A slightly different minimal energy regeneration device featured functional coupling between a sodium-driven ATP synthase and the NADH dehydrogenase (Complex I) with sodium-pumping activity (*51*). Coreconstitution of both enzymes confirmed sodium cycling as well as exclusive sodium-pumping activity of studied Complex I. Furthermore, the established sodium gradient was capable of driving ATP synthesis, while in its absence, the ATP synthase

11

was shown to hydrolyse ATP. This example showcased ATP regeneration alongside NAD$^+$ one and as such holds high value for bottom-up synthetic biology.

Finally, Biner and colleagues (*52*) recently made an extraordinary progress towards the construction of the artificial mitochondrion with the assembly of an artificial respiratory chain (ARC) in lipid vesicles. The latter comprised respiratory enzymes complex I, alternative oxidase and the ATP synthase, and was capable of sustained ATP production over several hours, using NADH as a substrate. The constructed energy module was successfully coupled upstream with the two NADH-yielding reactions, as well as downstream to drive the cell-free protein expression.

1.3.1 The artificial respiratory chain and mitochondrion

One of the goals of this work was to construct a chemically-driven energy regeneration module, which can be considered as the artificial respiratory chain (ARC). The energy module featured four essential components (functional parts):

- **Chemically-driven proton pump**, enabling the establishment of PMF,
- **ATP synthase**, harnessing the PMF to phosphorylate ADP into ATP,
- **NADH-dehydrogenase**, enabling the coupling between the energy and metabolic module,
- **Compartment**, enabling functionality of respiratory enzymes and the establishment of PMF.

For a proton pump, respiratory complex IV, cytochrome *bo₃* quinol oxidase (in this work referred to as "*bo₃* oxidase") was selected. The latter comprises four subunits (I–IV) containing two heme (*b* and *o₃*; subunit I) and one copper (Cu$_B$; subunit I) reaction centres, and catalyses 2-electron oxidation of ubiquinol and 4-electron reduction of dioxygen to water. The high affinity ubiquinone binding size (Q$_H$) was reported (*45*) to be located on the transmembrane region of subunit I of this enzyme. Due to this distinct position of a substrate binding site, *bo₃* oxidase, when reconstituted in vesicles, can be conveniently activated via the external ubiquinone addition regardless of the orientation of enzyme in the membrane (*44*). In contrast, this is not the case in another very similar and more commonly used oxidase, cytochrome c oxidase, featuring distal (with respect to the membrane) cytochrome c binding site, which is only externally accessible when the reconstituted enzyme (oxygen-reducing site) is facing inwards (*53*). Therefore, in order to activate the outwards-facing enzyme, prior membrane permeabilization is required (*44, 54*). *bo₃* oxidase was previously combined with the *E. coli*

ATP synthase by von Ballmoos and colleagues (*44*) in order to form a short respiratory chain ("SRC", Fig. 2). This minimal OXPHOS assembly was adapted in this work and it served as a basis for further ARC construction and stabilization as well as a benchmark system in various activity determinations. Furthermore, two variants of NADH-dehydrogenase were explored within the framework of this thesis. The first one was a fungal respiratory complex I isolated from *Yarrowia lipolytica*. This enzyme exhibiting a molecular mass of almost 1 MDa is consisting of at least 38 subunits and is considered amongst the largest and most complex (*55*). The enzyme-bound flavin mononucleotide (51 kDa subunit, (*56*)) catalyses the two-electron oxidation of NADH. The electrons are then passed through a series of FeS clusters to a final acceptor, ubiquinone, which is bound at the active centre located on the connecting fragment (IP), subunit 49 kDa. Complex I is a type 1 NADH dehydrogenase capable of proton translocation (whereby this action is proposed to be decoupled from the electron transfer, unlike in bo_3 oxidase; (*55*)) and in this work it was employed as a secondary proton pump. The second variant of NADH dehydrogenase explored in this work was the DT-diaphorase (NQO1). This much smaller and simpler enzyme has a molecular mass of 32 kDa and it consists of two identical subunits (*57*). Similar to complex I, it catalyses 2-electron oxidation of NAD(P)H (by the bound flavin adenine dinucleotide, final acceptor is ubiquinone). Unlike complex I, this type 2 NADH dehydrogenase it is not a proton pump. In fact, this enzyme is not membrane-associated and oppose to the complex I, the membrane-insertion is not required. This feature was exploited in this work to enable coupling between the energy and metabolic module without altering the activity of the short respiratory chain (SRC). When the latter was expanded by the addition of the complex I, the resulting ARC was denoted as the ARC 1. On the other hand, in the case where the ARC was expanded with the DT-diaphorase, the resulting ARC was denoted as the ARC 2 (Fig. 2). Finally, via the coupling between the energy and metabolic module, the construction of the minimal energy regeneration organelle – the minimal artificial mitochondrion – was envisioned. The latter was intended to be in future works enveloped in the outer compartment functionalized with substrate/product transporters and this fully formed organelle is referred to as the artificial mitochondrion. For the mentioned coupling, the so-called CETCH cycle (*58*) was selected as a model metabolic module. The CETCH is a reaction network comprising 17 enzymes (some are engineered), from 9 different organisms that is capable of continuous CO_2 fixation in vitro. Although most frequently, simple metabolic conversions are used to study coupling between different modules (*59*), the CETCH cycle offered an unprecedented opportunity to study the functionality of the energy module in a complex, cell-like environment. In this context, the effects of crowding on the output of ARC

could potentially be examined, along with the potential interactions between the CETCH enzymes and the ARC. Only just recently, the CETCH was coupled with the isolated photosynthetic membranes, which served as the energy module (*60*). Nevertheless, through the coupling between the CETCH and the ARC, the interactions between the two fully bottom-up constructed modules can be studied.
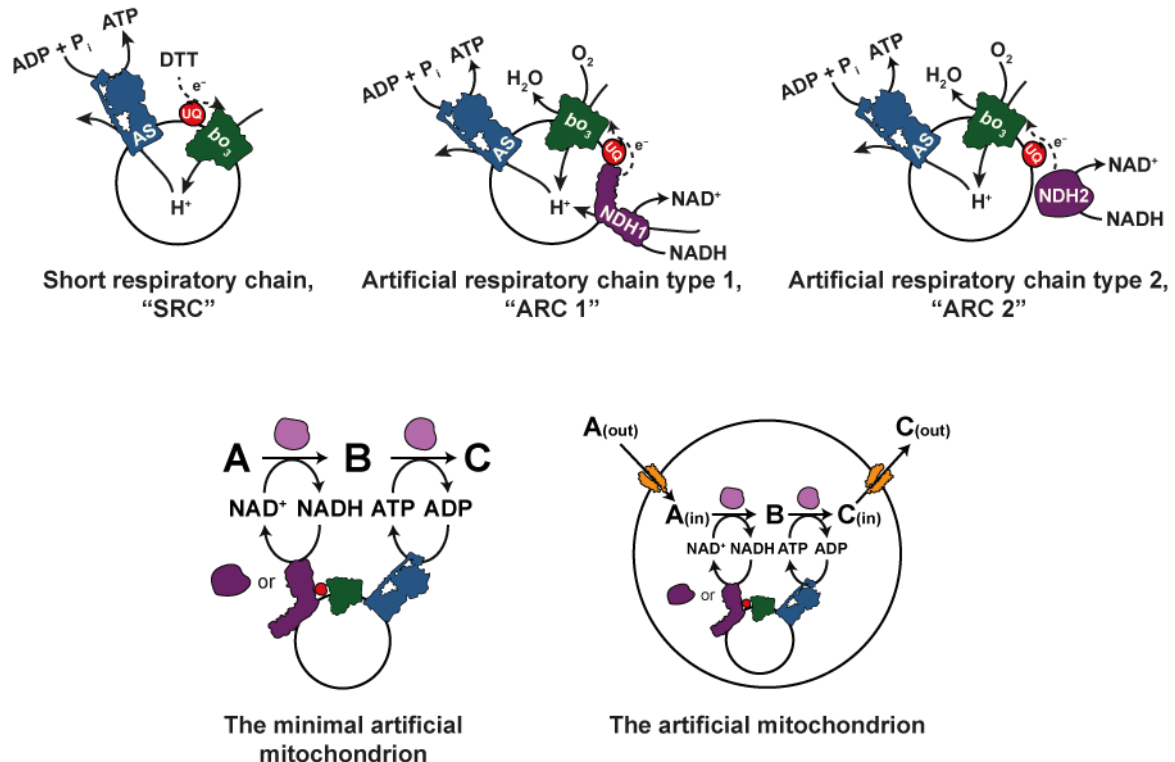
Fig. 2. Synthetic constructs employed in this work and the related terminology. By fully exploiting the concept of bottom-up SynBio, structures of increasing complexity can be build via sequential integration of functional parts. In this respect, artificial respiratory chains of different complexity were engineered. The short respiratory chain comprising *bo₃* oxidase (*bo₃*), ubiquinone (UQ) and ATP synthase (AS) inserted in different type of compartments could be expanded by either complex I (type 1 NADH dehydrogenase, NDH1) or DT-diaphorase (type 2 NADH dehydrogenase, NDH2) to form the ARC 1 and ARC 2, respectively. These respiratory chains could further be combined with the metabolic module (depicted with the conversion steps A, B and C with the related enzymes) to form and energy regeneration organelle, the minimal artificial mitochondrion. The final construction step would be the encapsulation of the latter in an outer compartment functionalized with the substrate/product transporters, thus assembling the fully-formed artificial mitochondrion.

14

1.3.2   Insertion of membrane proteins into compartments

Respiratory enzymes employed in this work were extracted from their native membranes and stabilized in detergent micelles to reduce their activity loss and decomposition. In order to restore their functionality and facilitate the coupling between them, their insertion into preformed compartments had to be accomplished. To this end, different detergents were used to mediate the protein insertion, and to optimize the reconstitution procedure, the strategy developed by the group of Jean-Louis Rigaud (*61-64*) and further improved by the group of Christoph von Ballmoos (*44, 54*) was followed. This strategy is based on the idea that the reconstitution procedure represents the reverse order of the protein extraction. In this context, preformed compartments (vesicles) are first supplemented with detergents through the entire range that causes the transformation of lamellar vesicles into mixed micelles. The protein of choice (or the combination of the several of thereof) is then added to the vesicle-detergent mixture, and its incorporation can be readily studied in each step of the lamellar to micellar transition after the detergent removal (*65*).

To evaluate the degree of vesicle solubilization upon the detergent addition, optical density of the vesicle suspension is monitored (most commonly at 540 or 600 nm) as a function of detergent concentration (*34, 62, 63, 66*). The solubilization process can be described by a three-stage model, also known as the equilibrium partition model (*67-69*), and can be quantitively visualized via changes in optical density of the lipid-detergent suspensions (Fig. 3). In the first stage, the detergent partitions into the lipid bilayer of liposomes until the membrane saturation point (R_{sat}) is reached. During this stage, detergent addition to preformed vesicles does not disrupt their integrity and only slight changes in turbidity can be seen, depending on the type of used detergent and lipids. During the second stage, detergent-saturated vesicles are disrupted and gradually dissolved into lipid-detergent mixed micelles, which can be observed as a significant decrease in optical density. The third and final stage is characterized by the complete solubilization of all vesicles into lipid-detergent mixed micelles and the suspension becomes optically transparent. The point at which all vesicles are dissolved is denoted as the total solubilization point (R_{sol}).
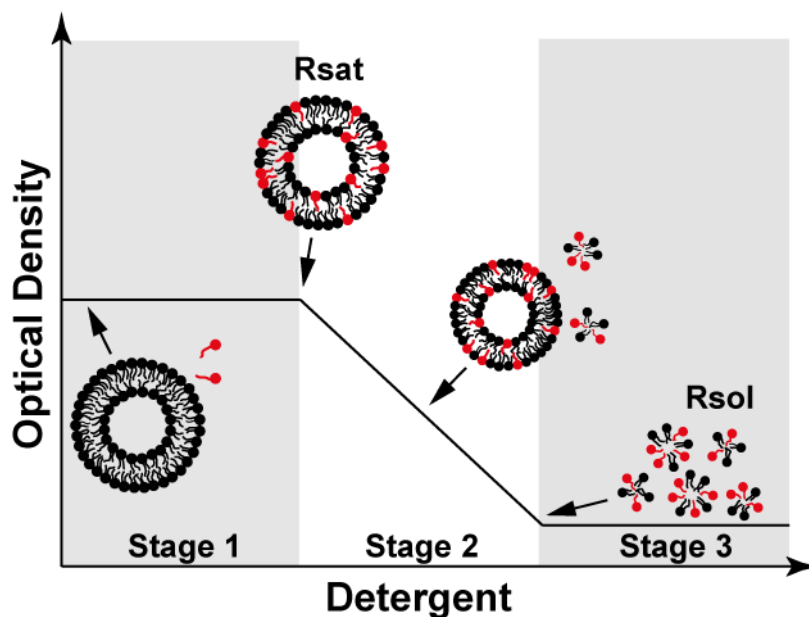
Fig. 3. Solubilization of vesicles with detergent. Indicated are the three stages of liposome solubilization with detergent. In the first stage, detergent (red) is partitioning in lipid bilayers until the point of membrane saturation (also denoted as the "onset solubilization") point (R_{sat}) is reached. During the second stage lipids (black) are leeched from vesicles into lipid-detergent mixed micelles. This continues until the vesicles are completely dissolved (R_{sol}) and lipid is contained entirely in mixed micelles. Redrawn based on the concept depicted in (*63*).

A similar progression of polymersome solubilization by detergents to the progression described above for liposomes was previously observed, although the first stage was absent in some of these systems, depending on the detergent of choice (*34, 70-72*). Two of such examples are solubilization of poly(butadiene)-poly(ethylene oxide) (PBd-PEO) vesicles with dodecyl maltoside (DDM) and Triton X-100 (TTX) by Rottet and colleagues (*71*) as well as solubilization of poly(ethyl ethylene)-poly(ethylene oxide) (referred to by authors as EO-EE) vesicles with TTX according to a report by Pata and colleagues (*71*). Interestingly, in contrast to the report by Rottet et al., Khan and colleagues (*34*) described different progression of solubilization of PBd-PEO vesicles with TTX, although in the case of the first report, a degree of polymerization was not specified and the observed differences could have originated in different polymer structure. Furthermore, it appears that the first solubilization state specified above was also missing in the cases where polymer was combined with lipids or another type of polymer to form hybrid vesicles (*34, 72*).

Finally, a variety of different detergents were reported to successfully mediate the insertion of membrane proteins. However, only few can be seen consistently aiding in protein reconstitutions that result in high retained activity of the inserted enzyme. By examining the

protein reconstitution reports, the selection of detergents tested in this work was narrowed to octyl glycoside, Triton X-100, sodium cholate, sodium deoxycholate and dodecyl maltoside (*44, 63, 64, 73, 74*). With the exception of sodium cholate, which efficiently mediated protein insertion when the enzyme was added during second stage of solubilization (*64*), all other listed detergents were most efficient at either R_{sat} or R_{sol}. Therefore, the reconstitution of the artificial respiratory chain was in this work analysed mostly with respect to the latter two points, although some examples of reconstitutions with sodium cholate during the second solubilization stage are also included.

1.4 FUSION AS A TOOL FOR SYSTEM INTEGRATION

The artificial respiratory chain and mitochondrion are synthetic construct featuring amphiphilic membranes as an essential component, which were functionalized with respiratory enzymes. In the final design of the artificial cell as envision by the MaxSynBio, replacement and repair mechanisms were not considered as a vital process of life and were excluded from the cell entirely. Therefore, the potential avenues for the restoration of the faulty membrane-bound synthetic constructs were explored in this work. In this context, the means of the potential module/system expansion were investigated. Ideally, an appropriate method of choice would not only allow for new enzymes to be added to the existing protein-functionalized compartments, but would also allow for the merger of the latter in order to form higher hierarchical units. All these criteria could be meet by employing membrane fusion as a tool for systems assembly and editing. Membrane fusion, one of the most fundamental processes in life, occurs when two separate membranes of adjacent vesicles or cells merge into a single continuous layer to form a larger fused cell or a vesicle (*75*). Both, in vivo and in vitro is usually induced by external agents called fusogens. While the most common fusogens are large molecules like proteins and peptides (protein-mediated fusion), a wide variety of different types of agents are able to mediate fusion of protein-free lipid bilayers by overcoming hydration and electrostatic forces. The exact mechanism (i.e., the way a fusogenic agent will induce the fusion process) of membrane fusion varies depending on the nature of the fusogen and the membrane (*76*). Taking into account the inherent fragile and sensitive nature of synthetic constructs (in particular membrane proteins) and the relatively low efficiency of a large portion of available fusogens, two fusion mediators were considered viable within the scope of this work – charged lipids and soluble N-ethylmaleimide-sensitive factor attachment protein receptor proteins (SNAREs). Charge-mediated fusion would require supplementation of compartments with a

fraction of charge lipids. These were previously reported to modulate (potentially inhibit) the activity of several membrane proteins (*77-79*) and are known to effect the enzyme insertion as well as the coupling between enzymes (*50, 80*). Furthermore, the utilization of membrane charge as a fusion mediator would require spiking of polymer compartments with charged lipids, which would decrease the overall stability of the system. For these reasons, SNAREs were selected as the assembly tool and were employed in the construction of the energy module.

SNAREs are the intracellular membrane fusion machinery driving the formation, assembly and maintenance of life as we know it. They are involved in a variety of processes, such as fertilization, cell transport, trafficking and growth, among others (*81*). Used in this work was a minimal SNARE fusion machinery, the so-called SNARE core complex (*82-84*) – full-length synaptobrevin (syb) and the acceptor complex comprising syntaxin, SNAP-25, and a C-terminal syb fragment (referred to as "ΔN complex") Fig. 4A. This ΔN complex is structured in such a way so that the synaptobrevin binding to free site at the N-terminus is accelerated, resulting in faster fusion as well as preventing the formation of dead-end 2:1 syntaxin:SNAP-25 complexes (*85, 86*). Through the zippering motion between the syb and the ΔN complex in the direction from the membrane distal N-terminus to membrane proximal C-terminus, fusing membranes are pulled into close proximity. The mechanic forced produced by SNAREs is used to overcome electrostatic repulsion arising from the charged membrane species, as well as hydration forces at around 2 nm distance (*87*). Several models were proposed to describe the mixing between the fusing membranes, whereby a stalk model developed by the group of Michael Kozlov (*88*) is the most widely accepted as plausible. According to the stalk hypothesis (Fig. 4B), the fusion is initiated via point-like membrane protrusion, which is then transformed into a stalk-shaped connection between two fusing monolayers. The stalk can then either expand further to form hemifusion diaphragm that transitions into fusion pore, or the stalk can be transformed directly into fusion pore. Finally, after the pore expansion, contents of the two fusing vesicles are combined into a single compartment. SNAREs were previously used as the assembly tool by Nordlund and colleagues (*54*), where they were used to reconstruct a fully functional bacterial respiratory chain, as well as to incorporate ATP synthase into native bacterial membranes which lacked this component.
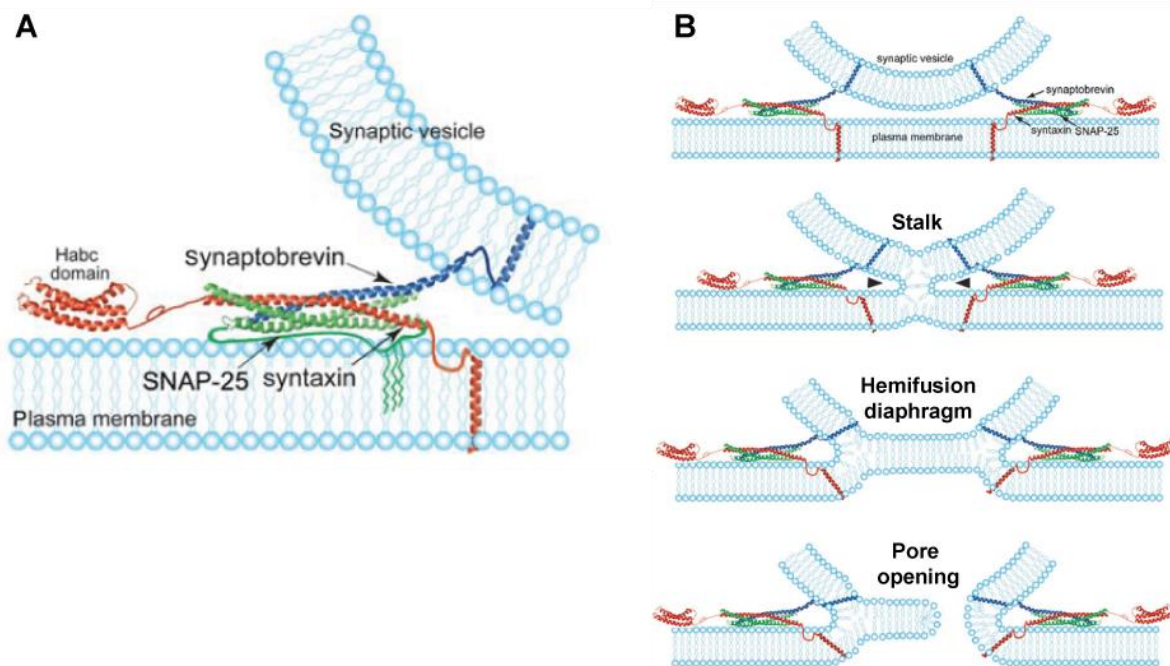
Fig. 4. SNARE-mediated membrane fusion. (**A**) Core fusion complex comprising synaptobrevin, SNAP-25 and syntaxin was used to form vesicles. In the truncated syntaxin used in this study, the Habc domain was removed. Truncated synaptobrevin fragment was attached to the syntaxin/SNAP-25 complex to promote rapid association with synaptobrevin. (**B**) SNARE-mediated fusion progression. The zippering action of SNAREs is used to exert the force required to bring the two fusing vesicles into close proximity. Then, a contact between the membranes is established, which develops into a stalk. The latter can then be transformed into a hemifusion diaphragm and finally into a pore, or a pore can be opened directly after the stalk formation. Adapted from (*89*) with the permission from Springer Nature.

The SNAREs were prior to this work never used to fuse polymer or hybrid membranes. In fact, only a handful of examples of the successful fusion of polymersomes can be found throughout the existing literature (*90-95*), whereby complete fusion (with content mixing) was to a sufficient degree demonstrated by Zhou and colleges (*95*) as well as Varlas and colleges (*90*). This is likely due to the robustness of this type of vesicles, in which the increased membrane thickness and bending stiffness has an antagonistic effect on fusion. Nevertheless, with the membrane thickness similar to natural membranes and considering the high fluidity of PDMS-*g*-PEO membranes, I hypothesized that the latter could potentially be fused via SNAREs and this hypothesis was tested in this work. Furthermore, I was aiming at evaluating the potential fusion intermediates, which would shed light onto the fusion progression in the context of polymer monolayers.

1.5 AIMS OF THIS WORK

In the context of the construction of a synthetic cell, currently the biggest challenges lie in defining which functions and how many of thereof should be mimicked for the cell to be considered as "living", and, furthermore, in defining the principles guiding the construction. What is very clear even at this stage, however, is that biomimetic life, much like its natural counterpart, is highly energy demanding. Therefore, a versatile energy regeneration module, which would enable continuous supply of adenosine triphosphate (ATP) and, potentially, other important co-factors, such as NAD^+, is highly sought after. Through means other than the aforementioned ATP-dependence, such module would ideally allow for integration with other life processes-mimicking modules, in particular with various metabolic conversions, where energy-rich side-products would be converted to ATP and the utilization of a sacrificial donor would therefore be avoided. Nevertheless, it is expected that the usefulness of such energy regeneration module would not be restricted only to the confines of synthetic biology. Tailored and controlled means of ATP regeneration are expected to have a large impact on other ATP-dependent applications, such as metabolic engineering and synthesis, as well as on a cell-free protein expression.

The main objective of this work was to construct chemically-driven energy regeneration module of sufficiently high energy output that would enable coupling with other energy-demanding constituents of the artificial cell. With respect to this, the CETCH cycle, a metabolic network comprising 17 enzymes from 9 different organisms was selected as a model metabolic conversion module the energy requirements of which were attempted to be met. Compositionally, the proposed energy module can be considered as an artificial respiratory chain (ARC) and in lines with the principle "keeping the essentials only" that was guiding its design, several functional parts were identified as crucial for its construction. The first and the most important one was the ATP synthase – a proton-driven rotary motor that catalyzed the formation of ATP from ADP and inorganic phosphate. The second one was a proton pump, which would establish a proton gradient used to drive the ATP synthesis – *bo₃* quinol oxidase (hereby referred to as "*bo₃* oxidase"). The third one was the NADH dehydrogenase, a connecting point between the metabolism and energy regeneration through which the electrons harnessed from the metabolites were fed to the ARC. The dehydrogenase was coupled with the proton pump via the fourth essential component – the electron shuttle. In the present case, this role was assumed by synthetic ubiquinone-1 (in figures referred to as "UQ"). Finally, a proton gradient could not have been established without the proton-tight compartment, a container in

which all other part could be integrated so that their function was enabled. Through the integration of the energy module and the metabolic cascade, an artificial organelle – the minimal artificial mitochondrion – could be formed.

The main objectives along with the secondary ones tackled in this work are listed below.

Construction of the artificial mitochondrion:

- o Construction and characterization of the ARC as the chemically-driven energy regeneration module.
- o Evaluation of the ARC activity under the condition relevant for the coupling between the energy and metabolic module (increased osmolarity, freezing/thawing, etc.).
- o Achieving coupling between the ARC and CETCH towards the formation of the minimal artificial mitochondrion.
- o Addressing the increased membrane permeability due to enzyme insertion.
- o Exploring avenues for enabling oxygen supply to energy modules.

Stabilization of the energy module:

- o Substitution of lipid compartments with polymer or lipid/polymer hybrid ones, and the related protein insertion in these compartments.
- o Evaluation and optimization of enzyme insertion in different types of compartments.
- o Functional and structural analysis of polymer-based compartments.
- o Characterization of the interplay between different compartments and the inserted respiratory enzymes.
- o Examination of the protective function of polymer with respect to oxidative damage.

Development of tools for the integration of functional modules and systems.

- o Examination module/systems integration via SNARE-mediated fusion.
- o Insertion of SNAREs into polymer-based compartments and characterization of the formed proteovesicles.
- o Analysis of SNAREs-mediated lipid and content mixing.
- o Analysis of pore opening and expansion in polymer-based compartments.
- o Examination of fusion intermediates of SNAREs-mediated fusion of polymer and hybrid compartments.
- o Establishment of versatile and biocompatible fusion platformed based on SNAREs.

1.6 STRUCTURE OF THE THESIS

To enable convenient navigation through this work, its contents are shortly summarized, below.

The assembly steps of the artificial mitochondrion are depicted in Fig. 5 and can be divided into four stages. During the first stage, parts comprising the organelle were isolated and purified. In parallel, compartments were formed from different amphiphiles and functionalized with the isolated parts (Fig. 5, Stage 1). Furthermore, several functional parts could be combined to form functional modules (Fig. 5, Stage 2). Since in, at the time, the current version of the artificial cell functional parts and modules could not be replaced or repaired, my next objective was to increase their stability and durability. Towards this end, lipid compartments were substituted for the ones made of graft co-polymer (polymersomes) or the ones in which said polymer was mixed with lipids to form hybrid vesicles. The reconstitution procedure was devised, which enabled simultaneous insertion of several enzymes comprising the ARC in the mentioned polymer-based compartments, and the enzyme activity was determined. The interplay between the respiratory enzymes and the man-made membranes was analyzed in greater detail. With respect to this, the membranes of proteopolymersomes and proteohybrids were inspected for the structural rearrangements and changes in permeability following the enzyme insertion, as well as for their interactions with detergents mediating protein reconstitution. Meanwhile, the enzyme insertion was examined extensively in lipid, hybrid and polymer compartments. In this context, the orientation and reconstitution efficiency were determined for each individual enzyme in every compartment type while inserted with several tested detergents. The final output of the energy module was then analyzed in the light of these reconstitution parameters. Finally, the protective function of the graft copolymer against reactive oxygen species (ROS) was assessed with respect to the preserved enzymatic activity as well as structural integrity of the compartments. All of the above-mentioned efforts can be found described and discussed in Chapter 3.1.

Since it was found that the optimal protein insertion can be achieved in single enzyme reconstitutions but not when several enzymes were reconstituted at once, means of module/system assembly alternative to protein co-reconstitution were explored. With respect to this, synaptic fusion machinery comprising SNAP receptor proteins ("SNAREs") was integrated in polymer and hybrid compartments and the minimal respiratory chain was assembled via SNARE-mediated fusion. The described fusion platform was examined for the

membrane and content mixing efficiency and, similar to the insertion of respiratory enzymes, the orientation and reconstitution efficiency of SNAREs in hybrids and polymersomes was analyzed. For the first time, fusion intermediates of the SNARE-mediated fusion of artificial membranes were described, and the fusion progression was discussed in the context of the measured pore opening dynamics as well as bending rigidity and surface charge of the membranes. SNAREs as a tool for system integration are described and discussed in Chapter 3.2.

The final goal was to couple the most active variant of the ARC with the CETCH cycle to form the basis of the artificial mitochondrion (Fig. 5, Stage 3). To achieve this, different NADH dehydrogenases were tested with the aim of introducing another proton pump to the module, thus increasing its efficiency. Membrane tightness was imperative for the establishment of proton gradient, used to drive ATP synthesis by the energy module. Therefore, increased membrane permeability, as a result of imperfect protein insertion, was tackled with the polymer-assisted membrane resealing and through other means. Furthermore, the activity of the ARC was evaluated under the operational conditions of the metabolic network and the energy module underwent the appropriate tunning, which enabled the coupling with the CETCH. Lastly, the functionality of the coupled system was assessed and an auxiliary oxygen supply system was developed to address its shortcomings. In this role, the oxygen release from the calcium peroxide particles was analyzed and the effect of particles on the activity of the ARC was evaluated. The respiratory tissue was proposed, which combines the essentials for continuous, versatile and efficient energy regeneration. The report on the coupling between the metabolic and energy module with the related above-mentioned objectives can be found in Chapter 3.3.

Finally, the step-wise construction of the artificial mitochondrion was envisioned carried out in a microfluidics setup. That is why in Fig. 5, the assembly progression is depicted as if taking place in different parts of the microfluidic channels. Unfortunately, the microfluidics were not used in this work. Nevertheless, with the currently available and rapidly improving technology (related to most importantly cell-free protein expression and microfluidics chip design), I find it very likely that the entire construction procedure could be carried out from start to finish in microfluidics, thus streamlining the artificial organelle/cell construction.
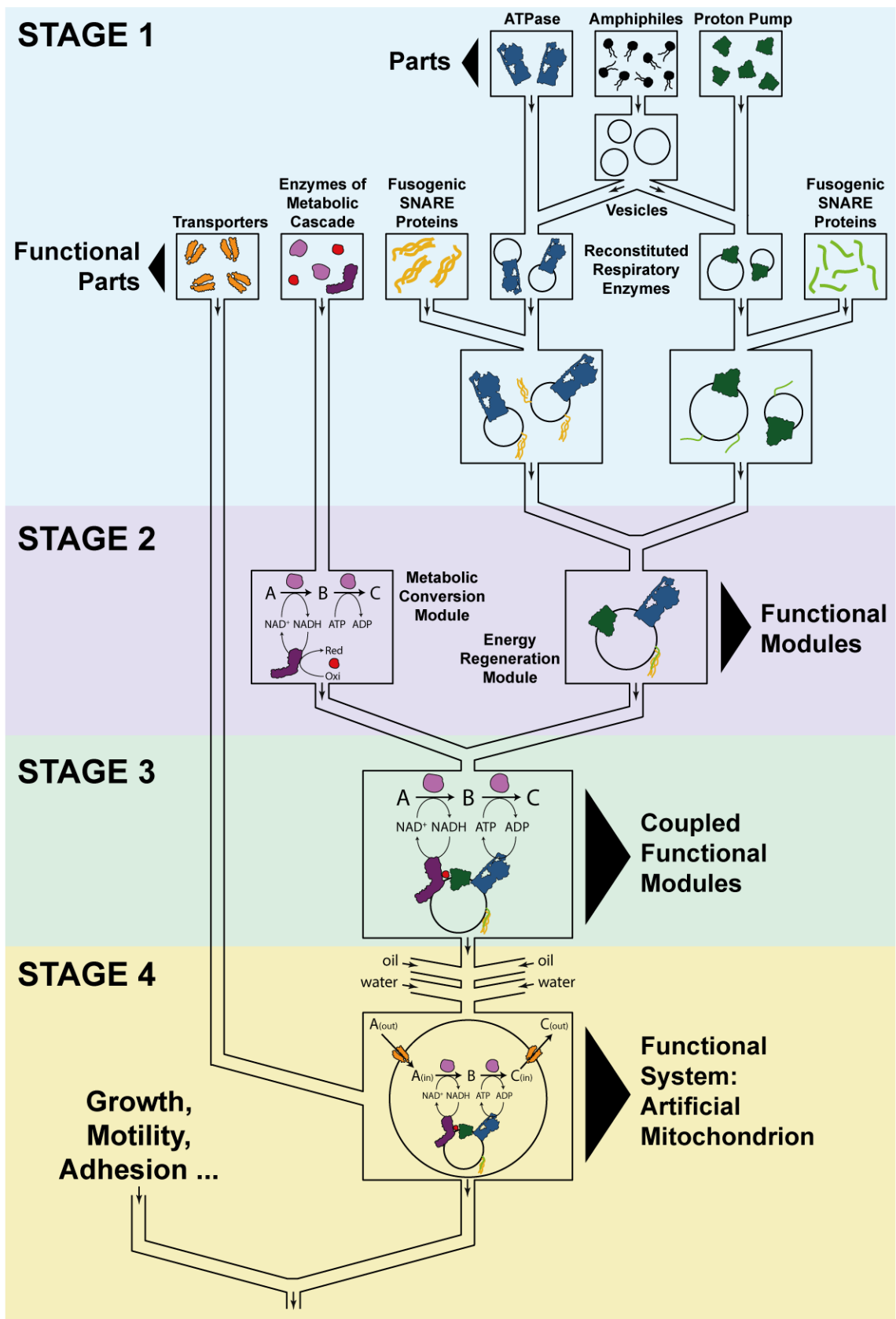
Fig. 5. Step-wise bottom-up construction of the artificial mitochondrion. Depicted are the four stages of the construction, as envisioned taking place in the microfluidics setup. The products of each assembly stage are indicated

2 MATERIALS AND METHODS

Chapters 2.1.1, 2.1.2, 2.1.4, 2.3.3 and 2.4.1–2.4.8 were reprinted (adapted) from L. Otrin et al., En route to dynamic life processes by SNARE-mediated fusion of polymer and hybrid membranes. *Nature Communications* 12, 4972 (2021) (*96*), licensed under CC BY 4.0 (https://creativecommons.org).

Chapters 2.3.4, 2.3.5, 2.3.13, 2.5.1, 2.5.3 and 2.5.8 were reprinted (adapted) with permission from L. Otrin et al., Toward Artificial Mitochondrion: Mimicking Oxidative Phosphorylation in Polymer and Hybrid Membranes. *Nano Letters* 17, 6816 (2017) (*1*). Copyright 2017, American Chemical Society.

Chapters 2.3.5, 2.3.7–2.3.10, 2.5.4 were reprinted (adapted) from N. Marušič, L. Otrin et al., Constructing artificial respiratory chain in polymer compartments: Insights into the interplay between *bo₃* oxidase and the membrane. *Proceedings of the National Academy of Sciences* 117, 15006 (2020) (*97*), licensed under CC BY 4.0 (https://creativecommons.org).

2.1 ENZYME PURIFICATION

2.1.1 Purification of ATP synthase

The *E. coli* F_1F_O ATP synthase was overexpressed in *E. coli* strain DK8(ΔuncBEFHAGDC and purified with the Ni^{2+}-NTA affinity chromatography (HisTrap FF crude, Cytiva, 11000458) as described previously (*98*) in the presence of octyl glucoside (Glycon Biochemicals, D97001-C), Na-deoxycholate (Merck, 302-95-4: 30970) and sodium Na-cholate (Merck, 206986-87-0: C6445). Following purification, the enzyme was flash-frozen in liquid nitrogen and stored at −80 °C. Enzyme concentration was determined with Specord 50 Plus spectrophotometer (Analytik Jena) using the previously determined extinction coefficient of 340000 M^{-1} cm^{-1} (*99*). Plasmid containing the sequence of His-tagged ATPase as well as the expression culture were kindly gifted by Prof. von Ballmoos, University of Bern.

2.1.2 Purification of *bo₃* quinol oxidase

The *E. coli bo₃* quinol oxidase cloned in plasmid pETcyo was overexpressed in *E. coli* strain C43(DE3)(ΔcyoABCDE) and purified as described by (*100*) in the presence of dodecyl maltoside (Merck, 69227-93-6: D4641), using affinity chromatography (HisTrap FF crude, Cytiva, 17528601). After the purification, enzyme was concentrated using Amicon Ultra-0.5 Centrifugal Filter Units with a nominal molecular weight limit (NMWL) of 100 kDa (Merck,

UFC510024). Concentrated enzyme was flash-frozen in liquid nitrogen and stored at −80 °C. Enzyme concentration was determined in 50 mM HEPES pH 8.0, 0.05 % (w/v) dodecyl maltoside, from the dithionite reduced minus oxidized α band of the enzyme (*101, 102*). Plasmid containing the sequence of His-tagged bo_3 quinol oxidase as well as the related expression culture were kindly gifted by Prof. von Ballmoos, University of Bern.

2.1.3   Purification of formate dehydrogenase

The *Mycobacterium vaccae* formate dehydrogenase sequence containing D221A mutation (*103*), which allowed for enzyme to accept $NADP^+$ as a substrate, was cloned into plasmid pET-21a(+)-*fdh* D221G generated previously (*104*) and overexpressed in *E. coli* strain BL21(DE3). The enzyme was purified via Ni^{2+}-NTA affinity chromatography (HisTrap FF crude, Cytiva, 17528601), eluted in 20 mM Tris-HCl pH 8.1, 500 mM NaCl and 500 mM imidazole (Merck, 288-32-4: 56749), and afterwards desalted with HiTrap desalting columns (Cytiva, 11000329) in 20 mM Tris-HCl pH 8.1, 200 mM NaCl. Eluted fractions were concentrated with Amicon Ultra-4 centrifugal filter units (Merck, UFC803024) with a NMWL of 30 kDa, supplemented with 20 % glycerol (Merck, 56-81-5: G5516), flesh-frozen in liquid nitrogen and stored at −80 °C. Enzyme concentration was determined on a Nanodrop 2000 (Thermo Scientific, ND-2000) using the calculated extinction coefficient of 58710 M^{-1} cm^{-1}. Plasmid containing the sequence of formate dehydrogenase was kindly provided by Prof. Erb, Philipps University of Marburg.

2.1.4   Purification of SNAREs

Syntaxin-1A (183-288) (*105*), synaptobrevin-2 (1-116) (*106*), SNAP-25a (1-206) (*82*) and truncated synaptobrevin-2 (49-96) (*85*), all originating from *Rattus norvegicus* were overexpressed in *E. coli* strain BL21(DE3) and purified with the combination of Ni^{2+}-NTA affinity (HisTrap FF crude, Cytiva, 17528601) followed by ion-exchange chromatography (Mono S 5/50 GL, Merck, GE17-5168-01 for the full-length and truncated synaptobrevin and Resource Q, Cytiva, 17-1179-01, for SNAP-25 and syntaxin) on Äkta system (GE Healthcare), as described previously (*107, 108*). All proteins with the exception of truncated synaptobrevin-2 were purified in the presence of stabilizing detergents Na-cholate (Merck, 206986-87-0: C6445) and CHAPS (Merck, 331717-45-4: C5070). An artificial SNARE acceptor complex (the "ΔN complex") comprising truncated synaptobrevin-2, syntaxin-1A and SNAP-25a was preassembled as described previously (*85, 86*) by mixing mentioned constituent at the 1.5:1:1 molar ratio, respectively. Peptide mixture was incubated at 4 °C overnight and purified on the

following day by ion-exchange chromatography (POROS HQ, Thermo Scientific, 4481315) in the presence of CHAPS. This ΔN complex is structured in such a way so that the synaptobrevin binding to free site at the N-terminus is accelerated, resulted in faster fusion as well as preventing the formation of dead-end 2:1 syntaxin:SNAP-25 complexes (*85, 86*). The concentration of synaptobrevin-2 and the ΔN complex was determined on Nanodrop 2000 using the calculated extinction coefficients of 13980 and 24325 $M^{-1}\,cm^{-1}$, respectively, or by using Pierce 660 nm protein assay kit (Thermo Scientific, 22660) in combination with spectrophotometer Synergy HT (Biotek). All mentioned constructs as well as the expression cultures were kindly gifted by collaboration partner Prof. Jahn, the Georg August University of Göttingen

2.1.5   Purification of complex I

Fungal complex I from *Yarrowia lipolytica* was a kind gift from Prof. Volker Zickermann, Goethe University Medical School. The enzyme was purified by Dr. Kristian Parey using the protocol, briefly described below.

Mitochondrial membranes from *Yarrowia lipolytica* WT strain (GB30) were isolated as described previously (*109*) and resuspended in 20 mM Na-borate (pH 7.9), 50 mM NaCl and 1.5 mM PMSF. Complex I was solubilized with dodecyl maltoside as detailed in (*110*), via step-wise addition of detergent to the membranes stirred on ice to a detergent-to-protein ratio of 1 g : 1 g. The enzyme was purified on the Ni-NTA Sepharose column (Bio-Rad) and eluted in 20 mM Na-phosphate (pH 7.2), 140 mM imidazole, 400 mM NaCl, 0.025% lauryl maltose neopentyl glycol (LMNG). The eluted enzyme was concentrated using Centriped centrifugal filter devices (Millipore), desalted on the TSK G4000SW column (TosoH Bioscience) and separated by size exclusion chromatography on an ÄKTA purifier chromatography system (GE Healthcare). Peak fractions were concentrated using spin devices (Vivaspin, 100,000 MWCO, Sartorius) and stored in 20 mM Tris/HCl (pH 7.2), 100 mM NaCl, 1 mM EDTA and 0.025% LMNG, at −80 °C.

2.2 LABELLING OF ENZYMES AND POLYMER

2.2.1   Labelling of *bo₃* oxidase with ATTO 514 (lipid and polymer partitioning experiments)

Deprotonated amino groups of *bo₃* oxidase were labelled with fluorescent dye ATTO 514 N-hydroxysuccinimidyl(NHS)-ester (Merck, 67455), as described in (*97*). Briefly, first,

the enzyme was dissolved in 20 mM HEPES, containing 0.05 % DDM, at 2.2 mg ml^{-1} and at pH = 8.2, at which high enough concentration of unprotonated and thus reactive amino groups was ensured. To enzyme, ATTO 514 dye, dissolved at 2 mg ml^{-1} in anhydrous DMSO (Merck, 67-68-5: 276855) was added at eightfold molar excess and the reaction mixture was incubated for 1.5 h at room temperature, protected from light, under agitation (250 RPM). Afterwards, the unbound dye was removed from the conjugate solution via size exclusion chromatography, on a column (internal diameter of 1.5 cm and length of 20 cm) filled with Sephadex G-25 resin, equilibrated with 20 mM HEPES (pH = 7.5), containing 0.05 % DDM. The degree of labelling (DOL), i.e., the average number of dye molecules coupled to enzyme molecule, was determined via absorption spectroscopy, using the equation provided by the manufacturer:

$$DOL = \frac{A\text{max} \times \varepsilon\text{prot}}{(A280 - A\text{max} \times CF280) \times \varepsilon\text{max}}$$
(Eq. 1)

In the above relationship, A_{max} is the absorbance of ATTO dye at the absorption maximum λ_{abs} (for ATTO 514 λ_{abs} = 511 nm), ε_{prot} is the molar extinction coefficient of bo_3 oxidase (calculated value of ε_{bo3} = 184720 M^{-1} cm^{-1}, for the denatured enzyme), A_{280} is the absorbance of ATTO 514 at the absorption maximum of proteins (280 nm), CF_{280} is the correction factor for dye specified by the manufacturer ($CF_{280\ (ATTO\ 515)}$ = 0.07) and ε_{max} is the extinction coefficient of dye at the absorption maximum λ_{abs} (ε_{max} = 115000 M^{-1} cm^{-1}). The DOL was determined to be 1.7 molecules of dye per enzyme.

2.2.2 Labelling of bo_3 oxidase with ATTO 488 (orientation determination of reconstituted enzyme)

Fluorescent dye ATTO 488 Nα,Nα-bis(carboxymethyl)-L-lysine, Nickel(II) complex (NTA) (Merck, 39625-250UG-F) was attached to His-tag of bo_3 oxidase. To 0.439 mg (3 nmol) of enzyme dissolved in 20 mM HEPES, pH 7.5, 200 mM KCl, 200 mM imidazole, 0.05% (w/v) DDM, ATTO 488, dissolved in HEPES, pH 7.5, 200 mM KCl, 30 mM imidazole, 0.05% (w/v) DDM at 2 mg ml^{-1} was added in tenfold molar excess. The conjugation mixture was incubated at 4 °C, protected from light, and agitated at 400 RPM, for 45 min. The non-conjugated dye was removed via size exclusion chromatography on Superose 6 Increase 10/300 GL (Cytiva, GE29-0915-96), equilibrated with 20 mM HEPES, pH 7.5, 200 mM KCl, 200 mM imidazole, 0.05% (w/v) DDM, on Äkta system. All protein-containing eluted fractions were pooled and the enzyme was concentrated with Amicon Ultra-0.5 Centrifugal Filter Units with NMWL of 100 kDa. Labelled enzyme was flash-frozen in liquid nitrogen and stored at −80 °C.

2.2.3 Labelling of PDMS-*g*-PEO with NBD, rhodamine, fluorescein, ATTO 550 and ATTO 647N

Polymer was fluorescently labelled via hydroxyl end groups of PEO chains conceptually following previously described protocol (*38*). In short, first, hydroxyl end groups were mesylated. Towards this end, PDMS-*g*-PEO was dissolved in dichloromethane (Merck, 75-09-2: 270997) and cooled down to 0 °C. Then, triethylamine (Merck, 121-44-8: T0886) was added at once, followed by a drop-wise addition of methanesulfonyl chloride (Merck, 124-63-0: 471259, dissolved in dichloromethane. Solvents were removed under vacuum first at room temperature and afterwards at 60 °C. In next steps, polymer was aminated. To achieve this, aqueous ammonia was added to PDMS-*g*-PEO mesylate and the reaction was vigorously stirred for 5 days at room temperature. Aminated polymer was then purified by dialysis against Milli-Q water using Pur-A-Lyzer dialysis chambers (Merck, PURX25005) with a molecular weight cut-off of 25 kDa, followed by drying under vacuum. Typical aminated polymer yield was 55-70 % (w/w). In next steps, fluorescent dyes in the form of NHS esters were conjugated to amine-modified polymer. To achieve this, succinimidyl 6-(N-(7-nitrobenz-2-oxa-1,3-diazol-4-yl)amino)hexanoate (NBD-X) (Thermo Scientific, S1167), 5/6-carboxy-tetramethyl-rhodamine succinimidyl ester (NHS-Rhodamine) (Thermo Scientific, 46406), ATTO 550 NHS-ester (Merck, 92835) and/or ATTO 647N NHS-ester (Merck, 18373) were first dissolved in DMSO at 40 mg ml^{-1}. To polymer, dissolved in tetrahydrofuran (THF) (Merck, 109-99-9: 401757), first, diisopropylethylamine at 12 mg ml^{-1} in THF was added, followed by the addition of dye in DMSO. The conjugation was performed over the course of 24 hours, at room temperature, under gentle agitation. Unconjugated dye was removed via dialysis (Pur-A-Lyzer chambers, 25 kDa MWCO) against basic water (pH = 10) for 6 days. The labelled polymer was then dried under vacuum and then resuspended in basic water and purified using size exclusion chromatography (manually packed column, sephadex G-25 resin, bed height of 20 cm and width of 1 cm, equilibrated with basic water). Eluted fractions containing dye-modified polymer were pooled and dried under vacuum. Finally, polymer was dissolved in chloroform:methanol (2:1, v:v), typically at 5 mg ml^{-1}.

2.3 FORMATION AND CHARACTERIZATION OF THE COMPARTMENTS

2.3.1 Formation of protein-free lipid, polymer and hybrid large unilamellar vesicles (LUVs)

Lipid used in all experiments, unless stated otherwise, was soy L-α-phosphatidylcholine (referred to as "soy PC", 95 %, Avanti Polar Lipids, 441601). Polymer used in this study was graft co-polymer poly(dimethylsiloxane)-*graft*-poly(ethylene oxide) hereby referred to as "PDMS-*g*-PEO". This polymer is commercially available and is sold by Dow Corning (Dow, DOWSIL OFX-5329 Fluid). The average viscosimetric molecular weight of 3000 g mol^{-1}, the 47 % weight fraction of ethylene oxide (2 arms of PEO per PDMS chain, on average) and the average degree of polymerization of 12 are reported in the data provided by the supplier. Furthermore, for all reconstitution experiments, unless stated otherwise in the related section, protein-free LUVs were prepared at 10 mg ml^{-1} with respect to lipid, polymer or hybrid content. All membrane constituents were dissolved in 2:1 chloroform-methanol (v/v) and stored at −20 °C until use, except for PDMS-*g*-PEO solution, which was stored at room temperature.

Protein-free vesicles were prepared as described in (*1*). For the preparation of liposomes, first, 10 mg of dissolved lipid were transferred into round-bottom glass vial and the solvent was evaporated under a gentle stream of nitrogen over 1 h. The nitrogen stream was strong enough to spread the solvent evenly on walls of the vial, facilitating the formation of thin lipid film upon solvent removal. In all case, unless described differently in the respective sections, thin films were then rehydrated with vesicle buffer, 20 mM HEPES (pH 7.5), 2.5 mM MgSO$_4$, 50 mg ml^{-1} sucrose, and resuspended by gently vortexing, until homogenous appearance of the suspension and until no more material could be observed on walls of the vial. Multilamellar vesicles (MLVs) formed in this way were then subjected to 6 freeze/thaw cycles (1 min freezing in lN$_2$, thawing in water bath at 35 °C, followed by vortexing at 900 rpm for 30 s). Finally, the size and lamellarity of liposomes in the suspension was unified by the extrusion (21 times) through polycarbonate filters with 100 nm pores size (Merck, Z373419) with the Mini-Extruder (Avanti Polar Lipids, 610020-1EA).

Hybrid LUVs were prepared comprising 30 mol% of soy PC and 70 mol % of PDMS-*g*-PEO as the starting material and were prepared in the exact same way as described for liposomes.

Polymersomes were prepared from PDMS-*g*-PEO as described in liposome preparation, except that the freeze/thaw steps were omitted. Furthermore, if polymer vesicles were intended for protein reconstitution, the appropriate amount of detergent of choice was supplemented to rehydration buffer (please see related sections for details).

2.3.2 Estimation of the loss of membrane constituents during preparation of LUVs

To determine the amount of lipid, polymer or hybrid mixture, which is removed from the vesicle solution due to the adsorption onto glass vials or onto polycarbonate filter during the extrusion process, different types of LUVs were prepared as described in Chapter 2.3.1. Towards this end, 10 mg of lipid, polymer or hybrid mixture in organic solvents were deposited into pre-weighted glass vials. Solvents were evaporated under gentle stream of nitrogen over 1 h and the formed thin films were weighted. Next, films were rehydrated with Milli-Q, vortexed at 900 rpm until no material was seen attached to the wall and until the suspension appeared homogeneous, and were extruded through polycarbonate filters with the pore sizes of either 100 or 200 nm, 21 times. The solutions of so-formed LUVs were then transferred into pre-weighted plastic tubes and lyophilized. After freeze-drying, the tubes containing vesicles were weighted again and the fraction of lost material was determined by comparing the mass of thin films with the mass of dry membrane constituents.

2.3.3 Determination of size and dispersity of LUVs by dynamic light scattering (DLS)

The intesity-based size distribution of LUVs and the dispersity of LUVs suspension was determined via dynamic light scattering on Zetasizer Nano ZS (Malvern). Illumination is provided by 633 nm helium-neon laser and the samples were measured in back-scattering detection mode at a fixed angle of 173°. Towards this end, 50 μl of LUVs suspension were transferred into quartz cuvette micro (Hellma, Z600415) and measured at 23 °C three times, each measurement consisting of 10 runs with 70 s duration. Intensity-based size distribution was reported as the average of three measurements, unless the sizing was inconsistent due to various effects, such as aggregation or sedimentation, in which case only measurements obtained prior to these effects taking place were considered. Reported are average values with standard error.

2.3.4 Preparation of protein-free polymer and hybrid giant unilamellar vesicles (GUVs)

Micron-sized hybrids were formed with the electroformation approach (*111*) at room temperature. First, thin hybrid film was created from hybrid mixture at various polymer-to-lipid ratios (10 mol % increments), containing 7.7 μM dye-functionalized polymer PDMS-*g*-PEO-fluorescein and 300 nM lipid dye L-α-phosphatidylethanolamine-N-(lissamine rhodamine B sulfonyl) (Rho-PE, Avanti Polar Lipids, 810150). Next, 50 μl of hybrid solution at 1 mg ml^{-1} were deposited on each of the two glass coverslips coated with indium tin oxide (PGO, CEC020S) with resistivity of 20 Ω sq^{-1}. Next, solvent was evaporated under gentle stream of nitrogen over 45 min. The electroformation chamber with approximate volume of 0.6 ml was then created by connecting both slides via silicone spacer with thickness of 1.2 mm. Chamber was filled with 0.1 M sucrose solution and a sine wave (2 V, 10 Hz) was applied for 40 min followed by squared wave (1 V, 2 Hz) for 1 min. Solution, containing GUVs was then carefully collected and 5 μl were deposited onto poly-L-lysine coated glass slides (Poly-Prep Slides, Merck, P0425-72EA). If only observation of larger GUVs (> 10 μm) was desired, the GUVs solution was first sedimented in 0.1 M glucose by transferring 50 μl of GUVs into 300 μl of glucose solution, and incubating at room temperature for 30 min. Then, larger GUVs were carefully collected from the bottom of the glucose solution and 5 μl were applied to poly-lysine slides, as described above. The solution was incubated on slides for 5 min prior to observation, which allowed for weak immobilization of GUVs.

Polymer GUVs were formed with the protocol described above for hybrids, only that polymer thin film was created by depositing 5 μl of 10 mg ml^{-1} polymer solution, supplemented with 7.7 μM dye-functionalized polymer PDMS-*g*-PEO-fluorescein, on both ITO-coated coverslips.

2.3.5 Analysis of protein-free polymer and hybrid GUVs via fluorescence microscopy

Protein-free GUVs prepared as described in previous section were imaged with Zeiss Axio Imager M equipped with a digital camera AxioCam MRm (FireWire 1394a). Vesicles were observed with either ×40/0.7 or ×100/1.3 (magnification/NA) objective lens. Samples were excited by HBO 100 short-arc 100 W mercury lamp (Zeiss) at 560 nm (Rho-PE) and at 494 nm (PDMS-*g*-PEO-fluorescein). Filter set 38 and 46 HE (Zeiss) were used to record the emission of excited dyes at 583 nm (Rho-PE) and at 518 nm (PDMS-*g*-PEO-fluorescein).

2.3.6   Protective function of PDMS-*g*-PEO against ROS

Lipid, polymer and hybrid *bo₃* oxidase-containing LUVs were prepared as described in (*97*). In summary, first, preformed vesicles were partially solubilized with the detergent. To achieve this, 0.1 % sodium cholate (final concentration, w/v) was added to 5 mg ml^{-1} liposomes, 0.2 % to 10 mg ml^{-1} hybrids and 0.4 % to 20 mg ml^{-1} polymersomes. In the case of polymersomes, sodium cholate was already included in the rehydration buffer during vesicle formation (*1*) to increase the solubilization efficiency. Next, the enzyme was added to vesicles at the lipid/hybrid mixture/polymer-to-protein ratio of 9550:1. This configuration assured similar protein content as well as vesicle concentration across all systems. The final protein content was 0.675 µM *bo₃* oxidase in liposomes, 0.449 µM in hybrids and 0.698 µM in polymersomes. Reconstitution mixtures were mixed briefly with short vortexing bursts and incubated at room temperature for 1.5 h. Afterwards, the detergent was removed by three sequential additions of Bio-Beads, 90 mg beads per 200 µl of reconstitution mixture were added in each step. Prior to measurements, four separate reconstitutions were pooled to average out the reconstitution-to-reconstitution variability.

Proteovesicles, prepared as described above, were then tested for their resistance to oxidative damage via exposure to ROS. The latter were introduced to vesicles in the form of ascorbate or ascorbyl free radical (A•), as described previously (*112, 113*). First, FeSO₄×7H2O (Merck, 7782-63-0: F8633) was dissolved in 1 mM Tris-HCl, pH 7.5, containing 100 mM sucrose, at 1.25 mM. Meanwhile, ascorbate stock solution at 25 mM was prepared freshly on the day of experiments, by dissolving sodium L-ascorbate (Merck, 134-03-2: 11140) in the same buffer as above. To test the influence of A•, 24 µl of *bo₃*-LUVs were mixed with 0.5 µl FeSO₄ solution (final concentration 25 µM) and 0.5 µl sodium L-ascorbate solution (final concentration 500 µM). The effect of ascorbate was tested in the same way, but the FeSO₄ solution was omitted and same volume of buffer was added instead. Treated proteovesicles were then mixed well by vortexing (600 RPM) and incubated for 30 min at room temperature. Afterwards, *bo₃* oxidase activity was determined via oxygen consumption using Oxytherm system, as described by (*1, 50*) with slight modifications. In the total measurement volume of 1 ml, the fraction of *bo₃*-LUVs was adjusted so that the same theoretical concentration of *bo₃* oxidase across all systems of ~13.5 nM was achieved. The enzyme was activated with 8 mM DTT and 40 µM of Q₁ (final concentrations) and the oxygen consumption was recorded at 22 °C while the solution was being stirred. Untreated proteovesicles were used as a reference when comparing the effect of ROS on enzyme activity. All measurements were carried out in

duplicates or triplicates and the t-test was conducted for statistical analysis (p < 0.05 indicated statistically significant difference). The oxygen consumption rates were reported as the average of 2–3 measurements, with standard deviation. Finally, to test the effect of ROS on the integrity of vesicles (to probe for potential vesicle collapse or degradation), size of proteovesicles was determined before and after treatment by DLS with same setup, as described in Chapter 2.3.3.

2.3.7   Passive proton permeability of protein-free LUVs

Passive proton permeability of LUVs was determined with protocol previously established for liposomes comprising lipids isolated from Archaea (*114*). For this purpose, first, choline-containing vesicles were prepared. Membrane impermeable choline$^+$ presents a static charge, which facilitates the exchange between alkali ions, in this case K$^+$ and protons upon proton entry into vesicles due to externally induced pH change (*115*). Lipid, polymer or hybrid thin films were prepared same as in Chapter 2.3.1 and were rehydrated in 50 mM 3-morpholinopropanesulfonic acid (MOPS) (Merck, 1132-61-2: 69947), pH 7.0, 75 mM KCl, and 25 mM choline chloride (Merck, 67-48-1: C7017) ("inner buffer") to a final concentration of 40 mg ml^{-1}. LUVs were then formed from these MLVs by subjecting them to 5 consecutive freeze/thaw steps (1 min freezing in lN$_2$, followed by thawing at 30 °C and vortexing for 1 min, freeze/thaw is omitted in polymersomes!) and 21× extrusion through polycarbonate membrane filters) with pore diameter of 200 nm (Merck, 610006). Next, outer vesicle buffer was exchanged for one with lower buffering capacity, 0.5 mM MOPS, pH 7.0, 75 mM KCl, and 75 mM sucrose ("outer buffer") on the size exclusion column (PD Minitrap G-25, Cytiva, GE28-9180-07) equilibrated with the outer buffer.

For permeability measurements, vesicles were first diluted to 1.5 mg ml^{-1} in 1.5 ml total volume of outer buffer in stirred 1.5 ml quartz cuvette (Hellma, 109004F-10-40). Material loss during extrusion and vesicle dilution after size exclusion chromatography was accounted for when calculating the amount of material needed per measurement. In the next step, potassium ionophore valinomycin (Merck, 2001-95-8: 94675; dissolved in DMSO) was added at 1 nmol per 1 mg of lipid/polymer/hybrid mix, which enabled potassium counter flux and prevented the establishment of inhibitory transmembrane electrical potential (Δψ), caused by the electrogenic influx of protons. To monitor the changes in external pH due to proton movement between vesicles outer solution and vesicles lumen, pyranine (Merck, 6358-69-6: H1529) was added at 10 μM final concentration. After equilibration, the external pH was lowered with the addition of 100 nmol H$^+$ (in the form of 50 mM H$_2$SO$_4$ stock solution). The influx of protons into

vesicles over time was then monitored as the increase of the pyranine fluorescence with the dye excited at 450 nm and the emission recorded at 508 nm. Finally, ionophore nigericin (Merck, 28643-80-3: N7143) dissolved in DMSO was added to vesicles to equilibrate the pH across the membrane. The pyranine signal was calibrated afterwards by the addition of small aliquots of acid (H_2SO_4) or base (KOH).

2.3.8 Passive proton permeability of *bo₃* oxidase-functionalized LUVs

Prior to enzyme reconstitution, lipid and hybrid proteovesicles were prepared as described in previous section. For proteopolymersomes preparation, 0.8 % (w/v) of sodium cholate was supplemented to inner vesicle buffer, which was used to rehydrate thin polymer film. Meanwhile, preformed liposomes and hybrids were partially solubilized with 0.8 % sodium cholate after the formation. Then, *bo₃* oxidase was added to all types of vesicles at the lipid/hybrid mixture/polymer-to-protein ratio of 9550:1. Reconstitution mixtures were then incubated at 4 °C for 30 min on a rocking platform. Detergent was removed with Bio-beads as described in Chapter 2.3.6 and the vesicles outer solution was exchanged to 0.5 mM MOPS, pH 7.0, 75 mM KCl, and 75 mM sucrose, via size exclusion chromatography as described in previous section. Passive proton permeability of *bo₃* oxidase-functionalized LUVs was then assessed in the exact same way as that of protein-free LUVs, described in previous section. Lastly, the size distribution of proteovesicles was determined by DLS as described in Chapter 2.3.3.

2.3.9 Calculation of proton permeability coefficients from the pH-dependant fluorescence changes of pyranine

Permeability coefficients in the absence of diffusion potentials can be calculated as the proton flux from the derivate of the external pH in relationship with time (*116, 117*), while accounting for several other factors, such as surface-to-volume ratio and the buffering capacity of all species, including lipids and polymer (*118*). In the current work however, the buffering capacity of lipids/polymer and of the buffer was neglected due to relatively small lipid/polymer content and proportionally lower surface-to-volume ratio of LUVs, and because of the low ionic strength of outer buffer (1 mM). Additionally, two proposed mechanisms were considered in data analysis: the formation of transient pores and the solubility-diffusion mechanism (*117*). The former was observed as the initial fast change of pH (steep initial jump) and was attributed to the random nature of pore opening exhibiting a Poisson distribution of the closing rates.

Meanwhile, the latter was reflected in the observed slower phase corresponding to a solubility-diffusion pathway (*119*). Since in the present case the pH changes were more accurately described by such a two-stage process, the data was fitted with the biexponential curve:

$$y = A_1 e^{-tk_1} + A_2 e^{-tk_2} + y_0 \qquad \text{(Eq. 2)}$$

In this equation, A_1 *and* A_2 are the amplitude of fluorescence signal, k is the first order rate constant of proton influx and y_0 the offset. Second (smaller) rate constant k_2 was used to calculate the permeability coefficients via previously proposed relation (*119*):

$$P_{H+} = k_2 \frac{R}{3} \qquad \text{(Eq. 3)}$$

Here, k_2 is the rate constant of slower stage of proton flux, mentioned above and the R indicates average radius of used (proteo)vesicles, as determined by the DLS.

2.3.10 Assessment of ROS damage on protein-free and bo3 oxidase-functionalized LUVs with cryo-EM

Protein-free and *bo3* oxidase-functionalized LUVs were prepared as described in Chapters 2.3.1 and 2.3.8. Prior to vitrification of samples, they were treated with either ascorbate or with ascorbyl free radical, as described in Chapter 2.3.6. After 30 min exposure to ROS, 3.5 μl droplet of the LUVs suspension was deposited onto a glow-discharged holey carbon grid (R2/1 type 200 Mesh, Quantifoil). Samples were then vitrified using Vitrobot Mark IV System (Thermo Scientific) and standard Vitrobot filter paper (Grade 595, Ø55/20mm, Agar Scientific, AG47000-100) at 4 °C and 95 % relative humidity. Vitrification was achieved with a blotting time of 6 s and a blot force of 2. The grid was then mounted onto a Thermo FEI Glacios 200 kV autoloader (Thermo Scientific) under cryo conditions. Images were acquired with Falcon 3EC direct electron detector (Thermo Scientific) in linear mode and a under a total dose of 50 e$^-$ Å^{-2}.

Several collaboration partners aided in sample preparation and imaging. Samples were vitrified by Fotis L. Kyrilis and images were captured by Farzad Hamdi, both affiliated with Interdisciplinary Research Center HALOmem & Institute of Biochemistry and Biotechnology, Martin Luther University Halle-Wittenberg, Biozentrum, Halle/Saale.

2.3.11 Functional reconstitution of respiratory enzymes of a short respiratory chain – *bo₃* oxidase alone or *bo₃* oxidase in combination with ATP synthase – into lipid, polymer and hybrid LUVs

Enzymes required for the construction of short respiratory chain, namely the *bo₃* oxidase and the ATP synthase were initially reconstituted in polymer and hybrid LUVs based on previously established principles governing successful membrane protein reconstitution (*64*). These principles were later successfully applied to bacterial respiratory enzymes (*44, 54*) by rigorous screening of optimal reconstitution conditions, in particular with respect to detergent selection, degree of vesicle solubilization and the selected method for detergent removal. This approach was in the early stages of the construction of artificial mitochondrion adopted also in this work and was proven to be an invaluable starting point. Furthermore, by adopting general methodology such as detergent concentration ranges along with detergent types, straight-forward comparison with the only existing similar system at that time was enabled, which served as a guideline for system optimization.

Following the mentioned preestablished approach for the reconstitution of the SRC, ATP synthase and *bo₃* oxidase were first reconstituted in liposomes, which served as a benchmark system, at the theoretical protein-per-liposome ratio of approx. 1 ATP synthase and 5 *bo₃* oxidase. To achieve this, the theoretical concentration of vesicles in suspension had to be calculated following the rationale described previously (*44*). With this approach, first, the average number of lipids per liposome is calculated following the equation:

$$N = 4\pi \frac{\left(\frac{d1}{2}\right)^2 + \left(\frac{d2}{2}\right)^2}{A}$$ (Eq. 4)

In this relation, N is the number of lipid molecules in a single liposome, d_1 is the inner diameter of a liposome (i.e., vesicle diameter determined via DLS minus thickness of the membrane, as assessed via cryo-EM imaging), d_2 is the outer diameter of a liposome (measured via DLS) and A is the surface area of the lipid head group (≈ 0.7 nm^2 for phosphatidyl choline (*120*)). For instance, an average liposome with the determined diameter of 105 nm and the membrane thickness of 5 nm contains approximately 94360 lipid molecules. This calculation assumes tight, perfect lipid packing, which is not the case in the actual biological systems, therefore the number of lipid molecules per liposome is slightly overestimated. Next, the concentration of lipids in a vesicle solution can be divided by the number of lipid molecules

required to form a vesicle with the determined average diameter, to calculate the theoretical concentration of vesicles in a liposome solution. For example, in the cases where the soy PC liposomes were prepared at 10 mg ml^{-1} (= 12.9 mM with respect to lipid content), the theoretical concentration of vesicles was 12.9 mM / 94360 = 0.14 μM. This meant that if the theoretical protein-per-liposome ratio of approx. 1 ATP synthase and 5 bo_3 oxidase was aimed at, 0.14 μM ATP synthase and 0.70 μM of bo_3 oxidase (final concentrations) were added to preformed liposome LUVs with the specified diameter. Average size of the vesicles was determined prior to every reconstitution to adjust for the small variations in their sizes. Furthermore, for polymersomes, same packing density of polymer in vesicles was assumed as for the lipids in liposomes.

Next, vesicles were partially solubilized by either sodium cholate, sodium deoxycholate or octyl glucoside, in the concentration range of 0.2 – 0.8 % (w/v) at 0.2 % increments. When the bo_3 oxidase was reconstituted alone in order to find the optimal reconstitution conditions from the insertion of this proton pump, vesicle buffer was added to partially solubilized vesicles instead of ATP synthase. The reconstitution mixture was the incubated at room temperature for 30 min under mild agitation (rocking platform), followed by the detergent removal either via size exclusion chromatography, dialysis or by Bio-beads. In the first case, following incubation, samples were applied to PD Minitrap G-25 column (Cytiva, GE28-9180-07), equilibrated with the vesicle buffer (20 mM HEPES (pH 7.5), 2.5 mM MgSO$_4$, 50 mg ml^{-1} sucrose) and eluted in same buffer. In the second case, reconstitution mixtures were transferred into QuixSep dialysis capsules (Carl Roth, H448.1) and dialysis membrane (Spectra/Por 7, 8 kDa NMWL, Avantor, 25223-672) was stretched across the capsule. Samples were then dialyzed overnight at 4 °C against 100 ml of vesicle buffer supplemented with 100 mM KCl. Finally, in the case of detergent removal by Bio-beads (SN2 Resin, Bio Rad, 1523920), the reconstitution mixture was supplemented with 100 mg of beads, added in a single step, followed by 2 h incubation at room temperature on a rocking platform. After that, beads were pelleted and the supernatant (proteoliposomes) was collected. Detergent removal by Bio-Beads led to highest activity of both reconstituted enzymes (the activity was only slightly higher than by using gel filtration, as proposed initially (*44*)), therefor from this point onward, this detergent removal technique was selected for all following reconstitution experiments, unless specified otherwise.

The reconstitution of ATP synthase and bo_3 oxidase in preformed hybrid LUVs was carried out as described above for liposomes, with slight modifications. The detergents were removed by Bio-Beads, but, to the reconstitution mixture, the beads were added in 3 subsequent

additions, 15 mg of beads each, followed by the 30 min incubation period, at room temperature, on a rocking platform. This facilitated slower detergent removal (speed of detergent removal via adsorption to beads is proportional to the amount of beads in the reconstitution mixture), which seemed to have led into more efficient enzyme reconstitution into this type of artificial membranes.

For the protein reconstitution in preformed polymer LUVs, it was crucial that the ATP synthase and bo_3 oxidase were not added at once, as in the case of liposomes and hybrids. Instead, ATP synthase was added first, followed by 15 min incubation at room temperature. Then, bo_3 oxidase was added followed by additional 20 min incubation at room temperature. Enzymes were added to preformed polymersomes which already contained the detergent of choice in the desired concentration, as described in Chapter 2.3.1. Finally, detergent was removed in the exact same way as described above for hybrids (i.e., step-wise addition of Bio-beads).

2.3.12 Determination of solubilization profiles of different types of protein-free LUVs with sodium cholate, sodium deoxycholate, Triton X-100, octyl glucoside and dodecyl maltoside

Sodium cholate ("SC", Merck, 206986-87-0: C6445), Sodium deoxycholate ("SDC", Merck, 302-95-4: 30970), n-dodecyl-β-D-maltoside ("OG", Merck, 69227-93-6: 850520P) and n-Octyl β-D-glucopyranoside ("OG", Glycon, D97001) were dissolved in Milli-Q water at 10 % (w/v) and were stored at room temperature (SC) or at −20 °C (SDC, DDM, OG) for no more than a year. Furthermore, Triton X-100 (Merck, 9002-93-1: 93443) was supplied as a 10 % (w/v) solution in water and was stored at room temperature and in the inert atmosphere to reduce peroxide formation.

Preformed LUVs were prepared as described in Chapter 2.3.1 at the concentration of 10 mg ml^{-1}, the only difference being that the detergents were not being included in rehydration buffer during polymersomes preparation. First, 100 µl of the LUVs solution were placed into quartz cuvette (Hellma, 104002B-10-40, 700 µl) and their baseline absorbance was recorded at 540 nm with Specord 50 plus spectrophotometer (Analytik Jena) at 22 °C, without stirring and with the vesicle buffer used as a reference. Next, detergent of choice in solution was added to vesicles in small increments, typically 0.2 µl of detergent per step. After each addition, cuvette with LUVs was gently flickered to mix vesicles and detergent, and incubated for 1 min at room

temperature to allow for equilibration and detergent partitioning into vesicles. In the case of DDM, vesicles were incubated with detergents for 5 min upon detergent addition due to relatively slower partitioning of this detergent (*121*). It was crucial that detergents were added gently and with patience, otherwise the solution would foam, hindering the absorbance measurements. The detergents were then continuously added until the absorbance of LUVs reached the value of that of a vesicle buffer, point at which vesicles were considered completely dissolved.

Solubilization profiles of different types of LUVs were analysed in accordance with the proposed three-stage solubilization model (*63, 68*). The saturation point (R_{sat}) and total solubilization point (R_{sol}) were defined with respect to the amount of added detergent and the related changes in LUVs absorbance. R_{sat} was defined as the detergent content, at which treated vesicles exhibited highest absorbance (liposomes) and before their absorbance started to decrease rapidly (hybrids, polymersomes). Moreover, R_{sol} was defined as detergent content at which the absorbance of vesicles reached the value determined for the solvent.

2.3.13 Determination of the detergent removal efficiency of Bio-beads during enzyme reconstitution in lipid, polymer and hybrid LUVs

Protein-free LUVs were prepared as described in Chapter 2.3.1 and the short respiratory chain was reconstituted into all LUV types as described in Chapter 2.3.11. During the reconstitution, Bio-beads facilitated detergent removal and protein insertion. The three reconstitution setups with respect to used detergent that produced the most active proteovesicles, namely lipid LUVs solubilized with 0. 6 % (w/v) sodium cholate as well as polymer and hybrid LUVs both solubilized with 0.1 % (w/v) of octyl glucoside, were then probed for the residual detergent following reconstitution. The analysis was performed by Eurofin Scientific with the following setup. Samples containing proteovesicles were dissolved in acetonitrile, separated using Agilent Zorbax Eclipse XDB-C18 column (Agilent, 100×2.1 mm, 3.5 μm) and analysed with the HPLC-MS/MS. The detection limit for tested detergents was $100 \ \mu g \ l^{-1}$.

2.4 CONSTRUCTION AND CHARACTERIZATION OF FUSION PLATFORM BASED ON SNARES

2.4.1 Preparation of SNAREs-free and SNAREs-inserted nano-sized lipid, polymer and hybrid vesicles with the co-micellization method

Proteovesicles were formed from mixed micelles upon detergent removal, loosely following the integration strategy described previously (*85, 86*), with considerable modifications. Common preparation steps are described in the non-indented text, while the diverging steps are encompassed in the indented one.

Soy phosphatidylcholine (Avanti, 95 %, 441601), polymer PDMS-g-PEO (Dow, DOWSIL OFX-5329 Fluid) or hybrid mixture (polymer:lipid = 7:3, mol:mol – this composition produces homogeneous, well-mixed hybrid membranes(*1*)), all dissolved in chloroform:methanol (2:1, v:v), were deposited into round-bottom glass vial.

> For the membrane mixing experiments, in addition to the dye-free vesicles, one population of vesicles was supplemented with 1.5 mol% of 1,2-dioleoyl-sn-glycero-3-phosphoethanolamine-N-(lissamine rhodamine B sulfonyl) (ammonium salt) – "Rho" (Avanti, 810150) and 1.5 mol % of 1,2-dipalmitoyl-sn-glycero-3-phosphoethanolamine-N-(7-nitro-2-1,3-benzoxadiazol-4-yl) (ammonium salt) – "NBD" (Avanti, 810144) and the lipid content (liposomes, hybrids) or polymer content was reduced proportionally. Both dyes were dissolved in chloroform:methanol (2:1, v:v), at 1 mg ml^{-1}.

> For the content mixing experiments, vesicles were supplemented with 0.5 mol % Rho (Avanti, 810150), dissolved as described above, and the lipid content (liposomes, hybrids) or polymer content was reduced proportionally.

Then, solvent was evaporated under gentle stream of nitrogen and the produced thin films were further dried under nitrogen for 1.5 h.

> Next, for the membrane mixing experiments, dry thin films were resuspended at the final concentration of 5 mM in 20 mM HEPES (Merck, 7365-45-9: H6147) (pH = 7.4/KOH), containing 150 mM KCl (Merck, 7447-40-7: P9541), 1 mM DTT (Merck, 3483-12-3: D9779) and 5 % (m [g]/100 ml) sodium cholate, by rigorous vortexing (approx. 1200 rpm) until all material was seen dislocated from the glass and

homogenously resuspended. This yielded lipid/polymer/(dyes)/detergent mixed micelles. Next, to micelles containing Rho/NBD, ΔN complex was added at the lipid/polymer/hybrid mixture:ΔN complex ratio of 1000:1 (mol:mol) and to the dye-free micelles, synaptobrevin was added at the lipid/polymer/hybrid mixture:syb ratio of 400:1 (mol:mol). Upon protein addition, reconstitution mixtures were mixed briefly with 3 short bursts (1000 RPM) and incubated at 23 °C for 5 min. Proteovesicles were then formed spontaneously upon the detergent removal via size exclusion chromatography on the PD Minitrap™ G-25 column (GE Healthcare) equilibrated with 20 mM HEPES (pH = 7.4/KOH), containing 150 mM KCl, 1 mM DTT. Eluted fractions containing lipid dyes were collected and pooled. Furthermore, volume-wise, corresponding eluted fractions containing dye-free vesicles were collected and pooled.

For the content mixing experiments, dry thin films were resuspended in 20 mM HEPES (pH = 8.0/KOH), containing 150 mM KCl, 1 mM DTT, 5 % Na-Cholate as described above. To one population of mixed micelles, first, ΔN complex was added at the lipid/polymer/hybrid mixture:ΔN complex ratio of 1800:1, followed by mixing with 3 short bursts. Next, after 5 min, ATP synthase was added at the lipid/polymer/hybrid mixture:ATP synthase ratio of 81000:1 (mol:mol) followed by brief mixing, as before. To another population of mixed micelles, synaptobrevin was added at the lipid/polymer/hybrid mixture:synaptobrevin ratio of 500:1 (mol:mol), and bo3 oxidase at the ratio of 27000:1 with intermediate mixing steps, as described above. Reconstitution mixtures were then incubated at 23 °C for 5 min. Proteovesicles were then formed spontaneously upon the detergent removal via size exclusion chromatography on the PD Minitrap™ G-25 column equilibrated with 20 mM HEPES (pH = 8.0/KOH), containing 150 mM KCl, 1 mM DTT and 40 mM KH_2PO_4 (Merck, 7778-77-0: P5655). All eluted fractions containing lipid dyes were collected and pooled.

For the cryo-EM imaging, vesicles were prepared in the exact same way as described for the membrane mixing experiments, except that the ΔN complex was reconstituted at the lipid/polymer/hybrid mixture:ΔN complex ratio of 1800:1 (mol:mol).

SNAREs-free nano-sized vesicles, used in the control experiments, were prepared in the exact same way as described above for SNAREs reconstitution, with the exception of SNAREs being omitted and replaced with 20 mM HEPES (pH = 8.0/KOH), containing 150 mM KCl, 1 mM DTT (as well as 40 mM KH_2PO_4 in the case of content mixing vesicles).

2.4.2 Determination of orientation of reconstituted SNAREs

Orientation of SNARE proteins incorporated into liposomes, polymersomes or hybrid vesicles, as described in Chapter 2.4.1, was assessed with protease (trypsin) digestion of intact and detergent-solubilized vesicles as adapted from (*105*). Briefly, 40 µl of vesicles were incubated either with 10 µl of buffer only (20 mM HEPES pH 7.4, 150 mM KCl), buffer and trypsin (Merck, 9002-07-7, final concentration 0.1 mg ml−1), or buffer, trypsin and Triton X-100 (Merck, 9002-93-1, final concentration 0.3 %). After 2 h incubation at 37 °C, samples were analysed by Tricine-SDS-PAGE (*122*). With respect to this, the band intensity of samples, treated with buffer only (total amount of inserted SNAREs) was compared with the band intensities of trypsin-treated samples (amount of inwards-facing SNAREs) and trypsin/Triton-treated ones (amount of indigestible intramembrane fragments of SNAREs). The fraction of outwards-facing SNAREs was then calculated by subtracting the inwards-facing SNAREs and indigestible fragments from the total amount of inserted SNAREs and dividing it by the latter.

The analysis of SNAREs orientation was carried out by collaboration partner Dr. Agata Witkowska, Max Planck Institute for Biophysical Chemistry, Göttingen.

2.4.3 Stability assessment of reconstituted SNAREs via the floatation assay

Integration stability and efficiency was evaluated with a flotation assay on a discontinuous Nycodenz (Progen, 1002424) gradient, as described (*105*). Briefly, reconstituted vesicles prepared as described in Chapter 2.4.1 were mixed with equal volume of 80 % Nycodenz dissolved in 20 mM HEPES (pH 7.4/KOH), 150 mM KCl and were overlaid first with 30 % Nycodenz and then with said buffer only. Following ultracentrifugation, reconstituted vesicles were partitioned in the uppermost (buffer) layer of the gradient, while the non-incorporated SNAREs as well as disassembled ΔN complex can be found in lower layers. The SNAREs content of different layers was analysed by Tricine-SDS-PAGE (*122*) and the amount of SNAREs, inserted in a stable manner (upmost layer) was compared with the total amount of SNAREs in all layers.

The analysis of SNAREs stability was carried out by collaboration partner Dr. Agata Witkowska, Max Planck Institute for Biophysical Chemistry, Göttingen.

2.4.4 Zeta potential and size determination of SNAREs-free nano-sized vesicles intended for membrane and content mixing

Zeta potential of protein-free vesicles employed in the membrane and content mixing experiments prepared as described in Chapter 2.4.1 was determined under experimental conditions with respect to solvent (buffer) composition, pH, temperature and presence of various related cofactors (UQ, ATP etc.). In this regard, protein-free vesicles (with or without 1.5 % of both Rho/NBD for membrane mixing and with 0.5 % Rho for the content mixing) were prepared as described above in either membrane mixing buffer (20 mM HEPES (pH 7.4/KOH), 150 mM KCl, 1 mM DTT; viscosity at 37 °C = 0.760 cP, refractive index at 37 °C = 1.3332) or in content mixing buffer (20 mM HEPES (pH 8.0/KOH), 150 mM KCl, 40 mM KH_2PO_4, 73.5 μM ADP, 58.7 nM ATP, 35.2 mM DTT, 0.6 mg ml^{-1} CLSII luciferin/luciferase reagent and 0.2 mM UQ; viscosity at 23 °C = 1.019 cP, refractive index at 23 °C = 1.3364), respectively. In parallel, for a comparison, all vesicles were also prepared in Milli-Q water. Prior to measurements, folded capillary zeta cells (Malvern Panalytical, DTS1070) were filled with either of two buffers or with Milli-Q, and a small volume (10 – 40 μl) of vesicles, with the concentration of 80 mg ml^{-1} was injected directly to the bottom of the cell. This so-called diffusion barrier technique minimized sample contact with the electrode and the resulting sample decomposition. Samples, intended for the content mixing were measured at 23 °C. Meanwhile samples, intended for membrane mixing were deposited into capillary cells, incubated at 37 °C for 30 min prior to measurements and then measured at 37 °C. All samples were measured with Zetasizer Nano ZS (Malvern Panalytical) using Smoluchowski approximation and monomodal analysis (i.e., fast field reversal) as well as general purpose mode (combination of fast and slow field reversal) when possible, both yielding very similar results. Measurements consisted of 10-300 runs each. Reported are mean zeta potentials acquired in separate measurements.

2.4.5 SNAREs-mediated membrane mixing and vesicles size changes following fusion

Vesicles intended for the membrane mixing experiments as described in Chapter 2.4.1 were first incubated at 37 °C for 30 min following preparation to preheat them. Then, vesicle population containing Rho/NBD was resuspended in preheated membrane mixing buffer (20 mM HEPES (pH 7.4/KOH), 150 mM KCl, 1 mM DTT) in stirred quartz cuvette. The NBD in tagged vesicles was excited at 460 nm and a baseline fluorescence emission of NBD at 535 nm

was recorded on Varian Cary Eclipse (Agilent), with the excitation/emission slits at the positions 10/10 and with the PMT voltage set at 480 V. Then, to initiate fusion, dye-free vesicles were added next. Final concentration of both vesicles was 0.4 mM each in a total reaction volume of 0.9 ml. Membrane mixing as an NBD dequenching was monitored until plateau was reached. After that, 10 % octyl glucoside resuspended in membrane mixing buffer was added stepwise (1-5 µl per addition) until maximal NBD dequenching was achieved. Typically, total NBD dequenching was reached at 0.53 % final concentration of OG in liposomes, 0.43 % in hybrids and 0.48 % in polymersomes. Measured changes in NBD emission were normalized using the initial NBD fluorescence as 0 % and the fluorescence of max. dequenched NBD upon OG addition as 100 %. In control experiments, SNAREs were omitted from vesicles. Reported are average values of at least two separate vesicle preparation with standard errors.

Intensity-based size distribution of vesicles before and after fusion was recorded with the Zetasizer Nano ZS as described in Chapter 2.3.3. The reported "before fusion" size estimation was recorded with the freshly prepared vesicles. Meanwhile, for the size estimation of vesicles after fusion, small aliquot of the membrane mixing reaction mixture was removed after reaction plateau was reached and prior to the addition of OG. After size was determined, measured volume was returned and OG was added to solubilize vesicles.

2.4.6 SNAREs-mediated content mixing via coupling of respiratory enzymes

Vesicles intended for the content mixing experiments were prepared as described in Chapter 2.4.1 and their intensity-based size distribution was recorded as described in Chapter 2.3.3. To content mixing buffer (20 mM HEPES (pH 8.0/KOH), 150 mM KCl, 40 mM KH_2PO_4, 73.5 µM ADP, 0.6 mg ml^{-1} CLSII luciferin/luciferase reagent), both populations of vesicles were added with their final concentration of 2.5 mM each, and a baseline luminescence signal was recorded with GloMax® 20/20 luminometer (Promega) at 23 °C. Next, known concentration of ATP (Merck, 34369-07-8: A7699) dissolved in Milli-Q water was added to enable signal calibration. Proton pumping action by *bo₃* quinol oxidase was initiated with the addition of (final concentrations) 35.2 mM of DTT dissolved in Milli-Q and 0.2 mM of ubiquinone 1, dissolved in DMSO, and a luminescence increase as a result of ATP synthesis by the ATP synthase was recorded. During measurements, samples were not stirred. The content mixing solutions were vortexed briefly every 5 min to enable oxygen supply and

homogenous redistribution in measured volume. It is worth noting that the vesicles started fusing as soon as they were mixed, while there was a 5-10 min delay with the ATP synthesis detection so that the baseline/calibration could be recorded. The ATP synthesis rates were determined from the fast initial steady-state synthesis via linear regression.

2.4.7 Determination of the pore edge tension of lipid, polymer and hybrid GUVs and the analysis of dye entry dynamics in porated vesicles

Protein-free GUVs were prepared using previously described electroformation method (*1*). In short, lipid, polymer or the hybrid mixture of the two (7:3, mol:mol) dissolved in chloroform at the concentration of 1 mg ml^{-1} was spread onto two ITO-coated conductive slides (about 25 µl total per slide) and the solvent was evaporated under a gentle stream of nitrogen over 1 h. Both slides were then connected via 2 mm thick Teflon spacer, which created a chamber with about 1.9 ml volume. Chamber was filled with 200 mM sucrose (Merck, 57-50-1: S7903) dissolved in Milli-Q and connected to a function generator. Vesicles were formed in the AC field of 1.5 V and 10 Hz at 23 °C over the course of 2 h. When lipid dyes were used, the electroformation was performed in the dark.

Membrane edge tension was measured according to the method reported in (*123*) with some modifications, and using the theory of pore closure as previously developed (*124*). The analysis described below was performed by collaboration partners Dr. Ziliang Zhao and Dr. Rafael B. Lira (both affiliated with Max Planck Institute of Colloids and Interfaces, Potsdam-Golm).

In short, GUVs prepared as described above, but instead in 200 mM sucrose solution containing 0.1 mM NaCl (Merck, 7647-14-5: S7653) were dispersed in 180 mM glucose (Merck, 50-99-7: G7528) solution and observed under phase contrast microscopy using an inverted microscope (Axiovert 135, Zeiss, Göttingen, Germany) equipped with a 40x (NA 0.6) Ph2 objective. Images were recorded using a high-speed camera Phantom v2512 (AMETEK) at 5 kfps. The obtained images were semi-automatically processed using ImageJ (NIH, USA) and analysed as described previously (*123*). Slow, linear 3rd stage of the pore closure was used in the analysis. For the electroporation, an electroporation chamber was formed by sticking two parallel copper conductive tape pieces (3M, 1101102) onto a glass coverslip, separated by 0.5 cm. A closed chamber was formed by placing parafilm perpendicular to the strips, forming a chamber approx. volume of 100 µl. Prepared GUVs were diluted 10-20 times in isosmolar

glucose solution and placed into the chamber for electroporation. The end of each tape was connected to a multiporator βtech pulse generator GHT_Bi500 (βtech, l'Union, France), and pulses of varying magnitude and time could be applied. If not mentioned otherwise, we applied a single DC pulse of 200 V and 4 ms duration. Since polymer GUVs often become permeable after the application of an electric pulse (see results), we exchange the GUVs in the chamber every time a pulse was applied and so vesicles were subjected to only one pulse.

The dye entry into electroporated GUVs was studied as in (*125*) with minor modifications. Studied GUVs, labelled with 0.5 mol% of a green dye NBD were dispersed in medium containing 2 µM of water-soluble dye sulforhodamine B (SRB) (3520-42-1: S1402), and were electroporated as described above. To test the long-term membrane permeability 5-10 minutes after the original poration, a second dye, ATTO 647 (ATTO-TEC) was added to the external solution of GUVs at the final concentration of 2 µM. Images were acquired using a Leica TCS SP5 confocal microscope (Wetzlar, Germany) using a 63x water-immersion objective (1.2 NA) at 512×512 pixels, 1 A. U., 400 Hz scanning speed and three line averages. To record fast electroporation dynamics in real time, videos were recorded with 128×128 pixels, at 1000 Hz scanning speed and one line average. NBD was excited at 488 nm using argon laser and its emission was detected at 495-550 nm. SRB and ATTO 647 were excited with a diode-pumped solid-state laser at 561 nm and 633, respectively, and detected at 564–615 nm and 640–690 nm. As in above, the GUV samples were discarded after a single electroporation.

2.4.8 Analysis of SNAREs-free and SNAREs-inserted vesicles as well as fusion intermediates in SNAREs-mediated fusion of polymer and hybrid vesicles

The SNAREs-inserted polymer and hybrid vesicles were prepared as described in Chapter 2.4.1. After the formation, first, vesicles were preheated at 37 °C for 30 min. Then, both populations of vesicles were mixed 1:1 (v:v) to initiate fusion and were being continuously stirred at 600 rpm at 37 °C. Between 3-12 minutes after the initiation, aliquots of fusing vesicles were collected and applied as a 3.5 µl droplets onto a glow-discharged R2/1 type 200 Mesh Quantifoil holey carbon grid. Samples were then vitrified using Vitrobot Mark IV System (Thermo Fisher Scientific) and standard Vitrobot Filter Paper (i.e., Ø55/20 mm, Grade 595) at 95 % relative humidity and at 4 °C. A blot force of 2 and blotting time of 6 s were applied for vitrification. The grids with applied samples were mounted onto a FEI Glacios 200 kV

autoloader under cryo conditions and were imaged Falcon 3EC direct electron detector in linear mode and a total dose of 50 e−/Å2. Acquired movies were collected at pixel size of 0.9612. Beam-induced motion correction was performed in RELION 3.0 (*126*) using the built-in implementation of MotionCorr2 (*127*).

Several collaboration partners aided in sample preparation and imaging. Samples were vitrified by Fotis L. Kyrilis and images were captured by Farzad Hamdi. Motion correction was applied by Prof. Panagiotis Kastritis. All mention colleagues are affiliated with Interdisciplinary Research Center HALOmem & Institute of Biochemistry and Biotechnology, Martin Luther University Halle-Wittenberg, Biozentrum, Halle/Saale.

2.5 ASSEMBY AND CHARACTERIZATION OF ENERGY REGENERATING CONSTRUCTS

2.5.1 Determination of *bo₃* oxidase activity via oxygen consumption

The activity of *bo₃* oxidase reconstituted in different types of preformed LUVs was determined as described in (*50*). Oxygen consumption measurements by the enzyme were performed with the Oxytherm system (Hansatech Instruments), comprising Clark-type Pt/Ag electrode (S1/MINI oxygen electrode disc), Peltier temperature control element and the electrode chamber. Data was recorded with the OxyTrace software (Hansatech Instruments). First, 20 µl of proteovesicles containing reconstituted *bo₃* oxidase were resuspended in 970 µl of 20 mM Tris-HCl (pH 7.5), 2.5 mM $MgSO_4$, 100 mM KCl, 2 mM DTT, and the baseline oxygen consumption was recorded. Next, the enzyme was activated with the addition of electron shuttle ubiquinone Q_1 (Merck, 727-81-1: C7956; dissolved in DMSO at 80 mM) at 20 µM final concentration and the enzyme turnover was recorded over several hours, at 22 °C and while the saples were stirred. In the control experiments, oxygen binding to the enzyme was blocked with 0.32 mM (final concentration) of KCN (Merck, 151-50-8: 60178; dissolved in measurement buffer at 40 mM). Additionally, the activity of *bo₃* oxidase in detergent micelles (as stabilized after the extraction and purification) as well as that of aggregated *bo₃* oxidase upon the detergent removal in the absence of vesicles or dispersed membrane constituents, was determined as described above.

2.5.2 Assessment of proton translocation activity by the *bo₃* oxidase in lipid LUVs

The proton pumping activity of *bo₃* oxidase reconstituted in liposomes via mediating detergent, which yielded highest enzyme activity with respect to oxygen consumption was evaluated with ratiometric pH sensitive dye pyranine as described in (*128*). This evaluation required determination of the fraction of residual pyranine outside of vesicles and the calibration of fluorescence changes of pyranine to the changes in internal pH.

First, lipid LUVs were prepared as described in Chapter 2.3.1 in 2 mM MOPS (pH 7.32) (Merck, 1132-61-2: M5162), 50 mM K_2SO_4, but were instead extruded through a polycarbonate filter with a pores size of 200 nm (Merck, Z373427) and were partially solubilized with 0.5 % (w/v, final concentration) of sodium cholate. To vesicles, 700 nM of *bo₃* oxidase was added and the reconstitution mixture was incubated on ice for 30 min, followed by detergent removal (90 mg of Bio-beads, added at once, and incubation for 1.5 h on a rocking platform). Then, proteoliposomes were supplemented with pyranine (Merck, 6358-69-6: H1529) at the 1 mM final concentration, and were subjected to 3 freeze/thaw cycles (30 s freezing in lN₂, thawing in water bath at 35 °C, 10 s vortex) in order to encapsulate this pH sensitive dye. Loaded proteoliposomes were then extruded through polycarbonate filter with pores size of 200 nm to unify their size, and the non-encapsulated pyranine was removed via size exclusion chromatography on the MiniTrap G-25 column (Cytiva, GE28-9180-07) equilibrated with 2 mM MOPS (pH 7.32), 50 mM K_2SO_4.

To measure proton pumping by the oxidase, 35 µl of proteovesicles were resuspended in 665 µl of 2 mM MOPS (pH 7.42), 50 mM K_2SO_4, and were equilibrated for 15 min at room temperature. Then, the oxidase was activated by the addition of 10 mM DTT and 0.15 mM ubiquinone Q_1 (final concentrations) and the pyranine emission was recorded at 510 nm while excited at 405 and 455 nm on Varian Cary Eclipse (Agilent). Samples were stirred in quartz cuvettes (Hellma, 109004F-10-40) at room temperature. Excitation/emission slits were set to 20/20, respectively, and the PMT voltage was set to 500 V.

Next, fluorescence changes of pyranine were calibrated to the changes in pH. To achieve this, 2 µl of pyranine loaded proteovesicles were resuspended in 998 µl of various buffers with various pH. Buffers used were 5 mM MES (pH 5.9, 6.16, 6.48) (Merck, 4432-31-9: M3671), MOPS (pH 6.79, 7.06, 7.30) and Tris (pH 7.60, 8.42). Next, vesicles were supplemented with 100 nM of ionophore nigericin (Merck, 28643-80-3: N7143) and 300 nM

of protonophore carbonyl cyanide 3-chlorophenylhydrazone (CCCP, Merck, 555-60-2: C2759), which facilitated equilibration of inner vesicle pH with the external. Vesicles were incubated at room temperature for 15 min and the fluorescence of encapsulated pyranine at various pH was afterwards measured as described above. The ratio of pyranine fluorescence at two different excitation wavelengths ($R = F_{405}/F_{455}$) was then plotted in dependence of pH and the experimental data was then fitted with the three-parameter logarithmic function:

$$y = a - b \times \ln (x + c) \tag{Eq. 5}$$

where y corresponds to pH and x to the fluorescence ratio R, described above. This enabled determination of constants a, b and c, which could then be used to calculate any pH from the measured fluorescence ratio R.

Next, the amount of residual pyranine, which was not removed on the size exclusion chromatography was determined. This enabled differentiation between the fluorescence response of encapsulated pyranine to internal pH changes inside vesicles and the fluorescence response of external pyranine with respect to external pH changes. To achieve this, 35 µl of proteovesicles were resuspended in 673 µl of 2 mM MOPS (pH 7.42), 50 mM K_2SO_4, 10 mM DTT. The total pyranine fluorescence (of internal and external pyranine) at this pH was then measured at 405 nm ($F_{tot(405,\ pH\ 7.42)}$) and at 455 nm ($F_{tot(455,\ pH\ 7.42)}$). Next, external pH was changed to 6.8 with the addition of 1 M HCl and total pyranine fluorescence at this different pH was recorded again at 405 nm ($F_{tot(405,\ pH\ 6.8)}$) and at 455 nm ($F_{tot(455,\ pH\ 6.8)}$). The fraction of internal pyranine was then calculated according to previously described equation (please see (*128*) for details):

$$x_{in} = \frac{F_{tot(405, pH\ 6.8)} - F_{tot(455, pH\ 6.8)} \times R(pH\ 6.8)}{F_{tot(405, pH\ 7.42)} - F_{tot(455, pH\ 7.42)} \times R(pH\ 6.8)} \tag{Eq. 6}$$

where x_{in} was the fraction of internal (encapsulated) pyranine, F_i (i = 405, 455 nm) were the measured fluorescence emissions at specified excitation and at specified pH (6.8, 7.42) and R was the ratio of fluorescence emissions at 405 and 455 nm ($R = F_{405}/F_{455}$) at the specified pH, calculated from the calibration curve described in previous paragraph. This allowed for the calculation of the fluorescence contribution of externally bound pyranine at any given pH (pH a) at 405 and 455 nm:

$$F_{ex(405,\ pH\ a)} = F_{tot(405,\ pH\ a)} - F_{tot(405,\ pH\ 7.42)} \times x_{in} \tag{Eq. 7}$$

and

$$F_{\text{ex}(455,\,\text{pH a})} = \frac{F_{\text{ex}(405,\text{pH a})}}{R(\text{pH a})} = \frac{F_{\text{tot}(405,\text{pH a})} - F_{\text{tot}/405,\text{pH 7.42}} \times x_{\text{in}}}{R(\text{pH a})} \qquad \text{(Eq. 8)}$$

where the $F_{\text{ex i}}$ (i = 405, 455 nm) was the fluorescence of external pyranine at different excitation wavelength (405, 455) and at desired pH (pH a), F_{tot} was the measured pyranine fluorescence at mentioned wavelengths and at specified pH, x_{in} was the fraction of encapsulated pyranine and the R was the ratio of fluorescence emissions at 405 and 455 nm calculated from the calibration curve for any desired pH a. Finally, fluorescence changed in internal pyranine as the result of proton translocation by the bo_3 oxidase could be calculated from the relation described below (for details please see supporting information of (*128*)):

$$F_{\text{in}(405,\,\text{pH a})} = F_{\text{tot}(405,\,\text{pH a})} - F_{\text{ex}(405,\,\text{pH a})} \qquad \text{(Eq. 9)}$$

and

$$F_{\text{in}(455,\,\text{pH a})} = F_{\text{tot}(455,\,\text{pH a})} - F_{\text{ex}(455,\,\text{pH a})} \qquad \text{(Eq. 10)}$$

where F_{in} corresponded to fluorescence intensity of encapsulated pyranine, F_{tot} corresponded to measured pyranine fluorescence and F_{ex} corresponded to calculated fluorescence emission of external pyranine, all at the specified wavelength (405, 455 nm) and at desired pH (pH a). Fluorescence ratio R of internal pyranine ($R_{\text{in}} = F_{\text{in405}}/F_{\text{in455}}$) could then be determined and inserted into calibration curve to calculate pH changes inside vesicles upon proton pumping by bo_3 oxidase.

2.5.3 Determination of respiration-driven ATP synthesis by the short respiratory chain

The ATP synthesis activity of SRC was recorded as described previously (*44*), with slight modifications. First, 10 μl of proteovesicles co-reconstituted with bo_3 oxidase and ATP synthase were mixed with 480 μl of measurement buffer, 20 mM Tris (pH 8.0), 20 mM K_2HPO_4 (Merck, 7758-11-4: 60353) 10 μl of luciferin/luciferase assay (CLSII, reconstituted in Milli-Q water at 10 mg ml^{-1} according to manufactures protocol, Merck, 11699695001), 0.035 mM ADP (ultrapure, Cell Technology) and 2 mM DTT (Merck, 3483-12-3: 10197777001) and the baseline was recorded. Next, signal was calibrated with the known amount of ATP (Merck, 34369-07-8: A7699) followed by activation of bo_3 oxidase with the addition of 0.02 mM ubiquinone Q_1. ATP synthesis was recorded at 22 °C and in the absence of stirring. In the control experiments, proton pumping by bo_3 oxidase was inhibited as described in previous section, while ATP synthase was inhibited with oligomycin (Merck, 579-13-5: 75351) at 5 μg ml^{-1}. Furthermore, proton gradient was abolished with protonophore carbonyl cyanide 4-

51

(trifluoromethoxy)phenylhydrazone (FCCP, Merck, 370-86-5, C2920) at 200 nmol per 1 mg of vesicles.

2.5.4 Analysis of *bo₃* oxidase partitioning in hybrid membranes via FRET between *bo₃*-ATTO 514 and PE-Rho/PDMS-*g*-PEO-Rho

Hybrid LUVs exhibiting homogeneous distribution of lipid and polymer (30 mol% of soy PC and 70 mol % of PDMS-*g*-PEO), containing 2 mol% of either a lipid dye PE-Rho or Rhodamine-modified polymer PDMS-*g*-PEO-Rho (the amount of non-labelled lipid/polymer was reduced proportionally) were prepared with the freeze/thaw/extrusion method. First, 5 mg of hybrid mixture in chloroform:methanol (2:1, v/v) were deposited into a round-bottom glass vial and the solvent was evaporated under a gentle stream of nitrogen for 1 h. Formed thin hybrid film was rehydrated with 1 mM Tris (pH 7.5), containing 100 mM sucrose, to a final hybrids concentration of mg ml^{-1} by gently vortexing until homogenous suspension was observed. Next, the multilamellar vesicles were subjected to 5 freeze/thaw cycles, 1 min freezing in lN₂ followed by thawing in water batch at 30 °C and 30 s of vortexing. Finally, the size and lamellarity of hybrids was unified by extrusion (21 times) through a polycarbonate filters with pores size of 100 nm (Merck, Z373419). Next, preformed hybrids were partially solubilized with 0.1 % (w/v) sodium cholate and the *bo₃* oxidase was added to vesicles at final concentration of 0.45 μM. The reconstitution mixture was incubated under mild agitation (on rocking platform) and at 4 °C for 30 min, followed by the detergent removal via Bio-Beads. The beads were supplemented to proteohybrids in 3 subsequent additions, 30 mg of beads per 200 μl of reconstitution mixture each, followed by 30 min incubation period, at room temperature on a rocking platform. After that, supernatant (reconstituted hybrids) was carefully collected and stored at 4 °C until measurements.

To determine enzyme partitioning in hybrid membranes, 20 μl of pre-cooled proteohybrids containing either of two dyes were dispersed in pre-cooled 0.8 ml of 1 mM Tris-HCl (pH = 7.5), 100 mM sucrose and the fluorescence emission of ATTO 514 (enzyme dye) at 533 nm was monitored while excited at 511 nm (slits position = 10/10, PMT = 800 V) in a Varian Cary Eclipse (Agilent) spectrophotometer at constant stirring and thermostated at 5 °C. Next, the dequenching of enzyme dye was induced with the addition of octyl glucoside in in 30 subsequent steps, 2 μl of 10 % (w/v) detergent each, and the changes in ATTO 514 emission

based on its interaction with rhodamine quencher was recorded. After each addition of OG, the samples were vortexed for 5 s.

2.5.5 Determination of the orientation and reconstitution efficiency of *bo₃* oxidase in LUVs reconstituted with various detergents at the membrane saturation (R_{sat}) and solubilization (R_{sol}) point

Lipid, polymer and hybrid LUVs were prepared as described in Chapter 2.3.1 but at the concentration of 10, 40 and 20 mg ml^{-1}, respectively (at nearly same molar concentration). Then, preformed vesicles were reconstituted with 0.33 µM (final concentration) of *bo₃*-ATTO 488 at membrane saturation (R_{sat}) and at total solubilization (R_{sol}) points (as determined in Chapter 2.3.12) with sodium cholate, sodium deoxycholate, dodecyl maltoside, octyl glucoside and Triton X-100 as mediating detergents. For polymersomes reconstituted at R_{sat}, detergent was already included in rehydration buffer during vesicle formation. During all preparation steps, the reconstitution mixtures/proteovesicles were protected from light to reduce photobleaching of the attached dye. Vesicles were reconstituted at 4 °C and during the detergent removal by Bio-beads, solutions were shake at 600 rpm at 4 °C. Following the reconstitution, proteovesicles were ultracentrifuged at 270000 g (rotor F50L, 096-247028, Thermo Scientific), at 4 °C for 90 min. This enabled separation of uninserted enzyme (contained in supernatant after ultracentrifugation step) from the reconstituted vesicles (pelleted). Supernatant was discarded and pellets were resuspended in 200 µl of 50 mM HEPES pH 7.5, 2.5 mM MgSO₄, and 50 mg ml^{-1} sucrose.

Fluorescence of *bo₃*-ATTO 488 in reconstituted vesicles was then recorded with Varian Cary Eclipse (Agilent) at the excitation wavelength of 501 nm, emission wavelength of 523 nm, with the slits positioned at 10/10 and with the PMT voltage set to 550 V.

In the next step, outwards-facing dye (meaning the outwards-facing enzyme) was removed by detaching the dye from the His-tagged enzyme. Initially, this was attempted by chelating Ni^{2+} from the His-Ni-dye complex by EDTA (Merck, 60-00-4: EDS). Unfortunately, the EDTA treatment was unreliable in polymersomes and hybrids, presumably due to the unknown interactions between the polymer and said chelator. Furthermore, the dissociation of mentioned complex was relatively slow even at relatively high concentration of EDTA (500 mM). Therefore, new strategy was devised for the dye removal.

In proteoliposomes, the fluorescence of ATTO 488 attached to the His-tagged *bo₃* oxidase was instead bleached with sodium dithionite (Merck, 7775-14-6: 157953) dissolved in Milli-Q (solution was prepared fresh prior to experiments). Sodium dithionite was added to proteoliposomes after their initial fluorescence was recorded as described above at the final concentration of 10 µM. Samples were mixed by flickering for about a minute and the fluorescence was recorded again with the same setup described as above. In this setup, the membrane impermeable sodium dithionite bleached only the fluorescence of outwards-facing dye (and enzyme), while the fluorescence of inwards-facing dye remained unchanged. This enabled the determination of the *bo₃* oxidase orientation.

In polymersomes and hybrids, sodium dithionite was observed reacting with the polymer component of the membrane, which led to polymer degradation and towards membrane permeabilization. The latter could be observed as the total bleaching of ATTO 488 fluorescence over time, until no fluorescence at all could be detected. Therefore, sodium dithionite could not be used to determine the orientation of *bo₃* oxidase in polymersomes and hybrids. Instead, the dye dissociation was induced with imidazole. First, vesicles were reconstituted as described above and their fluorescence was measured. Then, proteovesicles were pelleted via ultracentrifugation (90 min, 4 °C, 270000 g, same as in the initial ultracentrifugation step), were resuspended in 200 mM imidazole solution (prepared in Milli-Q) and were incubated at room temperature and protected from light for 30 min. Afterwards, dissociated dye was removed from the samples via Nycodenz density gradient. To achieve this, imidazole-treated vesicles were supplemented with 600 µl of 50 mM HEPES pH 7.5, 2.5 mM MgSO₄, and 50 mg ml^{-1} sucrose, and were transferred into open top polypropylene ultracentrifuge tubes (Beckman Coulter, 328874). Next, vesicles were first layered with the 1.8 ml of 75 % (w/v) Nycodenz (ProGen, 1002424) dissolved in the same buffer, and then with the 1.8 ml of 25 % (w/v) Nycodenz solution. Finally, 800 µl of vesicle buffer was placed on top of the gradient. Proteovesicles applied to Nycodenz gradient were then ultracentrifuged at 230000 g (rotor TH-660, Thermo Scientific; slow acceleration and deacceleration mode was selected to avoid disturbing the density gradient), for 1.5 h, at 4 °C. After this step, proteovesicles were partitioned in the upper vesicle layer of the gradient, while the detached dye could be found in the lower layers. Hence, the proteovesicles were collected from the top-most layer, pelleted via ultracentrifugation (90 min, 4 °C, 270000 g, same as in the initial ultracentrifugation step) and resuspended in vesicle buffer. Their fluorescence was then measured as described above.

The orientation of bo_3 oxidase was determined by comparing the fluorescence of proteovesicles after the reconstitution with the fluorescence following the sodium dithionite (proteoliposomes) or imidazole (proteohybrids and polymersomes) treatment. Furthermore, the fluorescence of 0.33 µM of bo_3-ATTO 488 was determined in 20 mM HEPES (pH 7.5), 0.05 % (w/v) dodecyl maltoside and compared to the fluorescence of bo_3-ATTO 488 in proteovesicles after the reconstitution to determine the reconstitution efficiency of bo_3 oxidase.

2.5.6 Determination of the orientation and relative reconstitution efficiency of ATP synthase in LUVs reconstituted with various detergents at the membrane saturation (R_{sat}) and solubilization (R_{sol}) point

Lipid, polymer and hybrid LUVs, prepared as described in Chapter 2.3.1, were reconstituted with ATP synthase (bo_3 oxidase was omitted here), as described in Chapter 2.3.11, at the theoretical concentration of 1 ATP synthase molecule per vesicle, but at 4 °C. All types of vesicles were reconstituted at membrane saturation (R_{sat}) and at total solubilization (R_{sol}) points as determined in Chapter 2.3.12 with sodium cholate, sodium deoxycholate, dodecyl maltoside, octyl glucoside and Triton X-100 as mediating detergents. After the addition of detergents, vesicles were incubated at 4 °C for 15 min to allow for detergent partitioning into the membranes. Upon detergent removal, proteovesicles were collected, concentrated with ultracentrifugation at 270000 g (rotor F50L, 096-247028, Thermo Scientific), at 4 °C for 60 min, and resuspended in 40 µl of vesicle buffer (50 mM HEPES pH 7.5, 2.5 mM MgSO$_4$, and 50 mg ml^{-1} sucrose).

The activity of reconstituted ATP synthase in the hydrolysis direction way measured according to previously described protocol (*128, 129*). Briefly, absorbance blank was recorded at 340 nm on Specord 50 Plus (Analytik Jena) with Tris (pH 7.5/HCl), 5 mM NaCl, 5 mM MgCl$_2$, 3 mM phospho(enol)pyruvate (Merck, 4265-07-0: 860077), 6 U of L-lactate dehydrogenase (Merck, 10127876001, 550 U mg^{-1}, 5 mg ml^{-1}), 5 U of pyruvate kinase (Merck, 10128155001, 200 U mg^{-1}, 10 mg ml^{-1}) and 40 µl of concentrated proteovesicles. Then, 0.25 mM NADH (dissolved in 10 mM Tris pH 8.5) was added and a baseline was recorded. ATP synthase was then activated by the addition of 2 mM ATP (resuspended in Milli-Q, pH adjusted to 7.0 with 1 M KOH) and the ATP hydrolysis rate of outwards-facing enzyme ("AHA1") was monitored indirectly as the NADH synthesis by lactate dehydrogenase for several seconds, until enough data points were captured to enable the determination of enzyme turnover. Next, 2 µM

of ionophore carbonyl cyanide 3-chlorophenylhydrazone (CCCP, Merck, 555-60-2: C2759) were added, which prevented the formation of inhibitory membrane potential and enabled determination of non-inhibited ATP hydrolysis rate ("AHA2") over several seconds, as described above. Finally, Triton X-100 was added at the concentration corresponding to total solubilization point R_{sol} of the measured type of vesicles, as determined in Chapter 2.3.12, to completely solubilize proteovesicles. Typically, 0.05 % (w/v, final concentration) of Triton were added, with care being taken not to exceed R_{sol} concentration, since any excess amount of detergent would stimulate the activity of ATP synthase, which would lead to overestimation of non-inhibited total hydrolysis rate. This enabled activation of all ATP synthase, regardless of the enzyme orientation, and the determination of ATP hydrolysis rate of inwards- as well as outwards-facing enzyme ("AHA3").

To determine ATP synthase orientation, the ATP hydrolysis rates of uninhibited outwards-facing enzyme (AHA2) was compared with the total hydrolysis by outwards- as well as inwards-facing enzyme (AHA3). Furthermore, relative ATP synthase reconstitution efficiency was calculated by normalizing ATP hydrolysis rates (AHA3) or different setups to the reconstitution setup, which yielded highest overall ATP hydrolysis (i.e., liposomes reconstituted with sodium cholate at R_{sol} for this detergent). This enabled direct comparison of different reconstitution setups with respect to ATP synthase integration, although the ATP synthase reconstitution efficiency was overestimated by the reconstitution efficiency of ATP synthase at R_{sol} for sodium cholate. To correct for this fact, comparison between the activity of ATP synthase, reconstituted with the mentioned configuration and of the ATP synthase, stabilized in detergent micelles only, was attempted. It was found that the activity of the latter was always increasing with the increasing concentration of stabilizing detergent (due to the aforementioned stimulative role of the detergent), which led to the overestimation of the actual hydrolysis rates. Therefore, the ATP synthase reconstitution efficiencies determined with this method are in this work reported as the relative values normalized to highest achieved hydrolysis with reconstituted enzyme.

2.5.7 Evaluation of the effect of freezing/thawing on the activity of short respiratory chain

Commercial attractiveness of biochemical formulations depends strongly, among other things, on their stability when stored over a longer period of time. Most often, formulations featuring vesicles are snap-frozen in liquid nitrogen and are stored at ultralow temperatures.

Furthermore, shipping of such material additionally requires freezing of the samples and then thawing before usage. In this context, the effect of freezing and subsequent thawing on the ATP synthesis by the short respiratory chain, comprising *bo₃* oxidase and ATP synthase was investigated.

Lipid LUVs, prepared as described in Chapter 2.3.1, were reconstituted as described in Chapter 2.3.11 at the theoretical ratio of 5 *bo₃* oxidase and 1 ATP synthase per vesicle. Following the reconstitution, proteoliposomes were aliquoted into 20 µl aliquots and were snap-frozen in liquid N_2. Then, these aliquots were kept submerged in nitrogen for 30 min before thawing. The latter was attempted in two ways. Some aliquots were thawed rapidly in warm water kept at 35 °C. Meanwhile, other aliquots were thawed slowly on ice over the course of 15-20 min. The ATP synthesis by SRC was then measured as described in Chapter 2.5.3.

2.5.8 Cryo-electron microscopy imaging of short respiratory chain

For cryo-EM examination the samples were vitrified using a Vitrobot (FEI) plunging device. A 5 µl of the sample dispersion was applied to a holey carbon coated TEM grid that has been glow discharged shortly before. After removing excess sample solution with a filter paper, the grid was immediately plunged into liquid ethane. For the subsequent examination, the specimen was transferred to a TEM (FEI Tecnai F20) keeping cryogenic conditions using a cryo-EM holder (Gatan 926). Conventional TEM imaging was done using an acceleration voltage of 200 kV. Micrographs were acquired with a 2k CCD Camera (Gatan US1000) under low dose conditions. Samples were prepared for cryo-EM imaging and recorded by Dr. Ingo Lieberwirth, Max Planck Institute for Polymer Research.

2.5.9 Tuning of ARC osmolarity to CETCH cascade

To facilitate coupling between the ARC and the CETCH cycle, and to avoid vesicle deformation due to osmotic imbalance, the osmolarity of ARC was adjusted to correspond to the osmolarity of the CETCH. In this respect, the osmolarity of CETCH was measured with the Osmomat 3000 (Gonotec) and was determined to be 1230 ± 13 mOsm kg^{-1}. Next, the osmolarity of vesicles buffer used for preparation of LUVs was tuned to match the measured value. To achieve this, high osmolarity vesicle buffer was prepared containing 20 mM HEPES (pH 7.5), 2.5 mM $MgSO_4$ and 809 mM sucrose. Likewise, ATP synthase measurement buffer was prepared with matching osmolarity, comprising 20 mM Tris (pH 8.0), 20 mM K_2HPO_4 and

685 mM sucrose. The ATP synthesis activity of SRC and ARC prepared in high osmolarity vesicles buffer and measured in the high osmolarity measurement buffer was then recorded with the setup described in Chapter 2.5.3.

2.5.10 Activity of SRC in hypoosmotic and hyperosmotic environment

Proteoliposomes were reconstituted with bo_3 oxidase and ATP synthase with 0.6 % (w/v) sodium cholate as the mediating detergent as described in Chapter 2.3.11 in 20 mM HEPES (pH 7.5), 2.5 mM $MgSO_4$ and 775 mM sucrose with the osmolarity of 1194 ± 10 mOsm kg^{-1}. Then, the ATP synthesis was measured following the protocol described in Chapter 2.5.3 in either hypotonic buffer (20 mM Tris pH 8.0, 20 mM K_2HPO_4, 50 µM $CaCl_2$, 200 µM $MgSO_4$ and 300 mM sucrose; 412 ± 5 mOsm kg^{-1}) or in hypertonic buffer (20 mM Tris pH 8.0, 20 mM K_2HPO_4, 50 µM $CaCl_2$, 200 µM $MgSO_4$ and 900 mM sucrose; 1561 ± 12 mOsm kg^{-1}).

Furthermore, changes in vesicles size when subjected to the above-mentioned osmotic shock were recorded via DLS, as described in Chapter 2.3.3, 1, 5, 10 and 15 min after they were mixed with either hypotonic or hypertonic buffer.

2.5.11 Determination of formate dehydrogenase activity

The activity of formate dehydrogenase, purified as described in Chapter 2.1.3, was determined spectrophotometrically (Specord 50 Plus, Analytik Jena) with either NAD^+ or $NADP^+$ as substrates and in a buffer intended for ARC1 integration. Towards this end, baseline was recorded with Tris (pH 8.0), 20 mM K_2HPO_4, 200 mM formate (Merck, 141-53-7: 71539) and 0.06-8 mM β-NAD^+ (Merck, 20111-18-6: N0632) or 0.06-8 mM $NADP^+$ (Merck, 24292-60-2: 10128031001). Next, the reaction was initiated with the addition of 0.2 mg ml^{-1} (final concentration) of FDH and the change in absorbance was recorded at 340 nm. To calculate the concentration of synthesized NADH/NADPH from the measured absorbance, the extinction coefficient $\varepsilon_{340} = 6300$ M^{-1} cm^{-1} was used, as provided by Merck.

2.5.12 Extension of the short respiratory chain with the type 2 NADH dehydrogenase, DT-diaphorase; coupling between dehydrogenase and bo_3 oxidase

Lyophilized NADH dehydrogenase DT-diaphorase (DTD) was purchased from Merck (D1315, > 100 U mg^{-1}, molecular weight $= 31000$ g mol^{-1} for monomer) and was

reconstituted at 2 mg ml^{-1} (64.5 µM) in Milli-Q, aliquoted, frozen in lN$_2$ and stored at −20 °C.

After this expansion, the enzymatic assembly comprising DT-diaphorase, bo_3 oxidase and ATP synthase was referred to as the artificial respiratory chain variant 1, or shorter ARC1. For measurements of the ATP synthesis activity of the ARC1, 20 µl of vesicles containing 5 bo$_3$ oxidase and 1 ATP synthase per vesicle, reconstituted as described in Chapter 2.3.11, were added to 450 µl 20 mM Tris (pH 8.0), containing 20 mM K$_2$HPO$_4$, 100 mM KCl, 2.5 mM MgSO$_4$, 0.4 mM NADH (Merck, 606-68-8: 10107735001) and a baseline was recorded. Then, 10 µM of ubiquinone Q$_1$ (final concentration) was added and the reaction mixture was incubated for 5 min at room temperature. Reaction was initiated with the addition of 2 µM of DTD (final concentration) and the oxygen consumption by the bo_3 oxidase was recorded with the Oxytherm system, as described in Chapter 2.5.1.

2.5.13 Coreconstitution of type 1 NADH dehydrogenase, complex I, with bo_3 oxidase and ATP synthase in lipid LUVs towards the construction of ARC2

Three large transmembrane respiratory complexes – complex I (NADH dehydrogenase), bo_3 oxidase and ATP synthase were inserted into lipid membranes to form the artificial respiratory chain variant 2 ("ARC2").

Lipid LUVs were formed using protocol described in Chapter 2.3.1 and their concentration in suspension was calculated as reported in the mentioned section, based on their average size as determined by DLS. Then, LUVs were partially solubilized by the addition of membrane saturating (R_{sat}) concentration of either sodium cholate (0.17 %, w/v, final), octyl glucoside (0.25 %, w/v, final) or Triton X-100 (0.07 %, w/v, final) and the suspensions were incubated at room temperature for 15 min to allow for detergent partitioning into membranes. In the next step, respiratory enzymes were added to partially solubilized vesicles. With respect to this, complex I was added at the theoretical ration of 3 enzymes per vesicle, while the bo_3 oxidase and ATP synthase were added at 1 and 2 enzyme(s) per vesicle, respectively. Furthermore, doubling the enzyme content was explored, as well as increasing only the number of copies of a specific enzyme, while keeping the number of other enzymes constant. The sequence at which enzymes were added to solubilized vesicles was the following. First, ATP synthase was added, followed by complex I and finally bo_3 oxidase. After each addition, the reconstitution mixture was briefly vortexed (3 short bursts at 500 rpm) and incubated for 5 min,

at 4 °C. Detergent was removed by two-step addition of Bio-beads, 45 mg of beads per 100 µl of reconstitution mixture, followed by 90 min incubation, at 4 °C, while aggitated at 600 rpm.

2.5.14 NADH oxidation by complex I reconstituted in ARC2 proteoliposomes

Oxidoreductase activity of complex I in ARC was measured by following the changes in NADH absorbance, as described in Chapter 2.5.6, with modifications. To 615 µl of 20 mM Tris pH 8.0, 20 mM K_2HPO_4, 50 µM $CaCl_2$, 200 µM $MgSO_4$, 100 µM ADP, 15 µl of ARC2 proteoliposomes were added along with 64 µM of ubiquinone Q_1, following by 2 min incubation at room temperature, and the blank was recorded. Complex I was then activated by 500 µM NADH and the proton translocation-dependant activity was recorded. Finally, 0.28 % (w/v) of Triton X-100 were added to vesicles, corresponding to detergent concentration, which facilitated total solubilization of vesicles. The changes in complex I turnover in this uninhibited state were then recorded.

2.5.15 Determination of ATP synthesis by ARC2

The ATP synthesis by ARC2 was determined following the protocol, described in Chapter 2.5.3, with minor modifications. First, 10 µl of ARC2 proteoliposomes were dispersed in 100 µl of 20 mM Tris pH 8.0, 20 mM K_2HPO_4, 50 µM $CaCl_2$, 200 µM $MgSO_4$, 100 µM ADP and 0.23 mg ml^{-1} CLSII reagent, and the baseline was recorded. After signal calibration with a known amount of ATP, the reaction was initiated by the addition of 500 µM of NADH along with 64 µM of ubiquinone Q_1 (final concentrations). Changes in luminescence correlating to ATP content were then recorded for up to two hours. Furthermore, the ATP synthesis in this system while circumventing the complex I was also recorded. In this case, DTT was added to measurements several minutes after NADH/Q_1 at the final concentration of 10 mM.

2.5.16 Coupling of the artificial respiratory chain to the oxidation of malate and formate – determination of oxygen consumption and ATP synthesis

The ARC2, consisting of ATP synthase, *bo₃* oxidase and NADH dehydrogenase, described in Chapter 2.5.12 was coupled with the simple metabolic conversion featuring oxidation of malate to oxaloacetate and NADH by L-malate dehydrogenase (MDH), or to oxidation of formate to CO_2 and NADH by the formate dehydrogenase (FDH). The MDH was

purchased from Merck (from pig heart, 10127256001) and was added at the concentration of 5 mg ml^{-1} (1200 U mg^{-1}), while the FDH was purified as described in Chapter 2.1.3.

To test the ATP synthesis driven by malate as sole energy source, to 445 µl of 20 mM Tris (pH 8.0 – optimal pH with respect to MDH activity would be around 9-10, compromise is made with respect to other enzymes of ARC1) containing 20 mM K$_2$HPO$_4$, 100 mM KCl, 2.5 mM MgSO$_4$ and 450 µM β-NAD$^+$ (Merck, 20111-18-6: N0632), 0.6 µl of MDH (3.6 U/ml) were added and the reaction mixture was incubated for 5 min at room temperature. Then, 0.27 µl of malate (from 2 M stock, 540 µM final conc.) was added to the mixture and the mixture was incubated further for 5 min, at room temperature. Next, 20 µl of vesicles, containing 5 bo$_3$ oxidase and 1 ATP synthase per vesicle, prepared as described in Chapter 2.3.11, were added to the measurement mixture and the baseline was recorded. Reaction was initiated by the addition of 4 µl Q$_1$ (10 mM stock) and 15 µl DTD (64.5 µM stock) and the oxygen consumption by the bo$_3$ oxidase was detected by Clark-type electrode in Oxytherm system, as described in Chapter 2.5.1. The setup for probing a formate-driven enzymatic cascade was the exact same, the only difference being that 200 mM formate was added to the reaction mixture instead of malate. While different, both of those values were relevant in the context of the CETCH cycle (*58*), in which these two substrates are represented at the specified concentrations.

In the case where the activity of ATP synthase was being measured, the reaction mixture described above was supplemented with 4 µl of ADP (8.45 mM stock) and 10 µl of luciferin/luciferase reagent CLSII at 10 mg ml^{-1} after the addition of malate/formate and the baseline was recorded. Afterwards, the ATP synthesis was measured as described in Chapter 2.5.3.

2.5.17 Coupling between the ARC2 and the CETCH cycle

To 120 µl 100 mM MOPS KCl (pH 7.5), containing 0.2 mg ml^{-1} carbonic anhydrase (MP Biomedicals, 02153879-CF), 2 mM ADP, 5 mM NADPH, 5 mM MgCl$_2$, 0.5 mM coenzyme A (Merck, 18439-24-2), 50 mM NaH^{13}CO$_3$ (Cambridge Isotope Laboratories), 20 mM K$_2$HPO$_4$, 0.1 mM coenzyme B12 (Merck, 68-19-9: V2876), 20 mM formate, 15 µl of lipid LUVs, reconstituted with ATP synthase (at 0.1 µM in vesicles) and *bo$_3$* oxidase (at 0.5 µM in vesicles) as described in Chapter 2.3.11, and preincubated with 50 µM of ubiquinone Q$_1$, were added. Then, 2 µM of DT-diaphorase was added, followed by the addition of enzymes of the CETCH cycle, as described in detail in (*58*). The reaction was started with the addition of 100 µM propionyl-CoA (synthesized as described in (*58*)) and the reaction mixture was carried out

at 30 °C for 2 h. Then, 9 µl were withdrawn from the mixture, quenched in formic acid at the final concentration of 4 % (v/v) and the 4-hydroxybutyrate and glyoxylate content in the withdrawn samples was analyzed by MS as described in (*58*). When supplied with the ARC1 module and the coupling protocol, the above-described reaction was assembled and carried out by collaboration partner Christoph Diehl (Max Planck for Terrestrial Microbiology, Marburg).

2.5.18   Resealing of lipid membranes upon protein insertion by Poloxamer 188

To probe into the membrane resealing capabilities of Poloxamer P188 (Merck, 9003-11-6: P5556) in the context of proteoliposomes, the surfactant was added to vesicles solubilized with various detergents and functionalized with SRC/ARC, after the reconstitution, below the critical micellar concentration for this detergent (0.04 mM). Towards this end, freshly reconstituted vesicles were supplemented with 0.02 mM of P188 and were incubated for 30 min, at 4 °C. Then, either the ATP synthesis activity of SRC/ARC-containing surfactant-treated vesicles was determined as described in Chapters 2.5.3 and 2.5.15, or the oxidoreductase activity of complex I was determined as described in Chapter 2.5.14. The activities of treated vesicles were then compared with the activities of untreated ones.

2.5.19   Auxiliary oxygen regeneration system

To sustain the prolonged activity of *bo₃* oxidase and to avoid oxygen depletion in measured systems, the auxiliary oxygen supply was developed, comprising calcium peroxide (CaO_2) microparticles in combination with the enzyme catalase.

To test the oxygen release by CaO_2 particles, first, baseline was recorded on the Oxytherm system with 20 mM Tris (pH 8.0), 20 mM K_2HPO_4. Next, 1 mg of CaO_2 particles were added to 1 ml of the measurement buffer and the changes in oxygen content were recorded. The hydrogen peroxide, a side product of particle degradation was in the following step converted to oxygen and water by the addition of 1 U of catalase (Merck, 9001-05-2: C9322) and the changes in oxygen concentration was recorded.

If the oxygen regeneration system was used to boost the activity of SRC, ARC, or the coupled system of ARC/CETCH, calcium peroxide particles in combination with catalase were added to the measurement buffer with composition described in Chapter 2.5.15, while everything else was kept the same. While several different concentrations of particles were tested for suitability, increasing particle content has not led to proportional increase in oxygen

release due to particle sedimentation and the related availability of active (dissolving) surface in measured solutions. Furthermore, higher particle content was seen to disturb the light-based measurements.

3 RESULTS

3.1 CONSTRUCTION, CHARACTERIZATION AND STABILIZATION OF THE ARTIFICIAL RESPIRATORY CHAIN

This section describes the sequential construction and characterization of the artificial respiratory chain, an energy module intended for the integration with the metabolic conversion module, in lipid vesicles. Furthermore, our strives to increase functional stability and durability of the respiratory chain by reconstituting it in polymer-based membranes are reported. Main objectives of this assembly stage of the artificial mitochondrion were:

a) Formation and characterization of lipid, polymer and lipid/polymer hybrid vesicles intended for protein insertion,

b) Integration of minimal OXPHOS machinery comprising *bo₃* oxidase and ATP synthase in these vesicles with different mediating detergents and detergent removal techniques as well as variable degree of membrane solubilization,

c) Determination of the reconstitution parameters such as enzyme integration efficiency and orientation in relation to the choice of detergent,

d) Elucidation of the interplay between various membranes and the inserted enzymes based on the changes in enzymatic activity as well as the changes in membrane properties upon enzyme reconstitution,

e) Probing for the protective properties of PDMS-*g*-PEO with respect to oxidative damage as well as for its biocompatibility.

3.1.1 Preparation and characterization of lipid, polymer and hybrid nano and microcompartments

At first, suitable nano-sized vesicles, intended for the insertion of respiratory enzymes were prepared. To increase long-term stability, PDMS-*g*-PEO was chosen due to its high reported fluidity and similar membrane thickness to the one of commonly used lipid membranes, as discussed in the introduction. Another important characteristic of this polymer

is its miscibility with lipids towards the formation of lipid/polymer hybrid vesicles (*38, 117*). This attribute is of particular importance in the context of membrane protein insertion considering the essential role of lipids as facilitators of MP activity. Cardiolipin, for instance, was shown to induce conformational changes in respiratory complex I (also used in this work), modulating the accessibility of the quinone to the enzyme (*130*). Similar essential role of cardiolipin in promoting enzymatic activity was also observed in other enzymes of respiratory chain, for example in cytochrome c oxidase (*131*) or in Complex III (*132, 133*), where the enzyme activity was reduced 28-50 % in the absence of this lipid. However, lipids are not only modulating enzymatic activity via their interactions with the substrate binding domains of MPs. As membrane building blocks, they are crucial determinants of membrane stiffness, curvature, charge, thickness and permeability, all of which are known to have a profound effect on the activity of integrated enzymes (*134-137*). With liposomes mimicking the natural highly optimized environment of MPs and with the polymersomes presenting the more stable and resistant man-made alternative, hybrids are, in this work, explored as a potential "the best of both worlds" compromise for the purpose of protein insertion. The lipids used in this study were extracted from soy beans and their lipid content is predominantly (95 %) phosphatidyl choline. As already discussed, highest activity was observed in particular with this extract in several reconstituted complex MPs (*44, 73, 138, 139*).

First, nano-sized lipid, polymer and hybrid vesicles were formed with the freeze/thaw and extrusion technique (*140*). With this approach, thin films comprising membrane constituents were first rehydrated with buffered solution resulting in spontaneous formation of multilamellar vesicles. Then, the size and lamellarity of the latter were reduced first via cycles of rapid freezing and thawing (this step is omitted in polymersomes) and further via the extrusion through pores of defined sizes. Size, dispersity and surface charge of so-formed vesicles were first analysed by DLS. Shown in Fig. 6A are typical intensity-based size distributions of different types of vesicles. The size of vesicles (with Z-averages of 104 nm for liposomes, 105 nm for hybrids and 102 nm for polymersomes) is closely reflecting the diameter of pores used in the extrusion step (100 nm). Furthermore, all types of vesicles were uniform in size with the relatively low determined polydispersity indices of 0.158 for liposomes, 0.151 for hybrids and 0.149 for polymersomes. It is important to note that the size of the vesicles varied between preparations, with sizes ranging from 88–123 nm across all formulations. This was mainly due to differences in buffer composition between different experiments and also due to small differences in membrane composition, for instance when lipid dyes were being

added to the system to enable imaging. Since in the initial experiments, enzymes were reconstituted into these preformed vesicles at the theoretical *enzyme per vesicle* concentrations, the observed size variability was accounted for in the calculations of the concentration of vesicles prior to reconstitutions, as described in Chapter 2.3.11. Finally, the vesicles prepared in 20 mM HEPES (pH 7.5), 150 mM KCl and 50 g l^{-1} sucrose were found to be neutral (≈ -10 to 10 mV) charge-wise, with the measured zeta potential of liposomes of 3.1 ± 0.2, hybrids of -0.97 ± 0.1 and polymersomes of -1.5 ± 0.1 mV (Fig. 6B). This indicated that the vesicles were prone to aggregation and sedimentation, underlining the importance of the suspension homogenization via mechanical agitation in various preparations steps as well as during measurements.
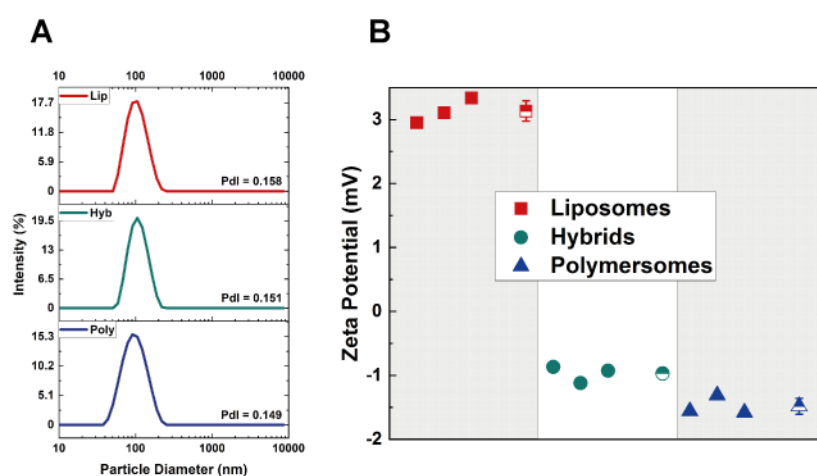
Fig. 6. Size and surface charge of lipid, hybrid and polymer LUVs. (**A**) Intensity-based size distribution of different types of compartments prepared with the freeze/thaw and extrusion method, as determined by DLS. Specified is the polydispersity index (PdI). (**B**) Zeta potential of different types of compartments. Each point represents an individual measurement. Average values with standard error are indicated with half-filled symbols. All data was recorded in 20 mM HEPES (pH 7.5), 150 mM KCl and 50 g l^{-1} sucrose, at 22 °C.

Next, the morphology of formed hybrid and polymer vesicles was determined by cryo-EM. Examples of different types of vesicles can be seen in Fig. 7 (polymer membrane seen as single fuzzy contour and lipid bilayer as characteristic double contour). The imaging revealed unilamellar hollow structures that were occasionally slightly elongated, likely due to the force applied to them during the extrusion. The membranes appeared the most relaxed in the case of polymersomes and the tensest in liposomes, while the intermediate relaxation was assumed by the hybrids. This suggested that the membrane tension was lower in polymersomes and hybrids in comparison to liposomes. Furthermore, the measured membrane thickness was 6.0 ± 1.1 nm

for polymersomes. Meanwhile, lipid domains in hybrids exhibited thickness of 4.1 ± 0.5 nm, while the thickness of polymer portion remained the same as in polymersomes (6.0 ± 0.7). Thickness of PDMS-*g*-PEO membranes was in the above-mentioned buffer slightly higher than the reported thickness of about 5 nm of such membranes in water (*36*), likely due to the swelling of PEO in the presence of salt, as observed in the simulations (*141*). Nevertheless, such minor divergence from the values observed in liposomes (3–5 nm) (*22*) did not lead into non-compensable hydrophobic mismatch between the membrane and inserted proteins. In fact, we recently showed that the PDMS-*g*-PEO polymer would compress around the inserted proteins (*97*) to match the thickness of their hydrophobic portion. Similar conformational adaptation can be observed in hybrid vesicles at polymer/lipid domain boundary (*142*).
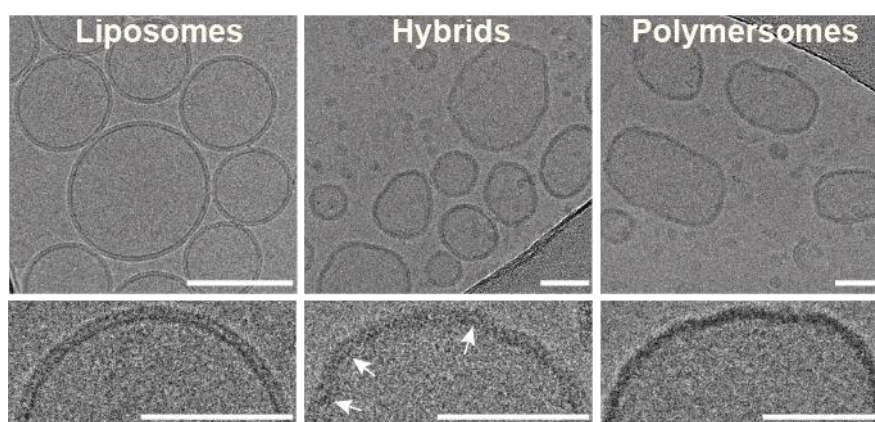
Fig. 7. Cryo-EM micrographs of lipid, hybrid and polymer LUVs. Enlarged portions of different types of membranes can be seen in bottom panels. Lipid-rich domains (double contour) of hybrid vesicles are indicated with white arrows. Scale bars are 50 nm. Defocus ≈ −2 μm.

In parallel, micron-sized hybrid vesicles were prepared with the electroformation procedure (*38, 111*), which enabled characterization of polymer and lipid distribution in hybrid membranes. While the hybrid vesicles comprising PDMS-*g*-PEO and either low or high melting transition temperature lipids (palmitoyl-2-oleoyl-sn-glycero-3-phosphocholine (POPC) and 1,2-dipalmitoyl-sn-glycero-3 phosphocholine (DPPC), respectively) were formed previously (*38, 117*), it was unclear whether hybrids comprising a heterogenous mixture of lipids can readily be formed in similar fashion. To enable visualization of polymer localization in prepared vesicles, PDMS-*g*-PEO was modified with fluorescent dyes, as described in Chapter 2.2.3. Similarly, fluorescent lipids were used to distinguish lipid-containing portions of the membrane. As with nano-sized vesicles, first, thin films comprising lipid and polymer at different molar ratios were formed on the ITO-coated glass surface, which were then rehydrated with buffered solution, in this case in the electric field. With the assistance of the latter, thin

films swelled until portions of them were seen budding off, forming giant unilamellar vesicles. These vesicles were then collected and imaged via the fluorescence microscopy. Previous report (*38*) suggested that homogenous distribution of lipids was observed in hybrids, which contained 20 (in the case of PDMS-*g*-PEO/POPC) or 40 mol% or less lipid (in the case of PDMS-*g*-PEO/DPPC). With the increased lipid content above the specified cut-offs, phase separation and the formation of lipid-rich and polymer-rich domains was reported. Similarly, in present work, the mentioned transition threshold determining architecture of hybrid vesicles was sought after. In the case of hybrids formed from soy lipids and PDMS-*g*-PEO, well-mixed membranes with no observable microscopic domains were seen in membranes featuring 30 mol % of lipid or less, while phase separated membranes were observed at higher lipid concentrations (Fig. 8). This is in agreement with behaviour of PDMS-*g*-PEO/POPC hybrids, which is unsurprising, considering the similar disordered organization (*97*) of lipids used in both studies, at room temperature. Furthermore, the stability of microscopic hybrids was probed for more than 40 days. Homogeneous hybrids remained stable – no phase separation was observed at later times and their structural integrity remained very high (insignificant number of vesicles were seen bursting during this time). On the other hand, this was not the case with heterogenous hybrids. Lipid domains of the latter were budding off several hours after the formation, leading to the complete fission between lipid and polymer. Similar finding was reported by Chemin et al. (*38*), where this phenomenon was reported to occur within hours. Nevertheless, following fission, formed liposomes and polymersomes remained stable for several weeks. With the compositional breakpoint determined, hybrid nano- as well as micro-sized vesicles could thereafter be prepared with either homogeneous or heterogeneous configuration. It is important to note that for all reconstitution experiments described in this work, only homogeneous hybrids (featuring 70 mol% of polymer and 30 mol% of lipid) were used so that the modules remained well-defined in the absence of fission. Nevertheless, phase-separated hybrids hold great potential for studying signalling and trafficking in protein/lipid assemblies (*i.e.,* lipid rafts) (*143*). The latter are also important targets of several antibiotics, therefor the proposed system could be used as a platform for studying drug-rafts interactions and development of novel therapeutics.
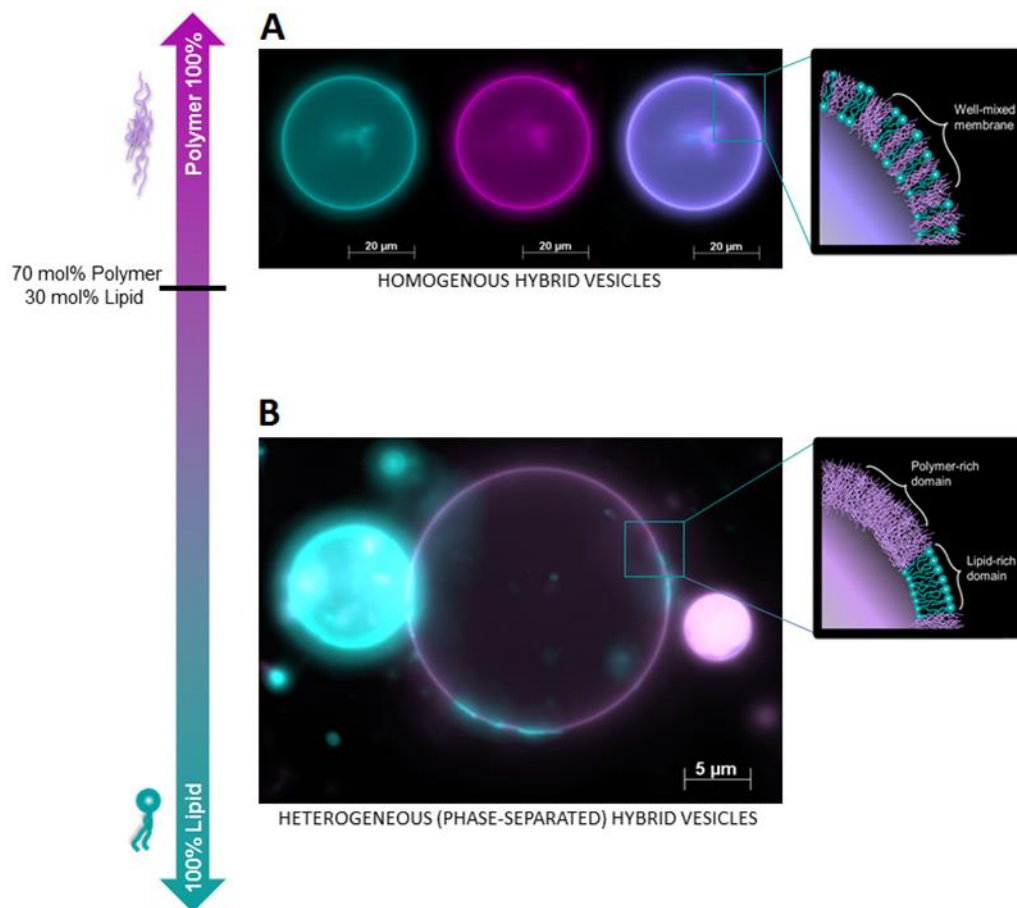
Fig. 8. An overview or different hybrid microcompartments obtained with the electroformation procedure with their corresponding fluorescent microscopy images. The distribution of polymer and lipid in hybrid polymer/lipid mixed membranes depends on their relative contents. At and above 70 mol% of polymer, hybrid membranes are homogeneous, exhibiting evenly distributed polymer and lipid (**A**). With the increasing lipid content, phase-separated membranes, exhibiting lipid-rich and polymer-rich domains were observed (**B**). With permission adapted from (*1*). Copyright 2017, American Chemical Society.

3.1.2   Build the ARC, Noah – reconstitution of *bo₃* oxidase as a first step of the ARC construction

The first construction step of the ARC assembly was the reconstitution of a proton pump, *bo₃* oxidase, in various nano-sized vesicles. The initial strategy was to expend on the pioneering works of, most notably, Rigaud and colleagues (*61, 64, 144*) as well as von Ballmoos and colleagues (*44, 50, 54, 145*). The reconstitution of membrane protein involves the unpredictable interplay between membranes, detergents, enzymes, and their environment. The search for the optimal conditions resulting in high activity of reconstituted enzymes most

frequently relies on trial and error and on screening of countless combinations and concentrations of different components of the reconstitution mixture. While in particular the effect of different concentrations of the mediating detergents on the activity of reconstituted enzymes is not entirely understood, some reported reconstitution setups consistently result in high MP activity. Two of such examples are the insertion of respiratory enzymes at the membrane saturating concentration of the specified detergent (octyl glycoside or Triton X-100) (*46, 64, 138*). Furthermore, sodium cholate is an another example of a reliable mediating detergent, although, interestingly, at the near membrane solubilizing concentration (*44, 54, 64*). Therefore, at first, these detergents were chosen for the reconstitution trials of ARC enzymes into polymersomes and hybrids. Meanwhile, sodium deoxycholate, while used with lesser frequency in reconstitutions, was successfully applied for disruption of rigid block copolymer membranes (*146, 147*). Without pre-existing information on the partitioning of detergents in PDMS-*g*-PEO, sodium deoxycholate was additionally selected as a potential candidate mediating the ARC assembly.

To achieve the functional insertion of *bo₃* oxidase in polymersomes and hybrids, preformed vesicles were partially solubilized with either of mentioned detergents in the previously reported (*50, 64*) most efficient detergent concentration range of 0.2–0.8 % (w/v). Furthermore, several detergent removal methods, namely removal by Bio-beads (*61*), dialysis (*148*) or by size exclusion chromatography (*54*) were explored. Next, the activity of the reconstituted enzyme in proteopolymersomes or proteohybrids was monitored as the oxygen consumption via Clark-type electrode (Fig. 9A). In parallel, *bo₃* oxidase was reconstituted in liposomes, which served as a pre-optimized benchmark system. The highest oxygen consumption rate (OCR) of 35.8 ± 0.7 nmol ml^{-1} min^{-1} in hybrids (Fig. 9C) was achieved with 0.4 % of octyl glucoside, while the highest rate achieved in polymersomes (Fig. 9D) was 34.9 ± 3.3 nmol ml^{-1} min^{-1}, using 0.2 % sodium cholate. In comparison, the highest OCR in liposomes, 38.7 ± 7.7 nmol ml^{-1} min^{-1}, was measured in vesicles reconstituted with 0.4 % of sodium cholate. Overall, more than 90 % of enzyme activity was retained in hybrids and polymersomes, which was a significant improvement over previous reconstitution attempt featuring polymer membranes. Khan and colleagues (*149*), for instance, reported 30 % of retained *bo₃* oxidase activity in hybrid vesicles comprising diblock copolymer PBd−PEO and POPC, although the absolute OCR values were not reported. In contrast, *bo₃* oxidase was entirely inactive when inserted in PBd−PEO polymersomes. It is worth noting that at this stage of the research, solubilization profiles of liposomes, polymersomes and hybrids with various

70

used detergents were still unknown. Nevertheless, they were analysed in detail later on and the findings are discussed in Chapter 3.1.7.1. For this reason, more detailed discussion on the bo_3 oxidase activity with respect to different mediating detergents can be found in the mentioned chapter. Finally, the OCR is a solid general representation of the enzymatic activity that takes into account the amount of integrated enzyme as well as the enzyme functionality. Furthermore, the OCR does not necessarily translate into the magnitude of the established proton gradient due to variability in enzyme orientation in the membranes. That is why the proton translocation activity was analysed in the overall most active system – bo_3 oxidase reconstituted in liposomes with 0.4 % of sodium cholate. This reconstitution setup was the most likely candidate for further expansion with other ARC enzymes, in particular with the ATP synthase, where the final output of the module would rely heavily on the established proton gradient. The changes in intravesicular pH due to the proton pumping action of bo_3 oxidase were determined with the pH sensitive ratiometric dye pyranine, which was encapsulated in vesicles. The changes in pyranine fluorescence revealed the acidification of vesicles lumen by approximately 1 ± 0.2 unit of pH in roughly 30 min (an example of pH measurement can be seen in Fig. 9B). The measured pH change was significantly higher than the one reported for similar setup by Berg et al. (*150*), where a pH decrease of 0.2 units inside of vesicles was observed. This was likely due to differences in bo_3 oxidase orientation across millions of proteovesicles – while slightly over 50 % of integrated enzymes transported protons towards vesicles lumen, a large fraction pumped in the opposite direction, which resulted in the overall low net pH change, as discussed by authors. That is why the proton translocation activity was also analysed on a single vesicle/enzyme level, where a larger pH change of 0.9–1.5 units was observed. We replicated this experiment on a single vesicle level in microfluidic chip and observed similar change in pH of 0.8 units after 30 min (*97*) in polymer GUVs reconstituted with bo_3 oxidase.
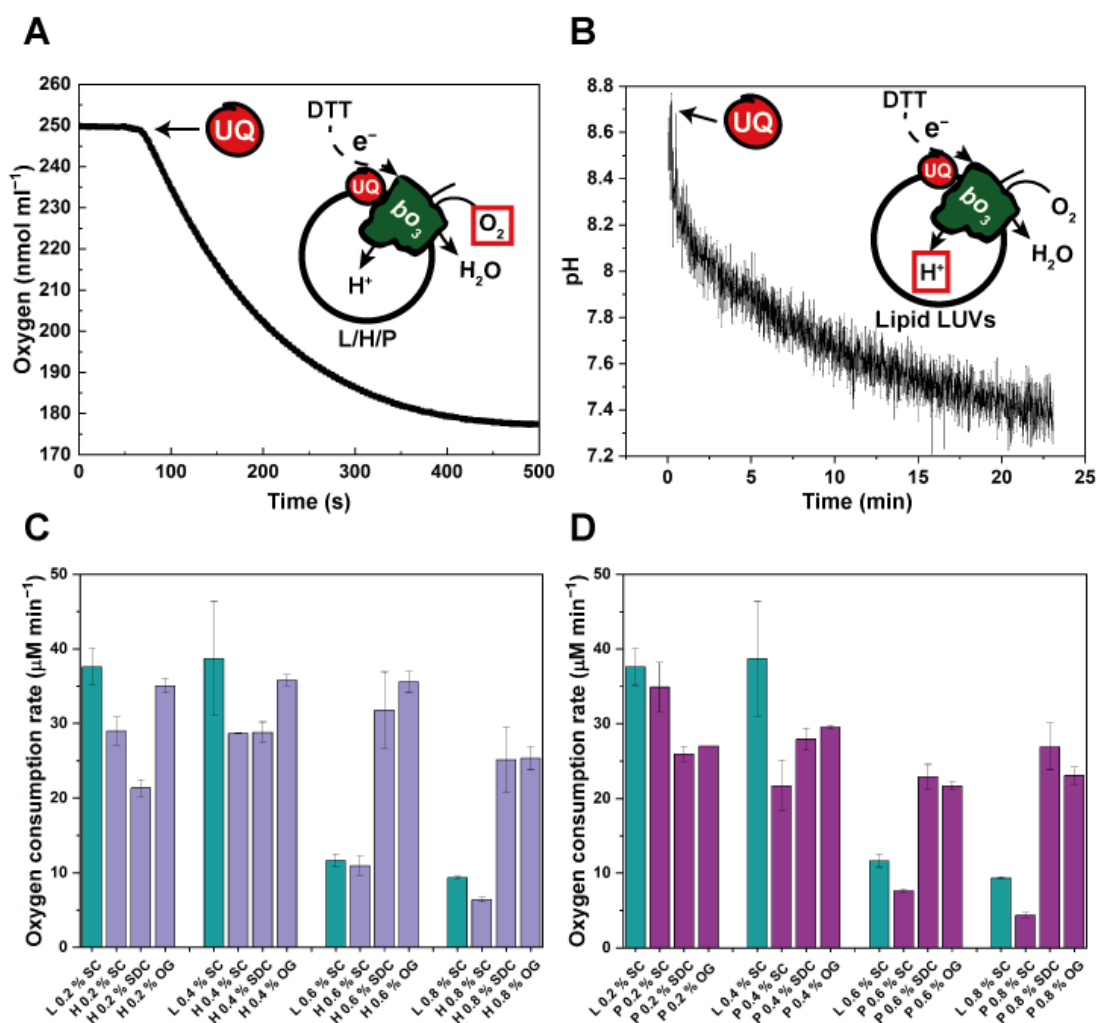
Fig. 9. The activity of *bo₃* oxidase in lipid, hybrid and polymer LUVs. (**A**) Changes in oxygen concentration due to the activity of *bo₃* oxidase in hybrid LUVs. At ~ 80 s mark, the reaction was initiated by the addition of ubiquinone-1 (UQ). The trace shown is for the hybrids reconstituted with 0.2 % sodium deoxycholate. The oxygen consumption rate was determined from the initial steady-state stage of the reaction. (**B**) Changes in the intravesicular pH as determined by the encapsulated ratiometric pH-sensitive dye pyranine based on the changes in dye fluorescence. Shown example was recorded in proteoliposomes reconstituted with 0.4 % of sodium cholate as the mediating detergent. At t = 0, proton pumping by *bo₃* oxidase was initiated by the addition of ubiquinone and the acidification of vesicle lumen was observed over several minutes. (**C**) & (**D**) The comparison of oxygen consumption rates of *bo₃* oxidase reconstituted into hybrid (H) and polymer (P) LUVs. The enzyme was reconstituted with 3 different mediating detergents, sodium cholate (SC), sodium deoxycholate (SDC) and octyl glucoside (OG) in the detergent concentration range of 0.2–0.8 % (w/v). The activity of *bo₃* oxidase in hybrid and polymer LUVs was compared to the highest achieved enzyme activity in liposomes (L) (natural membranes). Shown are averages of three separate reconstitutions with standard errors. With permission adapted from (*1*). Copyright 2017, American Chemical Society.

72

Next, the effect of different detergent removal methods on the activity of the oxidase was determined. Towards this end, hybrids and polymersomes were reconstituted with either 0.2 or 0.4 % of sodium cholate and the detergent removal was facilitated either by adsorbent beads, dialysis or gel filtration (SEC). Highest *bo₃* oxidase activity was recorded in hybrids reconstituted with Bio-beads or SEC (Fig. 10A), while the dialysis was seen to facilitate enzyme insertion with lesser efficiency. Interestingly, the opposite was observed in the case of polymersomes, where dialysis outperformed two other methods (Fig. 10B). Both, Bio-beads as well as SEC are known to be relatively rapid methods for detergent removal (in the case of the beads this depends on their concentration; nevertheless, this method is still comparatively much faster than dialysis). It would appear that faster removal over shorter period of time is preferred in hybrids, likely because it pairs better with the rapid reorganization of lipids in the vicinity of the enzyme (discussed in the following Chapter 3.1.5). Meanwhile, slow detergent removal via dialysis over several hours (overnight) facilitated efficient enzyme insertion in polymersomes. Nevertheless, such long incubation period could present significant problem when cointegration of several enzymes is considered, especially having in mind high temperature sensitivity of a variety of MPs. Ishmukhametov and colleagues (*98*), for instance, report rapid activity loss of ATP synthase isolated with their procedure, while stored on ice. Therefore, Bio-beads appear to be the best option for enzyme reconstitution in liposomes and hybrids, while only a small portion of enzyme activity is sacrificed in polymersomes when this method is selected over dialysis.
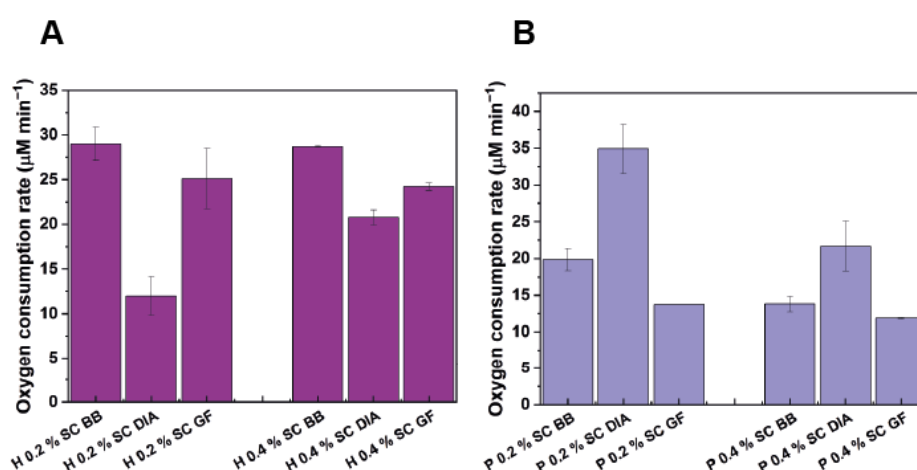
Fig. 10. The effects of different detergent removal techniques on the activity of the reconstituted *bo₃* oxidase. Oxygen consumption rates of *bo₃* oxidase in hybrid (H) vesicles (**left**) or polymer (P) vesicles (**right**) reconstituted with 0.2 and 0.4 % of sodium cholate (SC). Detergent was removed by either Bio-beads (BB), dialysis (DIA) or gel filtration (GF). Shown are averages of two separate reconstitutions with standard errors.

Lastly, all types of vesicles were probed for residual detergents following enzyme reconstitution. Towards this end, *bo₃* oxidase was inserted with the two highest performing detergents – sodium cholate and octyl glucoside, while the detergent removal was facilitated by Bio-beads. Proteovesicles were then analysed by HPLC-MS/MS, which revealed that more than 99.9 % of detergents in all tested systems were successfully removed (Table 1) with the described procedure. Detergents are known to have a profound effect on membrane properties. Of particular importance in the context of artificial mitochondrion construction is the increased membrane permeability (*151, 152*) governed by membrane-inserted detergent, along with the specific inhibitory effect of specific detergents on various membrane proteins. With respect to the latter, Triton X-100, for example, was reported as specific inhibitor of respiratory Complex I (*153*). Therefore, the efficient enzyme insertion in the presented system was just as important as the efficient detergent removal afterwards.

Table 1. The efficiency of the detergent removal from lipid, hybrid and polymer proteovesicles as determined by HPLC-MS/MS. In different types of vesicles, *bo₃* oxidase and ATP synthase were reconstituted with either sodium cholate (SC) or octyl glucoside (OG). Detergents were removed via Bio-beads. The detection limit for tested detergents was 100 μg l^{-1}. With permission adapted from (*1*). Copyright 2017, American Chemical Society.

	Liposomes	Hybrids	Polymersomes
Reconstitution amount of SC	0.6 %	/	/
Reconstitution amount of OG	/	0.1 %	0.1 %
Residual amount of SC (MS)	2800 μg l^{-1}	/	/
Residual amount of OG (MS)	/	< 100 μg l^{-1}	< 100 μg l^{-1}
Detergent removal efficiency	99.95 %	> 99.99 %	> 99.99 %

3.1.3 Second step of the ARC construction – reconstitution of ATP synthase

Following the successful insertion of *bo₃* oxidase into different types of vesicles with high preserved enzyme activity and the successful establishment of proton gradient, the latter could then be used to drive the ATP synthesis. The exploitation of this driving force required co-insertion of ATP synthase along with the proton pump in different types of vesicles, forming the short respiratory chain (SRC). For this purpose, liposomes were reconstituted with highest

performing detergent in that setup, sodium cholate. On the other hand, octyl glucoside was chosen as the mediating detergent in hybrids and polymersomes due to the high overall activity of *bo₃* oxidase reconstituted with this detergent in said vesicles. Furthermore, because the highest *bo₃* oxidase activity was recorded at the lowest tested concentrations of detergents, ATP synthase was additionally reconstituted at 0.05 and 0.1 % of octyl glucoside. Respiration-driven ATP synthesis was then detected by converting ATP into luminescence (Fig. 11A) using luciferin/luciferase reporter assay (*154*). In accordance with the mentioned trend observed in *bo₃* oxidase reconstitutions, the highest activity of a short respiratory chain was observed at the lowest tested amounts of octyl glucoside (Fig. 11B). With the overall highest ATP synthesis achieved in liposomes reconstituted with 0.6 % of sodium cholate, about 56 % of the activity was retained in hybrids and about 32 % in polymersomes (Fig. 11C). Successful co-insertion of two complex transmembrane proteins into man-made membranes was without precedent at the time and remains state-of-the-art at the time of writing. Furthermore, with this setup, ATP synthesis was maintained over several hours, and the physiological levels (0.5–5 mM) of ATP could be reached, which is a prerequisite for driving a large number of biological and biomimetic processes.
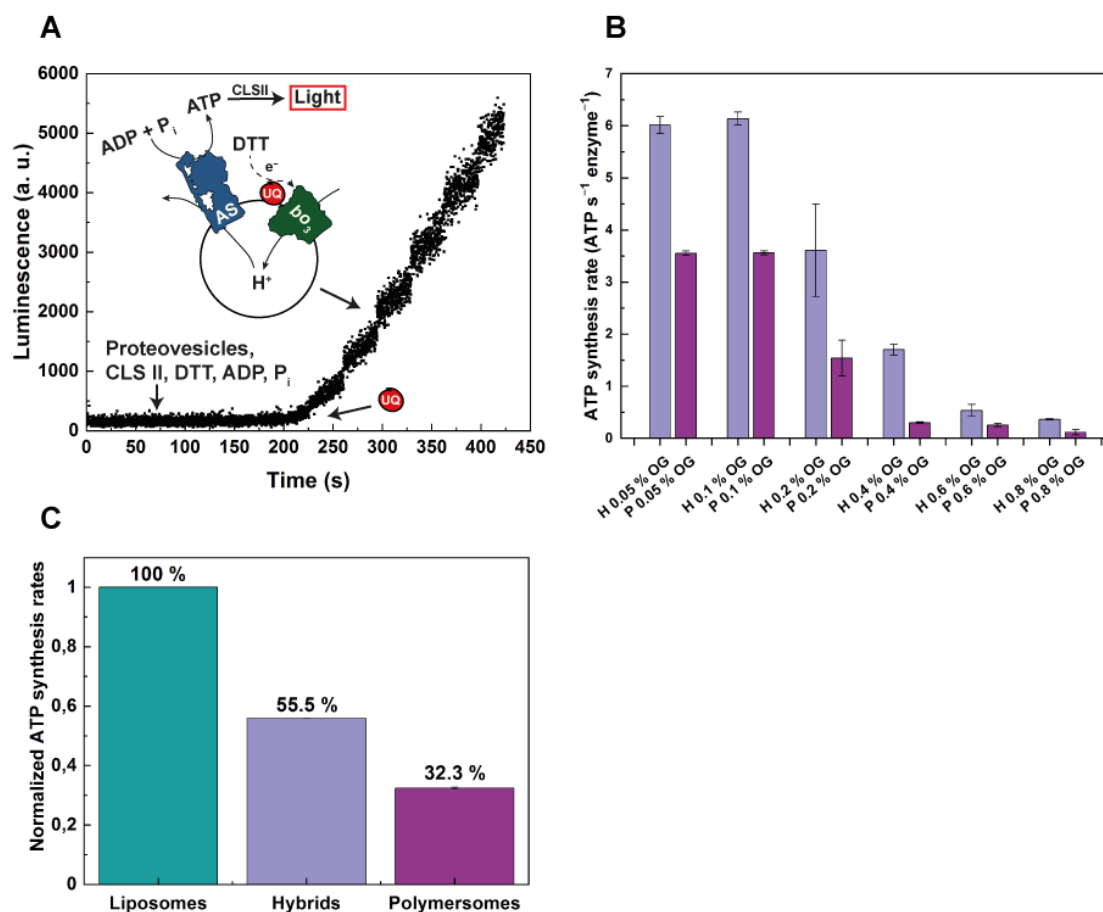
Fig. 11. ATP synthesis by the short respiratory chain in lipid, hybrid and polymer LUVs. (**A**) Respiration-driven ATP synthesis was detected based on the luminescence signal produced by the coupled luciferin/luciferase reporter system. Proton translocation by *bo₃* oxidase (*bo₃*) was initiated at t = 200 s by the addition of ubiquinone-1 (UQ) and the activity of ATP synthase (AS) was recorded. The signal was calibrated against a known amount of ATP. The trace shown is for the hybrids reconstituted with 0.05 % octyl glucoside. (**B**) The comparison of respiration-driven ATP production rates of the short respiratory chain reconstituted in hybrid (H) and polymer (P) LUVs. The respiratory chain was reconstituted with various amounts (0.05–0.8 %) of octyl glucoside (OG). While *bo₃* oxidase remained highly active at higher tested detergent concentrations, the highest activity of ATP synthase was obtained at the lower detergent contents. Shown are the average values of three different measurements with standard errors. (**C**) The comparison of highest obtained ATP synthesis rates in different types of vesicles. ATP synthesis in hybrids and polymersomes is normalized to that measured in liposomes (the most active setup). With permission adapted from (*1*). Copyright 2017, American Chemical Society.

The prerequisites for the successful ATP synthesis by SRC were: (1) suitable membrane thickness that enabled insertion of respiratory enzymes as well as promoted their function via sufficient hydrophobic matching, (2) suitable membrane architecture capable of facilitating conformation changes of embedded enzymes and diffusion of cofactors, such as ubiquinone,

(3) proton-tight membrane, (4) sufficiently high enzyme reconstitution efficiency and correct orientation. Even though the slightly more than 1 nm difference in thickness between polymer and lipid membrane could be observed by cryo-EM as discussed in Chapter 3.1.1, the compression of PDMS-*g*-PEO around the inserted enzyme enabled hydrophobic matching. While this phenomenon was likely less important in the case of *bo₃* oxidase, which exhibits mostly hydrophobic structure, hydrophobic matching was crucial for functionality of ATP synthase. The dominating hydrophilic segment of the latter was the one facilitating phosphorylation of ADP via rotational movement of the involved subunits and large hydrophobic mismatch would likely hinder the movement, inhibiting enzyme activity. Similar adjustment of polymer membrane thickness was reported by Itel and colleagues (*155*), where PMOXA-*b*-PDMS-*b*-PMOXA membranes with thickness of about 9 to 13 nm were seen compressing to match the thickness of inserted proteins with their size ranging from 3.3 to 7.1 nm. They further showed that the high flexibility of PDMS, which facilitated rapid membrane reorganization and resulted in membrane fluidity similar to the one of lipid bilayers was the key factor for MP insertion. High membrane fluidity and low viscosity largely determine the lateral mobility of membrane-inserted enzymes and cofactors (*155, 156*). In the case of *bo₃* oxidase it is crucial that the ubiquinone can readily diffuse to the binding site of the enzyme. The fluidity of commonly used block copolymers is typically relatively low in comparison with lipid membranes. In this context, a diffusion coefficient of polymer of 0.22 ± 0.06 µm² s⁻¹ was measured for PBd₄₀-*b*-PEO₃₀ polymer membranes (*157*), while the reported diffusion coefficient for lipids in DOPC lipid membranes was 10.0 ± 0.4 µm² s⁻¹ (*158*). Such large difference in membrane fluidity appears to be the reason behind hindered functionality of the inserted MPs, therefore, we checked whether PDMS-*g*-PEO provided fluidity similar to the natural environment. Toward this end, we measured lateral mobility of protein, polymer and lipid in liposomes, hybrids and polymersomes via the fluorescence recovery after photobleaching (FRAP) (*97*). To enable this, *bo₃* oxidase was labelled with the fluorescent dye ATTO 514, while lipid and polymer were labelled with rhodamine. We found that the diffusion coefficient of *bo₃* oxidase in hybrids and polymersomes was roughly 30 and 65 % lower than the one measured in liposomes, respectively. Interestingly, the diffusion of *bo₃* oxidase in hybrid membranes (6.9 ± 1.7 µm² s⁻¹) was faster than the diffusion of lipid (4.8 ± 0.8 µm² s⁻¹) and polymer dye (6.2 ± 1.4 µm² s⁻¹). We attributed this to the association of lipids with the enzyme, which resulted in the decreased lipid mobility. An experimental setup was designed to probe for this effect – details can be found in Chapter 3.1.5. Overall, we found that both, enzymes and lipids (relevant in the context of ubiquinone diffusion), can readily diffuse in

hybrid as well as polymer membranes with their lateral mobility matching that of lipid membranes. This also hinted at the decreased ATP synthesis in hybrids and polymersomes not being related to either the difference in polymer membrane thickness or the membrane fluidity. Hence, membrane proton permeability (3) and the above-described reconstitution parameters (4) were investigated in greater detail. The passive proton permeability of polymer and hybrid protein-free and protein-functionalized membranes is described in Chapter 3.1.4. Additionally, the analysis of enzyme orientation and reconstitution efficiency can be found in Chapters 3.1.7.2 and 3.1.7.3. The calculated ATP synthesis rates assumed the same reconstitution efficiency (amount of inserted enzyme) and same enzyme orientation across all setups, which led to underestimation of ATP synthesis in hybrids and polymersomes (Fig. 11C) (please see also Chapter 3.1.7).

3.1.4 Passive proton permeability of nano-sized compartments

Passive proton permeability (more accurately denoted as the net proton-hydroxy permeability (*116*)) is arguably the most important attribute of compartments in the context of ATP synthesis because it is essential for the establishment and sustainment of proton gradient. In this work, passive proton flux across various types of protein-free and protein-functionalized membranes was measured via pH sensitive ratiometric dye pyranine, which was added to vesicles exterior. Furthermore, encapsulated choline (static, membrane impermeable charge) as well as potassium were used to enable unhindered proton translocation, as described in Chapter 2.3.7. Transmembrane pH gradient was then induced by the addition of acid to vesicles outer solution and the proton influx was recorded as the change in pyranine fluorescence (Fig. 12A). The recorded data were fitted with the biexponential decay function and the permeability coefficients (P_{H+}) of compartments were then calculated from the second rate constant k_2, as described in Chapter 2.3.9.

Pristine (protein-free) PDMS-*g*-PEO LUVs were found to be the least permeable of all tested LUVs, with the determined P_{H+} of $2.1 \pm 1.1 \times 10^{-7}$ cm s^{-1} (Fig. 12B). Meanwhile, very similar but slightly higher permeability was observed in liposomes and hybrids with the measured permeability coefficients being 7.1 ± 1.9 and $11.1 \pm 1.4 \times 10^{-7}$ cm s^{-1}, respectively. While no data on PDMS-*g*-PEO membranes permeability was previously reported, the reported values for proton permeability of protein-free liposomes vary over several orders of magnitude (*128, 159-162*), which is likely due to difference in employed setups (pH dye used, temperature, magnitude of induced pH change, etc.) as well as calculation approaches. Drawing parallels

between these systems and the setup, presented in this work would be trivial, therefore, I only include and discuss comparisons with related setups. Interestingly, we observed similar highest permeability of hybrid vesicles on a single-vesicle level (giant vesicles were trapped in microfluidic chip and the pH difference was induced by outer solution exchange (*97*)), where we determined P_{H+} of 24.2 ± 2.0 × 10^{-7} cm s^{-1}, At the same time, giant liposomes and polymersomes had similar permeability coefficients of 1.4 ± 0.2 and 2.3 ± 0.1 × 10^{-7} cm s^{-1}, respectively. Furthermore, highest permeability of hybrid LUVs was also observed by Kleineberg and colleagues (*72*) with pyranine encapsulated in vesicles and with slightly higher induced pH difference. This observed increased permeability of hybrids on nano and micro level can be attributed to phase separation in these vesicles and the related increase proton flux at the polymer-lipid boundaries. To probe for this effect, we intentionally formed giant hybrid vesicles with such composition, so that the lipid microdomains could be seen (*97*). The permeability of so-formed phase-separated hybrids was about three times higher than that of homogeneous hybrids (7.1 ± 1.9 × 10^{-6} cm s^{-1} vs. 24.2 ± 2.0 × 10^{-7} cm s^{-1}), which confirmed that the passive proton permeability correlated with the dynamics of domain formation. Moreover, small difference in determined P_{H+} between nano- and micro-sized vesicles, which did not vary by more than one order of magnitude can be attributed to various factors. First, the LUVs are measured in bulk and the determined average permeability values do not necessarily reflect the heterogeneity of the sample (*119*). Furthermore, in the bulk assays, the integrity of LUVs is not always guaranteed, and there are additional differences in size, packing density and curvature of vesicles. These assumptions were supported by the observed minor (approx. 9%) difference in passive proton permeability between polymer LUVs and GUVs, where the structure of polymer monolayer should be largely preserved, regardless of the size. Meanwhile, largest discrepancies were observed in hybrids, where the composition cannot be perfectly controlled, leading to the formation of vesicles with disperse lipid content, and consequently lipid domains (*163*).
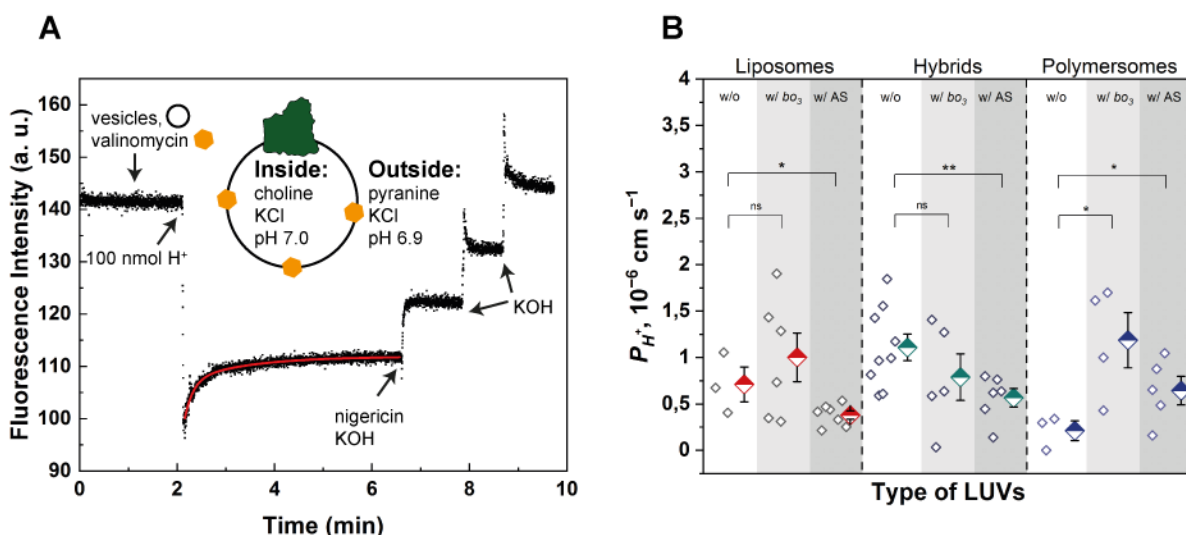
Fig. 12. Passive proton permeability of protein-free and protein-containing lipid, hybrid and polymer LUVs. (**A**) A pH gradient was applied to vesicles via the external addition of acid and the proton flux towards vesicle interior was monitored as the changes in fluorescence intensity of pH-sensitive ratiometric dye pyranine (excitation, 450 nm; emission, 508 nm). Compensatory movement of potassium ions was facilitated by the potassium ionophore valinomycin. Signal was calibrated with the known amounts of acid/base in the presence of protonophore nigericin. Data were fitted with biexponential function ($y=A_1e^{-tk1}+A_2e^{-tk2}+y_0$) (red trace) to determine second rate constant k_2, which enabled the calculation of permeability coefficients P_{H+}. Shown is the trace for the batch of polymer LUVs reconstituted with ATP synthase. (**B**) P_{H+} of protein-free LUVs (w/o; white area) and protein-containing LUVs with bo_3 oxidase (w/ bo_3; gray area) or ATP synthase (w/ AS; dark-gray area). Each diamond represents a separate measurement on LUVs in bulk. Average values are presented with half-filled diamonds and mean error. a.u., arbitrary units; ns, not significant for P > 0.05; *P ≤ 0.05; **P ≤ 0.01; ***P ≤ 0.001.

Next, passive proton permeability of protein-functionalized LUVs was determined (Fig. 12B). The increased permeability upon the insertion of bo_3 oxidase was observed for liposomes and polymersomes (10.0 ± 2.6 and $11.9 \pm 3.0 \times 10^{-7}$ cm s^{-1}, respectively). Unfortunately, the literature on membrane permeability changes upon protein insertion is very scarce. Nevertheless, similar increased permeability was previously observed in liposomes following the insertion of bacteriorhodopsin (*164*). MPs reconstitution is proposed to cause imperfections in lipid bilayer, likely leading to increased membrane permeability (*74*). Meanwhile, the insertion of MPs into PDMS-*g*-PEO membranes likely results in loosening of the monolayer, which further leads into increased membrane permeability (as well as expedited diffusion, as discussed in previous section). Intriguingly, loosening of polymer membranes was also observed upon the insertion of ATP synthase (with determined P_{H+} of $6.4 \pm 1.5 \times 10^{-7}$ cm s^{-1}),

featuring smaller transmembrane domain compared to *bo₃* oxidase and, overall, much different enzyme architecture. Remarkably, decreased proton permeability was observed in hybrids following the insertion of either of the two respiratory enzymes. The P_{H_+} of $7.9 \pm 2.5 \times 10^{-7}$ cm s^{-1} was determined upon the insertion of *bo₃* oxidase and $5.7 \pm 1.0 \times 10^{-7}$ cm s^{-1} upon the insertion of ATP synthase. This effect could be observed in the nano-sized as well as in the micro-sized vesicles (*97*), where in the latter even more pronounced permeability decrease from 24.2 ± 2.0 to $2.6 \pm 0.2 \times 10^{-7}$ cm s^{-1} could be seen in the case of the insertion of *bo₃* oxidase. This was further accompanied by the membrane thickness increase in the enzyme surroundings, as observed via cryo-EM, which led me to believe that the decreased permeability of proteohybrids relates to the reorganization of the membrane by protein insertion. In this context, lipid molecules are proposed to localize at the protein insertion spots, counteracting the polymer loosening. To explore the latter hypothesis in greater detail, I investigated lipid and polymer partitioning in proteohybrids.

3.1.5 Lipid and polymer partitioning in proteohybrids

The partitioning of either lipid (PE-Rho) or polymer dye (PDMS-*g*-PEO-Rho) with respect to *bo₃* oxidase tagged with ATTO 514 dye and inserted in hybrid LUVs was analysed. In this scenario, the emission of the FRET donor ATTO 514 would be quenched by the FRET acceptor rhodamine when the lipid dye localizes in close proximity to the reconstituted enzyme. Next, the distance between the FRET couple was gradually increased by stepwise dissolution with detergent octyl glucoside and the ATTO 514 dequenching was monitored.

The dequenching profiles differed significantly between the two systems. Most notably, the initial emission intensity of the protein dye was significantly lower with the lipid dye (i.e., quenched), hinting at preferred lipid localization in the vicinity of *bo₃* oxidase (Fig. 13A, mechanism presented in Fig. 13C). Moreover, the addition of octyl glucoside up to the point of total vesicle solubilization (marked as OG R_{sol}) led to relatively small increase in the emission of ATTO 514 (Fig. 13A, steps 1 and 2). This was a further indication of persistent quenching by protein-associated lipids rather than by merely proximal ones (note that the distance between the latter and the enzyme should increase with increasing surfactant resulting in proportional dequenching, which was observed only partially and shortly). Furthermore, while rapid dequenching of the protein dye was observed upon total solubilization to mixed (lipid/polymer/detergent/*bo₃* oxidase) micelles (Fig. 13A, "OG R_{sol}"), ATTO 514 was quickly requenched again (Fig. 13A, step 4), presumably due to lipid relocation to the protein. Finally,

when octyl glucoside was added at the critical micellar concentration (denoted as "OG CMC"), gradual ATTO 514 dequenching was observed, which was likely a result of PE-Rho leaching to detergent micelles as well as delipidation of bo_3 oxidase.
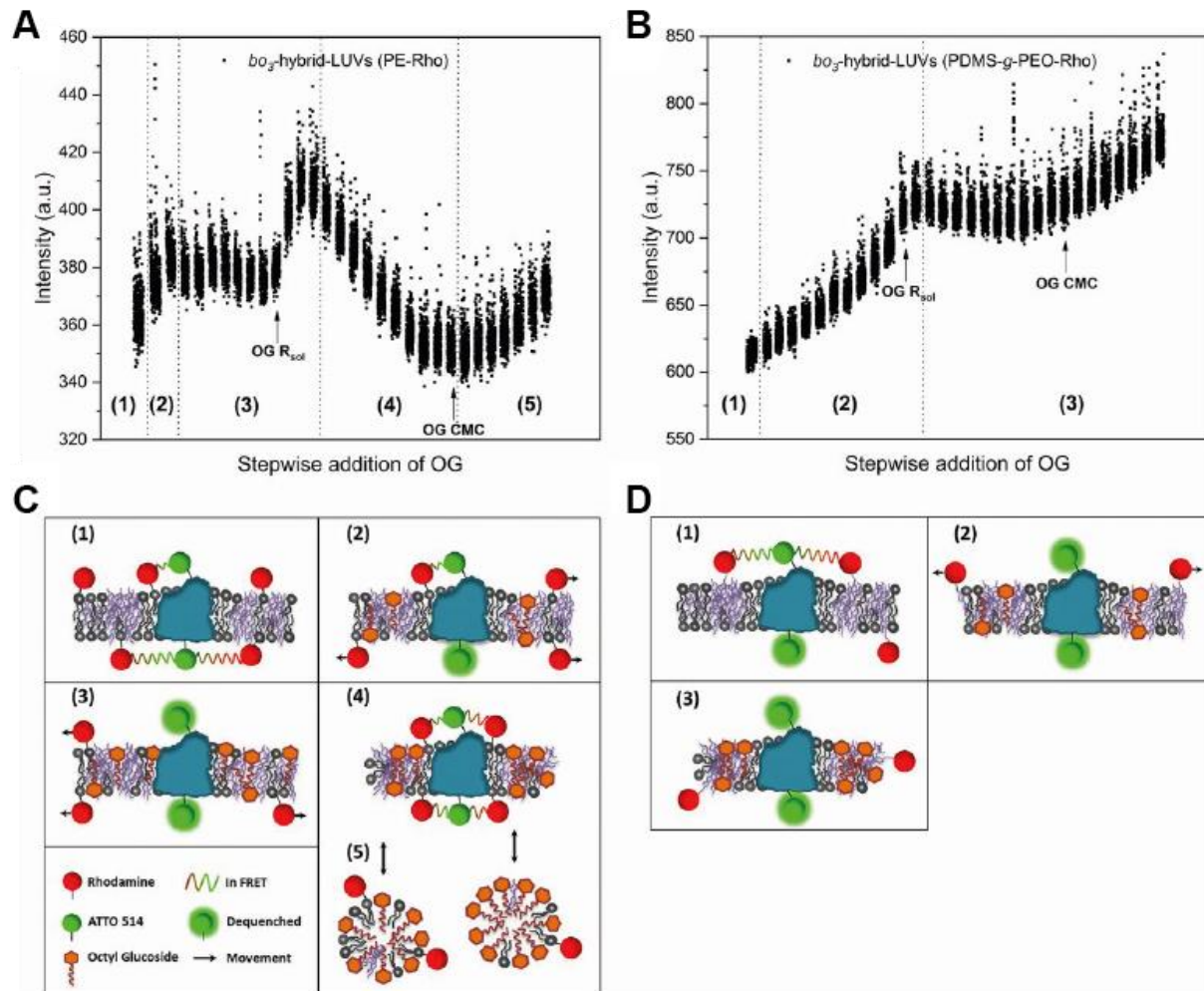
Fig. 13. The FRET-based analysis of lipid and polymer partitioning in the vicinity of bo_3 oxidase, integrated in hybrid membranes. bo_3 oxidase tagged with the FRET donor (ATTO 514) was reconstituted in hybrids containing either fluorescently tagged lipid (PE-Rho), when lipid partitioning was being analyzed (**A**) or fluorescently tagged polymer (PDMS-*g*-PEO-Rho), when polymer partitioning was analyzed (**B**). While in close proximity, rhodamine quenched the emission of ATTO 514, which was being excited. Dequenching was induced by gradual disruption of the membranes via stepwise addition of the detergent octyl glucoside (OG). Two important points are marked on plots (**A** and **B**): the concentration of OG, at which all hybrid LUVs were dissolved to mixed micelles (OG R_{sol}), and the critical micelle concentration of OG (OG CMC). The separate mechanistic steps of the experiment for the partitioning of the lipid or polymer dye are schematically depicted in (**C**) and (**D**), respectively. a.u., arbitrary units. Adapted from (*97*), licensed under CC BY 4.0.

In contrast, the higher initial emission of ATTO 514 with PDMS-g-PEO-Rho (i.e., less quenching) indicated larger lateral distance between enzyme and polymer. The dilution of the hybrid membranes resulted in continuous linear dequenching of the polymer dye until the OG R_{sol} (Fig. 13B, step 2) and similar steady increase was observed in the micellar phase (Fig. 13B, step 3). Both, the initial fluorescence intensity as well as the dye dequenching dynamics observed in the described experiment involving labelled polymer were strong indicators of random localization of polymer with respect to the enzyme and its unrestricted mobility, in contrast to the sustained intimate localization of lipids. This distinct positioning of the membrane constituents around the enzymes in hybrid membranes might have also be the reason behind the preserved activity of *bo₃* oxidase over time (*97*). Nevertheless, this arrangement likely resulted in the increased enzyme susceptibility to ROS and the overall lower stability of proteohybrids when compared to proteopolymersomes, because of the potential protein aggregation due to delipidation. This hypothesis was tested and is described in more detail in the following chapter. Lastly, the proposed entrapment of lipids was in line with their slower diffusion in the polymer membrane after protein insertion (*97*) in contrast to the increased overall membrane fluidity.

It was previously proposed that block copolymer membranes can adjust their thickness to the size of MP, whereby in the case of hydrophobic mismatch between smaller MPs (channels) and thicker PMOXA-*b*-PDMS-*b*-PMOXA membrane (9 to 13 nm) hydrophobic domains around the inserted MPs showed significant compression, explained by the flexibility and low viscosity of PDMS (*155*). Cryo-EM revealed that the PDMS-*g*-PEO membrane also compressed in the proximity of the protein (Fig. 14B). Meanwhile, the opposite behaviour was observed in the hybrid membrane: The thickness around the integrated protein increased (average thickness changed from 4.9 ± 0.17 to 5.3 ± 0.54 nm), which could be due to lipid accumulation in the protein surrounding (*97*). This rearrangement was most likely the reason behind the resealing of hybrids upon the insertion of *bo₃* oxidase and the determined decreased membrane permeability. In contrast, lipid membranes did not demonstrate adaptation of the thickness to the protein insertion (Fig. 14A), which was reflected in the increased proton permeability. This apparent sealing of the hybrid membrane by the MPs can be considered as a beneficial phenomenon, which would sustain pH gradients across the membrane, while making use of the hybrid membrane chemistry.
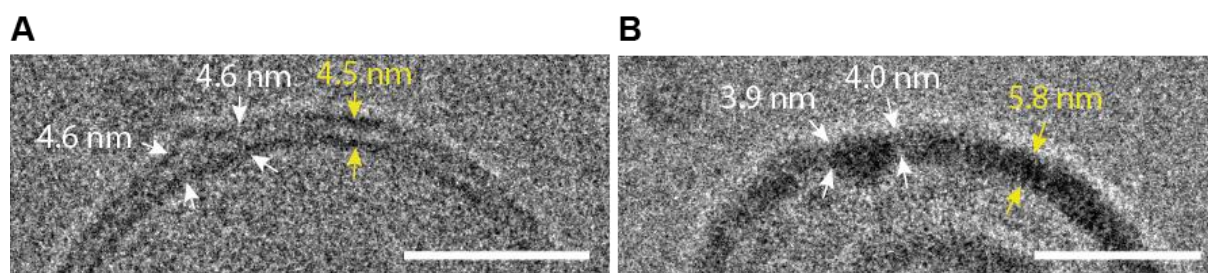
Fig. 14. Adaptation of lipid and polymer membrane to the insertion of *bo₃* oxidase. (**A**) No compression or expansion of lipid bilayer in the vicinity of the inserted enzyme (indicated with white arrows) relative to the average membrane thickness (yellow arrows) could be observed in proteoliposomes. (**B**) In contrast, significant compression of polymer monolayer could be seen in the enzyme surroundings (white arrows) in proteopolymersomes, while the distant membrane segments remained comparatively thicker. Scale bars are 25 nm.

3.1.6 Protective function of PDMS-*g*-PEO against ROS

High proton motive force and the reduced state of enzymes and cofactors of the electron transport chain have been linked to increased production of reactive oxygen species (ROS) in mitochondria (*165, 166*). ROS can induce peroxidation of lipids (unsaturated fatty acids) or cleave ester bonds and thus disrupt the bilayer arrangement, which may in turn inactivate MPs and increase membrane permeability (*167, 168*). With respect to this, partially or completely replacing the lipids with synthetic polymers, which are less prone to oxidation and hydrolysis, would increase the overall system stability. Therefore, this was the main motivation behind the attempted protein insertion in PDMS-*g*-PEO membranes, described in this study. Nevertheless, I postulated that the protective function of this polymer with respect to enzyme activity could only come into effect in cases where the inserted enzyme is enveloped in polymer and thus resistant to delipidation and direct damage by ROS. Importantly, as discussed in previous chapter, this condition was not met in hybrid membranes, in which the localization of lipids was observed directly and indirectly in the enzyme surroundings. To examine the potential protective function of PDMS-*g*-PEO against ROS, different types of LUVs functionalized with *bo₃* oxidase were exposed to oxidative stress by incubation with ascorbate or ascorbyl free radical, following the established protocols (*112, 113*). The activity of *bo₃* oxidase in untreated and ROS-treated vesicles was then measured via the oxygen consumption using the Clark-type electrode, as described in Chapter 2.5.1. Furthermore, ROS-treated proteovesicles were inspected for deformations by cryo-EM and the integrity of vesicles (changes in vesicle size due to decomposition, bursting or enzyme extrapolation) was examined with DLS.

The DLS analysis revealed no changes in vesicle size after the incubation of proteovesicles with either ascorbate or ascorbyl radicals. This suggested that the vesicles were not bursting, however, the poration of membranes and the related content leakage could not be excluded. To probe for this effect, we encapsulated water-soluble dye carboxyfluorescein in different types of vesicles and treated them with ROS (*97*). After treatment, dye leakage was detected in lipid vesicles while, remarkably, no leakage could be seen in hybrids or polymersomes. This indicated that ROS treatment compromised the integrity of lipid bilayers, while the integrity of polymer-based membranes was seemingly preserved. Furthermore, proteovesicles were inspected for subtle changes associated with surface modifications and/or compromised membrane tightness (due to local perturbations, for instance, pores) via cryo-EM. In this context it could be seen that a portion of liposomes exhibited bilayer defects manifested as either visible pores or irregular membrane surface (Fig. 15B). On the contrary, no difference between the ROS-treated and untreated samples was observed in both hybrids and polymersomes.

The observed membrane disruptions in liposomes by ROS could potentially lead towards delipidation of bo_3 oxidase and consequently to enzyme aggregation and deactivation (we previously demonstrated complete loss of bo_3 oxidase activity in the absence of stabilizing amphiphiles (*97*)). In the next step, the effects of ROS on the activity of integrated enzymes were analysed. In this context, a protective function of PDMS-*g*-PEO was revealed – after 30 min of the exposure of proteovesicles to free radicals, bo_3 oxidase in polymersomes retained 73 ± 6 % of the initial activity, while the enzyme in liposomes retained only 10 ± 4 % (Fig. 15A). It is important to note that the activity decrease in proteopolymersomes was statistically nonsignificant. Furthermore, bo_3 oxidase performed slightly better in treated hybrids than in treated liposomes, although the enzyme activity was mostly lost after the treatment of proteohybrids with ascorbyl radical. One of the reasons behind the observed deactivation of bo_3 oxidase in liposomes and hybrids could be damage sustained by the enzymes during the direct attack of disruptive species on the reconstituted MPs. On the other hand, bo_3 oxidase could have been deactivated due to delipidation caused by the membrane disruption by ROS. To differentiate between the two options, the effects of ROS on the enzyme alone were tested (i.e., bo_3 oxidase, which was not reconstituted in a membrane but was instead stabilized in detergent micelles). With respect to this, no loss of enzyme activity was observed upon the treatment. In fact, the oxygen consumption in treated samples was slightly increased,

presumably due to direct reduction of hemes by ascorbate (with OCR being 25.5 ± 3.4 vs. 20.8 ± 3.5 μM min^{-1}, treated vs. untreated enzyme, respectively).
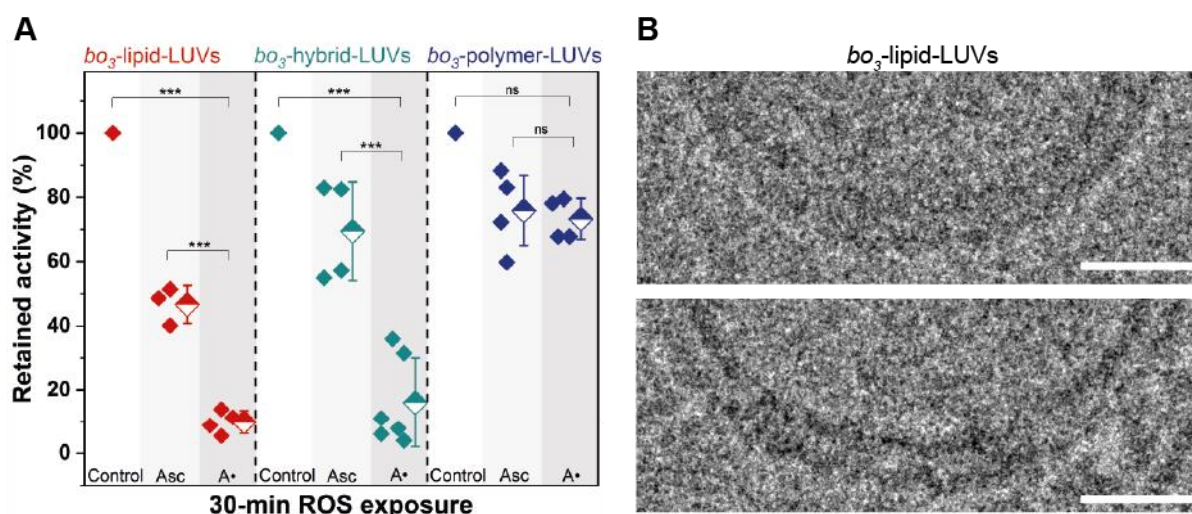
Fig. 15. The effects of ROS on proteovesicles. (**A**) Activity retention of *bo₃* oxidase after incubation with ascorbate (Asc) and ascorbyl free radical (A•) for 30 min. For 100% (control) activity of untreated *bo₃*-LUVs was taken (two to three repeats). Individual data are shown as filled diamonds; average values are shown as half-filled diamonds and standard error. ns, not significant for $P > 0.05$; ***$P \leq 0.001$. (**B**) Micrographs of proteoliposomes treated with ascorbyl free radical. After treatment, vesicles could be seen featuring transversal bilayer disruptions (upper panel) as well as localized disturbances of the monolayer (indentations) (bottom panel). Scale bars are 10 nm. Defocus ≈ -2 μm. Adapted from (*97*), licensed under CC BY 4.0.

Based on these experiments, the proposed direct damage to the reconstituted enzymes by ROS could be excluded. Instead, *bo₃* oxidase in liposomes and hybrids was postulated to lose the activity due to delipidation. In liposomes, membrane disruptions were confirmed by the leakage of the encapsulated dye as well as via cryo-EM analysis. Meanwhile, localization of lipids in the vicinity of inserted enzymes was observed in hybrid vesicles, as discussed in the previous chapter. These localized assemblies would likely be as susceptible to ROS as lipid bilayers and the ROS treatment of vesicles would therefore result in the enzyme delipidation and deactivation. Nevertheless, some portion of the enzyme in hybrids remained highly active even after the treatment, which is likely the portion contained in the predominantly polymer vesicles. These observations emphasize the importance of a stable scaffold (compartments) even in the cases when the integrated MPs are otherwise resistant to ROS. The revealed chemical resistance of the tested graft copolymer substantiates its suitability to accommodate the complete electron transport chain and to counteract the detrimental influence of ROS (produced by Complex I in particular) on the respiratory enzymes. Lastly, the structural

86

integrity of the membrane is imperative for reaction compartmentalization or for potential applications, such as the ones related to the cargo delivery.

3.1.7 Orientation and reconstitution efficiency of bo_3 oxidase and ATP synthase in lipid, hybrid and polymer LUVs

Large differences were observed in ATP production by SRC reconstituted with various detergents in different types of vesicles and at different degree of vesicle solubilization, as discussed in Chapter 3.1.3. Several factors were identified that could have led to this observed discrepancy: (1) different biocompatibility of vesicles, (2) insufficient solubilization of vesicles by detergents, (3) different membrane insertion efficiency and (4) different orientation of inserted enzymes. The appropriate membrane thickness and flexibility of PDMS-g-PEO membranes (Chapter 3.1.1), along with their high, diffusion-promoting fluidity (Chapter 3.1.3), low bending rigidity (*97*) and low permeability (Chapter 3.1.4) would suggest excellent compatibility of these membranes with respiratory enzymes. On the other hand, the enzyme reconstitution efficiency as well as orientation were previously reported to show correlation with the degree of membrane solubilization and are, furthermore, dependant on the choice of detergent (*44, 50, 63, 64, 74*). In this chapter, the mentioned dependencies are analysed in detail. The idea here was to reconstitute SRC in lipid, hybrid and polymer LUVs solubilized with various detergents to a various degree, determine the orientation and the reconstitution efficiency of ATP synthase as well as bo_3 oxidase, and, finally, to measure the ATP synthesis of these differently prepared modules. This would enable the comparison between the tested reconstitution parameters and the final output of the modules. In Chapter 3.1.3, the degree of vesicle solubilization was adapted from the existing literature related to proteoliposomes, as described, taking into consideration the previously achieved high enzyme activity. Nevertheless, it was unknown if the degree of liposome solubilization is also reflected in hybrids and polymersomes. To be more specific, let us take a look at the reconstitution of ATP synthase, for instance, for which high activity was observed when reconstituted in liposomes with Triton X-100 or octyl glucoside at the membrane saturating concentration of detergents (*61, 64, 144*). It was not clear whether the same concentrations of detergents, which saturated lipid membranes would also saturate hybrid and polymer ones. Furthermore, it was unknown if the interactions between detergents and polymer are similar to those between detergents and lipid. To elucidate these factors, first, solubilization profiles of lipid, polymer and hybrid LUVs with different detergents were recorded. In the next step, enzymes of SRC were reconstituted in different vesicles at the membrane saturating (R_{sat}) as well as membrane solubilizing (R_{sol})

concentrations of each detergent, as identified from the solubilization profiles. Since the degree of membrane solubilization can be considered a continuous spectrum, any degree of solubilization could have been selected for the enzyme reconstitution. Nevertheless, the two selected degrees are important inflection points. The saturation point denotes the maximum capacity of membranes for tested detergent, at which vesicles integrity is still preserved. Moreover, the total solubilization point indicates detergent concentration at which vesicles are completely dissolved and their constituents are contained in the lipid (polymer)/detergent mixed micelles. When enzymes are added to either of the two, vastly different course of reconstitution can be seen upon the detergent removal, as discussed in Chapter 1.3.2. Briefly, enzyme reconstitution at R_{sat} (the "direct reconstitution") usually, in liposomes, results in lower enzyme insertion efficiency (considerate portion of enzyme does not end up inserted in membranes). However, the enzymes are inserted with largely uniform, preferred orientation. On the other hand, enzyme reconstitution at R_{sol} results in comparatively higher insertion efficiency but mostly random enzyme orientation (with the percent of inwards/outwards facing enzymes being close to 50:50) was observed (*50, 62, 74*). While the rest of the spectrum can be considered variating between these two modalities, in some cases, the most efficient reconstitutions can be achieved with detergent concentrations somewhere between R_{sat} and R_{sol}, an example of which was the ATP synthase reconstituted with sodium cholate (*1, 50, 64*). Nevertheless, these two extremes are commonly chosen as starting points in reconstitution attempts, while the fine tuning with respect to detergent concentration can be done later. For these reasons, reconstitution of SRC here was performed at R_{sat} and R_{sol} of detergents, while I stress once more that these two points by no means indicate the maximal achievable activity.

3.1.7.1 Solubilization profiles of different types of LUVs with various detergents

Preformed lipid, hybrid and polymer LUVs were solubilized by the gradual addition of either sodium cholate, sodium deoxycholate, octyl glucoside, Triton X-100 or dodecyl maltoside. These detergents were previously shown to be reliable reconstitution mediators for MP insertion into liposomes, as discussed in Chapter 1.3.2. While otherwise significantly different in, among other attributes, their chemical nature, charge, structure and membrane partitioning kinetics, these tested surfactants can generally be divided into two groups based on the mechanism of membrane solubilization in dependence to the speed of detergent flip-flop between outer and inner monolayer. If detergent molecules cannot flip to the inner layer or they flip slowly, the accumulation of detergent in outer layer induces mass imbalance between both

layers as well as increased positive curvature of outer layer (*68, 169*). These effects lead into the formation of membrane invaginations and, furthermore, into budding of mixed lipid/detergent micelles (*170, 171*). Such membrane solubilization is relatively slow, considering separate monolayer solubilization and slow detergent partitioning from solution to monolayer, hence the detergents which exhibit this mechanism of action can be considered as slow solubilizing detergents. The examples of the latter used in this study are sodium cholate and sodium deoxycholate. On the other hand, in the case where detergents are capable of rapid flip-flopping and partitioning in the lipid inner layer, the trans-bilayer equilibration results in membrane perturbation and the formation of microscopic transient pores. Eventually, micellization of the whole membrane can be seen to occur (*169, 172*). Detergents exhibiting the described course of action can be classified as the fast solubilizing and are in this study represented by octyl glucoside, Triton X-100, and dodecyl maltoside. It is worth noting that for the former, secondary aggregation was also observed at high lipid concentration, leading to an increased turbidity at the end of the solubilization process (*62, 173*). Finally, to determine the membrane saturation and the total solubilization point for tested detergents, the changes in the absorbance of vesicles were monitored at 540 nm (*34, 174*). The total solubilization point was defined as a point at which the minimal absorbance value was reached, in accordance to the proposed three stage membrane solubilization model (*63, 67, 175*), described in the introduction (Chapter 1.3.2). This point could be consistently observed and determined across all tested systems. The membrane saturation point, however, which is usually observed as the point of maximal absorbance, could not be defined in same way between liposomes, hybrids and polymersomes considering large differences in membrane architecture and interactions with detergents that separate these systems. The specifics of the determined R_{sat} in various systems can be found in their corresponding segment.

Destabilization profiles of detergent-treated lipid LUVs perfectly conveyed the mechanism of action differences between slow and fast solubilizing detergents, as described above. In the case of liposomes treated with octyl glucoside, Triton X-100 or dodecyl maltoside (Fig. 16), first, the detergents accumulated in bilayer, which was reflected in the apparent increase in optical density of vesicles, up to the point where the membranes were saturated with detergents (R_{sat}). Membrane saturation was most pronounced in the case of dodecyl maltoside, where nearly sixfold increase in absorbance was measured, showcasing comparatively high capacity of lipid membranes for said detergent. Saturation was followed by gradual membrane disintegration, which could be seen as a rapid decrease in absorbance of vesicle solution, ending

in total solubilization of vesicles (R_{sol}). Interestingly, in the case of dodecyl maltoside, when this point was reached, treated samples became highly turbid (pronounced milky appearance), which suggested secondary aggregation mentioned above. The presence of these aggregates could have negatively affected protein insertion and should be considered where the activity of respiratory enzymes reconstituted with R_{sol} for dodecyl maltoside is analysed.
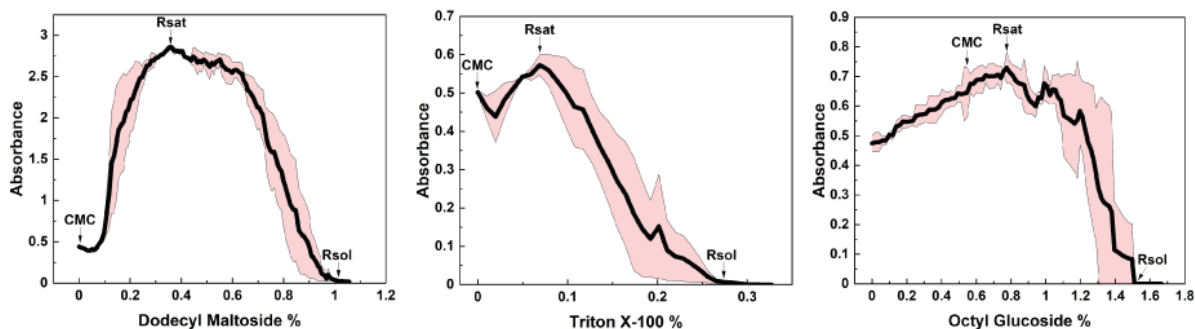
Fig. 16. Solubilization profiles of lipid vesicles treated with dodecyl maltoside, Triton X-100 or octyl glucoside. Detergents were supplemented to 0.2 ml of preformed lipid LUVs in small increments and changes in the absorbance of vesicles were recorded at 540 nm. Specified are the membrane saturation (R_{sat}) and total solubilization (R_{sol}) point, as well as when the critical micellar concentration (CMC) of the tested detergent was reached. Average values of three different measurements and the standard errors are depicted with black and red, respectively.

On the other hand, large differences in solubilization profiles of liposomes recorded with slow solubilizing detergents could be seen (Fig. 17). The initial slow partitioning of sodium cholate in outer lipid monolayer resulted in slight decrease in optical density of vesicles, followed by much faster drop in absorbance, presumably when membrane budding occurred. The inflection point between these two events was therefore chosen as the membrane saturation point. In the case of sodium deoxycholate, comparatively faster initial detergent partitioning could be seen, resulting in even faster absorbance decrease compared to sodium cholate. This was likely accompanied by membrane budding from the very start. Nevertheless, this was followed by momentarily increase in optical density of samples, seemingly due to partitioning of said detergent into inner layer (*121*) upon the dissolution of outer one, which again proceeded with steep absorbance decrease due to membrane budding. The very similar nature of the initial decrease in absorbance and of the following another one further suggested that the budding already occurred at the very start of solubilization. In the case of sodium deoxycholate, the point after which the second stage of budding have been seen, was chosen as the membrane saturation point. Finally, it is worth noting that in the case of fast solubilizing detergents, detergent micelles (in solubilization profiles the detergent concentration, at which micelles are

90

formed – the critical micellar concentration, CMC, is indicated) were present in samples from the very start. The presence of micelles could have had a stabilizing effect on added enzymes during reconstitution, which could have negatively affected enzyme membrane insertion efficiency.

Fig. 17. Solubilization profiles of lipid vesicles treated with sodium cholate or sodium deoxycholate. Detergents were supplemented to 0.2 ml of preformed lipid LUVs in small increments and changes in the absorbance of vesicles were recorded at 540 nm. Specified are the membrane saturation (R_{sat}) and total solubilization (R_{sol}) point, as well as when the critical micellar concentration (CMC) of the tested detergent was reached. Average values of three different measurements and the standard errors are depicted with black and red, respectively.

The solubilization of hybrid LUVs was highly reminiscent of the solubilization of liposomes with the slow solubilizing detergents considering the absence of the initial increase in absorbance due to membrane saturation. Instead, a very short-lasting spikes in absorbance were observed following the initial decrease in vesicle turbidity, and the point of maximal recorded absorbance of this transient stage was denoted as the membrane saturation point (indicated as "R_{sat}" in the related Figs. 18 and 19). This temporal increase was likely due to the detergent incorporation into lipid domains of hybrid vesicles and this stage might have been slightly staggered due to the more frequent detergent-polymer interactions considering the higher polymer content of hybrids. Furthermore, the initial drop in absorbance could have been a result of polymer or lipid leeching out of hybrid membranes by detergents, as in the case of liposomes. Nevertheless, the loosening of polymer monolayer due to the incorporation of detergent could have also resulted in the decreased vesicle absorbance. We observed similar effect upon the insertion of MPs into polymersomes, which resulted in the increased membrane permeability and enhanced diffusion in this system (Chapters 3.1.3 and 3.1.4). Interestingly, in cases where detergent micelles were not present in hybrid samples during detergent treatment

(octyl glucoside, sodium deoxycholate), nearly linear decrease in sample absorbance was recorded, hinting at even and steady solubilization of hybrids (Fig. 18).
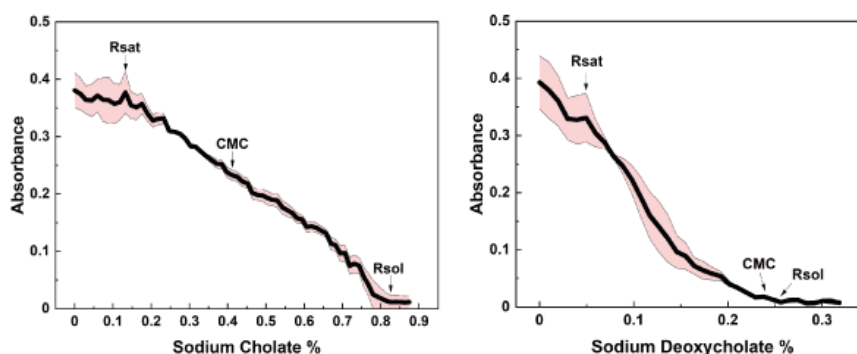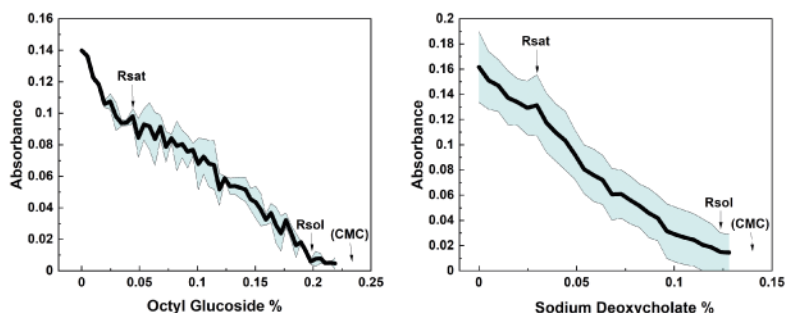

Fig. 18. Solubilization profiles of hybrid vesicles treated with octyl glucoside or sodium deoxycholate. Detergents were supplemented to 0.2 ml of preformed hybrid LUVs in small increments and changes in the absorbance of vesicles were recorded at 540 nm. Specified are the membrane saturation (R_{sat}) and total solubilization (R_{sol}) point. Critical micellar concentration (CMC) of the tested detergent was not reached in these systems. Average values of three different measurements and the standard errors are depicted with black and green, respectively.

On the contrary, in the presence of detergent micelles (sodium cholate, Triton X-100, dodecyl maltoside), rapid membrane solubilization was followed by much slower one, likely reflecting a difference in the exchange speed of lipid and polymer between the vesicles and mixed micelles (Fig. 19). As in the case of liposomes, the presence of detergent micelles in the reconstitution mixtures requires further consideration in the analysis of enzyme activity. Furthermore, secondary aggregation of DDM was detected upon total solubilization of hybrids. Finally, it is worth noting that a similar solubilization progression of POPC/PBd-*b*-PEO hybrid vesicles with Triton X-100, featuring two distinct stages – slower and faster solubilization – was reported by Khan and colleagues (*149*), regardless of large differences between said polymer and PDMS-*g*-PEO. Moreover, such solubilization progression could even be seen in hybrids comprising two different types of polymer (*72*).
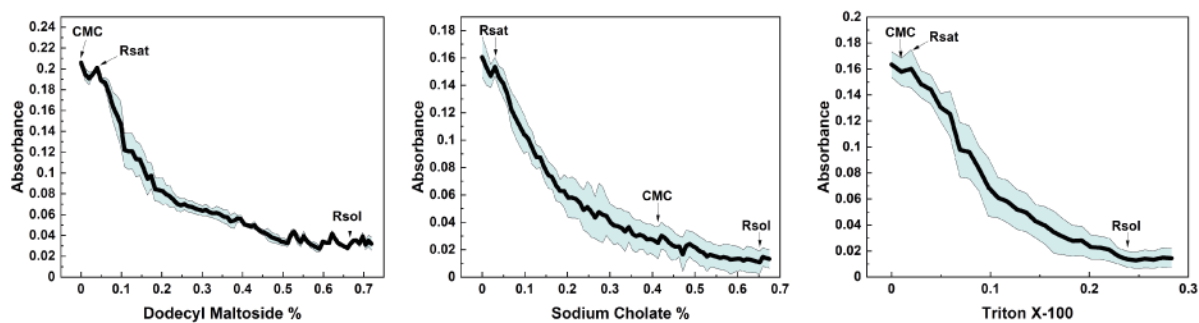
Fig. 19. Solubilization profiles of hybrid vesicles treated with dodecyl maltoside, sodium cholate or Triton X-100. Detergents were supplemented to 0.2 ml of preformed hybrid LUVs in small increments and changes in the absorbance of vesicles were recorded at 540 nm. Specified are the membrane saturation (R_{sat}) and total solubilization (R_{sol}) point, as well as when the critical micellar concentration (CMC) of the tested detergent was reached. Average values of three different measurements and the standard errors are depicted with black and green, respectively.

Finally, very similar solubilization profiles of polymer LUVs treated with various detergents could be observed. The initial slower solubilization, which likely indicated detergent partitioning into polymer monolayer, was followed by more rapid decrease in vesicle absorbance, which presumably specified the leeching of polymer from the vesicles. The inflection point between the two stages was designated as the membrane saturation point (R_{sat}). Interestingly, this point was seen to occur at about 15 % of detergent concentration required for total solubilization of vesicles, consistently, across all tested detergents. Moreover, in the case of polymersomes, detergent micelles were only present in samples treated with either Triton X-100 or dodecyl maltoside. Lastly, similarly to liposomes and hybrids, secondary DDM aggregation was observed in solubilized polymersomes, further suggesting very similar nature of tested lipid and polymer, based on the presence of these assemblies.
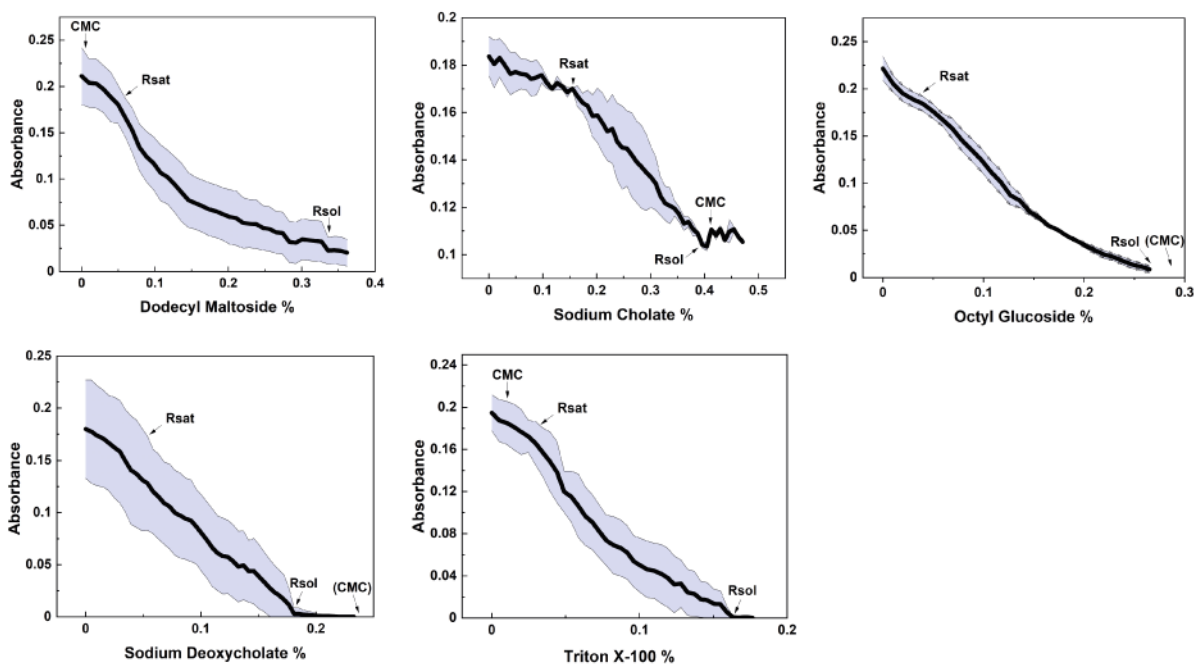
Fig. 20. Solubilization profiles of polymer vesicles treated with dodecyl maltoside, sodium cholate, octyl glucoside, sodium deoxycholate or Triton X-100. Detergents were supplemented to 0.2 ml of preformed polymer LUVs in small increments and changes in the absorbance of vesicles were recorded at 540 nm. Specified are the membrane saturation (R_{sat}) and total solubilization (R_{sol}) point, as well as when the critical micellar concentration (CMC) of the tested detergent was reached. Average values of three different measurements and the standard errors are depicted with black and blue, respectively.

The determined R_{sat} and R_{sol} values for tested detergents in different types of vesicles are compiled in Table 2, and these detergent concentrations were used for the reconstitution of *bo₃* oxidase and ATP synthase for the analysis of enzyme orientation and reconstitution efficiency.

Table 2. The determined membrane saturation (R_{sat}) and total solubilization points (R_{sol}) of lipid, hybrid and polymer LUVs for different detergents. Data was compiled from the solubilization profiles obtained by gradual supplementation of preformed vesicles with detergents. Starting material were 2 mg of vesicles in 0.2 ml of buffered solution. R_{sat} and R_{sol} were expressed as percent mass of the detergent (m/v).

	Liposomes		Hybrids		Polymersomes	
	R_{sat} (%)	R_{sol} (%)	R_{sat} (%)	R_{sol} (%)	R_{sat} (%)	R_{sol} (%)
Sodium cholate	0.13	0.83	0.03	0.65	0.16	0.40
Sodium deoxycholate	0.05	0.26	0.03	0.13	0.03	0.18
Octyl glucoside	0.77	1.51	0.03	0.20	0.04	0.27
Triton X-100	0.07	0.27	0.02	0.24	0.02	0.16
Dodecyl maltoside	0.35	1.10	0.04	0.67	0.05	0.34

3.1.7.2 Orientation and reconstitution efficiency of bo₃ oxidase in lipid, hybrid and polymer LUVs

The correctly oriented *bo₃* oxidase is one of most important prerequisites for the establishment of sufficient proton gradient in vesicles, capable of driving the synthesis of ATP. Considering the high symmetry of this enzyme with respect to structure, hydrophobicity and surface charge, the insertion of *bo₃* oxidase with predominantly preferred single orientation is not expected. In fact, largely mixed orientation of the inserted enzyme (albeit with only slightly larger fraction of inwards-facing enzyme) was previously reported (*44, 50, 150*), despite the fact that the enzyme was inserted into partially solubilized vesicles, the method which usually results in some degree of uniformity orientation-wise. Nevertheless, the successful ATP synthesis in mentioned systems (*44, 50*) served to showcase the importance of sufficiently high enzyme reconstitution efficiency. After all, correct orientation of the enzyme matters very little, if the enzyme itself does not end up inserted in membranes with sufficiently high concentration (and, on a similar note, does not end up co-inserted with the ATP synthase in shared vesicles). Therefore, my goal was to investigate how the orientation and reconstitution efficiency of *bo₃* oxidase can be modulated in different types of vesicles based on the choice of detergent and on the degree of vesicle solubilization. Towards this end, the fluorescently labelled enzyme was reconstituted in lipid, polymer and hybrid LUVs, which were partially (at R_{sat}) or entirely (at

R_{sol}) solubilized with either sodium cholate, sodium deoxycholate, octyl glucoside, Triton X-100 or dodecyl maltoside. The fluorescence of the enzyme in vesicles and in the reconstitution mixture could then be compared to determine the enzyme reconstitution efficiency (for details please see Chapter 2.5.5). Furthermore, the fluorescent dye could be selectively removed from the outwards-facing enzyme only (His-tag facing outwards) by disassembling the His-Ni-dye complex with imidazole (competitive binding) or by fluorophore bleaching with sodium dithionite (Fig. 21). This enabled estimation of the fraction of inwards-facing enzyme, which was unaccessible to mentioned treatments.
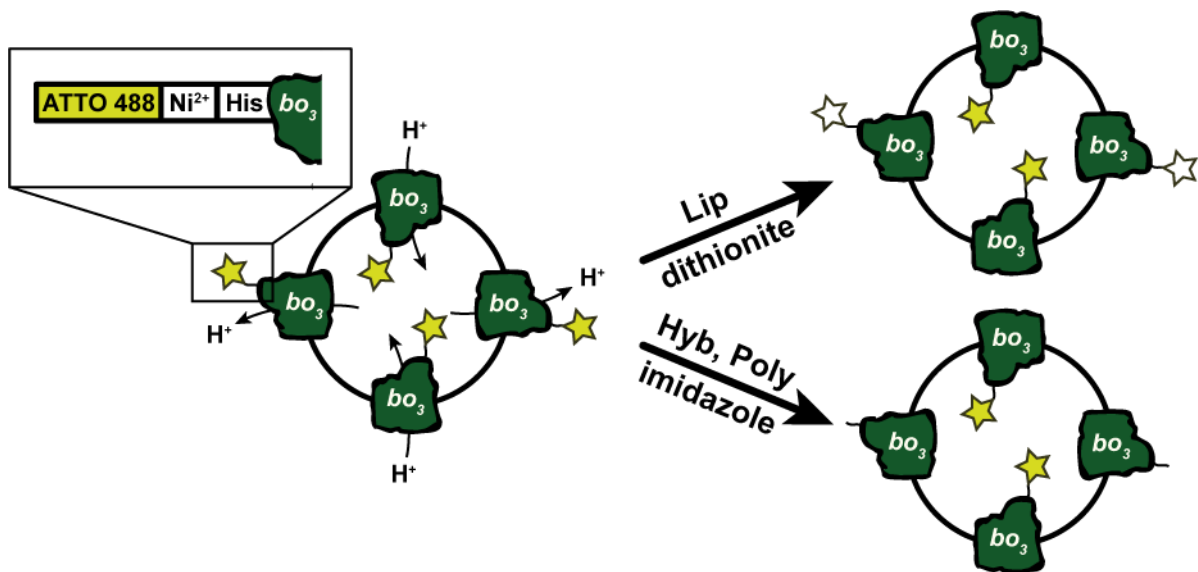
Fig. 21. Determination of the orientation of *bo₃* oxidase in different types of vesicles. The enzyme contained His tag on the C-terminus of the subunit II (pointing in direction of proton translocation) to which the fluorescent dye (ATTO 488) was attached via the His-Ni-NTA affinity binding. In proteoliposomes, the fluorescence of the accessible (outwards-facing) dye could be bleached by dithionite. Meanwhile, in proteohybrids and proteopolymersomes the accessible dye was detached entirely from the enzyme by the competitive binding of imidazole and the detached dye was removed from proteovesicles on a density gradient. By measuring and comparing the fluorescence of proteovesicles before and after the treatment, the orientation of *bo₃* oxidase was determined.

The analysis of *bo₃* oxidase orientation in liposomes revealed that the highest fraction of inwards-facing enzyme was achieved with the fast solubilizing detergents – Triton X-100, dodecyl maltoside and octyl glucoside (Fig. 22). With respect to these, proteoliposomes prepared with dodecyl maltoside at the membrane saturating detergent concentration contained 79.4 ± 12.2 % of correctly oriented enzyme. Similarly, the majority of proteoliposomes that were reconstituted with Triton X-100 at the R_{sat} of this detergent, exhibited comparably high (71.9 ± 6.7 %) correct orientation of *bo₃* oxidase. Octyl glucoside was an exception within the

group of detergents with similar course of action, considering the best enzyme orientation was achieved following the total solubilization of liposomes with this detergent. Nevertheless, the degree of correct orientation achieved in this way, 58.1 ± 10.0, was still slightly lower than the ones achieved at R_{sol} of dodecyl maltoside and Triton X-100 – 64.2 ± 5.8 and 58.7 ± 1.6 %, respectively.
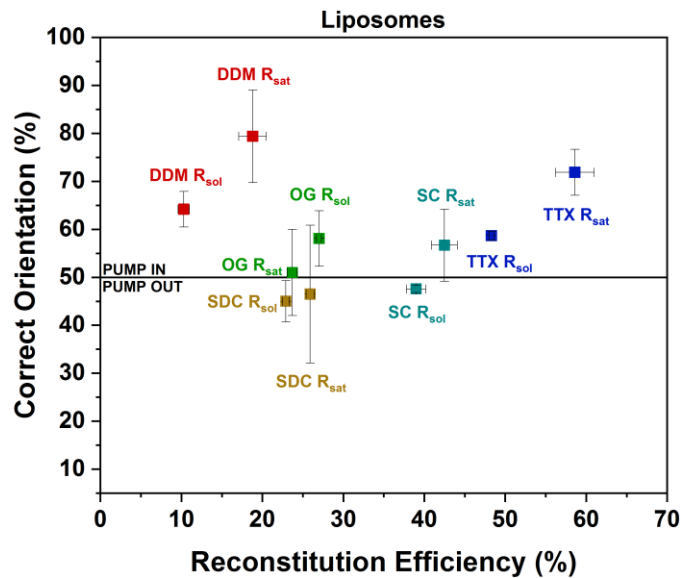
Fig. 22. Orientation and reconstitution efficiency of *bo₃* oxidase inserted in lipid LUVs with different detergents. Preformed vesicles were either saturated (R_{sat}) with detergents or completely dissolved (R_{sol}) to form lipid/detergent mixed micelles. Orientation of *bo₃* oxidase was determined based on the accessibility of enzyme-attached (unilaterally) dye to bleaching agent (sodium dithionite). Reconstitution efficiency was determined by comparing fluorescence intensity of labelled enzyme in the reconstitution mixture and in proteoliposomes. Each point represents the average value of at least 4 different measurements (separate reconstitutions) with the standard error.

In contrast, reconstitutions of *bo₃* oxidase featuring slow solubilizing detergents – sodium cholate and sodium deoxycholate – resulted mostly in enzyme insertion with mixed orientation (the fractions of the inwards- vs. outwards-facing enzyme being nearly 50:50). The only exception were proteoliposomes reconstituted at R_{sat} of sodium cholate, in which 56.7 ± 13.2 % of enzyme was oriented correctly. Interestingly, similar orientation of *bo₃* oxidase (slightly over 50 % correct, as deducted from the net proton influx in their system) was reported in the works of von Ballmoos and colleagues (*44, 50*), in which the enzyme was reconstituted with sodium cholate at or near R_{sat} of this detergent. Furthermore, equal findings are reported by Berg and colleagues (*150*) for this reconstitution setup. The above-described findings are somewhat counterintuitive. Based on the differences in the course of membrane solubilization

between slow and fast solubilizing detergents, one might expect to observe enzyme insertion with preferred orientation in cases, where only an outer lipid layer is dissolved (slow detergents), hence forming an asymmetrical enzyme insertion point with respect to hydrophobicity and electrostatic repulsions. Nevertheless, preferred enzyme orientation was instead achieved in the perturbated bilayers (fast detergents). In these systems, detergent contents were above their CMC and the presence of detergent micelles could have modulated the enzyme insertion, affecting bo_3 oxidase orientation. In contrast, no particular relationship between the reconstitution efficiency of bo_3 oxidase and the course of action of detergents was observed. Overall, slightly better enzyme insertion was achieved at the membrane saturating detergent concentrations (Fig. 22), although the insertion efficiencies varied significantly between tested setups. The most efficient insertion was achieved with Triton X-100, where 58.6 ± 2.4 % of the enzyme was inserted successfully, while the least efficient setup appeared to be reconstituted with dodecyl maltoside, where only 10.3 ± 1.7 % of the enzyme ended up inserted in membranes. In the latter setup, secondary aggregates of dodecyl maltoside were observed in samples containing entirely dissolved vesicles, likely hindering the formation of proteoliposomes upon detergent removal, which resulted in poor enzyme insertion. Furthermore, the most efficient enzyme insertion seen at R_{sat} of detergents was somewhat surprising, considering higher insertion efficiencies reported in systems formed via micellization method (63, 64, 74). Nonetheless, the differences between R_{sat} and R_{sol} setups were minor, usually within 5 %, with the obvious exceptions being dodecyl maltoside (secondary aggregates at R_{sol} but not at R_{sat}) and Triton X-100 (unknown reasons).

On average higher correct orientation of bo_3 oxidase was achieved in proteohybrids when compared to proteoliposomes (approx. 67 vs. 58 %, respectively) (Fig. 23). Vesicles reconstituted with dodecyl maltoside at R_{sat}, in particular, were seen standing out as in the case of liposomes, by featuring 83.7 ± 2.3 % correctly inserted enzyme. On a similar note, fast solubilizing detergents could be on average seen performing better than the slow solubilizing ones, although the difference between the two groups is not as pronounced as in liposomes. This is particularly interesting considering the predominant polymer content of hybrids and thus monolayer architecture. Nevertheless, it appears that the lipid nanodomains present in these assemblies might have had a leading role in deciding enzyme orientation, as suggested by apparent similarities between proteoliposomes and proteohybrids with respect to this reconstitution parameter. Importantly, better than 50 % correct orientation was achieved with all tested detergents in hybrid vesicles, which makes this type of vesicles a promising candidate

98

for the construction of artificial respiratory chain or for other gradients-driven applications. Furthermore, on average slightly more efficient insertion of bo_3 oxidase was achieved in proteohybrids compared to proteoliposomes (approx. 39 vs. 32 %, respectively). With respect to this, octyl glucoside at R_{sol} was identified as the best mediator, resulting in 57.8 ± 2.0 of bo_3 oxidase inserted in membranes. In comparison, the highest achieved enzyme insertion efficiencies in hybrids and liposomes were nearly the same (57.8 vs. 58.6 %, respectively), further suggesting high degree of biocompatibility of this polymer architecture. The poorest enzyme insertion was recorded in samples reconstituted with sodium deoxycholate, comparable to the one determined in samples formed with dodecyl maltoside at R_{sol}, where secondary aggregates were detected. It is important to note that similar poor performance of sodium deoxycholate was observed in liposomes, hinting at predominant detergent-lipid interactions in this hybrid system. Interestingly, better insertion of bo_3 oxidase was achieved when the enzyme was added to the mixture of fully solubilized vesicles (at R_{sol}). This effect was expected, although not observed, in liposomes. This was likely due to the presence of additional detergent (in the form of polymer), which facilitated efficient mixing between lipid/polymer/detergent micelles and the detergent-stabilized enzyme.

Fig. 23. Orientation and reconstitution efficiency of bo_3 oxidase inserted in hybrid LUVs with different detergents. Preformed vesicles were either saturated (R_{sat}) with detergents or completely dissolved (R_{sol}) to form lipid/detergent mixed micelles. Orientation of bo_3 oxidase was determined based on the accessibility of enzyme-attached (unilaterally) dye to chelator (EDTA). Reconstitution efficiency was determined by comparing fluorescence intensity of labelled enzyme in the reconstitution mixture and in proteohybrids. Each point represents the average value of at least 4 different measurements (separate reconstitutions) with the standard error.

Polymer LUVs facilitated efficient insertion of bo_3 oxidase with predominantly correct orientation, although the performance of detergents varied significantly in these vesicles. On average, the fraction of inwards-facing enzyme was the same as in hybrids, approx. 67 % (Fig. 24). In the absence of lipids, the orientation of enzyme seemingly depended much more on the type of detergent as well as degree of membrane solubilization, instead on the course of detergent action. In this context, high performance of some slow-acting in addition to some fast-acting detergents was determined. Triton X-100 at R_{sat}, along with sodium cholate at R_{sol} mediated the insertion of bo_3 oxidase with 82.8 ± 2.6 and 84.6 ± 4.8 % correct orientation, respectively. Interestingly, this correct insertion was seemingly less dependent on the degree of membrane solubilization. Instead, it appears that it was related to the particular detergent type, likely due to specific dynamics of detergent partitioning in graft polymer membranes, which unfortunately at the time of writing remain entirely unknown, and should be addressed in future works. Nevertheless, high degree of correct orientation was achieved with Triton X-100 and sodium cholate at membrane saturation as well as at total membrane solubilization, further underlining the importance of a wider detergent screening that could potentially enable identification of even better insertion mediators. Moreover, the average reconstitution efficiency of bo_3 oxidase in polymersomes (~66 %) was significantly higher than in liposomes or hybrids, with highest efficiencies determined for sodium deoxycholate at R_{sat} (53.9 ± 3.7 %) as well as at R_{sol} (60.2 ± 9.6 %). The trend of detergent performance being related to the detergent type and not to the course of action or the degree of membrane solubilization could be seen also with respect to the enzyme reconstitution efficiency. Here, the best performing detergents facilitated efficient insertion at R_{sat} or R_{sol}, with the obvious exception being octyl glucoside, with which efficient insertion was achieved at R_{sol}, while the predominantly correct orientation was achieved at R_{sat}.
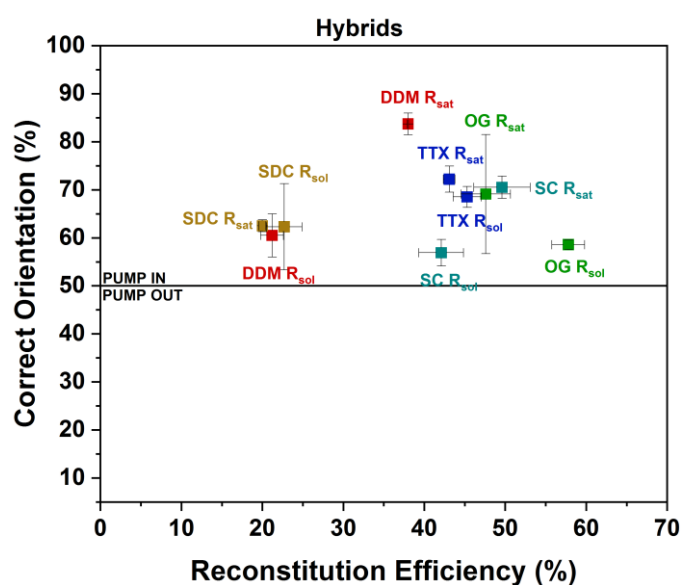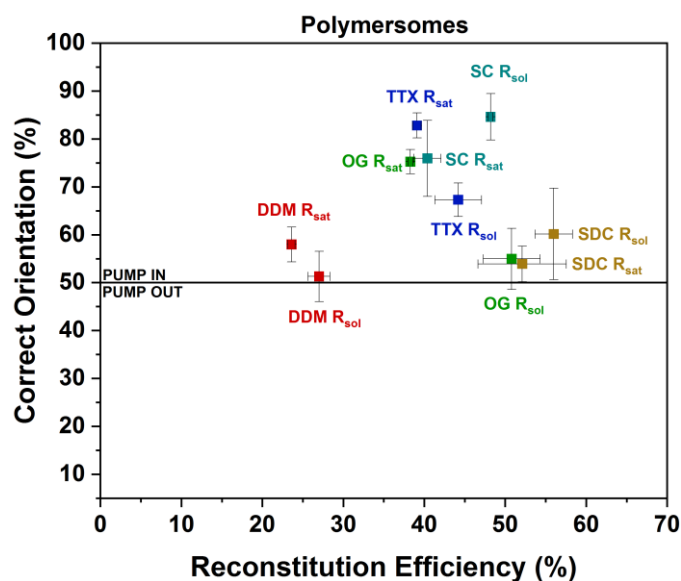
Fig. 24. Orientation and reconstitution efficiency of _bo₃_ oxidase inserted in polymer LUVs with different detergents. Preformed vesicles were either saturated (R_{sat}) with detergents or completely dissolved (R_{sol}) to form lipid/detergent mixed micelles. Orientation of _bo₃_ oxidase was determined based on the accessibility of enzyme-attached (unilaterally) dye to chelator (EDTA). Reconstitution efficiency was determined by comparing fluorescence intensity of labelled enzyme in the reconstitution mixture and in proteopolymersomes. Each point represents the average value of at least 4 different measurements (separate reconstitutions) with the standard error.

The above-discussed findings clearly demonstrate the similarities between liposomes and hybrids with respect to the insertion of largely symmetric and hydrophobic membrane proteins. This, along with the apparent differences between liposomes/hybrids and polymersomes suggests that the interactions of detergents with lipid and not polymer portion of hybrid vesicles dictates enzyme insertion. Perhaps this is because lipids can be more promptly exchanged between vesicles and micelles, while the partitioning coefficients of much larger polymer molecules are comparatively lower. The findings also demonstrate that the orientation as well as insertion efficiency of _bo₃_ oxidase can be controlled to a large extent by the detergent choice in polymersomes, and, in parallel, with the degree of membrane solubilization in hybrids and liposomes. In many cases, the correct orientation is achieved at the expense of lower insertion efficiency and vice versa. Nevertheless, determination of the reconstitution parameters is invaluable for the assessment of the final output of the module, as well as for the application-tailored system design where most often some attributes are more important than others. This is particularly true for the gradients facilitators, such as proton pumps, where the correct orientation of the pump has much higher impact on the system than the high insertion efficiency, the parameter which can more easily be remedied in other ways.

101

Finally, it is important to note that the determined enzyme orientation in batch does not necessarily reflect the potentially highly variable and heterogeneous enzyme distribution on a single vesicle level. On the contrary, high proton influx is expected in vesicles featuring high degree of correctly oriented enzyme, while no gradient is established in vesicles which contain predominantly outwards-facing enzyme. If one considers further random co-insertion of ATP synthase into such heterogeneous population of vesicles, increasing the concentration of *bo₃* oxidase in energy modules (either by including more enzyme in the reconstitution mixture or by increasing its reconstitution efficiency) is expected to result in higher number of vesicles capable of driving ATP synthesis. This phenomenon was previously observed by von Ballmoos and colleagues (*44*) (also (*50*)), with some limitations. In particular, the increased membrane permeability at high protein contents must be considered, due to its diminishing effect on the formation of a proton gradient (*74, 97*). Remarkably, we observed hybrid membrane resealing upon protein insertion (*97*), which can be exploited in future for the reconstitution of energy modules at high protein densities.

3.1.7.3 Orientation and reconstitution efficiency of ATP synthase in lipid, hybrid and polymer LUVs

The output of the energy module is directly dependant on the amount of the reconstituted ATP synthase, degree of the correct orientation of this enzyme as well as its specific activity. Here, the enzyme orientation is not as important (while still very important!) as in the case of *bo₃* oxidase. Mixed orientation of the latter actively diminished the net proton influx, inhibiting ATP synthesis, while the mixed orientation of the former only proportionally reduces the amount of active enzyme, thus lowering the rate of ATP synthesis. On the other hand, ATP synthesis depends directly on the amount of successfully inserted enzyme. To determine the orientation of ATP synthase, enzyme activity in proteovesicles in the hydrolysis direction was analysed. Towards this end, different types of vesicles reconstituted with ATP synthase were coupled with enzymatic cascade featuring pyruvate kinase and lactate dehydrogenase (Fig. 25A). In this coupled system, ATP available to the ATP synthase is regenerated from phosphoenolpyruvate by pyruvate kinase. The pyruvate produced in this reaction is then converted to lactate by lactate dehydrogenase, while NADH was being oxidized to NAD⁺. The changes in absorbance of NADH at 340 nm can then be monitored, which are directly proportional to the amount of ATP hydrolized by the ATP synthase. In this setup, ATP is produced by the coupled system outside of vesicles, hence, only outwards-facing ATP synthase can access and hydrolize it, enabling the estimation of enzyme inserted with this

orientation. In the next step, proteovesicles are completely dissolved by detergent and the inwards- as well as outwards-facing enzyme is exposed to ATP. The total ATP hydrolisis in samples could then be determined and compared to the hydrolysis of outwards-facing enzyme to estimate the degree of correct (outwards-facing) orientation (Fig. 25B).
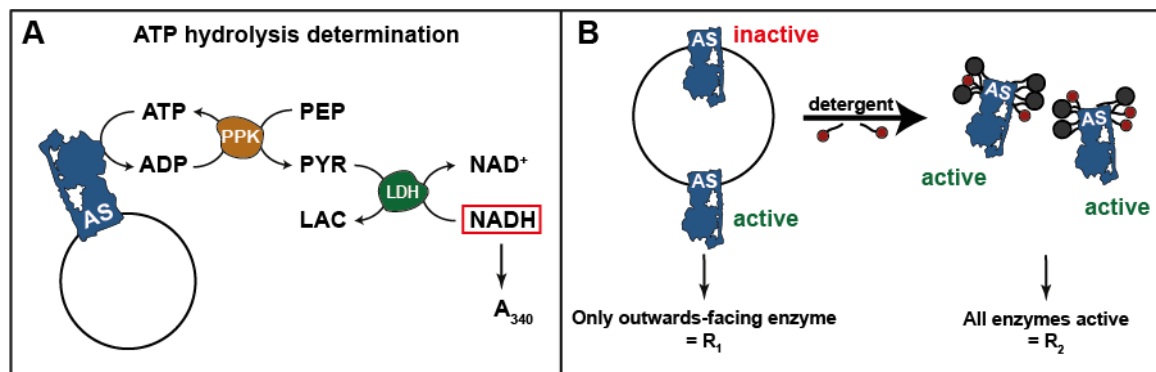
Fig. 25. ATP hydrolysis determination in different types of vesicles reconstituted with ATP synthase. (**A**) Proteovesicles were coupled with the reporter system comprising polyphosphate kinase (PKK) and lactate dehydrogenase (LDH), which enabled indirect detection of changes in the concentration of ATP. In the coupled system, phosphoenolpyruvate (PEP) was converted to pyruvate to enable continuous resupply of ATP. Next, pyruvate (PYR) was converted to lactate (LAC) by lactate dehydrogenase (LDH), while NADH was simultaneously oxidized to NAD^+. The consumption of NADH corresponding to the ATP hydrolysis could then be monitored spectrophotometrically at 340 nm. (**B**) Orientation of ATP synthase was determined by comparing the ATP hydrolysis rate of proteovesicles (R_1) with that of enzyme stabilized in micelles (R_2). In proteovesicles, only outwards-facing enzyme was accessible by ATP and could be activated. On the other hand, when proteovesicles were dissolved with detergent to form mixed micelles, all enzyme could be activated. Orientation was then determined by comparing R_1 and R_2.

Furthermore, hydrolysis in samples was compared to the determined highest one to extrapolate relative reconstitution efficiencies. Ideally, this parameter would be determined by comparing the activity of vesicle-inserted enzyme after reconstitution with the activity of the same concentration of the enzyme that was used in reconstitutions, but instead stabilized in detergent micelles. However, stimulatory effect of detergents on hydrolysis by ATP synthase was previously reported (*176*), due to the detergent interactions with the ε subunit of the enzyme. Interestingly, similar effect of several detergents, among others Triton X-100 on the activity of ATP synthase in micelles was observed in this work (Fig. 26). Considering the notoriously tight association of some detergents with membrane proteins, it could not be excluded that minute amounts of residual detergents after the reconstitution could have altered

the ATPase activity, leading to the overestimation of the enzyme reconstitution efficiency. Therefore, the hydrolysis activities obtained with various detergents are compared among themselves instead, and the relative reconstitution efficiency is reported.
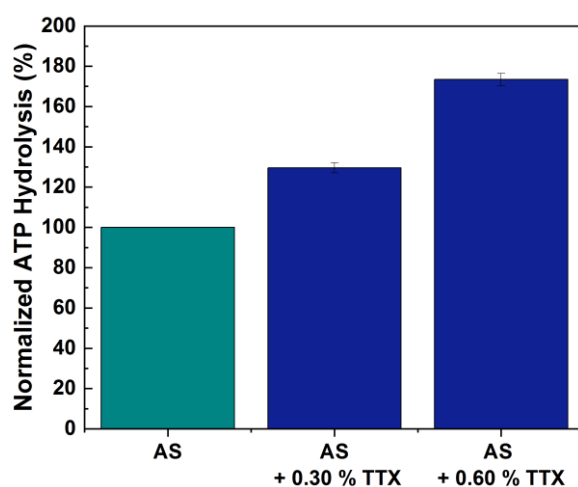
Fig. 26. ATP hydrolysis by ATP synthase stabilized in micelles in the absence and presence of Triton X-100. To the ATP synthase stabilized in the elution buffer containing octyl glucoside, sodium cholate, sodium deoxycholate and phosphatidylcholine (**AS**), Triton X-100 was added at either 0.3 % (**AS + 0.3 % TTX**) or 0.6 % (**AS + 0.6 % TTX**) final concentration (w/v) and the changes in ATP hydrolysis were recorded. The activities of ATP synthase after the addition of Triton X-100 were normalized to the enzyme activity determined in the absence of this detergent.

The analysis of ATP synthase orientation in all systems revealed high variability between the samples as well as within most samples. For this reason, each measurement (representing separate reconstitution) on proteoliposomes (Fig. 27A), hybrids (Fig. 27B) or polymersomes (Fig. 27C) is indicated with individual symbol and the values are not averaged. In rare cases, continuum of the degree of correctly orientated enzyme within a sample was determined, as, for instance, in the case of polymersomes reconstituted with octyl glucoside at R_{sat} (Fig. 27C, lane 3). In the majority of cases, however, samples could be seen featuring two or more distinct vesicle populations with different average correct orientation between populations. A few of such examples are liposomes reconstituted with sodium cholate at R_{sat} (Fig. 27A, lane 5), hybrids reconstituted with sodium deoxycholate at R_{sol} (Fig. 27B, lane 8) and polymersomes reconstituted with Triton X-100 at R_{sol} (Fig. 27C, right-most lane).
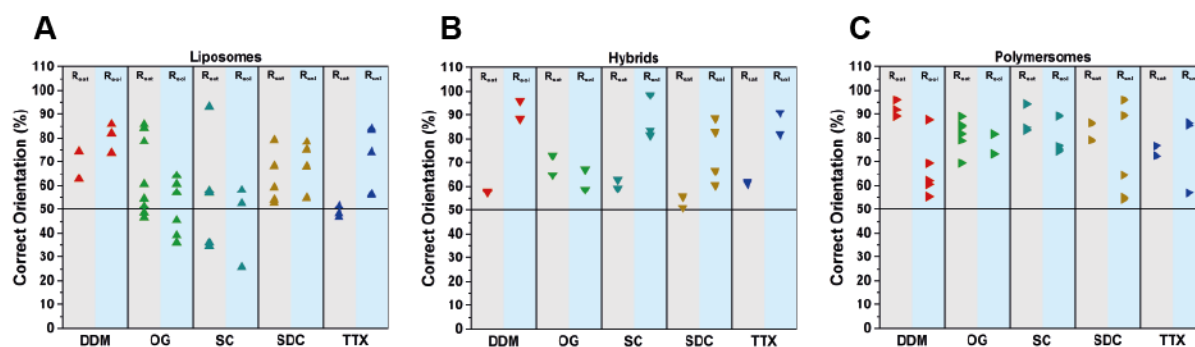
Fig. 27. Orientation of ATP synthase in lipid (A), hybrid (B) and polymer (C) LUVs. Preformed vesicles were reconstituted with ATPase at the membrane saturating (R_{sat}, grey lanes) or solubilizing (R_{sol}, blue lanes) concentration of either dodecyl maltoside (**DDM**), octyl glucoside (**OG**), sodium cholate (**SC**), sodium deoxycholate (**SDC**) or Triton X-100 (**TTX**). Enzyme orientation was determined based on the hydrolysis activity of proteovesicles. Each point represents a separate reconstitution.

In principle, this could be expected in reconstitutions where vesicles were completely dissolved by detergents and proteovesicles were formed from mixed micelles (*63, 64, 74*), considering the mixed and random orientation of ATPase in this scenario. However, this phenomenon was observed consistently between tested samples, independent on the type of detergent or the degree of membrane solubilization. This could be due to several reasons. First, unlike *bo₃* oxidase, which was stabilized with a single detergent, dodecyl maltoside, purified ATP synthase was stabilized with several amphiphiles – octyl glucoside, sodium cholate, sodium deoxycholate and phosphatidylcholine (*98*). Therefore, the dynamics of enzyme exchange between complex micelles and tested vesicles in the case of ATPase was expected to be much different from what could be expected in the case of *bo₃* oxidase. For the latter, simple dilution of the enzyme below CMC of stabilizing detergent was sufficient to promote dissociation of detergent and the related association of the enzyme with vesicles. While similar micellar dissociation could be argued even in the case of composed mixed micelles, the presence of lipids introduces additional level of complexity as well as additional mediator of protein insertion. In fact, we observed tight association of lipids with inserted enzyme in hybrid vesicles (*97*), which was not significantly disturbed even at relatively high detergent content in samples. This would suggest that the ATP synthase was reconstituted as lipid/enzyme assembly and the lipid content of these assemblies is speculated to play an important role in enzyme insertion. Furthermore, heterogeneity of ATPase with respect to orientation could have originated from slight variations in the degree of membrane solubilization within the same sample. Presumably, the supposed high sensitivity of ATPase to the latter could have resulted in the related highly variable outcome with respect to the enzyme insertion, which, in

105

comparison, was not seen in the reconstitutions of *bo₃* oxidase. To speculate further, such presumed high sensitivity could have been related to the lipid content in isolated enzyme. The detergent added to the reconstitution mixture would therefore be partitioning into preformed vesicles, as well as into lipid assemblies enveloping ATPase. The result of this would likely be variable membrane solubilization and the corresponding variable correct orientation. All things considered, highest average correct orientation of ATP synthase was achieved in polymersomes with about 78 % of the enzyme facing outwards, while about 72 and 61 % of the enzyme was determined facing outwards in hybrids and liposomes, respectively. Furthermore, dodecyl maltoside consistently mediated the insertion of ATPase with the correct orientation in liposomes and hybrids at R_{sol}, as well as in polymersomes at R_{sat}. Overall best enzyme orientation (93.2 % correct) in liposomes was accomplished with sodium cholate at R_{sat}, which is consistent with previously published value of 97.2 % for a very similar system (*128*), although large variations within a sample were recorded in this work, as discussed above. Most reliable detergent for the enzyme insertion in liposomes and hybrids, on the other hand, was determined to be dodecyl maltoside at R_{sol}. ATPase reconstituted with this setup exhibited highest average correct orientation along with the lowest variability within the two samples (80.4 ± 6.1 and 92.2 ± 5.3 % respectively). As in the case of *bo₃* oxidase, large similarities between liposomes and hybrids were observed with respect to detergent performance, further hinting at the preferred or at least more impactful interactions of detergents with lipids in these assemblies. Finally, dodecyl maltoside at R_{sat} performed best in polymersomes and turned out to be the most reliable, yielding 92.4 ± 3.4 % correctly inserted enzyme.

While very similar detergent performance could be seen with respect to the orientation of the reconstituted ATP synthase across all tested setups, this was not the case when the enzyme reconstitution efficiency was being considered. Interestingly, hybrids facilitated the most efficient overall enzyme insertion, with on average about 52 % of ATPase successfully inserted in membranes (Fig. 28B). The average value in liposomes was slightly lower (approx. 42 %), nevertheless, the overall highest insertion efficiency was achieved in this type of vesicles using sodium cholate as the mediating detergent (Fig.27A). Remarkably, the highest ATP synthesis was determined in liposomes reconstituted with sodium cholate across the literature (*44, 50, 54, 128*) as well as in our lab (*1*), which corelates well with the high insertion efficiency of ATP synthase determined for this setup. In fact, this relationship between the efficiency of ATPase insertion and the output of the module can be further seen in hybrids as well as in polymersomes (Chapter 3.1.3, Fig. 11C), and is analysed in more detail in the following

chapter. Finally, relatively low (below 40 %) insertion efficiencies were determined in polymersomes in all tested setups. Considering the enzyme reconstitution in polymersomes being tied to the postulated loosening of polymer monolayer (*97*), the insertion of larger lipid/ATPase assemblies in this type of vesicles might have been hindered. This claim is additionally supported with much better insertion of ATP synthase in hybrids, in which comparatively higher proton permeability (= looser structure; Chapter 3.1.4) was determined. Moreover, the insertion efficiency of *bo₃* oxidase in polymersomes was nearly the same as in liposomes, further suggesting that the reasons behind poor ATPase insertion originated in the enzyme itself and are likely only to a lesser extent related to the membrane architecture or the detergent of choice. Finally, as in the case of *bo₃* oxidase, poor ATP synthase insertion with dodecyl maltoside at R_{sol} was discerned, presumably due to the interference of secondary aggregates with the enzyme insertion.
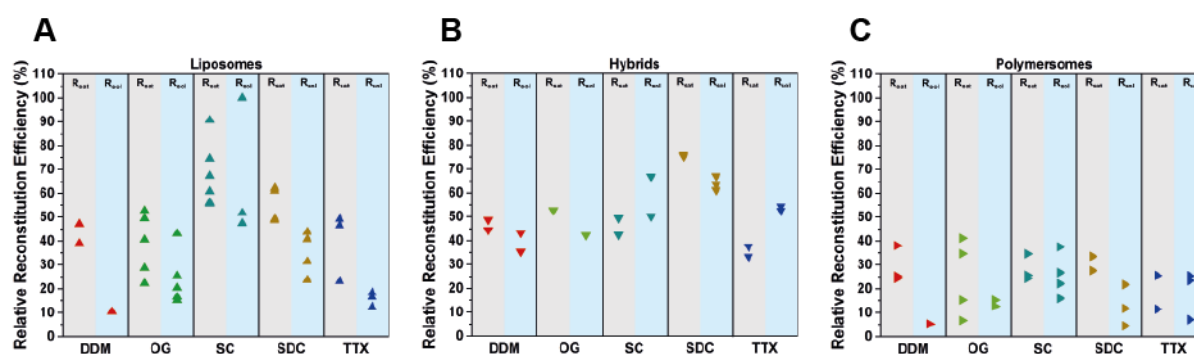
Fig. 28. Relative reconstitution efficiency of ATP synthase in lipid, hybrid and polymer LUVs. Preformed vesicles were reconstituted with ATPase at the membrane saturating (R_{sat}, grey lanes) or solubilizing (R_{sol}, blue lanes) concentration of either dodecyl maltoside (**DDM**), octyl glucoside (**OG**), sodium cholate (**SC**), sodium deoxycholate (**SDC**) or Triton X-100 (**TTX**). ATP hydrolysis rates (R_2) in different setups were compared with the highest obtained enzymatic activity to extrapolate relative insertion efficiencies. Each point represents a separate reconstitution.

3.1.7.4 ATP synthesis by the SRC reconstituted with various detergents in lipid, hybrid and polymer LUVs

Following the determination of the orientation and the reconstitution efficiency of ATP synthase and *bo₃* oxidase, both enzymes were coreconstituted in lipid, polymer and hybrid LUVs with various detergents at membrane saturation as well as solubilization point, and the ATP synthesis in these modules was measured. This enabled the comparison between the mentioned reconstitution parameters and the final output of the energy module. To account for the variability between the reconstitutions, each module was reconstituted and measured

separately at least six times. Finally, it is important to note that in the determination of ATP synthesis rates, a 100 % insertion efficiency and correct orientation of ATPase was assumed, leading to the underestimation of the actual activity of tested modules. Although the rate correction was proposed (*50*), the idea here was to compare raw output of the modules as measured, without determining the actual enzyme turnover. This reflected the activity of the modules as a whole in relation to the determined reconstitution parameters.

The ATP production measurements revealed highest activities of the energy modules reconstituted with sodium cholate in liposomes (Fig. 29A), octyl glucoside and sodium deoxycholate in hybrids (Fig. 29B) and with octyl glucoside in polymersomes (Fig. 29C). By comparing the highest average activities of proteohybrids and proteopolymersomes to the highest measured activity of proteoliposomes, it could be seen that roughly 55 and 36 % of the activity was retained in these polymer-based modules, respectively. Remarkably, this coincided well with the determined insertion efficiency of ATPase in these types of membranes (Chapter 3.1.7.3, Fig. 27), discussed in previous chapter. To inspect this relationship in greater detail, all determined reconstitution parameters for both enzymes were combined and plotted as a single parameter, the functional incorporation efficiency. The latter was derived by accounting for the enzyme reconstitution efficiency range, which was then corrected to further reflect the determined range of the correct enzyme orientation. For instance, in the case of liposomes reconstituted with ATP synthase using octyl glucoside at R_{sat}, the determined reconstitution efficiency was seen varying between 22.3 and 52.7 %, which meant that roughly between one fifth to one half of the enzymes added to the reconstitution mixture would end up inserted in membranes. Then, 46.6 to 85.7 % of the reconstituted enzymes could be seen inserted with the correct orientation and were able to facilitate ATP synthesis in the coupled module. Hence, the 10.4 to 45.2 % (the obtained ranges of 10.4–11.8 and 24.6–45.2 % were consolidated) of the inserted enzymes were functionally incorporated, which indicated that they were inserted successfully <u>and</u> with the correct orientation. The functional incorporation efficiencies of *bo₃* oxidase and ATP synthase were then plotted separately and overlayed with the ATP synthesis data collected in these modules to enable the comparison.
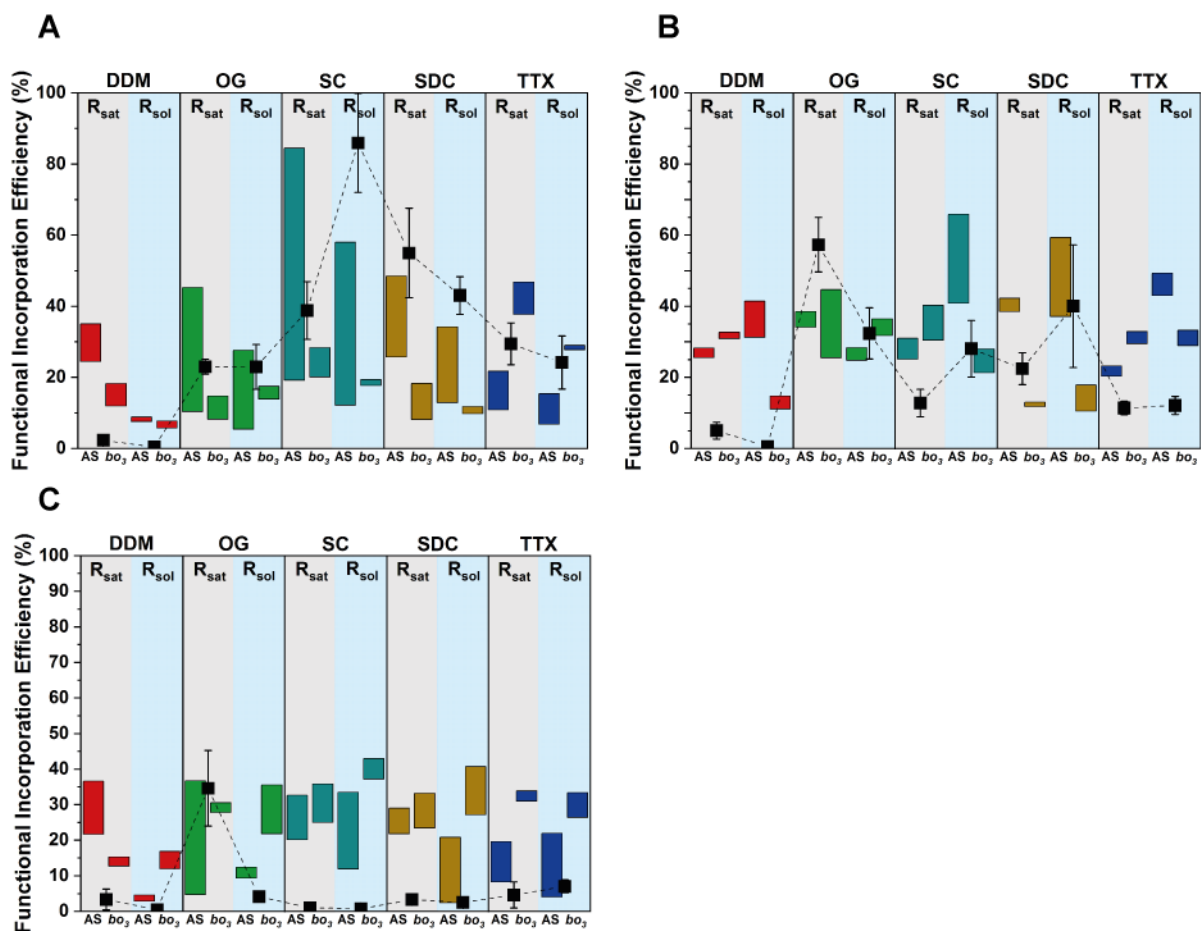
Fig. 29. Functional incorporation efficiency of *bo₃* oxidase (*bo₃*) and ATP synthase (AS) in lipid (A), hybrid (B) and polymer (C) LUVs. The two enzymes were reconstituted in preformed vesicles at the membrane saturating (R_{sat}, grey lanes) or solubilizing (R_{sol}, blue lanes) concentration of either dodecyl maltoside (**DDM**), octyl glucoside (**OG**), sodium cholate (**SC**), sodium deoxycholate (**SDC**) or Triton X-100 (**TTX**). The determined enzyme orientation and reconstitution efficiency in different setups were combined into a single parameter – functional incorporation efficiency. Overlaid (black trace) is the average ATP synthesis measured in different setups, with standard error. To determine the ATP synthesis, each sample was reconstituted two times and each reconstitution was measured in quadruplicate.

As mentioned above, a strong relationship between, in particular, the ATP synthase insertion efficiency and the final output of the modules could be seen in liposomes (Fig. 29A) and hybrids (Fig. 29B). In fact, high functional insertion of ATPase was a reliable predictor of the related high synthesis activity by the modules in all cases except in the case of dodecyl maltoside. While some fractions of both enzymes were seen functionally inserted, the ATP synthesis in modules constructed by dodecyl maltoside was negligible. As discussed in Chapter 3.1.7.1, secondary aggregation of this detergent at R_{sol} likely hindered the enzyme insertion.

Furthermore, the removal of detergent, which could be seen partitioning into inner membrane layer to an astonishing degree of membrane saturation (please see the solubilization profile of liposomes with dodecyl maltoside, Chapter 3.1.7.1, Fig. 16) poses significant challenge. Unfortunately, modules constructed with dodecyl maltoside were not tested for the presence of the residual detergent. Nevertheless, it is highly likely that this detergent was not sufficiently removed from the membranes upon protein insertion, resulting in low ATP synthesis rates in the related modules across all tested membranes. Somewhat of an outlier were also hybrids reconstituted with Triton X-100, in which higher ATP synthesis could be expected, following the trend observed in other tested setups. It is important to note though that the reconstitution parameters were determined for each enzyme separately, while the final activity of the modules depends on the successful coinsertion of both enzymes. Regrettably, at this point, the interactions between enzymes during the coinsertion remained unknown and should be addressed in future works. In this context, it would be important to see if the reconstitution parameters obtained on proteovesicles containing a single enzyme are also relevant in multi-enzyme scenarios. In any case, these finding showcase the potential of single enzyme reconstitutions via optimized protocols, followed by the enzyme integration and the assembly of functional modules and systems, for instance through fusion. While the prediction of the activity of energy modules correlated very well with the ATPase insertion efficiency in liposomes and hybrids, this trend could not be seen in polymersomes (Fig. 29C). In this type of membrane, the highest activities were obtained with the two fast solubilizing detergents - octyl glucoside and Triton X-100, with the former exhibiting significantly better performance than all other tested detergents. I observed this discrepancy in my previous work (*1*), where the highest ATP synthesis in polymersomes was achieved at very low concentrations of octyl glucoside (below R_{sat}), while the activities obtained with other detergents were significantly lower. The reasons behind this observation are not entirely clear, and, more broadly speaking neither is the mechanism of enzyme insertion into graft copolymer monolayers, along with the factors determining the outcome of the insertion. An appreciable improvement to the enzyme reconstitution procedure in polymersomes was made by detergent supplementation to polymer during the vesicle formation (instead of adding the detergent later and thus attempting solubilization of already formed vesicles) as well as the changed, stepwise addition of Bio-beads during the detergent removal phase (*1*). This drastically increased the enzyme insertion efficiency, leading towards major improvements of the output of the modules formed in this way. In parallel, this also suggested that there is still plenty of room for further optimization, where minor yet very impactful changes could further be made to the reconstitution procedures.

One of such changes would be enzyme reconstitution in polymersomes at even lower detergent concentrations or even in the absence of detergents. Astonishingly, I attempted the latter as a proof of concept only and recorded about 6 % activity with this setup relative to the highest activity measured in liposomes, which is higher than the activities obtained with all tested detergents, bar octyl glucoside at R_{sat} and Triton X-100 at R_{sol}. Moreover, passive proton permeability of proteopolymersomes reconstituted with different detergents should be determined to offer a potential insight into disproportionate ATP synthesis rates with respect to protein content of polymer membranes. Taking into account polymer monolayer loosening upon protein insertion (Chapter 3.1.4), imperfect insertion could have resulted in leaky membranes. The latter was in hybrids remedied by the membrane resealing facilitated by lipids but remained unaddressed in polymersomes. As a potential solution for this problem, I explored the Poloxamer P188 as a resealing agent (discussed in more detail in the upcoming Chapter 3.3.2), although in liposomes only, due to time constrains. Finally, as mentioned above, it is worth noting that the enzyme coinsertion in polymersomes could have resulted in poorer reconstitution of each individual enzyme. This hypothesis is somewhat supported by the observed decreased output of hybrids-based modules in comparison to proteoliposomes, in which the ATP synthesis rates remained relatively high (about 60 % of that determined in liposomes) regardless of the relatively higher polymer content (70 %, n/n) of hybrids.

3.2 SNAREs AS TOOLS FOR SYSTEMS INTEGRATION

In a previous section it was demonstrated that the efficient insertion of MPs with a desired orientation can be achieved in different types of membranes depending on a choice of detergent and a degree of membrane solubilization. The related insertion optimization requires rigorous screening for the ideal reconstitution conditions and, more often than not, the latter are found to differ significantly between the various enzymes. This was showcased in Chapters 3.1.7.2 and 3.1.7.3 with respect to ATP synthase and bo_3 oxidase, where achieving the optimal insertion efficiency as well as the orientation of the two enzymes reconstituted individually required the employment of different detergents at different concentrations. Nevertheless, previous chapter also exemplified that the final output of the energy module correlated in particular with the insertion efficiency of ATP synthase. Hence, in the construction of the ARC, efficient insertion of the ATPase was prioritized above everything else, resulting in suboptimal insertion of all other enzymes. These findings can be generalized to the scenarios where simultaneous insertion of several enzymes is attempted, where the differences between the

optimal reconstitution procedures must be considered carefully and compromises must be made to ensure the successful coreconstitution.

On the other hand, simultaneous integration of several enzymes via fusion can be exploited in order to circumvent the above limitations. In this scenario, each enzyme is reconstituted separately under optimal conditions and the fusogens are added to them. Following fusion, enzyme orientation is preserved, while the reconstitution efficiency with consideration to a complete module depends on the fusion efficiency. Furthermore, the most suitable fusogen must be selected to fit the requirements of a particular system. In the context of the ARC assembly, the fusogen of choice must have a potential to facilitate several rounds of fusion without being depleted, thus enabling stepwise insertion of multiple enzymes. Moreover, said fusogen must also not hinder the membrane insertion of the respiratory enzymes, so that their optimal reconstitution can be achieved. As discussed in more detail in the Introduction (Chapter 1.4), SNARE fusogenic proteins were identified as the only candidate fitting these criteria and the ARC integration via SNARE-mediated fusion is explored in detail in this section. Furthermore, the respiratory enzymes were integrated in polymer and hybrid membranes to enhance the structural and functional stability and durability of the energy module, as discussed in the previous section. Several PDMS-*g*-PEO characteristics of high potential to promote membrane fusion were observed, in particular its low bending rigidity, sufficient fluidity and comparatively low membrane thickness (Chapter 3.1) (*1, 97*). Nevertheless, despite this, one of the biggest challenges that I tackled in this work was achieving a natural phenomenon – a SNARE-mediated fusion – in this man-made material. The insertion of SNAREs into polymer-based membranes as well as the journey to achieving membrane and, finally, content mixing in these systems is described in this section. Finally, the latter also describes the mechanisms governing the successful fusion in this system and discusses key fusion intermediates, observed by cryo-EM.

3.2.1 Reconstitution of SNAREs via comicellization and characterization of the formed proteovesicles

First, a minimal SNARE fusion machinery – full-length synaptobrevin (syb) and the acceptor complex comprising syntaxin, SNAP-25, and a C-terminal syb fragment (referred to as "ΔN complex") – was reconstituted into polymer and lipid/polymer hybrid vesicles, and in parallel into liposomes, which served as a natural benchmark. The employed ΔN complex is structured in such a way so that the synaptobrevin binding to free site at the N-terminus is

accelerated, resulting in faster fusion as well as preventing the formation of the dead-end 2:1 syntaxin:SNAP-25 complexes (*85, 86*). As discussed in detail in the previous section, several strategies could potentially be explored for the insertion of SNAREs into different membranes. Among others, SNAREs could be reconstituted into preformed vesicles by the direct insertion method (at or around R_{sat} of vesicles) or into totally solubilized vesicles (at or above R_{sol}) using the so-called co-micellization method. It was previously shown that the proteovesicles formed via direct insertion exhibit more homogeneous sizes and protein densities than the reconstitution method involving detergent cosolubilization of proteins and membrane constituents (*177*). Nevertheless, the co-micellization yielded slow but efficient lipid mixing at high protein densities and variable amounts of lipid mixing at moderate protein densities, while the larger, more homogenous proteoliposomes prepared by the direct method yielded almost no lipid mixing at moderate protein densities. For this reason, the so-called co-micellization method was employed in this work by using mixed micelles of SNAREs and amphiphiles, with sodium cholate as the mediating detergent. The latter was chosen based on its excellent performance in enzyme reconstitutions (Chapter 3.1.7) and it was supplemented to different types of membranes in several-fold excess (5 % w:v; in comparison, R_{sol} of liposomes, hybrids and polymersomes for sodium cholate was 0.83, 0.65 and 0.4 %, respectively, as determined in Chapter 3.1.7.1), which ensured their total solubilization. SNARE-functionalized nano-sized proteovesicles were then spontaneously formed upon detergent removal via size exclusion chromatography (Fig. 30).
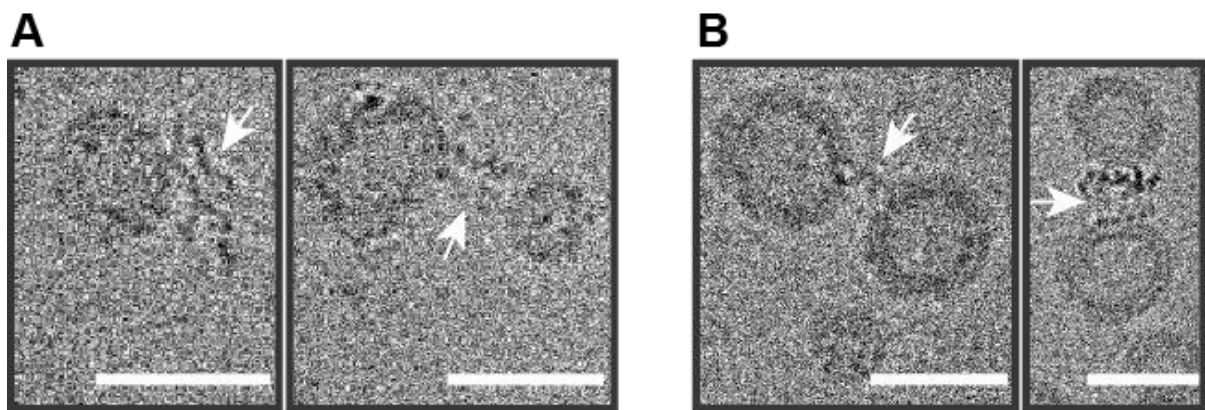
Fig. 30. Reconstitution of SNAREs into polymersomes and hybrids. SNAREs, indicated with white arrows, were inserted into polymer (**A**) and hybrid (**B**) vesicles via detergent removal on the size exclusion chromatography. Scale bars are 30 nm. Adapted from (*96*), licensed under CC BY 4.0.

Bearing in mind that only SNAREs with correct (outward) orientation at the membrane will contribute to membrane fusion, their alignment was analysed via proteolytic digestion

(*105*). To proteovesicles, a serine protease trypsin was added either in the presence or absence of detergent. When trypsin was added alone, only outwards-facing SNAREs were digested while the inwards-facing ones were inaccessible to this enzyme. Meanwhile, the total solubilization of vesicles by supplemented detergent enabled hydrolysis of all SNAREs, regardless of their orientation. Next, the SNARE fragments were analysed by SDS-PAGE, which enabled the determination of the correctly-oriented enzyme. Said analysis revealed syb insertion with at least 84 % and ΔN complex with over 95 % correct orientations in all types of examined membranes, with the best overall orientation achieved in polymer vesicles (Fig. 31A). A similar trend of a more uniform outward orientation of the ΔN complex was observed previously in lipid vesicles (*105*), although to a lesser extent compared to this work. Furthermore, the stability and efficiency of inserted SNAREs was assessed with a flotation assay (*105*). Firm insertion of the membrane-spanning domains of SNAREs is a prerequisite for the exertion of a mechanical force necessary to induce fusion. With the membrane architecture significantly different from lipid bilayers, it was not clear whether the SNAREs can be inserted in polymer membranes with high enough stability to facilitate this action. Furthermore, the goal was also to probe for the potential undesired interactions between polymer and ΔN complex, which could lead into dissociation of the latter. In the floatation approach, proteovesicles are separated from the poorly incorporated/unstable SNAREs on a density gradient via ultracentrifugation. The reconstituted vesicles partitioned in the uppermost (buffer) layer of the gradient, while the non-incorporated SNAREs as well as disassembled ΔN complex could be found in lower layers. The SNAREs content of different layers was analysed by Tricine-SDS-PAGE and the amount of SNAREs, inserted in a stable manner (upmost layer) was compared with the total amount of SNAREs in all layers to discern the reconstitution efficiency. A stable and efficient integration of SNAREs was observed in all types of membranes with less than 10 % protein loss upon ultracentrifugation (Fig. 31B). This suggested that the equal application of force can be expected by the correctly inserted SNAREs across all tested systems.
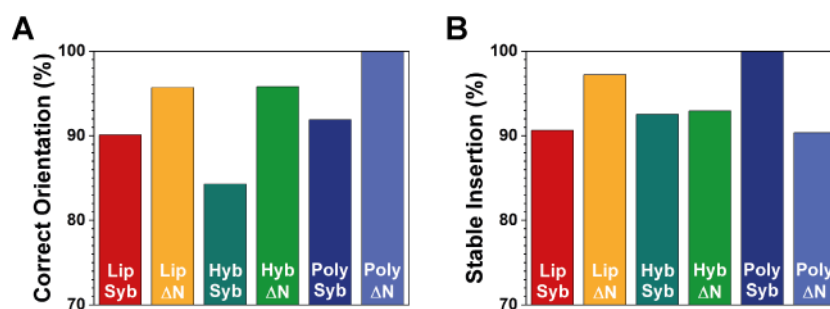
Fig. 31. Characterization of SNARE-free and SNARE-functionalized vesicles. (**A**) Fraction of outwards-facing synaptobrevin (syb) and ΔN complex (ΔN) in lipid (Lip), hybrid (Hyb) and polymer (Poly) vesicles, determined by proteolytic digestion and fragment analysis via SDS-PAGE. (**B**) Fraction of stably inserted SNAREs determined by a flotation assay on a density gradient. Adapted from (*96*), licensed under CC BY 4.0.

Following the successful and stable incorporation of SNAREs with predominantly correct orientation in the synthetic membranes, next, the proteovesicles were placed in an environment that kept the system minimal, well-defined and versatile. This was necessary in order to ensure the unhindered activity of respiratory enzyme following fusion and to demonstrate the much wider applicability of the proposed fusion platform. Towards this end, unless specifically stated otherwise, moderately buffered solution containing only HEPES, KCl and dithiothreitol (DTT), at physiological pH, osmolarity and ionic strength was used. Besides due to its stabilizing effect on the MPs, KCl was selected since it is known for its relatively weak interactions with phospholipids (*178*) as well as with poly(ethylene oxide) (*141*). This enabled more accurate assessment of SNAREs as the predominant fusion mediator across all tested membranes by minimizing the contribution of ions/agitation towards membrane fusion. Furthermore, KCl enabled the neutralization of the charged species that were introduced to the membranes in the form of membrane dyes (discussed separately, below), which allowed the observation of the fusion of artificial membranes in their near-native form with respect to surface charge. Since KCl was previously shown to induce membrane swelling (*141*), this effect was probed for by cryo-EM by measuring the membrane thickness of polymersomes as well as of the polymer (Fig. 30B, single fuzzy contour) and lipid (Fig. 30B, two parallel contours) nanodomains of hybrid vesicles, with and without SNAREs. The flexibility of PDMS-*g*-PEO allowed for the adaptation of membrane thickness to enable hydrophobicity matching with the inserted enzymes (Chapter 3.1.1), therefor the potential salt-induced changes in thickness were not expected to hinder the activity of MPs. Nevertheless, these changes could have potentially affected the fusion process. A fairly constant thickness of PDMS-*g*-PEO was determined in

polymersomes (6.6 ± 0.55 nm) and in hybrids (6.1 ± 0.33 nm), while the lipid domains of the latter were on average 4.9 ± 0.33 nm thick. Interestingly, compared to vesicles formed in sucrose solution with low buffering capacity (*97*), the polymer swelled by nearly 20 %, while the thickness of lipid bilayers remained unchanged. Furthermore, no significant thickness change was observed in any of the membrane compositions upon SNAREs insertion.

Finally, the presence of salts (*179, 180*) and the reconstitution of MPs (*97, 181-183*) can result in considerable changes of the membrane bending modulus κ – an important parameter governing the energy of a membrane and one of the several energetic barriers to fusion, with respect to the high curvature of the stalk (*184*). To assess the effect of KCl, lipid dyes and inserted SNAREs on the bending rigidity of polymer and hybrid vesicles, vesicle size was scaled up to the micron range via fusion/electroformation. With this method, giant unilamellar vesicles (GUVs) were formed in 5 mM HEPES (pH 7.4) containing 5 mM KCl and their κ was determined via fluctuation (flickering) spectroscopy (*185*). Even though the salt concentration had to be considerably lowered (compared to the membrane mixing experiments) in order to facilitate the formation of GUVs, this setup enabled valuable information to be gained on the influence of the aforementioned factors. These experiments were carried out by the collaboration partner Nika Marušič and the acquired data will be in more detail discussed in her thesis. Here, I include only a short summary to enable the more wholesome interpretation of the SNARE-mediated fusion in these novel systems. Indeed, nearly 50 % decrease of the bending rigidity in protein-free polymersomes and hybrids formed in KCl was seen compared to the ones grown in sucrose (*97*). This observation is consistent with the previously reported effect of salts on neutral and charged lipid membranes (*179, 180*) in conjunction with the polymer loosening effect upon insertion of charged species (*97*). Addition of the lipid dyes DOPE-N-(lissamine rhodamine B sulfonyl) (Rho) and DPPE-N-(7-nitro-2-1,3-benzoxadiazol-4-yl) (NBD) to polymer and hybrid vesicles led to further substantial softening. This was likely due to increased salt screening via the additional membrane charge introduced by Rho and NBD (*180, 181*). In contrast, the insertion of syb resulted in only moderate increase of the bending modulus in both polymersomes and hybrids, while the ΔN complex had no statistically significant effect. This outcome does not correspond to our previous findings (10) on membrane softening upon insertion of large transmembrane and multidomain proteins (*bo₃* oxidase), likely reflecting considerable differences in protein size, architecture, charge and concentration. In fact, a similar increase in the bending rigidity was previously reported for DNA, anchored in lipid membranes (*186*), a system that is more reminiscent of our current setup.

3.2.2 SNARE-mediated membrane mixing in lipid, polymer and hybrid vesicles

Next, I examined whether SNAREs are able to induce membrane mixing in synthetic membranes. Towards this end, one population of each type of vesicles was supplemented with the FRET couple Rho/NBD and reconstituted with the ΔN complex. Meanwhile, synaptobrevin was inserted in vesicles containing no dyes. With this setup (Fig. 32), membrane mixing can be followed by the dequenching of NBD upon fusion, which results from the dilution of labelled proteovesicles with unlabelled ones.
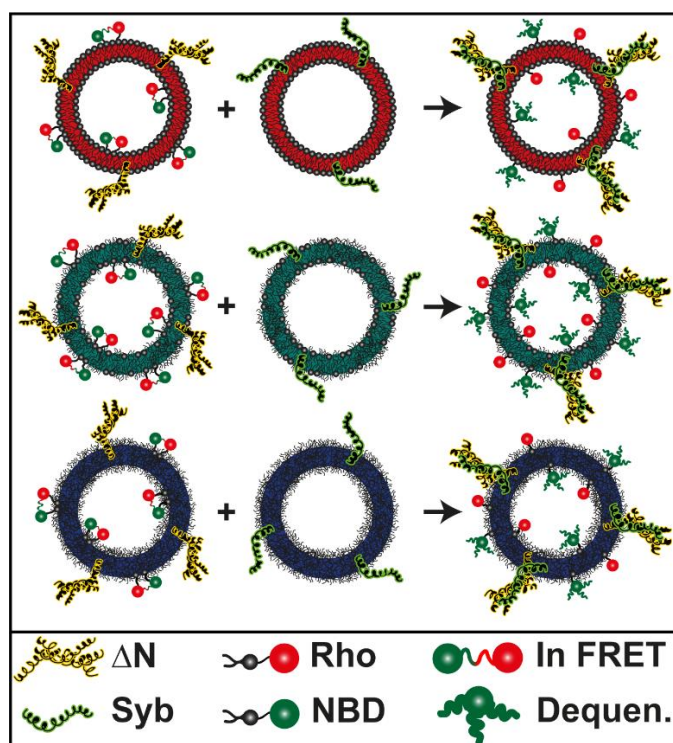
Fig. 32. Schematic representation of the SNARE-mediated membrane mixing setup. For this purpose, two separate populations of lipid (red), hybrid (green) or polymer (blue) proteovesicles were formed. One population contained FRET couple Rho/NBD and was reconstituted with ΔN complex. In this population, the emission of NBD was quenched via proximal Rho. The second population contained no dyes and was reconstituted with synaptobrevin. Following fusion, dye-containing membranes were diluted with the dye-free membranes, resulting in NBD dequenching and in corresponding increase in its emission. Adapted from (*96*), licensed under CC BY 4.0.

Thereby, KCl neutralized the additional surface charge from Rho/NBD and thus minimized the electrostatic repulsion between the vesicles (a comparison between the zeta potential of different vesicles in water and in the measurement buffer can be seen in Fig. 33A and B). In addition, in the control experiments, SNAREs were omitted from the vesicles, while

everything else was kept the same in order to assess the sole contribution of KCl on the membrane mixing of vesicles under mild agitation.
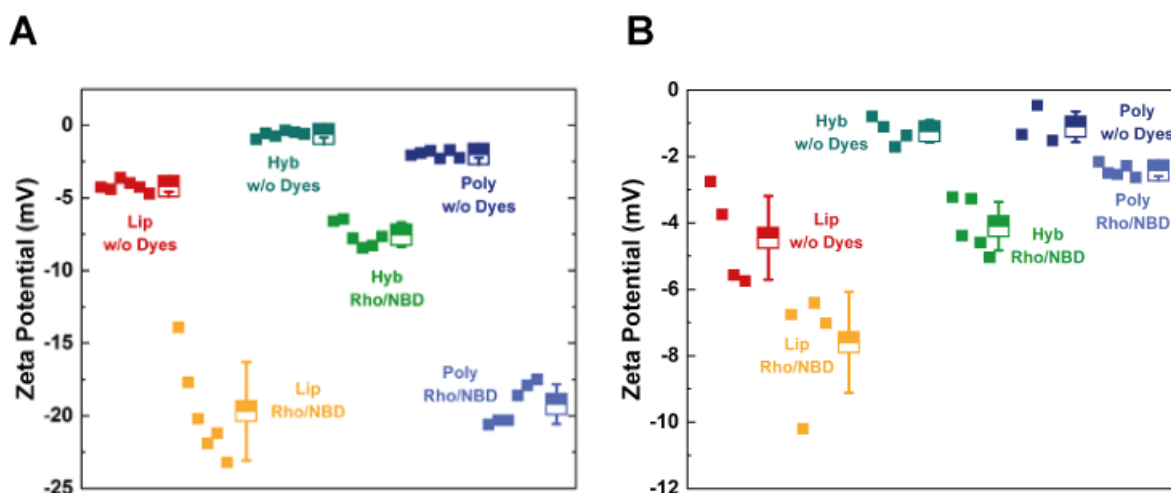
Fig. 33. Zeta potential of vesicles, intended for membrane mixing. (**A**) Dye free as well as dye-containing (Rho/NBD) vesicles were prepared in Milli-Q water and the zeta potential was measured at 37 °C. Shown are separate measurements with averages and standard errors. Significant contribution of added lipid dyes to the overall membrane charge can be seen in all cases, but in particular in liposomes and polymersomes. (**B**) The nearly neutral zeta potential of polymer-containing vesicles promotes membrane mixing. The surface charge, introduced by lipid dyes was neutralized with KCl. Adapted from (*96*), licensed under CC BY 4.0.

Compared to proteoliposomes, a very similar initial fast stage of membrane mixing was observed in proteopolymersomes and proteohybrids (Fig. 34A–C). Nonetheless, while the NBD fluorescence in proteoliposomes reached a plateau after about 2 h, a progressive increase at slower but steady rate was measured in both polymer-containing systems. This led to higher membrane mixing on average, whereby no saturation was seen over the duration of the experiment (Appx. Fig. 55). The fluorescence-based measurements were also complemented with the vesicle size determination via DLS before and after fusion. The reported "before fusion" size estimation was recorded with the freshly prepared vesicles. Meanwhile, for the size estimation of vesicles after fusion, small aliquot of the membrane mixing reaction mixture was removed after reaction plateau was reached and prior to the solubilization of vesicles by octyl glucoside. Similarly, DLS showed an increase in vesicle size in all tested systems after 2 h (Fig. 34, E-G). Interestingly, in polymersomes and hybrids, which exhibited more polydisperse populations of vesicles, the vesicle growth could be seen throughout the population, suggesting high fusion potential of the smaller (~30 nm) as well as the larger (< 100 nm) vesicles. Furthermore, the size of the vesicles could be seen increased by more than a

factor of the square root of two (= binary coupling), which indicated that the vesicles on average underwent several rounds of fusion. Some degree of membrane mixing was also observed in SNARE-free vesicles, albeit absent of the rapid initial stage, characteristic for SNAREs, which substantiated their predominant role as the fusion mediator. Interestingly, the overall faster membrane mixing in proteohybrids was obviously not a result from superimposition of unmediated fusion, which indicated sustained operation of SNAREs. On the other side, the proteins appear to expedite the anticipated saturation as evidenced by the comparison between SNARE-functionalized and SNARE-free liposomes (Fig. 34A), which should be valid for the polymer systems as well but at later times. Finally, variations in the total membrane mixing within identical systems were previously reported for proteoliposomes (*177*). This effect was probed for in proteopolymersomes and the variability in the membrane mixing over several separate reconstitutions was measured, with values ranging from 18 to 24 % after the 2 h benchmark, defined by the proteoliposomes (Fig. 34D).
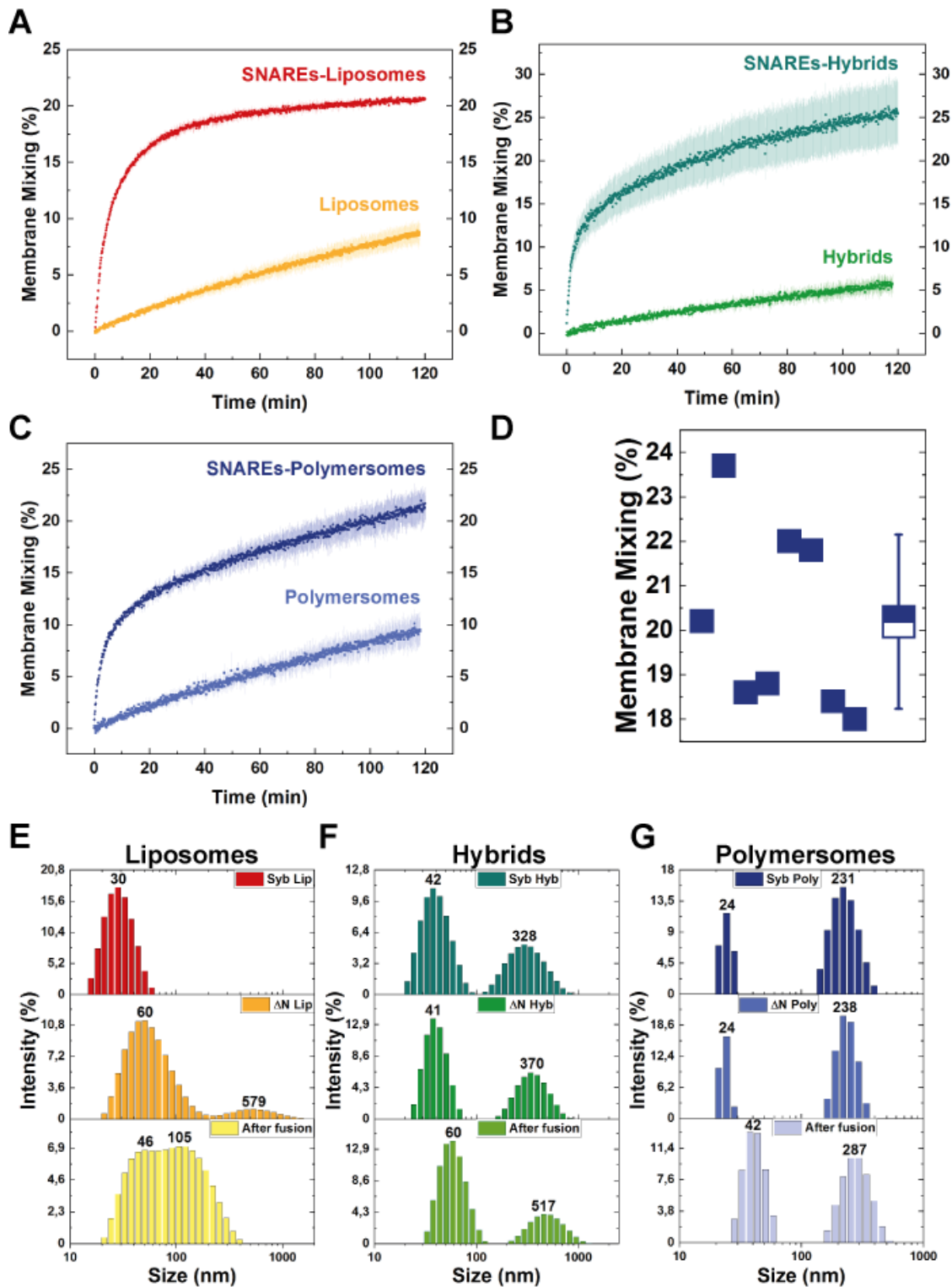
Fig. 34. Membrane mixing upon SNARE-mediated fusion. (A–C) Comparison of SNARE-induced and spontaneous membrane mixing in different amphiphiles. (**D**) Variability of SNARE-mediated membrane mixing in polymersomes. (E-G) Intensity-based size distribution with indicated peak values of different vesicles upon synaptobrevin or ΔN complex reconstitution before and after fusion. Vesicles increase corresponding to several rounds of fusion can be seen on bottom-most panels. All data was recorded at 37 °C. Adapted from (*96*), licensed under CC BY 4.0.

3.2.3 Pore opening dynamics in lipid, polymer and hybrid membranes

The observed membrane mixing in polymer and hybrid vesicles provided a strong evidence for the early steps of fusion, namely docking and hemifusion. However, membrane mixing does not allow to draw definite conclusions about pore opening and expansion, which are crucial during later stages and enable lumen of the two vesicles to merge. To gain insights into these later steps, the different types of protein-free micron-scaled vesicles were prepared with the electroformation approach and they were porated in electric fields to observe the closure dynamics of micron-sized pores. Then, the images of the porated vesicles were collected and semi-automatically processed using ImageJ software. The pore closure was analysed as described previously (*123*), whereby the slow, linear 3rd stage of the pore closure was used in the analysis of the pore edge tension.

Typical pore closure profiles of the three types of vesicles can be seen in Fig. 35A. These profiles strongly indicated that the pores in polymersomes and hybrids were more stable and remained open for considerably longer times. Furthermore, the determined pore edge tension values are compiled in Fig. 35B. The value of the edge tension for benchmark lipid membranes used in this study of 16.4 ± 7.4 pN is in the lower range of values found for commonly used pure lipids like POPC (25.8 ± 6.4 pN), whereas the edge tension in polymersomes (7.9 ± 4.2 pN) and hybrids (8.9 ± 2.3 pN) was even lower.
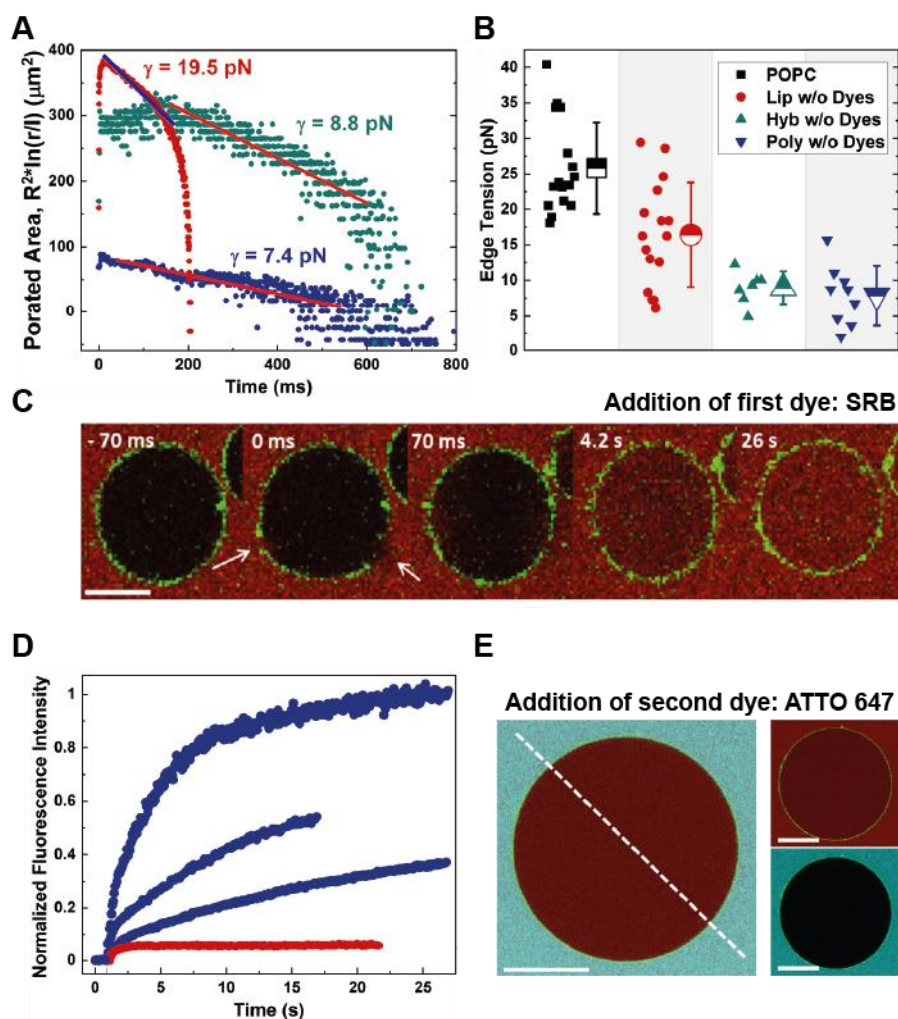
Fig. 35. Pore opening dynamics in different vesicles. (**A**) Typical pore closure dynamics of a lipid (red), polymer (blue) and hybrid (green) vesicles. Vesicle radius is denoted by R, pore radius by r, which is rescaled by the length $l = 1$ micron to avoid applying a logarithm to a dimensional parameter. The slopes of the data are used to determine the edge tension (γ) from the third stage of slow pore closure (blue line in the case of liposomes and red lines in the case of polymersomes and hybrids indicate linear regression). The pores in polymersomes and hybrids are more stable and remain open for longer times. The determined pore edge tension values are compiled in (**B**), each point representing a single GUV measurement. (**C**) Time-lapse of SRB entry into polymer GUV after electroporation. Micron-sized pores (indicated by white arrows) close in the first ~100 ms after the pulse. Entry of dye was detected even after the closure of the large pores, indicating the presence of persistent sub-micron pores below optical resolution or out of the focal plane. Scale bar represents 30 µm. (**D**) SRB dye entry profiles of several polymer GUVs (blue) indicate differences in pore size, number and lifetime. For comparison, typical dye entry profile of lipid GUV is depicted in red. (**E**) Absence of the second dye (ATTO 647 marked in cyan) in the vesicle lumen, added 5–10 min after SRB reveals closure of all pores. Fluorescence profiles of the depicted GUV along the indicated line can be found in Fig. 36. Scale bars represent 30 µm. Adapted from (*96*), licensed under CC BY 4.0.

During electroporation it was noticed that several minutes after the electric pulse was applied and microscopic pores were seen to have closed, some polymer vesicles lost contrast originating from the loss of sugar asymmetry across their membranes (GUVs were prepared in a sucrose solution and were afterwards diluted in a glucose solution to promote their sedimentation and weak immobilization). To examine the porated vesicles more closely for the presence of persistent submicron pores, the vesicles were electroporated in the presence of the water-soluble and membrane impermeable dye sulforhodamine B (SRB) to observe the potential content leak. About a third of the polymersomes could be seen remaining porated up to several minutes after the application of the pulse. A representative course of the dye entry can be seen in Fig. 35C but the dynamics varied greatly (Fig. 35D), which suggested that the defects differ in number and size. Finally, the resealing of the submicron pores at later times was investigated by the addition of a second dye of similar size (ATTO 647) 5–10 min after electroporation. In all instances, in which the polymersomes were permeable to SRB, ATTO 647 was not observed in the lumen of giant vesicles (Fig. 35E, Fig. 36). This indicated that the remaining submicron pores in the PDMS-*g*-PEO membranes eventually closed.
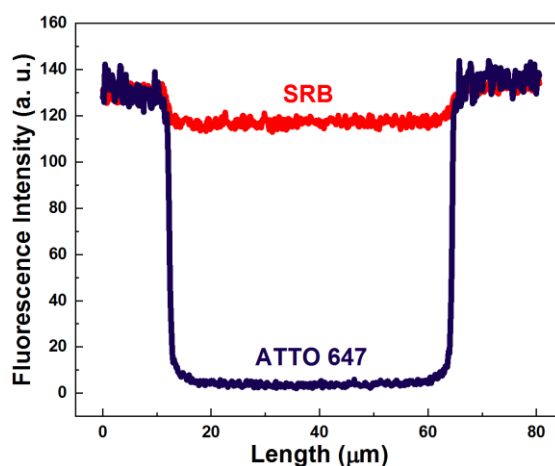
Figure 36. Dye content of the electroporated polymer vesicle. Polymer GUV, depicted in Fig. 35E was porated in the presence of water-soluble dye sulforhodamine B (SRB), which was able to diffuse into the vesicle through formed pores and was detected in the lumen of the vesicles. Several minutes later, after the closure of micron-sized pores was observed, a second dye, ATTO 647 was added to this vesicle, to check for the presence of submicron pores. Dye presence was not detected inside of the vesicle, indicating complete membrane resealing after this period of time. Adapted from (*96*), licensed under CC BY 4.0.

3.2.4 SNARE-mediated content mixing in liposomes, polymersomes and hybrids determined via respiratory coupling

Next, the content mixing of fused polymer and hybrid vesicles was examined, primed by the SNARE-induced pore opening and expansion. This was approached by co-reconstituting one vesicle population, containing the ΔN complex with ATP synthase and another population, containing synaptobrevin with *bo₃* quinol oxidase (Fig. 37A). The reduction of *bo₃* oxidase via ubiquinol led to translocation of protons across the membrane, establishing a proton gradient, which was then used by ATP synthase for the coupling of ADP and inorganic phosphate to ATP. In this setup, the reducing power was provided by DTT, while synthetic ubiquinone 1 (UQ) was used instead of bacterial ubiquinone 8. The essence of this functional assay was that ATP synthesis could be achieved only when both enzymes are integrated into a shared compartment, thus enabling the bioenergetic coupling.
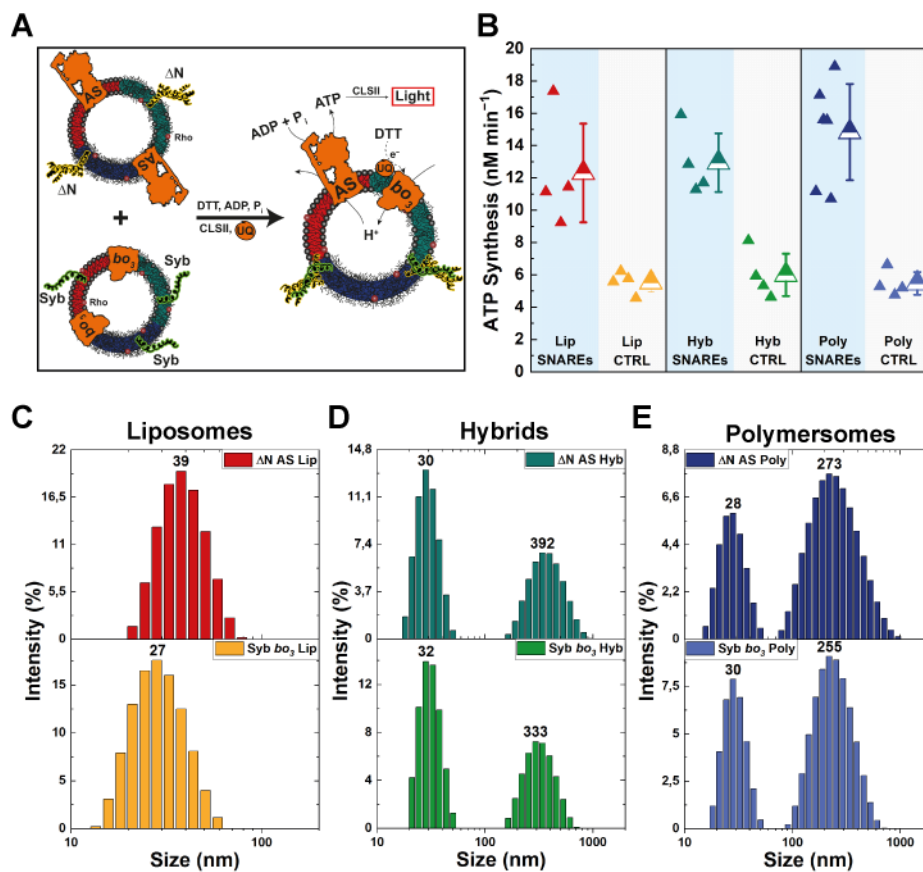
Fig. 37. **SNARE-induced content mixing in different vesicles.** (**A**) Content mixing was assessed via functional coupling between two enzymes of the bacterial respiratory chain: the proton pump *bo₃* oxidase and the proton gradient consumer ATP synthase. Each enzyme was co-reconstituted separately with either synaptobrevin or the ΔN complex. Upon successful fusion, the gradient established upon

activation of *bo₃* oxidase with DTT was used by ATP synthase for ATP production. ATP was converted to luminescence signal via the luciferase/luciferin reporter system (CLSII). (**B**) Comparison of ATP synthesis rates after SNARE-free or SNARE-mediated fusion of different vesicles indicated higher coupling efficiency in the presence of SNAREs. Each point corresponds to a single measurement. Highest SNARE-mediated content mixing was achieved in polymersomes. (**C**–**E**) Intensity-based size distribution of different vesicles co-reconstituted with synaptobrevin (syb) + *bo₃* oxidase (*bo₃*) or with the ΔN complex and ATP synthase (AS). Adapted from (*96*), licensed under CC BY 4.0.

For more reliable comparison, the vesicle formation procedure was carefully tailored so that all co-reconstituted vesicles described here would better match the ones employed in membrane mixing experiments (Chapter 3.2.2). With respect to this, the sizes of vesicles between the experiments were roughly matched to exclude the discrepancies in the content mixing due to dissimilar membrane tension (Fig. 34E–G, Fig. 37C–E). Furthermore, the surface charge of proteovesicles introduced in the form of membrane dyes as well as enzymes was neutralized with KCl to minimize the electrostatic repulsion between the fusing vesicles (Fig. 38).
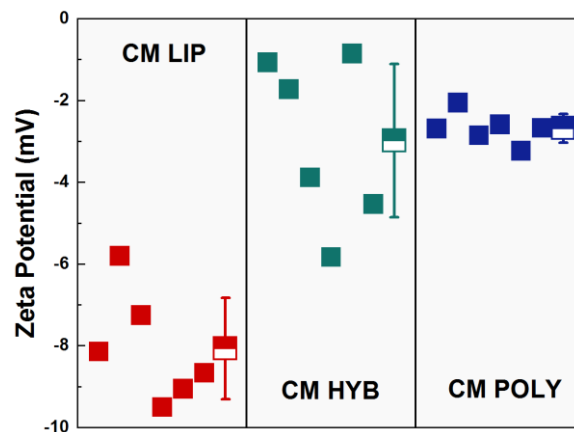
Fig. 38. Zeta potential of vesicles, intended for content mixing in content mixing buffer. Content mixing vesicles were prepared in content mixing buffer containing all cofactors, which were otherwise present in the related measurements (20 mM HEPES [pH 8.0/KOH], 150 mM KCl, 40 mM KH_2PO_4, 73.5 μM ADP, 58.7 nM ATP, 35.2 mM DTT, 0.6 mg ml^{-1} CLSII luciferin/luciferase reagent and 0.2 mM UQ). Zeta potential was measured at 23 °C. Shown are separate measurements with average values and standard errors. Composition of vesicles was tailored to match the surface charge of vesicles, employed in membrane mixing experiments, to enable more straight-forward comparison. Adapted from (*96*), licensed under CC BY 4.0.

Nevertheless, some changes had to be made to the content mixing setup in comparison to the membrane mixing one in order to accommodate both respiratory enzymes, such as increasing the pH from 7.3 to 8.0 and lowering the temperature from 37 to 23 °C. The necessary

co-factors (phosphate, ADP) were also supplied along with the reporter luciferin/luciferase system to enable the functional testing. In this respect, we previously reported a decrease in the bending rigidity of liposomes, polymersomes and hybrids upon the insertion of bo_3 oxidase (*97*). All mentioned changes could affect the early stages of vesicle fusion, manifested by membrane mixing, therefore the main focus here was solely on the analysis of the content mixing.

To measure the content mixing, first, the two populations of vesicles were combined and, following short incubation, proton pumping by bo_3 oxidase was initiated with the addition of DTT and UQ. As a result, successful ATP production in both SNARE-functionalized and SNARE-free vesicles was observed, although synthesis in the latter subsided rapidly (Fig. 39A), while the SNARE-mediated fusion resulted in a steady rate over more than an hour (Fig. 39B). The sole presence of various salts and cofactors, in combination with the energy provided by mechanical agitation, appears to suffice for some degree of fusion (consistent with the membrane mixing experiments). However, in the absence of guided mechanism, binary to the enzyme integration, this fusion is less efficient and random with respect to the functional coupling, which altogether leads to transient activity that cannot be sustained. The several-fold higher ATP synthesis rates achieved via SNARE-mediated fusion (Fig. 37B) further support this claim. The observed transient activity in SNARE-free vesicles was likely related to the lifetime of the pores. The pore opening in polymer-containing vesicles could have potentially been induced by the membrane mixing. In this scenario, the resulting pores could remain open for up to several minutes, as suggested by the pore opening experiments, described in the previous segment. Nevertheless, in the absence of SNAREs, pores would eventually close leading to a decoupling between the two inserted respiratory enzymes. On the other hand, SNAREs not only stabilized pores in SNAREs-functionalized vesicles, but also facilitated pore expansion resulting in the permanent content mixing and the related enduring respiratory coupling.
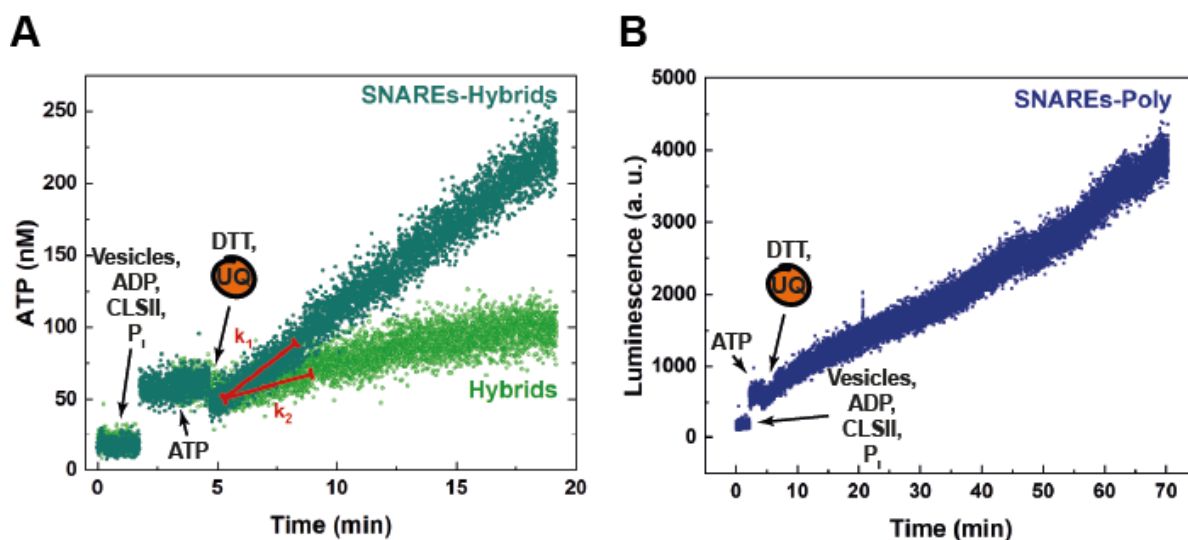
Fig. 39. SNARE-mediated content mixing hybrid and polymer vesicles. (**A**) Comparison between SNARE-induced and SNAREs free content mixing in hybrid vesicles detected via ATP synthesis. One population of vesicles, containing ΔN complex and ATP synthase, was mixed with a second population, which contained synaptobrevin and bo_3 quinol oxidase in the presence of cofactors required for ATP synthesis and for the detection of the latter. After signal calibration with known amount of ATP, ubiquinone along with the electron donor DTT were added to initiate proton pumping by the bo_3 oxidase. The established proton gradient was used to drive ATP synthesis by the ATP synthase only in the case where both enzymes were integrated in same vesicles (i.e., upon successful fusion). ATP synthesis rate of SNARE-containing vesicles (k_1) and SNARE-free vesicles (k_2) was determined from the initial steady-state stage. While the comparatively significantly lower ATP synthesis in SNARE-free vesicles was seen to subside after several minutes, high ATP synthesis rates were sustained in SNARE-containing vesicles for more than an hour. (**B**) Extended SNARE-induced content mixing in polymer vesicles. Adapted from (*96*), licensed under CC BY 4.0.

Finally, comparable ATP synthesis rates were observed between SNARE-integrated liposomes, polymersomes and hybrids, with polymersomes exhibiting slightly higher activity than the other two platforms. However, this observation alone does not factor in the different protein integration efficiencies of both respiratory enzymes in these types of membranes. In fact, the reconstitution efficiency of ATP synthase (the most important parameter determining the final output of the module) was in polymersomes and hybrids about 30 and 60 % of that in liposomes, respectively, as discussed in Chapter 3.1.7.3. Accounting for these differences by normalizing the ATP synthesis to the amount of reconstituted enzyme will lead to even better performance of polymer membranes. Furthermore, a direct comparison could be made between the output of the energy module when the two enzymes were simultaneously reconstituted in different vesicles with sodium cholate at the R_{sol} (Chapter 3.1.7.4), and when the enzymes were

under same conditions reconstituted separately and then integrated via SNAREs. Remarkably, the SNAREs-aided integration resulted in nearly same ATP synthesis across all tested vesicles, as described above. Meanwhile, the output of the module coreconstituted in hybrids (Chapter 3.1.7.4, Fig. 29B) was about 33 % of that in liposomes, while almost no (< 0.9 %) ATP synthesis was detected in polymersomes (Chapter 3.1.7.4, Fig. 29C). This showcased the immense potential of SNAREs as tools for enzyme integration, enabling the circumvention of the suboptimal reconstitution conditions often otherwise unavoidable in the coreconstitutions. In any case it can be concluded that suitable membrane properties like the lower edge tension led to easier pore opening and expansion, facilitating efficient SNARE-mediated fusion in both polymer and hybrid vesicles. Finally, the SNAREs-mediated pore opening in polymer monolayers remains one of many unexplored mysteries, which promises a great adventure.

3.2.5 Fusion intermediates of SNARE-mediated polymersome and hybrid fusion

Moreover, the fusion intermediates during the membrane and content mixing stages could be captured with cryo-EM. Even though it is impossible to follow the process by destructive imaging, and the mixing of vesicle populations generates additional stochasticity, a plausible SNARE-mediated fusion progression in polymer and hybrid proteovesicles was reconstructed by comparison with natural systems (*177*) and molecular simulations (*187, 188*). Another argument for the postulated sequence was the fact that later intermediates were prevalent upon longer incubation times (Fig. 42 – included at the end of this chapter for coherence reasons).

A docking stage of proteopolymersomes (Fig. 40-I, Appx. Fig. 56) was observed, which likely had proceeded towards the exvagination of a small membrane portion of a single vesicle, leading to the formation of unilateral stalk (Fig. 40-II). Thus, a local point contact, which was also observed in some cases of liposome fusion (*189*), was established between the stalk and the proximal membrane (the act of "kissing"), which should in turn have initiated membrane mixing and led to the emergence of a narrow hemifusion diaphragm (Fig. 40-III). It should be noted that the terminology was adopted from lipid bilayers to provide an analogy, although PDMS-*g*-PEO forms predominantly monolayers and therefore hemifusion loses its original meaning. Presumably, the diaphragm expanded further and thinning of membrane at the juncture, likely at the point of initial contact, was observed (Fig. 40-IV, Appx. Fig. 57). Furthermore, the pore opening (Fig. 40-V, Appx. Fig. 58) at the diaphragm extremity

(previously observed in simulations (*187*)) suggested potential colocalization of the points of initial contact, membrane thinning and pore opening. Finally, the resulting fused polymersomes featured persistent indentations, as well as occasional inclusions (bits of polymer membrane), likely remnants of the fusion diaphragm (Fig. 40-VI).
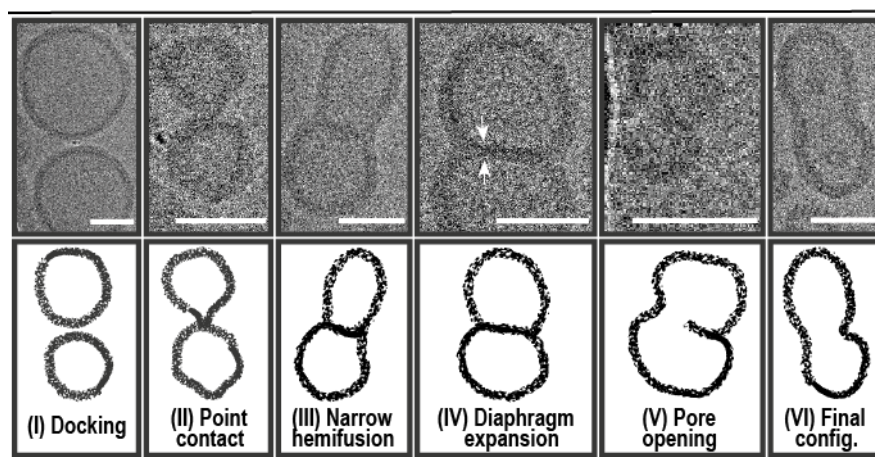
Fig. 40. Proposed fusion intermediates of SNARE-mediated polymersome fusion. Following vesicle docking (**I**; for enlarged image please see Fig. S9) local point contact is established between the vesicles (**II**), leading towards membrane mixing and emergence of hemifusion diaphragm (**III**). While the latter is expanding (**IV**), membrane thinning (shown with white arrows, enlarged in Fig. S10) can be observed at the juncture, indicating the location of eventual pore opening (**V**). Such position of fusion pore was previously observed in the simulations (*187*). Slight lateral deformations in the newly fused vesicles along with less frequent inclusions in the lumen are likely remnants of the hemifusion diaphragm (**VI**). Scale bars represent 30 nm. Adapted from (*96*), licensed under CC BY 4.0.

In contrast to proteopolymersomes, different steps of the fusion process were discovered in proteohybrids (Fig. 41). Docking stage in the latter was superseded by a long contact between the fusing vesicles, at the distance of about 2.5 nm. Remarkably, such contact was most frequently established between the polymer-rich domain of one vesicle and the lipid-rich domain (in a form of a bilayer) of another one (Fig. 41-I). Seemingly, the membrane mixing between the outer lipid layer and polymer monolayer originated at the lateral edge of the protruding lipid domain, and was propagated towards the opposite side (Fig. 41-II, Appx. Fig. 59). Such "hybrid membrane zippering" likely resulted in a state of transient hemifusion, in which lipid-rich monolayer domains (Fig. 41-II&III, exhibiting higher contrast compared to the polymer) were stabilized within the polymer monolayer. This temporary state was potentially resolved by membrane reorganization and the formation of lipid domains outside of the contact, leading to the formation of the characteristic configuration of hemifusion diaphragm, as in polymersomes (Fig. 41-IV). In all hybrid cases, pore opening was observed

in a more central region of the diaphragm (Fig. 41-V), which continued with pore expansion, diaphragm dissolution and, finally, membrane relaxation (Fig. 41-VI).
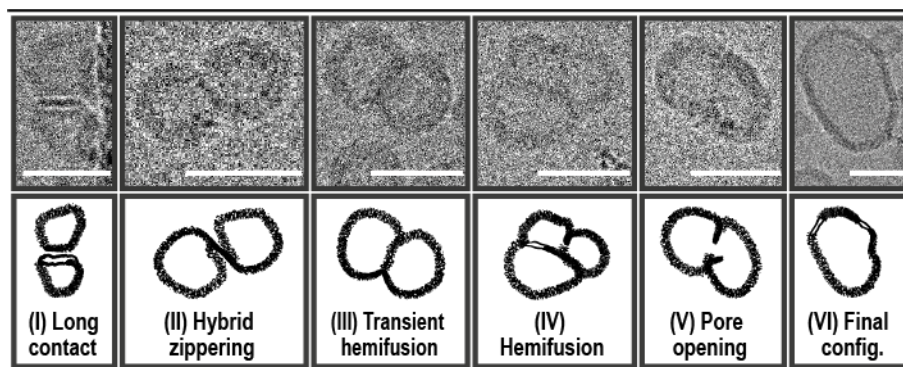
Fig. 41. Proposed fusion intermediates of SNARE-mediated fusion in hybrids. Long contact is established between the lipid-rich domain (bilayer) of one fusing vesicle, and the polymer-rich domain of another (**I**). The initial contact between the fusing membranes occurs at the lateral edge of the protruding bilayer and it further develops into crosswise membrane mixing (process of "hybrid zippering", **II**). Transient fusion diaphragm, exhibiting lipid-rich monolayer stabilized in polymer monolayer is observed (**III**) before stable lipid bilayers are formed in newly mixed hybrid diaphragm (**IV**). The fusion pore was formed in more central region of the juncture (**V**), as previously observed in simulations (*188*). No inclusions or deformations can be observed in fused vesicles (**VI**). Scale bars represent 30 nm. Adapted from (*96*), licensed under CC BY 4.0.

Unfortunately, only a handful of examples of polymersome fusion exist in literature at the time of writing and the fusion intermediates are to some extent described in a single work only (*95*). With that in mind, my goal here was to describe the intermediates observed in the SNARE-mediated fusion of hybrids and polymersomes to the best of my ability with the aid of the findings derived from liposome fusion research. Nevertheless, some parallels could be drawn between the fusion of hyperbranched polymersomes (*95*) comprising poly(3-ethyl-3-oxetanemethanol) core and many poly(ethylene oxide) arms (HBPO-*star*-PEO) and PDMS-*g*-PEO polymersomes used in this study. In both cases a softly protruding rim could be observed marking a location where the initial point contact between the fusing vesicles was established. In the case of hyperbranched polymersomes, protrusions could be seen in both vesicles, similar to liposome fusion (*177*). Meanwhile, in graft copolymer membranes tested in this work, protrusion could be observed in only one of the two fusing vesicles (Fig. 40-II). In both cases, however, the point of the initial contact was afterwards expanded towards the formation of a fusion diaphragm, although the fusion progression could not be resolved to greater detail by Zhou and colleagues using the light microscopy. Interestingly, the pore opening in HBPO-*star*-

PEO vesicles was induced by ultrasound, while the pores in PDMS-*g*-PEO opened spontaneously, although their expansion and the related full content mixing were mechanically tied to SNAREs, as discussed in previous chapters. Furthermore, remnants of the fusion diaphragm (bits of polymer membrane) could be seen in both cases in the lumens of vesicles following fusion. Finally, unprecedented fusion progression could be observed in hybrid vesicles, in which most notably the interactions between the lipid bilayers and polymer monolayers could be seen. How these initial long contacts are resolved in a hemifusion direction requires further exploration, likely aided by the cryo-electron tomography.
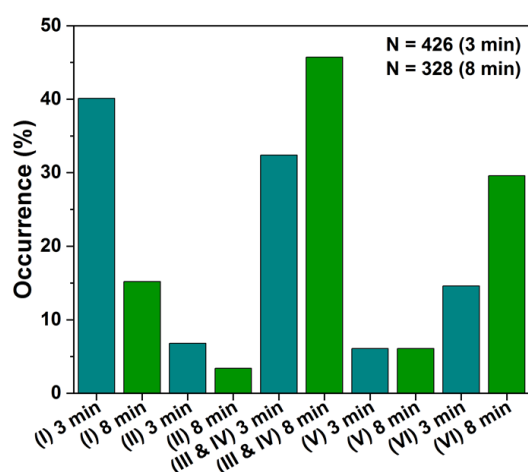
Fig. 42. Intermediates frequency in SNARE-mediated fusion of hybrid vesicles. Shown is the comparison between different intermediates, as depicted in Fig. 41, observed by cryo-EM after 3 min and 8 min from the initiation of fusion. After 8 min of SNARE-mediated fusion, the early fusion intermediates (I and II) were observed with significantly lower frequency, while the later ones (III-VI) were more frequent. Transient phenomena (hybrid zippering, II, and pore opening, V) were rare occurrences. Denoted with *N* is the number of observed fusion events. Adapted from (*96*), licensed under CC BY 4.0.

3.3 ASSEMBLY, CHARACTERIZATION AND OPTIMIZATION OF THE ARC AND ITS COUPLING WITH THE METABOLIC MODULE TOWARDS THE FORMATION OF THE MINIMAL ARTICIFIAL MITOCHONDRION

This section is dedicated to coupling between the artificial respiratory chain and metabolic conversion cascade – the CETCH cycle. Towards this end, the first goal was to provide a constant supply of the reduced ubiquinone to respiratory chain, which is a prerequisite for a continuous ATP synthesis over longer periods of time (up to several hours). For this reason, the short respiratory chain (ATP synthase/*bo₃* oxidase) was expanded by the addition of NADH:ubiquinone oxidoreductase (referred to as the "NADH dehydrogenase" throughout

this section) towards the formation of the artificial respiratory chain (ARC). The NADH dehydrogenase in this module connected the enzymes of the metabolic cascade with the two respiratory enzymes via the universal electron donor and common metabolite – NADH. In the next step, the either of the two products of choice of the CETCH cycle (malate and formate) was converted to NADH to power the ARC. With respect to this, two metabolic adapters – malate dehydrogenase (MDH) and formate dehydrogenase (FDH) were explored. The coupling between ARC and CETCH required freezing/thawing of the energy module, which is why the effects of freezing on the activity of the ARC were tested. Furthermore, said coupling also required operation of ARC under unusual conditions, namely at high and inconstant osmolarity. Fort this reason, the activity of the ARC under these conditions was assessed. With the ARC appropriately tuned to enable coupling with CETCH, the turnover of the cycle while powered by the ARC was then analysed. Finally, this section also describes my attempts to address the two weaknesses of the energy module. First one being the very limited supply of oxygen – a substrate essential for the establishment of a proton gradient by the bo_3 oxidase. In the unfortunate absence of cardiovascular system and breathing, I explored reoxygenation of the ARC by calcium peroxide particles. Lastly, on an entirely proof-of-concept basis, I made first steps towards resealing of lipid membranes, permeabilized due to protein insertion, via Poloxamer P188.

3.3.1 Complex I as the secondary proton pump of the energy module – two is not always better than one

From the very start, the ARC was not designed to be a stand-alone module. Instead of being modulated by the external trigger, such as the light, the ARC was intended to be connected with the metabolic conversion module. The goal was to exploit the reducing equivalents provided by the metabolic reactions of choice to produce ATP in the most efficient known way – amplified in accordance to the principles of oxidative phosphorylation. The challenging part was the absence of certainty about the envisioned metabolism of the artificial cell in its final form. With respect to this, many substrates and their related conversions were considered throughout the years and throughout several design iterations, to either fuel the cell or to bestow it with specific functionalities (as well as to prime it for various applications). What became clear, however, was that the very high versatility and adaptability of the energy module was required so that the coupling between it and a variety of the most diverse other modules would be enabled. For these reasons, I chose NADH as an electron mediator facilitating the coupling between the metabolism and the energy regeneration. Not only is

NADH one of the universal electron carriers that is produced in a wide range of metabolic reactions but there is another distinct advantage to it – the NADH:ubiquinone oxidoreductase, the enzyme through which the reducing equivalents can be fed to the respiratory chain, can be a proton pump. Indeed, the type 1 NADH dehydrogenase, also known as the complex I, facilitates proton translocation across the membrane and, in concert with other proton pumps, contributes to the establishment of a proton gradient. In nature, this synergistic action of the several proton pumps can then be converted into the incredible output of respiratory chains in terms of ATP, which I attempted to replicate in a biomimetic module. Towards this end, I expanded the short respiratory chain comprising bo_3 oxidase and ATP synthase with the fungal complex I (NADH dehydrogenase) and thus formed the first version of the artificial respiratory chain (ARC 1). Unfortunately, our attempts at purifying a reasonably active complex I at the very end of my doctoral studies did not bear fruit and I, instead, had to make do with a very limited quantities of the enzyme generously gifted by Prof. Volker Zickermann, Goethe University Medical School. For this reason, I was not able to approach the reconstitution of complex I as I approached the insertions of other respiratory enzymes – by exploring in detail the related reconstitution parameters, so to guide me through the optimization process. Instead, here, I inserted complex I in liposomes with sodium cholate, octyl glucoside and Triton X-100. Liposomes were selected as the compartments of choice because they facilitated the highest activity of SRC and were therefore, the best candidate for coupling, considering the high energy requirements of the coupled modules. Furthermore, the three mentioned detergents were consistently reported to mediate the successful insertion of respiratory enzymes, which I also observed and discussed in detail in Chapter 3.1. There are some advantages of total membrane solubilization with the mentioned detergents in the context of complex I insertion, such as slightly higher enzyme reconstitution efficiency as well as lesser increase in membrane permeability after the enzyme insertion (*74, 138*). Nevertheless, mostly mixed orientation (40–65 % correct) of complex I in systems reconstituted at the R_{sol} of the mediating detergents is reported in the works of Dröse and colleagues (*74*). In contrast, the orientation of complex I in similar systems, which were instead reconstituted at R_{sat}, was mostly correct (70–100 %). In the context of the ARC, complex I was intended to play a role of a secondary proton pump (besides bo_3 oxidase), thus enhancing the proton gradient generation relative to SRC. This would only be possible in a scenario where the proton gradient generated by one of the correctly-inserted proton pumps is not diminished by another, incorrectly-inserted one, hence inhibiting the ATP synthesis. Therefore, the correct orientation of the inserted complex I was a deciding factor when the degree of membrane solubilization with the detergents of choice was

considered, and the sodium cholate, octyl glucoside and Triton X-100 were employed at their R_{sat} concentrations, as determined for liposomes used in this study in Chapter 3.1.7.1.

The reconstitution of the ARC 1 started with the saturation of preformed liposomes with the mediating detergent. Then, enzymes were added in a specific order, based on a priority. First, ATP synthase was added, since comparatively lower reconstitution efficiency for this enzyme was determined compared to bo_3 oxidase and complex I (*74*), and the presence of any additional interferences (other enzymes) in the reconstitution mixture might further cripple its insertion, thus diminishing the output of the module. Next, complex I was added due to its lower reconstitution efficiency compared to bo_3 oxidase and its critical role in the activity of the ARC as well as coupling. Finally, bo_3 oxidase was added to the mixture. Each enzyme addition was followed by 15 min incubation period, at 4 °C and under gentle agitation. Interestingly, if all enzymes were added to the liposomes nearly at once, in a quick succession, and were incubated simultaneously, while everything else was kept the same, the output of the ARC 1 was nearly 60 % lower. This indicated that the enzyme coreconstitutions can be considered a dynamic and competitive process, which requires further in-depth analysis with respect to the reconstitution parameters of each individual enzyme in this multienzyme assembly. In this context, said parameters determined in single enzyme reconstitutions are not necessarily valid. Furthermore, complex I, bo_3 oxidase and ATP synthase were added to liposomes at the lipid-to-polymer ratio of 29700:1, 89000:1 and 44500:1, respectively, which roughly corresponded to a theoretical ratio (please see Chapter 2.3.11) of 3 complex I, 1 bo_3 oxidase and 2 ATP synthase per vesicle, respectively, if even enzyme distribution across all vesicles is assumed. Doubling the enzyme load in liposomes resulted in no significant increase in ATP synthesis, while tripling the load was accompanied by nearly complete loss of the ARC 1 activity. Von Ballmoos and colleagues (*44*) previously demonstrated a limited scalability of protein content in a similar setup featuring terminal oxidase in combination with ATP synthase. In their setup, the ATP synthesis rate increased with the increasing concentration of the proton pump up to 10 bo_3 oxidase per vesicle, while no increase in output was detected beyond this point. While discussing her work (*73*), Prof. Verkhovskaya, University of Helsinki, noted that a similar effect was observed in her research on complex I and oxidases, presumably due to the increased passive proton permeability of lipid membranes upon enzyme insertion at higher concentrations. The increased permeabilization of lipid vesicles was also determined in this work (Chapter 3.1.4) in the cases when bo_3 oxidase/ATP synthase were reconstituted separately at the lipid-to-protein ratio of about 9500:1. Hence, it is likely that simultaneous insertion of

several enzymes, one of which possessing a comparatively very large transmembrane segment, could drastically increase membrane permeability to the point where the proton gradient would have dissipated. Moreover, a certain fraction of impurities is introduced to membranes with each different enzyme, contributing to further membrane permeabilization. Taking everything into consideration, the total content of respiratory enzymes in the ARC 1 (defined above) was kept the same as the protein content in SRC, *i.e.,* 6 enzymes per vesicle, to avoid the undesired changes in membrane properties.

First, the ATP synthesis by the ARC 1 energy modules reconstituted with different detergents was determined. The respiratory chain was activated by the addition of 500 µM of NADH and the activity of ATP synthase was recorded based on the luminescence signal produced by the coupled luciferase reporter system (please see Chapter 2.5.15 for details). The highest output rate of 0.13 ± 0.05 ATP s^{-1} enzyme^{-1} was measured in ARC reconstituted with octyl glucoside at the R_{sat} (Fig. 43A). Meanwhile, significantly lower ATP synthesis was recorded in energy modules reconstituted with the other two detergents. The ARC reconstituted with sodium cholate and Triton X-100 exhibited 32 % (0.09 ± 0.03 ATP s^{-1} enzyme^{-1}) and 75 % (0.03 ± 0.01 ATP s^{-1} enzyme^{-1}) decreased output compared to the mentioned, most active reconstitution. This relation (octyl glucoside > sodium cholate > Triton X-100) between the determined activities in principle matches the degree of the correctly oriented ATP synthase (Chapter 3.1.7.3), although the differences between the tested detergents with respect to enzyme orientation were much smaller (fraction of the correctly inserted ATPase was, on average, 63.7, 56.1 and 48.9 % when reconstituted with octyl glucoside, sodium cholate and Triton X-100 as the mediating detergents, respectively). Furthermore, no relationship could be found between the determined reconstitution parameters for *bo₃* oxidase (Chapter 3.1.7.2) and the ATP synthesis activities of ARC 1. Therefore, next, the activity, orientation and the insertion efficiency of complex I in ARC was analysed. Towards this end, the enzyme turnover was measured under same conditions as the ATP synthesis, only that in this case, the concentration of NADH was monitored based on its absorbance. The complex I activity measurements revealed a story very similar to ATP synthesis. The enzyme was most active when reconstituted with octyl glucoside (9.67 µmol min^{-1} mg^{-1}) and significantly less active when reconstituted by either sodium cholate (5.76 µmol min^{-1} mg^{-1}) or Triton X-100 (2.97 µmol min^{-1} mg^{-1}) (Fig. 43B). It is important to note that in these measurements, only outwards-facing enzyme (the N segment located outside of vesicles) could access NADH and was, therefore, activated.
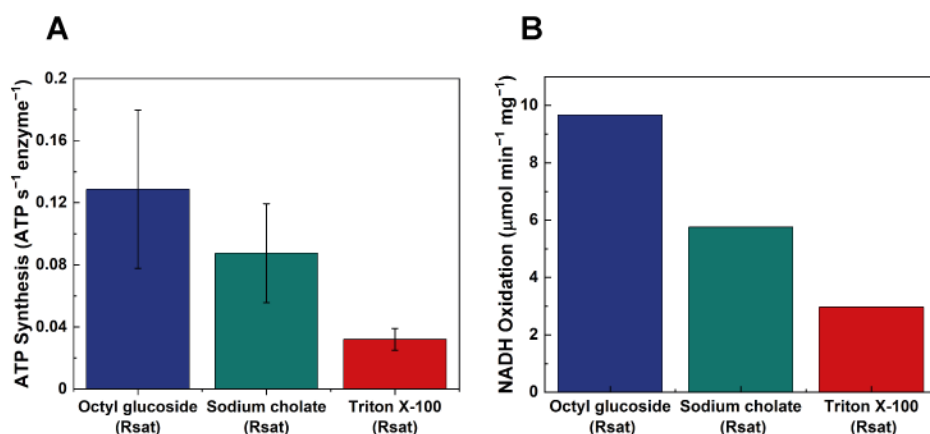
Fig. 43. ATP synthesis and NADH oxidation by the ARC 1. The respiratory chain was reconstituted with either octyl glucoside, sodium cholate or Triton X-100 as mediating detergents at their membrane saturation point (R_{sat}). (**A**) ATP synthesized by the ARC 1 was converted to the luminescence signal by the coupled luciferin/luciferase reporter system. Shown are the average values of the initial steady-state ATP synthesis of three separate reconstitutions with standard errors. (**B**) The initial steady-state NADH oxidation by the ARC 1 reconstituted with different detergents.

Next, to determine the orientation of complex I, ARC 1 proteovesicles were dissolved with detergent and the activity of the enzyme in micelles was measured. In this case, NADH was available to all enzymes. The portion of the correctly oriented complex I was 74, 72 and 66 % when reconstituted with octyl glucoside, sodium cholate and Triton X-100, respectively, which was in a good agreement with the degree determined by Dröse and colleagues (*74*) of about 70 % in single enzyme reconstitutions. Very similar orientation of complex I between different reconstitutions suggested that the differences in its activity instead correlated with the reconstitution efficiency of the enzyme when inserted with different detergents. Furthermore, the highest activity was reported when complex I was inserted alone in liposomes using Triton X-100 as a mediating detergent (*74*), followed by octyl glucoside and sodium cholate, while similar enzyme orientation was reported for all detergents. In that case, the highest enzyme turnover was also considerably higher than the one determined in this work (about 20 µmol min^{-1} mg^{-1} vs. 9.67 reported here). This data suggests that the reconstitution efficiency of complex I was notably impacted (and significantly reduced) by the presence of other enzymes. With respect to this, in future reconstitution attempts, different order of enzyme addition should be tested to determine whether the insertion of complex I can be improved by such straight-forward adjustment. Nevertheless, a good correlation can be seen between the ATP synthesis by the ARC 1 (octyl glucoside:sodium cholate:Triton X-100 = 100:68:25 %) and the complex I content in the energy module (octyl glucoside:sodium cholate:Triton X-100 = 100:60:31 %).

This comparison assumes that the membrane properties were roughly the same between tested setups after the enzyme insertion. Finally, these findings underline the equal importance of the optimal insertion of complex I and ATP synthase in these assemblies, while the variance in the insertion of bo_3 oxidase appears to be less impactful. For this reason a different ARC architecture, recently published by Biner and colleagues (52) could be seen as a very promising and exciting alternative. In their case, complex I was coinserted with the ATPase, while the alternative oxidase was supplemented to vesicles while stabilized in micelles. This way, the oxidase did not influence the insertion of other two enzymes. Furthermore, complex I in their setup served as the only proton pump and, considering the relatively high correct orientation of said enzyme, it might be an appealing substitute for bo_3 oxidase. Nevertheless, that architecture is very similar to the SCR and does not allow for the amplification of the generated proton gradient via simultaneous action of several proton pumps, which was the main motivation behind the formation of ARC 1.

Unfortunately, the very limited ARC 1 reconstitution attempts did not yield sufficiently active energy module, which could be used for coupling. While the access to complex I was being established so that the reconstitution of the ARC 1 could be optimized, I devised an alternative plan that would enable coupling between the metabolic cascade and the ARC despite the suboptimal performance of the ARC 1. Hence, in meantime, I explored the expansion of SRC with type 2 NADH dehydrogenase – DT-diaphorase (DTD). The version of the artificial respiratory chain, which contained DTD was denoted as the ARC 2. This enzyme is cytosolic (water-soluble) instead of transmembrane and therefore not a proton pump. As such, it does not influence the insertion of other respiratory enzymes nor does it alter the membrane properties. Because of this, the expansion of the SRC with DTD was not expected to significantly change the output of the SRC, which could be reconstituted with its optimal configuration according to the findings discussed in Chapter 3.1.7.4. Moreover, DTD could readily be added to SRC-containing proteoliposomes to couple them with metabolism, which enabled better control over the DTD/proteoliposomes content in the coupled systems. Finally, the tuning of ARC 2 simply required adjusting the concentration of DTD until the maximal ATP synthesis, as determined in SRC with the DTT as the electron donor, was matched or surpassed. It was determined that this was the case when 700 nM of DTD was supplemented per 10 µl of SRC proteoliposomes, which contained 40 µM of ubiquinone-1, as well as 0.6 µM of bo_3 oxidase along with 0.1 µM of ATP synthase. The ATP synthesis activity of the ARC 2 was then measured via luminescence and compared to the activities of the ARC 1, the most active SRC (reconstituted

in liposomes with 0.6 % of sodium cholate (Chapter 3.1.3), which is roughly between R_{sat} and R_{sol} for this detergent; Chapter 3.1.7.1) as well as ATP synthase alone (turnover data for the used ATP synthase fraction was provided by Dr. Thomas Heitkamp, University Clinic Jena). The ATP output of different variants of the energy module can be seen in Fig. 44. This data assumes that the entirety of ATP synthase, which was added to the reconstitution mixtures, ended up inserted in membranes (i.e., a 100 % reconstitution efficiency is assumed). A significant portion of the activity of ATP synthase was lost upon the enzyme coreconstitution with the bo_3 oxidase, when compared to the activity of ATPase, which was reconstituted alone. The activity of the latter was determined by inducing 1.2 units of a pH difference across the membrane, in accordance with the highest determined magnitude of the proton flux produced by bo_3 oxidase in the SRC (Chapter 3.1.2). There are several reasons potential reasons behind this decrease. Most likely, the reconstitution efficiency of ATP synthase was considerably lower in the coinsertion scenario due to the potentially competitive nature of protein reconstitutions. Furthermore, the interactions between enzymes during coreconstitution could potentially result in suboptimal enzyme orientations in SRC and the related lower synthesis in said module. Finally, the induced pH difference in a single enzyme experiments was relatively high considering the variations in proton pumping activity of bo_3 oxidase, which produced 0.8 to 1.2 units of a pH difference in the SRC. Nevertheless, a great portion of the ATPase activity was preserved and the output of the SRC was more than sufficient to energize most of the potentially coupled energy-consuming processes. Furthermore, the activity of SRC was matched by the ARC 2, which was not surprising, considering that the DTD, which was added externally to the preformed module, had no effect on the reconstitution of the SRC, nor any observable effect on its functionality. The ARC 2 was the most active energy module produced in this work and was therefore selected to be trialed first in the preliminary coupling with the CETCH cycle. Finally, compared to other versions of the respiratory chain, the ARC 1 was the least active. Its output of about 0.13 ATP s^{-1} enzyme^{-1} would be sufficient to drive some less demanding ATP-dependant processes, which take place at the lower concentrations of ATP (in the approx. 1–500 µM range). Nevertheless, it its current iteration, the ARC 1 would likely not be able to drive the relatively energy-demanding CETCH cycle. Further optimization of this the most complex artificial respiratory chain ever produced at the time of writing is required, which I regret not being able to finalize over the duration of my doctoral study.
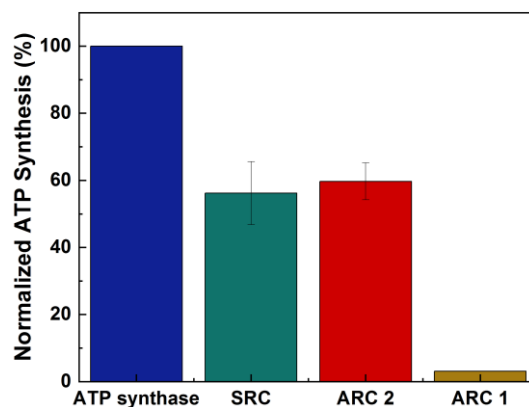
Fig. 44. Energy output of various energy regeneration modules. ATP synthesis by the short respiratory chain (SRC) as well as the artificial respiratory chains type 1 and 2 (ARC 1, ARC 2) were normalized to the ATP output of the ATP synthase reconstituted individually. The latter was activated by the acid-base transition, while the SRC and ARCs were energized by 0.5 mM NADH. ATP synthesized by the energy modules was converted to the luminescence signal by the coupled luciferin/luciferase reporter system. Shown are the average values of the initial steady-state ATP synthesis of at least four separate reconstitutions with standard errors.

3.3.2 The effects of freezing/thawing, osmolarity on the activity of the energy module, and membrane resealing with Poloxamer 188

When the coupling between the energy-demanding processes and energy modules in the form of functionalized liposomes is considered, the effects of the osmotic pressure are, more often than not, overlooked. On one hand, proteovesicles are prepared in solvents, which are intended to stabilize them and facilitate the activity of integrated enzymes. Meanwhile, energy consumers, for instance metabolic cascades, can be seen featuring a variety of substrates, cofactors and enzymes, all suspended in the appropriate solvent of choice. The potential problems may arise when, upon coupling, proteovesicles are supplemented to another module and the osmolarity inside proteovesicles does not match the one of their environment. In this scenario, the osmotic pressure, which is applied to the vesicles, can cause their deflation/inflation and, in the worst case, bursting. All these effects can profoundly destabilize the energy module due to changes in membrane permeability, coupling distances between the respiratory enzymes or membrane tension and curvature. Furthermore, in the worst-case scenario, disintegration of vesicles would result in a complete and irreversible deactivation of the module. To account for these effects, first, the osmolarity of the energy module as well as the CETCH cycle was measured. Throughout this work, the energy module was prepared in the

139

vesicle buffer, comprising 50 mM HEPES pH 7.5, 2.5 mM $MgSO_4$, and 50 mg ml^{-1} sucrose. The measured osmolarity of this solvent was 191 mOsm kg^{-1} and it was not significantly affected by the presence of proteovesicles. On the other hand, the osmolarity of CETCH was determined at different time points to account for the variability in the concentration of different metabolites with respect to the current stage of the cycle. Astonishingly, the average osmolarity of the CETCH was staggering 1230 mOsm kg^{-1} and it could be seen fluctuating from 1228 mOsm kg^{-1} at the start of the reaction, to 1200 mOsm kg^{-1} at the 60 min mark, and then again to 1390 mOsm kg^{-1} at the 90 min mark, when the cycle was terminated. These measurements revealed significant discrepancy between the osmolarity of the CETCH and the ARC, therefore further tuning of the ARC was required to correct for this difference. Towards this end, the vesicle buffer was supplemented with roughly 810 mM of sucrose, until the matching osmolarity was achieved. Nevertheless, the ARC osmolarity of 1230 mOsm kg^{-1} was now significantly higher than the osmolarity of bacterial cytoplasm, the natural environment of the respiratory enzymes used in this study, the typical values of which are around 300 mOsm kg^{-1} (*190*). Therefore, the osmolarity of the measurement buffer was further adjusted to 1230 mOsm kg^{-1} and the ATP synthesis by the ARC under these conditions was measured. Remarkably, on average 32 % higher output of the energy module was determined in the solvent featuring high sucrose content (Fig. 45). Whether the increased activity of the ARC in this context was related to the increased osmolarity in general or to the sucrose itself as an osmolyte remains unclear and should be explored further.
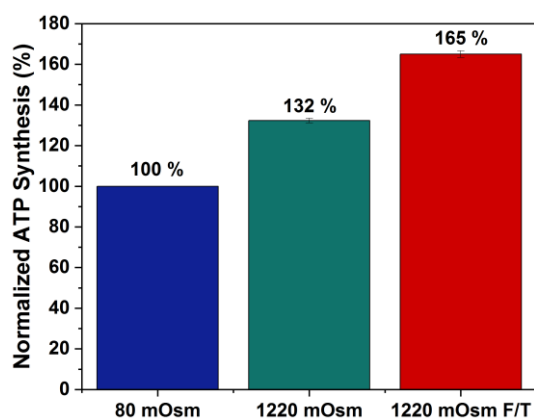
Fig. 45. The effects of increased osmolarity and a freezing/thawing on the output of the SRC. The short respiratory chain was prepared in either low (80 mOsm kg^{-1}) or high (1220 mOsm kg^{-1}) osmolarity buffer. Osmolarity of the measurement buffer was adjusted to match the osmolarity of the vesicle buffer and the ATP synthesis by the SRC was determined via luminescence produced by the coupled luciferin/luciferase reporter system. All osmolarity adjustments were done using sucrose. The SRC reconstituted in the high osmolarity buffer was subjected to a single cycle of freezing in liquid nitrogen

(1 min), followed by the thawing on ice (2 min) and the ATP synthesis by the treated SRC was determined (1220 mOsm F/T). Shown are the average values of three different measurements with standard errors.

Next, the effects of the osmotic pressure on the activity of the ARC were investigated. As briefly mentioned above, the osmolarity of the CETCH could be seen fluctuating under the operating conditions by about 200 mOsm kg^{-1}. To put this value into context, in the previous report by Hupfeld and colleagues (*191*), a 150 mOsm kg^{-1} difference could be seen resulting in the sweeling or shrieking of nano-sized liposomes, whereby in particular the magnitude of the swelling was strongly related to the average size of the vesicles. In this respect, nearly insignificant swelling could be seen in smaller (~200 nm) vesicles. Instead, when the hypotonic conditions were applied to these vesicles, the influx of water could be seen being compensated by the pore opening and the related content release, instead of by the swelling of vesicles. Furthermore, in a similar study conducted on the liposomes made of various natural lipid isolates (a system which strongly resembled lipids used in this study), a significant leakage could be seen in all setups at the applied osmotic difference of 160 mOsm kg^{-1} (*192*). If same was true for the liposomes comprising soy lipids, the pore opening in the ARC proteoliposomes would result in the dissipation of the established proton gradient and in total deactivation of the energy module. To probe for the dynamic osmolarity range of the ARC vesicles, the latter were subjected to hypertonic stress of 300 mOsm kg^{-1} difference or hypotonic stress of 600 mOsm kg^{-1} difference, and the ATP synthesis under these conditions was determined. Furthermore, the size of the ARC vesicles under osmotic pressure was analysed via dynamic light scattering. With respect to this, the osmolarity difference was notably higher in the hypotonic direction because the vesicle shrinkage is considerably harder to detect with this method, considering the insignificant decrease in vesicle diameter upon deflation (excess membrane in shrunk vesicles was contained in folds, while the diameter itself changed very little). Nevertheless, 600 mOsm kg^{-1} difference in the context of deflation was not expected to have such drastic effect on vesicles as the same difference in the inflation direction would have, since no content release or bursting was expected to happen. When subjected to hypertonic conditions, the ARC vesicles were seen shrinking from 116 to 100 nm (Fig. 46A, blue trace). Interestingly, the ATP synthesis under these conditions remained basically unchanged (Fig. 46B). This was somewhat surprising considering the highly-folded structure of mitochondria and its stimulatory effect on the oxidative phosphorylation. Folding in the mentioned organelles drastically increases their inner membrane surface, which results in the increased protein content in these membranes.

Furthermore, the volume of interlamellar space is increased, while the distance between lamellas remains relatively short. In comparison, the concentration of respiratory enzymes in the ARC vesicles was drastically lower than that in mitochondrial membranes. Hence even though membrane folding was expected to decrease the average distance between enzymes (and thus enhance coupling and potentially enhance the ATP synthesis), this would have little to no effect when only a couple of enzymes were contained in the same vesicle (and thus were still separated by the about 100 nm difference). On the other hand, when subjected to hypotonic stress, the soy PC vesicles with the inserted respiratory enzymes were seen swelling from 116 to 167 nm (Fig. 46A, red trace). Remarkably, their size remained stable over several weeks, which indicated the absence of pore opening and content release. Moreover, the ATP synthesis was slightly higher in swollen vesicles, although statistically insignificant (Fig. 46). All things considered, these experiments demonstrated the unhindered activity of the energy module under the osmotic pressure of at least 300 mOsm kg^{-1}, which meant that no further tuning in that regard was required to facilitate coupling with the CETCH.
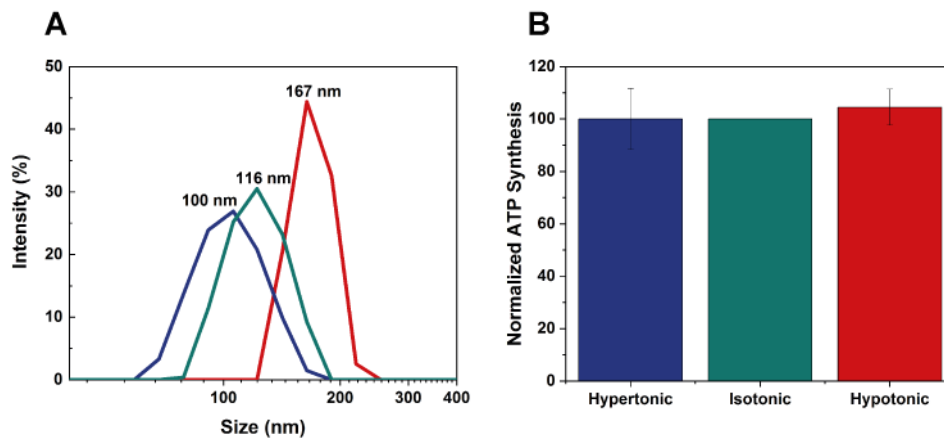
Fig. 46. The effects of osmotic stress on the SRC. (**A**) Intensity based size distribution of the SRC proteoliposomes in either isotonic (green), hypertonic (blue) or hypotonic (red) buffer with specified peak values. Osmolarity was adjusted with sucrose. To achieve hypertonic and hypotonic conditions, ΔM of 300 and 600 mOsm kg^{-1} was applied, respectively. (**B**) The initial steady-state ATP synthesis by the SCR under hypertonic, isotonic or hypotonic conditions, as determined via luminescence produced by the coupled luciferin/luciferase reporter system. Shown are the average values of at least 4 different measurements with standard errors.

Moreover, the coupling between the ARC and the CETCH required the shipping of the energy module to the collaboration partners. To enable this, the ARC vesicles had to be frozen, kept on dry ice over several days, thawed by the recipient and activated. The cycles of freezing and thawing are known to disrupt lipid membranes and this effect can be exploited in a variety

142

of applications, from bacterial transformation (*193*) to vesicle formation, employed in this study (Chapter 2.3.1). Nevertheless, upon thawing, vesicles could exhibit the increased membrane permeability, which would inhibit the ATP synthesis. To probe for this effect, small aliquots of the ARC liposome suspension were flash-frozen in liquid nitrogen over 30 s. Then they were either thawed slowly, on ice, or rapidly, at room temperature and their activity was measured. Remarkably, following a single freeze/thaw cycle, the ATP synthesis in proteovesicles was on average 65 % higher from the one in freshly reconstituted vesicles (Fig. 45), while no significant difference could be seen between the slow and rapid thawing. On the other hand, when this same batch of previously frozen proteoliposomes was subjected to a second freeze/thaw cycle, its energy output decreased by nearly 80 %. This suggested the presence of membrane deformations (imperfections in the organization of lipid bilayers) induced by the protein insertion and detergent digestion, which appeared to have been mended over the course of membrane remodelling due to the rapid changes in temperature. This resulted in the decreased membrane permeability, which could subsequently be altered by another temperature shock. An alternative explanation for the observed increase in ATP synthesis would be reconfiguration of proteovesicles with respect to protein content. In this context, freeze/thaw treatment could induce membrane mixing and fusion of random vesicles, yielding reorganized proteoliposomes with more favourable enzyme distribution. Nevertheless, this hypothesis could not be supported by the experimental evidence. No change in vesicle size could be detected upon either of the two freeze/thaw cycles. Furthermore, it is unlikely that only first reconfiguration would be favourable across five different reconstitutions, while the second one would always result in poorer enzyme distribution and lower ATP synthesis. Finally, high sucrose content in the ARC suspension was expected to act as a considerable cryoprotectant, substantially preserving the integrity of the vesicles. These experiments uncovered the compatibility of the ARC vesicles with the commonly used storage and shipment methods. Nevertheless, the vesicles were subjected to only one freeze/thaw cycle in all coupling experiments to avoid the activity loss.

The above-described freeze/thaw experiments have led me to the potentially important conclusion – membrane imperfections, as a result of protein insertion, could potentially be mended at later times to increase the output of the energy module. In this context, the deformations in lipid bilayers localized at the protein insertion spots should likely be discriminated from the non-protein-related deformations (Fig. 47B).

To induce resealing of permeabilized membranes, I was looking for an approach which would be less disruptive and more controllable than the freeze/thaw cycles. In this regard, tri-block polymer, Poloxamer P188 (Fig. 47A), was identified as a resealing agent of a high potential. P188 is used in a variety of biomedical applications to treat damaged tissues in the cases when cell disruptions are extensive or when there is an underlying pathology that reduces the membrane repair capacity of a cell (*194, 195*). When added to the membranes in concentrations below its CMC, P188 inserts selectively into damaged membranes exhibiting low surface pressure ($\sim$22 mN m^{-1} at 30 °C, roughly corresponding to the maximal surface pressure applied by P188 on a pure water phase (*196*); in comparison, normal surface pressure of lipid bilayers is about 30 mN m^{-1}), uninfluenced by the lipid headgroup electrostatic repulsion. Upon the polymer insertion, surface pressure of the membranes is increased and P188 gets squeezed-out, resealing membranes in the process. Apart from its beneficial properties as a resealing agent, P188 was reported to also serve as a scavenger of free radicals (*197*), a function invaluable in the context of the oxidative phosphorylation. Taking all these facts into consideration, I attempted to treat permeabilized ARC vesicles with Poloxamer 188 to tighten the membranes and increase the output of the energy module. These experiments were performed at the very end of my doctoral studies and were, thus, purely exploratory in nature. A substantial follow-up is required to fully understand the benefits and limitations of P188 when used as a tool in synthetic biology.
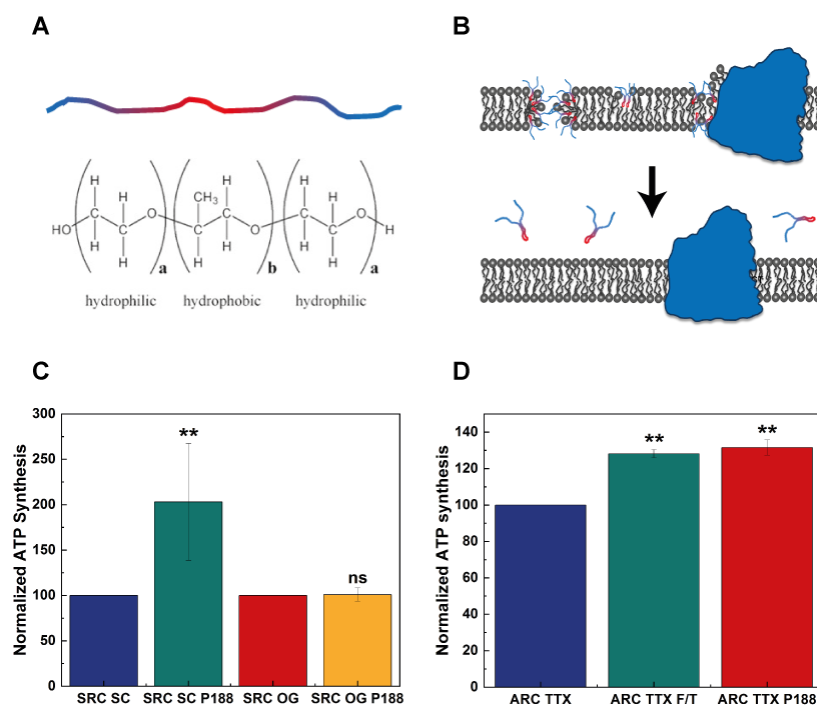
Fig. 47. Resealing of lipid membranes of the SRC by Poloxamer 188. (**A**) structure and schematic representation of Poloxamer 188. Hydrophilic portions of this block co-polymer are colored blue and the hydrophobic portion is colored red. (**B**) Drawing of the course of lipid membrane resealing by Poloxamer 188. With hydrophobic region, polymer is inserted into perturbations in lipid bilayer formed during the reconstitution of the energy module. The insertion results in bilayer resealing and the ejection of Poloxamer. (**C**) ATP synthesis by the SRC reconstituted with either sodium cholate (SC) or octyl glucoside (OG) and either untreated or treated with Poloxamer 188 (P188), as determined via luminescence produced by the coupled luciferin/luciferase reporter system. (**D**) Comparison of the ATP synthesis by the ARC reconstituted with Triton X-100 (TTX) untreated and either subjected to a single cycle of freezing (F/T) in liquid nitrogen (1 min), followed by the thawing on ice (2 min), or treatment with Poloxamer 188 (P188). Shown are the average values of at least 3 different reconstitutions and treatments, with standard errors. ns, not significant for $P > 0.05$; **$P \leq 0.01$.

To test the membrane resealing by Poloxamer 188, the ARC was reconstituted with either octyl glucoside, Triton X-100 or sodium cholate at the membrane saturation points (R_{sat}) of these detergents. Then, an aliquot of the ARC vesicles was supplemented with P188 at 50 µM (40 % CMC, (*196*)) and incubated at room temperature for 30 min. Finally, the ATP synthesis in treated and untreated vesicles was measured and compared. Interestingly, the increase in ARC activity upon P188 treatment was observed in vesicles reconstituted with sodium cholate (Fig. 47C) and Triton X-100 (Fig. 47D), while no change was observed in vesicles prepared with octyl glucoside. Furthermore, sodium cholate vesicles in particular received a significant activity boost (the ATP synthesis was on average doubled!) due to

Poloxamer treatment, although large variation could be seen between separate reconstitutions. Since it was very important that the P188 was added to vesicles below its CMC and yet in sufficiently high concentrations to facilitate membrane resealing (*197*), these variations could be due to small differences in Poloxamer content between different experiments. A more moderate (approx. 30 %) increase in ATP synthesis could be seen in the ARC vesicles assembled with Triton X-100 as a mediating detergent. Remarkably, the effect of Poloxamer on these vesicles was comparable to the effect of a single freeze/thaw cycle (Fig. 45). In contrast, no observable effect of P188 could be seen in the ARC vesicles reconstituted with the aid of octyl glucoside. These large differences in P188 resealing between the three ARC preparations could potentially suggest the related differences in membrane defects caused by membrane solubilization with different detergents. Furthermore, it remains unclear whether the Poloxamer could reseal membrane perturbations that are localized in the proximity of membrane proteins. It can be speculated that the effect of P188 on the ARC liposomes was dependant on the type of membrane damage, whereby in some cases the membranes were disrupted in the vicinity of inserted enzymes and could not be resealed by P188 (octyl glucoside), while in other cases (sodium cholate, Triton X-100), lipid bilayers were disrupted independently of the inserted MPs and the Poloxamer 188 could facilitate resealing.

3.3.3   Coupling between the energy (ARC 2) and metabolic (CETCH cycle) module

After the ARC was optimized with respect to its output and composition to enable coupling with the metabolic conversion module, next, preliminary coupling with the CETCH cycle (*58*) was attempted. The latter is a reaction network comprising 17 enzymes that converts CO_2 into organic molecules. With respect to this, the iteration of CETCH that was being used in the coupling experiments converted CO_2 into malate – between 400 and 600 µM of this dicarboxylic acid were being produced over 90 min. Furthermore, the cycle was being energized by the two energy sources – formate and polyphosphate. Formate was being used by the formate dehydrogenase to regenerate NADPH, a substrate which was required in 4 different steps of the cycle. Meanwhile, polyphosphate was exploited by the polyphosphate kinase to phosphorylate ADP to ATP and the latter was then driving the conversion of 4-hydroxybutyrate to 4-hydroxybutyryl-CoA via 4-hydroxybutyryl-CoA synthetase (HBS). Although most frequently, simple metabolic conversions are used to study coupling between different modules (*59*), the CETCH cycle offered an unprecedented opportunity to study the functionality of the energy module in a complex, cell-like environment. In this context, the effects of crowding on

the output of ARC 2 could potentially be examined, as well as the potential interactions between the CETCH enzymes and the ARC liposomes.

When the CETCH was examined for the potential points of coupling with the energy module, several promising candidates were identified. First off, malate could have been converted to NADH by the malate dehydrogenase to feed the ARC and to produce ATP. Malate was a prime candidate for the conversion since its accumulation could be seen inhibiting the CETCH cycle (*58*). The problem was, however, that this substrate was being produced at the later stages of the cycle, while the ATP was required from the very start. Moreover, malate was synthesised in relatively low quantitates, likely insufficient for the unhindered functionality of HBS. As such, malate was not considered further, although the valid option to convert it to ATP in order to stimulate the cycle remained available. The second candidate, through which the coupling was enabled was formate. By exploiting the latter, polyphosphate as a second sacrificial substrate could then be eliminated from the cascade, and the CETCH would now require only a single energy source. Furthermore, such elimination would make this reaction network more suitable for various biotechnological applications.

Figure 48. Coupling between the ARC 2 and the CETCH cycle towards the formation of the minimal artificial mitochondrion. ATP was produced by the ARC 2 employing formate as the energy source and it was used to drive the conversion of 4-hydroxybutyrate to 4-hydroxybutyryl-CoA by the

CETCH cycle. The two species which were analysed to determine the activity of the coupled system are indicated in red.

Nevertheless, as mentioned, relatively small quantities of ATP are required to drive the CETCH cycle in contrast to the comparatively high consumption of NADPH by the cycle. Hence, the competition between the CETCH enzymes and the ARC for the NADPH could lead to inhibition of the two modules. This would not have been an issue in the case of ARC 2, where the concentration of the non-membrane-inserted NADH dehydrogenase (DTD) could be adjusted so that a larger portion of NADPH was being fed to the CETCH and not the ARC. In contrast, the situation would be different if the ARC 1 was considered, because such fine control over the complex I content of this energy module would likely be unachievable. Luckily, this dilemma was quickly resolved by the fact that the time remaining before the end of my doctoral studies only allowed for a single coupling attempt, and for this occasion, the ARC 2 was selected due to its superior output compared to the ARC 1. Nevertheless, a minor adjustment was made to the module to throttle the substrate distribution between the ARC and the CETCH. Formate was being simultaneously converted to NADPH as well as NADH, while the affinity of formate dehydrogenase for the NAD^+ (Km = 3.7 mM) was considerably lower than its affinity for $NADP^+$ (Km = 0.6 mM) (Fig. 49). Meanwhile, in the ARC, the affinity of DTD for the NADH was higher than the affinity of this enzyme for NADPH (200 vs. 140 µM, respectively) (198). This setup enabled the examination of the coupling between the ARC and the CETCH under the conditions slightly more relevant for the ARC 1 – the module yet to be explored in this context. With that, a more straight-forward comparison between the ARC 1 and 2 as the components of a modular synthetic cell was enabled.
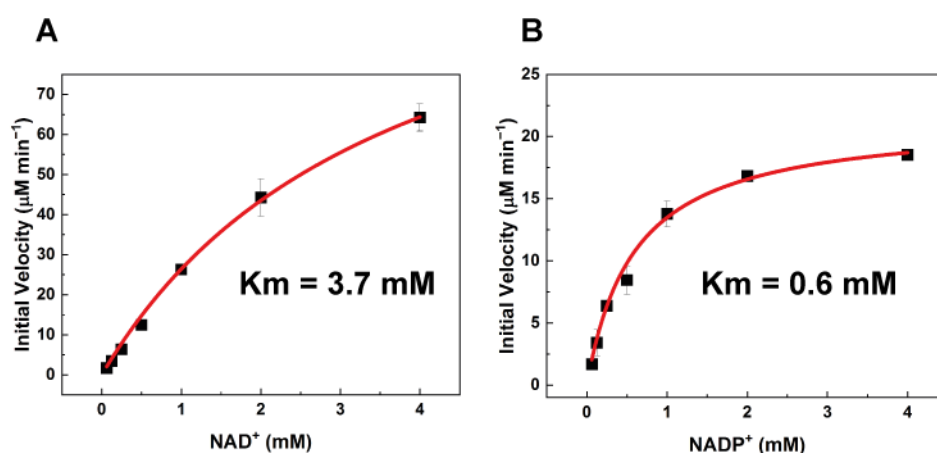

Figure 49. Conversion of formate to either NADH (A) or NADPH (B) by formate dehydrogenase. The activity of formate dehydrogenase was recorded spectrophotometrically, at 340 nm, in Tris (pH

8.0), 20 mM K_2HPO_4, 200 mM formate and 0.06–8 mM β-NAD$^+$ or 0.06–8 mM NADP$^+$. Data was fitted with the Michaelis–Menten equation to determine the affinity (Km) of formate dehydrogenase for the two substrates (indicated). Each point represents the average value of three different measurements with standard error.

Finally, the ARC 2 with a composition described in Chapter 3.3.1, was supplemented to the CETCH cycle to facilitate the regeneration of ATP. At different time points, small aliquots of the coupled system were collected, quenched in formic acid and analysed by mass spectrometry. In this regards, two metabolites were measured. Glycolate was detected as one of the several products of the cycle and its concentration reflected the efficiency of the CETCH. Meanwhile, the analysis of 4-hydroxybutyrate enabled the determination of the ARC efficiency. Up to 31 % of the CETCH efficiency was achieved while the cascade was being fuelled by the ARC 2 instead of the polyphosphate/polyphosphate kinase system or via direct supplementation of ATP (Fig. 50A). The turnover of the coupled cycle was relatively high during the first 15 min of the reaction, after which it decreased considerably and then remained relatively constant. The reasons behind this inhibition could be either the insufficient ATP synthesis by the ARC or the disruption of the cascade via the presence of lipid vesicles in the system. To discriminate between the two options, the 4-hydroxybutyrate content was analysed (Fig. 50B). The analysis revealed the accumulation of 4-HB, meaning that the insufficient amount of ATP was present in the reaction mixture to drive the conversion of 4-HB to 4-HB-CoA. This was somewhat surprising, considering the relatively high output of the energy module as measured in the first 15 min of the reaction (Chapter 3.3.1, Fig. 44). Furthermore, importantly, the efficiency of the coupled system was not seen increasing when the energy module was supplemented to the CETCH in larger quantitates. This suggested the potentially overlooked intrinsic problem with the ARC, so to explore this mystery further, the activity of ARC 2 over the extended periods of time was analysed. An extraordinary phenomenon was revealed during this analysis and is discussed in the next segment.
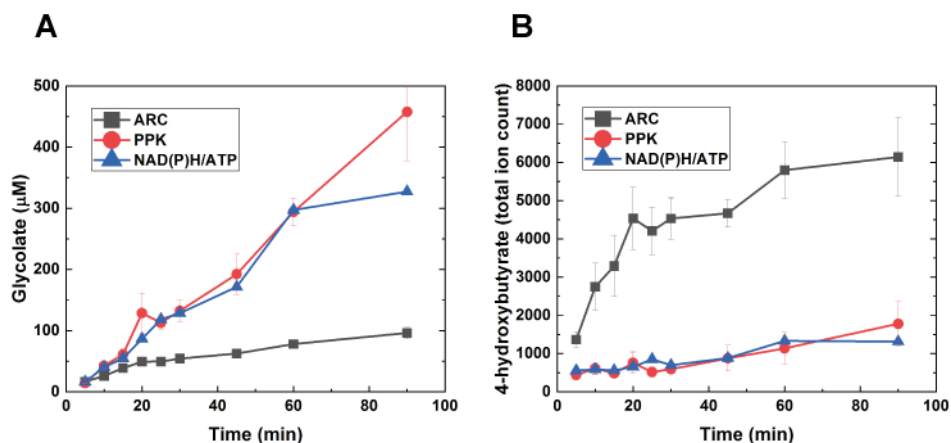
Fig. 50. The activity of the CETCH cycle energized by the ARC 2. Changes in glycolate (**A**) and 4-hydroxybutyrate (**B**) concentration during the turnover of CETCH, driven by either ARC 2 (black), polyphosphate kinase (PPK, red) or a single excess addition of NAD(P)H/ATP (blue). Content of intermediates was analyzed via mass spectrometry. Shown are the average values of 3 different measurements with standard errors.

3.3.4 The auxiliary oxygen resupply system based on calcium peroxide particles

To elucidate the reasons for the decreased output of the ARC in a coupled system over longer periods of time (> 1 h), first, the ATP synthesis was determined within a similar time frame in the uncoupled module. With respect to this, all substrates were supplemented in several-fold excess to avoid depletion. Right after the activation of the module, relatively high steady-state ATP synthesis could be detected for several minutes (Fig. 51). Astonishingly, however, this period of synthesis was followed by a steep and rapid decrease in the ATP signal, which appeared to have indicated that the ATP was being hastily consumed.
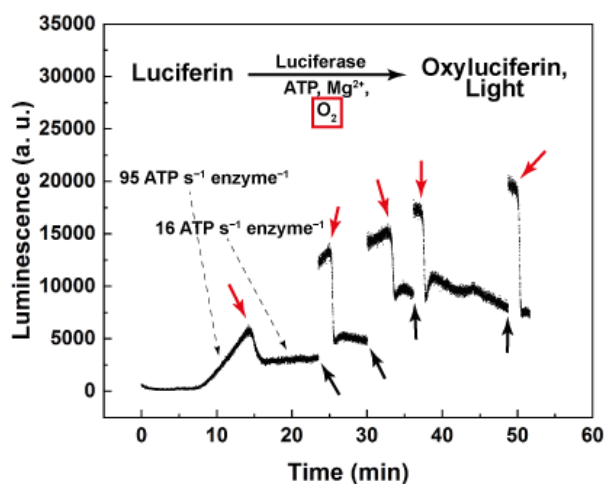
Fig. 51. Activity of the ARC over the extended period of time. ATP produced by the ARC was converted to light (black trace) by the coupled luciferin/luciferase reporter system via the reaction noted in the inset. For the detection of ATP, oxygen was required. Points in time when oxygen was depleted in the measured system are indicated with red arrows. Upon depletion, the system was reoxygenated via vigorous mixing, as indicated with black arrows. During the measurement, system was not mixed outside of the specified time points. The ATP synthesis rates of the ARC in the presence of oxygen and after its depletion are specified with the dashed arrows.

One of the explanations for this change could be that the ATP was being hydrolysed in the measured samples. In the absence of a proton gradient, ATP synthase can switch from ATP synthesis to hydrolysis (*199*), and in this case, the latter would indicate deactivation of proton pumps of the energy module. Energised by a vast electron pool maintained by the reducing agent dithiothreitol (DTT), unhindered activity of *bo₃* oxidase was expected for at least one hour. Nevertheless, to probe for the unlikely substrate depletion, fresh DTT, ubiquinone or the two together were added to the reaction to restart the synthesis. Neither of these additions could be seen successfully restarting the energy module, which indicated that the electron supply was not the underlined problem. Furthermore, this ATP depletion could be seen scaling with the concentration of *bo₃* oxidase in the measured samples. When taken together, these findings led me towards another potential cause – an overlooked and mostly forgotten, second substrate of *bo₃* oxidase – oxygen. The oxygen depletion in the measured samples would have to distinct side effects. First one and more obvious one was the lower activity of *bo₃* oxidase and potentially complete enzyme deactivation. The latter was not expected in practice due to oxygen diffusion from the gas phase overlaying the samples. Nevertheless, even if the enzyme was not completely inactive, the activity of *bo₃* oxidase that was depending on the oxygen diffusion would be considerably diminished. On the other hand, a second, far less obvious

151

reason was related to the reporter system, which was used to detect ATP. The ATP detection by the CLSII system was based on the conversion of luciferin to oxyluciferin by the enzyme luciferase (*154*). During this conversion, the ATP was being consumed and a signal in the form of luminescence was emitted. However, apart from ATP, another substrate was required for this reaction – oxygen. Therefore, the oxygen depletion by the *bo_3* oxidase would not only hinder the ATP synthesis due to the decreased activity of the mentioned proton pump, but would also disable the detection of the produced ATP by luciferase. Hence, in both cases, oxygen diffusion would be the rate limiting step of the coupled reactions. To test for this hypothesis, as soon as the decrease in ATP was detected during the ATP synthesis measurements, the samples were aerated by vigorous mixing and then measured again (Fig. 51, black arrows). Indeed, this step resupplied the reaction mixtures with sufficient amounts of oxygen to enable the detection of ATP synthesis for several minutes, until the next depletion. During this time, the high ATP content in the samples was revealed, and the ATP synthesis appeared to have followed the expected trajectory suggested by the initial steady-state. Based on these observations, I was able to confirm that the ATP in the samples was, in fact, not being hydrolysed. Instead, it was synthesized as well as detected at slower rates, limited by the diffusion of oxygen. This claim was additionally supported with the oxygen measurements via Clark-type oxygen-sensing electrode on the Oxytherm system. With respect to this, in parallel to ATP synthesis determination, I measured oxygen content in the activated energy module, which enabled the comparison between the two (Fig. 52). Unsurprisingly, a strong relation between the oxygen depletion and the decrease in ATP synthesis/detection could be observed within a given time frame. It is important to note that the oxygen was depleted slightly faster in the samples where the ATP was being measured than suggested by the oxygen measurements, considering that during the latter samples were being stirred, while this was not the case during the ATP determination.
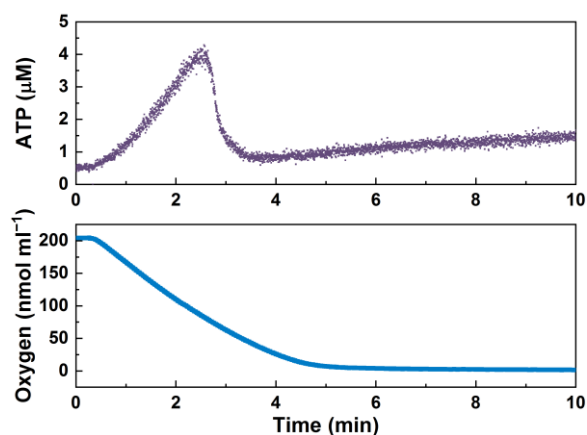
Fig. 52. ATP synthesis and oxygen consumption by the ARC. The changes in ATP concentration (top trace) due to the activity of the energy module were detected via luciferin/luciferase reporter system. In parallel, oxygen consumption by the bo_3 oxidase in the ARC (bottom trace) was monitored with the Clark-type electrode. The fast initial ATP synthesis in the well-aerated samples ($t \approx 0–2.5$ min) was followed by a much slower one ($t \approx 3$ min and onward), limited by the oxygen diffusion after its depletion.

The above-described experiments undoubtedly underlined the importance of the oxygen supply for the unhindered and continuous functionality of the energy module devised in this study and for any related coupled system. Indeed, in nature, considerable portions of the cellular infrastructure of organisms are dedicated to oxygen detection and resupply and countless strategies to achieve the latter have emerged throughout the course of the evolution. As we have reached the point where we can mimic oxidative phosphorylation with the efficiency more and more similar to the one of natural systems, it has become a necessity that the auxiliary support systems are also being mimicked alongside it. When I was contemplating the potential solutions for addressing the reoxygenation of the ARC vesicles, I sought after different areas of research that were tackling a similar problem. The most fitting homology could be found between my module and tissue engineering, whereby in both cases respiratory vesicles/seeded cells require constant artificial resupply of oxygen. In tissue engineering, the latter is most frequently and most successfully tackled via the employment of various oxygen release materials (reviewed extensively by Gholipourmalekabadi and colleagues (*200*) and Ashammaki and colleagues (*201*)), most notable of which are sodium percarbonate, fluorinated materials as well as hydrogen, magnesium and calcium peroxide. In particular the latter has been shown to be the most promising oxygen generator due to its relatively high solubility in water and the related rapid oxygen release as well as due to the comparatively higher purity (around 70 %) of the commercially-available formulations (*202, 203*). Calcium peroxide particles were shown to

react with water to form either oxygen, hydrogen peroxide or a combination of both (*204*). In these scenarios, oxygen was released mainly at higher pH (> pH 9) and temperature (> 22 °C), while in particularly lower pH (< pH 7) seemed to have favoured the hydrogen peroxide release. In the context of the artificial mitochondrion, several criteria must be met to make any considered oxygen release material suitable for the supplementation. First, the oxygen generator should be harmless to biological material and biologically inert. Second, the oxygen should be released from the material at the sufficiently high rate, which would enable unhindered functionality of the ARC. Third, ideally, the samples would be reoxygenated evenly, spatially and temporally, to promote the highest potential output of the ARC. With respect to these criteria, calcium peroxide microparticles were tested for biocompatibility with the energy module. Even though the supplementation of said particles at higher concentrations would directly correspond to higher amounts of the released oxygen in measured systems, unfortunately, there was a limit at which calcium peroxide could be added to the ARC samples. It was determined that this limit was 4 mg of particles per 1 ml pf the proteoliposomes solution. At the higher particle contents, ATP synthesis measurements (based on the detection of the luminescence signal) would be disturbed due to the absorption and scattering of light by the particles, and the determination of the ARC output was disabled.

To test the calcium peroxide microparticles in the role of the auxiliary oxygen supply system, first, the oxygen release by the particles was first measured via a Clark-type electrode. Towards this end, 1 mg of particles were dissolved in the ARC/CETCH coupling buffer (20 mM Tris pH 8.0, 20 mM K_2HPO_4, 50 µM $CaCl_2$, 200 µM $MgSO_4$ and 685 mM sucrose) and the oxygen release rate by the particles in the presence or absence of catalase was determined. Considering the expected aforementioned release of hydrogen peroxide at pH < 9 during the decomposition of calcium peroxide particles, enzyme catalase was added to reactions in order to facilitate the conversion of hydrogen peroxide to molecular oxygen and water. The enzyme was supplemented at 1 U per 1 ml of reaction mixture (one unit will decompose 1.0 µmole of H_2O_2 per min at pH 7.0 and at 25 °C). Such significant excess amount of enzyme was added to promote rapid removal of the formed hydrogen peroxide, so that oxidative damage in the module and the related deactivation of respiratory enzymes could be avoided. It is also important to note that the dispersion of particles in the mentioned buffer was relatively stable due to the high sucrose content. This enabled oxygen release measurements for up to approximately 8 minutes, while afterwards a large portion of particles would sediment onto the electrode and inhibit the detection of changes in the oxygen content in samples. Furthermore,

the sedimentation of particles also decreased their active surface and their accessibility to water, therefore, decreasing the oxygen release. Finally, the dynamic range of the oxygen electrode in the Oxytherm system was about 0–40 % O_2, as reported by the manufacturer. Considering the solubility of oxygen in water of about 1220 nmol min^{-1} at 25 °C (*205*), the changes in oxygen content could only be detected below 650 nmol min^{-1}. The particles alone could be seen releasing oxygen at the average rate of 20.9 ± 0.1 nmol min^{-1} (Fig. 53A, yellow trace). The oxygen release rate was increased to 84.3 ± 0.1 nmol min^{-1} when catalase was added to the particles (Fig. 53A, green trace), which indicated that the prevailing product (> 70 %) of particle decomposition at pH 8 was hydrogen peroxide. If one considers the oxygen release rate of calcium peroxide of 84.3 nmol min^{-1} and assumes the particle purity of 70 % (as reported by the manufacturer), 1 mg of particles would therefore completely dissolve in roughly 2 hours. The oxygen consumption rate of the most active variant of the ARC was about 40 nmol min^{-1} per 10 μl of proteovesicles (OCR here is purposely expressed per specified quantity of vesicles to enable direct comparison with the oxygen requirements of the coupled ARC/CETCH system), which meant that 1 mg of calcium peroxide would theoretically be able to sustain the ARC activity for about 4 hours. To test this assumption, the ATP synthesis by the ARC was recorded in the presence and absence of calcium peroxide particles. In the absence of the regeneration system, oxygen in measured samples was depleted by *bo₃* oxidase in about 2 minutes after the activation of the ARC (Fig. 53B). On the other hand, when calcium peroxide particles were supplemented to the samples, the steady-state ATP was sustained for roughly 8 minutes and, remarkably, the output of the ARC was increased 2-fold. Unfortunately, the synthesis recordings beyond the specified time point were unreliable due to particle sedimentation. The latter was particularly problematic in the context of the luminescence measurements, which were conducted in plastic vials featuring disadvantageous diameter-to-height ratio. In this setup, the surface of sedimented particles was severely reduced, which drastically limited the oxygen release. With respect to this, beyond the 8 min mark, the diffusion of oxygen between the particle sediment and the solution was even lower than the one between the overlaying gaseous phase and the solution, considering the lower diameter of the measurement vessel at the bottom compared to the top. Furthermore, importantly, catalase could not be included in the ATP synthesis measurements because of a high background noise caused by the enzyme. Therefore, the ARC inhibition due to oxidative damage caused by hydrogen peroxide could not be excluded in this setup.
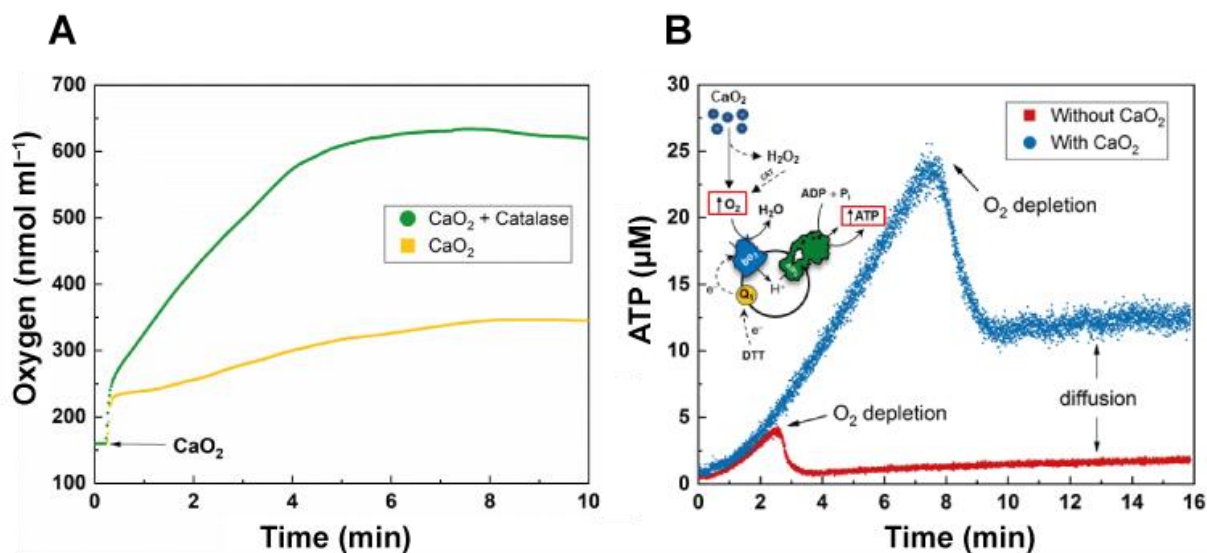
Figure 53. Calcium peroxide microparticles as the auxiliary oxygen supply system. (**A**) CaO_2 particles were hydrated with the measurement buffer at pH 8.0 prompting the oxygen as well as hydrogen peroxide release (yellow trace). The latter could be converted to oxygen and water via catalase, which was supplemented to the particles (green trace; 1 U of enzyme per ml), to stimulate more efficient oxygenation of the solution. Oxygen content in the samples was detected via Clark-type electrode. Compared are the initial quasi-steady-state oxygen release rates from CaO_2 in the presence of absence of catalase. (**B**) Calcium peroxide particles were supplemented to the energy module to promote the prolonged activity of *bo₃* oxidase. With that, the ATP synthesis by the ARC 2 at the initial fast synthesis rate was significantly extended. Catalase was not included in this reaction, therefore oxidative damage to the ARC by hydrogen peroxide was likely to occur. ATP synthesis was detected via the coupled luciferin/luciferase reporter system.

Based on the preliminary testing, calcium peroxide was identified as a high potential candidate for the efficient reoxygenation of the energy module, despite some limitations of the measurement setups. A minute amount of the particles could be observed releasing oxygen at the rate sufficient to support the activity of the ARC for several hours. The toxic side product of particle degradation under operational conditions of the ARC, hydrogen peroxide, could readily be converted to oxygen by catalase to avoid damaging the energy module. With respect to this, calcium peroxide could be considered biocompatible. Furthermore, good temporal control of oxygen release could be achieved, as long as the particle dispersion remained stable. Future challenges with respect to the implementation of calcium peroxide particles as the oxygen regeneration system lie mostly in assuring sufficient spatial control of particle distribution. The latter was in the current setup (to a limited extent) achieved primarily because of the relatively high viscosity of the solvent, which contained high concentrations of sucrose.

156

The unfortunate downside was the decreased solubility of oxygen in the buffered solution due to the high sugar content (*206, 207*). Major progress in this direction was already made in the applications related to tissue engineering. In this context, the oxygen releasing particles were frequently integrated into scaffolds built from different polymers, among others, poly(lactic-co-glycolic acid) (*208*) and PDMS (*209*). The encapsulation of the particles not only assured their homogeneous distribution in the system, but also enabled the control over the size of the reaction surface and, therefore, over the rate of oxygen release from the particles. Moreover, the scaffolds themselves were used to immobilize and position the cells. In future works, this principle could be applied to the energy modules in order to produce a highly sophisticated artificial respiratory tissue (Fig. 54). Lastly, cointegration of calcium peroxide and respiratory enzymes in PDMS membranes could be explored in more detail with the hopes of achieving substrate channelling that could potentially lead to increased output of the respiratory-driven energy modules.
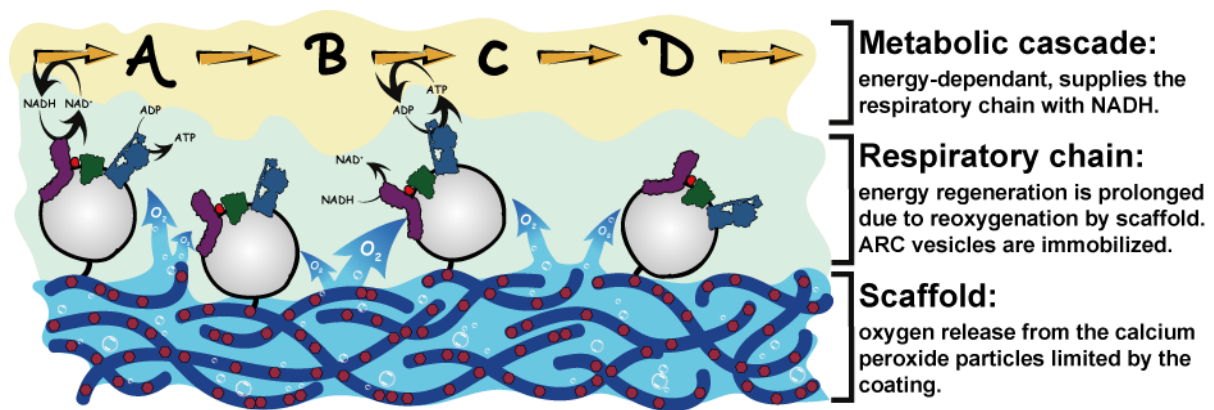
Fig. 54. The proposed artificial respiratory tissue. Calcium peroxide particles (red) are enclosed in polymer fibers (dark blue), which are crosslinked into a scaffold/matrix. The mentioned coating enables fine control over the oxygen release rate from the particles by limiting their active surface, homogeneous aeration of the assembly as well as immobilization of the ARC vesicles towards the formation of the respiratory tissue. The latter could potentially be applied to a solid surface and overlaid with the reaction of choice that requires continuous regeneration of ATP/NAD(P)$^+$ and oxygen supply.

4 CONCLUSIONS

The energy regeneration module was constructed to enable continuous supply of adenosine triphosphate and, potentially, other important co-factors, such as NAD^+ to other energy-demanding biomimetic modules comprising the artificial cell. This energy regeneration module can be considered as the artificial respiratory chain, consisting of five functional parts: the ATP synthase, a proton pump, an electron mediator, a NADH dehydrogenase and a compartment. Furthermore, the ARC was coupled with the metabolic cascade to form the energy regeneration organelle – minimal artificial mitochondrion. Construction of the latter was done in several stages, all defined by main objectives. Considering the short-lived nature of biological parts in the absence of the repair and replacement mechanisms, the most important objective of this work was to enhance the stability and durability of the energy module. Stabilization of the latter was also of particular importance due to the potential oxidative damage done to the module during its operation by the ROS that are produced by respiratory enzymes. The enhancement of the energy module was attempted via replacement of the fragile natural parts with man-made ones. Unfortunately, chemical mimicking of complex MPs such as the rotary engine ATP synthase, nearly perfected through millions of years of evolution, was at this time beyond my reach. On the other hand, significant progress could be achieved by augmenting the common delimiter and an essential component of the energy module – lipid membranes. Towards this end, graft co-polymer PDMS-*g*-PEO was chosen due to its ability to self-assemble into polymersomes, which exhibit similar membrane thickness and fluidity to the one of lipid membranes (*38, 210*). Furthermore, this polymer is known to be miscible with lipids, which enables the formation of hybrid vesicles featuring lipid content tailored to match the functional requirements of various membrane proteins. First, detergent-based reconstitution protocol was developed, which enabled the insertion of minimal oxidative phosphorylation machinery (*bo$_3$* oxidase and ATP synthase) into hybrid and polymer membranes. In parallel, the two respiratory enzymes were reconstituted into liposomes, which served as a benchmark system. While the activity of the proton pump was almost entirely preserved in these synthetic membranes, some portion of the ATPase activity was lost and the output of the polymer-based energy modules was proportionally reduced (*1*). Therefore, my next goal was to optimize their performance to either match or surpass that of the lipid-based ones. The mentioned reconstitution was the first example of the successful functional insertion of several complex membrane proteins in man-made membranes, which meant that in order to improve the output of the energy modules, the interplay between the polymer membranes and the inserted enzymes had to be elucidated. This

was approached from two directions – by characterization of the membranes and by analysis of the enzyme insertion and activity.

First, I probed the membrane architecture of proteohybrids and proteopolymersomes. Interestingly, in the former, membrane thickening in the vicinity of the inserted enzymes was observed with cryo-EM and was postulated to be due to the preferential partitioning of lipids in this area. This specific association between lipids and proteins in hybrid membranes was directly confirmed via a FRET-based experiments and indirectly via the observed decreased membrane permeability following enzyme reconstitution. In contrast, protein insertion in polymersomes resulted in the loosening of the polymer monolayer, membrane thinning and the observed increase in membrane permeability. Furthermore, looser polymer membranes facilitated enhanced diffusion of proteins as well as membrane constituents, while the diffusion of lipids was hindered in hybrid membranes due to their association with the enzymes (*97*). While beneficial in some aspects, the preferential localization of lipids in proteohybrids made the inserted proteins prone to delipidation and deactivation. Indeed, the exposure of proteohybrids to ROS resulted in nearly complete deactivation of bo_3 oxidase, while almost no activity loss was detected in proteopolymersomes. In this context, cryo-EM imaging revealed significant damage done to lipid bilayers in liposomes and hybrids by ROS, although the integrity of these vesicles was not completely diminished (vesicles were not bursting), as revealed by the DLS as well as the dye leakage experiments (*97*). To exclude the enzyme deactivation due to the direct damage of bo_3 oxidase, the enzyme alone stabilized in detergent micelles was also exposed to ROS. Complete retention of enzyme activity after the exposure to ascorbyl radical confirmed that the main weakness of the energy modules was, indeed, lipids. Therefore, the reconstituted enzymes were deactivated due to delipidation, resulting in enzyme aggregation and deactivation.

After the effects of protein insertion on the characteristics of functionalized hybrid and polymer membranes were elucidated, the reconstitution procedure itself and the resulting configuration of the inserted enzymes was analysed in greater detail. In this respect, it was crucial to understand the interactions between the mediating detergents and different types of membranes, so that the enzymes could be inserted under well-defined conditions. Furthermore, another essential piece of information was the enzyme orientation and reconstitution efficiency when inserted in different membranes with different detergents at different detergent concentrations. In this context, solubilization profiles of liposomes, hybrids and polymersomes with various detergents were first recorded. This enabled the determination of membrane

saturation (R_{sat}) and total solubilization (R_{sol}) point for tested detergents, both of which being membrane states consistently proven to be of great importance for the successful protein insertion (*44, 50, 54, 61, 63, 64, 73, 74, 138*). Efficient solubilization of hybrids as well as polymersomes could be achieved with all tested detergents, while large similarities were observed particularly between liposomes and hybrids. This suggested the predominant interactions between detergents and lipid domains of hybrid vesicles. Furthermore, the presence of detergent micelles in vesicle solutions resulted in two-stage solubilization of hybrids, whereby during the slower stage, membrane constituents were presumably exchanged between micelles and vesicles. Next, *bo₃* oxidase and ATP synthase were reconstituted in hybrids and polymersomes at the R_{sat} and R_{sol} of various detergents and the enzyme orientation as well as the reconstitution efficiency was analysed. The analysis revealed that the enzyme insertion could be influenced to a greater extent by the choice of detergent and the degree of membrane solubilization. Similarities were once more observed between liposomes and hybrids with respect to the orientation of *bo₃* oxidase, where fast solubilizing detergents (Triton X-100, octyl glucoside, dodecyl maltoside) could be seen mediating the enzyme insertion with predominantly correct orientation. This further implied the preferred interactions between detergents and lipids, and the potential role of lipid nanodomains in hybrid vesicles as protein insertion spots. Moreover, very similar reconstitution efficiency of *bo₃* oxidase was determined in all types of membranes, which was in a good agreement with the measured similar enzyme activities in these membranes. With this, a high potential of PDMS-*g*-PEO membranes as a platform promoting the efficient insertion of largely hydrophobic proteins at high protein densities was revealed, which could potentially have an impact on a variety of applications (desalting/filtering, gradient formation, transmembrane transport, etc.). On the other hand, a vastly different story could be seen in the experiments involving the reconstitution of ATP synthase. Over 80 % correct orientation of this enzyme could be achieved in all types of membranes, depending on the choice of detergent. Nevertheless, significantly lower reconstitution efficiency of ATP synthase was observed in polymer vesicles when compared to liposomes. Remarkably, the activity of the short respiratory chain reconstituted with different detergents in different types of membranes was strongly correlated with the reconstitution efficiency of ATP synthase. Surprisingly, the energy module was less active than expected in polymer membranes, despite their determined high biocompatibility, which could be due to the increased membrane permeability in these assemblies following the co-insertion of several enzymes. Since the insertion parameters were determined in vesicles reconstituted with individual enzymes, the disadvantageous interaction between several enzymes during their co-

reconstitution could also not be excluded and should be explored in more detail in future works. Nevertheless, the determined relationship between the tested detergents and the final configuration of the inserted enzymes served as invaluable information guiding the construction of the energy module and is of immediate importance for any similar system.

To enable the step-wise assembly of multiprotein artificial respiratory chains with the preserved optimal configuration of each individual enzyme, SNARE-mediated fusion was explored. With respect to this, the minimal fusion environment was defined with as wide as possible biocompatibility in mind. Apart from HEPES, and DTT to reduce the SNAREs, the only other additive was KCl, which is commonly used to stabilize MPs and was chosen due to its comparatively weaker interaction with membranes. Thereby, KCl neutralized the surface charges introduced by lipid dyes, which minimized the electrostatic repulsion between vesicles, and additionally stimulated fusion by lowering the bending rigidity of polymersomes and hybrids. The latter effects led to measurable events of unmediated fusion, both in content and membrane mixing experiments, but the significantly slower initial kinetics of the latter do not lessen the orthogonality of the SNARE-based approach. Remarkably, I observed fusion of polymersomes and hybrids with identical or better efficiency than in lipid vesicles. This is particularly exciting with respect to the previously mentioned decrease in the functional integration of ATP synthase with increasing polymer proportion. In fact, I demonstrated that the current strategy can be employed as a useful practical tool for the integration of bioenergetic apparatus in all tested amphiphiles, paving the way to further applications for protein trafficking in natural and synthetic membranes. Moreover, for the first time, polymersome fusion was observed on a nano-scale and the related fusion intermediates were described. Of particular interest in this context was the observed membrane mixing between the lipid bilayers and polymer monolayer in a process described as "hybrid zippering". The details behind the latter remain an alluring puzzle yet to be solved.

We previously observed several PDMS-*g*-PEO characteristics of high potential to promote membrane fusion, in particular its low bending rigidity, sufficient fluidity and comparatively low membrane thickness (*1, 97*). Here, the low edge tension was identified as another key material property that enabled easier pore opening and thus facilitated content mixing. Even though the structure and nanomechanics of the nascent fusion pore of potentially proteolipid character and the complex energy landscape of liposome fusion have not been fully resolved yet, there are indications that pore formation may be the dominating factor in the experimentally determined lumped activation energy of $\sim$30 k_BT in phosphatidylcholines (*211*). In any case,

it is safe to conclude that the joint contribution of easier bending and pore stability leads to a lower apparent activation energy for fusion in the polymer membrane compared to lipids. Thus, the 5 k_BT (*212*) of mechanical work, exercised by SNAREs at the conclusive stage of fusion will more easily overcome the energetic barrier and less cooperative effort would be required to achieve synaptic rates.

In line with the demonstrated biocompatibility, protective properties, and enhanced fusion ability of PDMS-*g*-PEO, alongside the established role of polymersomes in drug delivery, SNARE mediation opens new ways for targeted administration of encapsulated small molecules and biologicals. Though in addition to the above characteristics, a suitable polymer needs to be cellularly degradable and/or easily eliminated. Having secured that, the prime synaptic arena of SNAREs instantly motivates exemplary scenarios for the symptomatic treatment of neurological disorders like Parkinson's disease; such synthetic synaptic vesicles would directly (re-)activate dopaminergic neurons, while preventing systemic clearance. Moreover, the demonstrated orthogonality of PDMS-*g*-PEO to the respiratory enzymes suggests that further functionalization of materials with matching mechanical properties via targeting peptides and antibodies (for instance to cross the blood-brain barrier and thus ease the administration) is attainable as well. Yet the role of SNAREs is much more diverse and I hope that the current findings, which demonstrate that similar principles of protein-mediated fusion apply for polymer membranes as well, will stimulate multiple novel applications in synthetic biology and biomedicine. Furthermore, the biological congruity of SNAREs allows for immediate employment of natural NSF/SNAP recycling machinery to enable directed and sustained fusion, in contrast to one-off physicochemical triggers such as electrostatic attraction or bulk control by osmotic pressure. This exciting concept will be addressed in future works. Such a virtually inexhaustible process will be particularly relevant for recursive phenomena like the growth of membrane in the context of proliferation and construction of the artificial cells.

Finally, while the reconstitution of respiratory enzymes in polymer-based membranes was being optimized and SNAREs as a tool for system integration were being developed, I attempted the construction of the artificial mitochondrion. To enable coupling between the artificial respiratory chain and the metabolic cascade, the most active SRC – ATP synthase and *bo₃* oxidase reconstituted in liposomes – was first extended by the addition of NAHD dehydrogenase. My initial plan was to expand the SRC with another proton pump and with that increase the efficiency of the energy module. Alas, the simultaneous insertion of now three

respiratory enzymes emerged as a challenging task due to the unpredictable nature of such coreconstitution, resulting in relatively poor activity of the ARC 1. With this, the immense importance of the alternative tools for systems assembly, such as integration through SNARE-mediated membrane fusion, was highlighted once more. My firm believe with respect to the co-reconstitution approach, however, is that even such complex system can be optimized in a similar fashion to the optimization of the SRC, although unfortunately most likely through rigorous process of trial and error. In the meantime, to supply the energy to metabolic cascade at the sufficiently high rate, in parallel, I expanded the SRC with another variant of NADH dehydrogenase, which did not require membrane insertion. This way, the high activity of SRC was preserved, which enabled coupling with the proposed model metabolic cascade – the CETCH cycle. To prepare ARC 2 for said coupling, the osmolarity of the module was tuned to match the one of the cycle under operational conditions. To account for the dynamic changes in osmolarity during the turnover of CETCH, the output of the energy module was tested under the applied osmotic stress. Furthermore, the ARC 2 was subjected to freezing/thawing to probe for the stability of the module upon storage at ultralow temperatures. Remarkably, the activity of ARC 2 was preserved under significantly altered turgor pressure and was increased after a single freeze/thaw cycle. This beneficial membrane remodeling via the externally applied force suggested the potential presence of membrane imperfections, likely due to the protein insertion.

This led me to believe that a more controlled membrane reorganization could therefore be induced in the ARC vesicles with a goal of reducing membrane permeability and the related dissipation of the established proton gradient. Towards this end I employed Poloxamer 188, a block co-polymer, which is used in medical purposes to treat the damage done to cell membranes in vivo. Astonishingly, in some variants of the artificial respiratory chain, the supplementation with P188 resulted in drastically improved output of the energy module, urging the further exploration. Appropriately tuned and optimized ARC 2 was then coupled with the CETCH cycle to form the minimal artificial mitochondrion. The coupled system used a single energy source – formate – and was running continuously over several hours. The efficiency of the energy supply was about one third of the of the expected one and the accumulation of 4-hydroxybutyrate, a substrate of the ATP-dependant reaction, was detected. To investigate the reasons behind the ARC 2 inhibition, the activity of the ARC 2 under prolonged period of time was measured. It was determined that the energy module was inhibited by the oxygen depletion, hence my next objective was to design an auxiliary oxygen supply system. Towards this end, calcium peroxide particles were identified as a suitable

reoxygenation agent capable of extended oxygen release with high enough rate do drive the activity of bo_3 oxidase and the ARC for several hours. The particles were supplemented with the enzyme catalase in order to convert a harmful by-product of CaO_2 hydration, hydrogen peroxide, to oxygen and water. The significantly extended high initial activity of the ARC 2 in the presence of the oxygen supply system was observed, underlining the immense importance of cofactor resupply in biomimetic constructs. To avoid particle sedimentation and to facilitate homogeneous reoxygenation of the system, the encapsulation of CaO_2 in a form of oxygen supply matrix was proposed. For the time being, unfortunately, the artificial mitochondrion remains incomplete in the final construction phase. To form a truly near-autonomous artificial organelle capable of cell-like respiration, the coupled ARC/CETCH lack an external compartment featuring integrated substrate/product transporters. Nevertheless, when taken together, the experiments described in this work showcase the immense potential of the artificial respiratory chain as the energy supply module in the context of biomimetic constructs, or more broadly for various biotech applications. By experiencing countless obstacles related to protein coreconstitution and stabilization, membrane reorganization and cofactor supply, one can truly appreciate the marvels of a system in which these obstacles were successfully overcame – natural cells. I am looking with excitement and impatience towards the day when the complexity and elegance of natural systems will be accomplished, and perhaps surpassed, in biomimetic construct. In the meantime, luckily, the ARC 1 requires further optimization to help me pass the time!

Literature

1. L. Otrin *et al.*, Toward Artificial Mitochondrion: Mimicking Oxidative Phosphorylation in Polymer and Hybrid Membranes. *Nano Letters* **17**, 6816 (2017).
2. L. Otrin *et al.*, Artificial Organelles for Energy Regeneration. *Advanced Biosystems* **3**, 1800323 (2019).
3. C. A. Hutchison *et al.*, Design and synthesis of a minimal bacterial genome. *Science* **351**, aad6253 (2016).
4. A. A. K. Nielsen *et al.*, Genetic circuit design automation. *Science* **352**, aac7341 (2016).
5. Y. Shao *et al.*, Creating a functional single-chromosome yeast. *Nature* **560**, 331 (2018).
6. J. Luo *et al.*, Karyotype engineering by chromosome fusion leads to reproductive isolation in yeast. *Nature* **560**, 392 (2018).
7. X. Luo *et al.*, Complete biosynthesis of cannabinoids and their unnatural analogues in yeast. *Nature* **567**, 123 (2019).
8. D.-K. Ro *et al.*, Production of the antimalarial drug precursor artemisinic acid in engineered yeast. *Nature* **440**, 940 (2006).
9. F. Meng *et al.*, The second decade of synthetic biology: 2010–2020. *Nature Communications* **11**, 5174 (2020).
10. R. Kwok, Five hard truths for synthetic biology. *Nature* **463**, 288 (2010).
11. P. Schwille *et al.*, MaxSynBio: Avenues Towards Creating Cells from the Bottom Up. *Angewandte Chemie (International ed. in English)* **57**, 13382 (2018).
12. I. Ivanov *et al.*, Directed Growth of Biomimetic Microcompartments. *Advanced Biosystems* **3**, 1800314 (2019).
13. A. Akbarzadeh *et al.*, Liposome: classification, preparation, and applications. *Nanoscale Res Lett* **8**, 102 (2013).
14. S. Deshpande *et al.*, On-chip microfluidic production of cell-sized liposomes. *Nature Protocols* **13**, 856 (2018).
15. B. Yu *et al.*, Microfluidic methods for production of liposomes. *Methods Enzymol* **465**, 129 (2009).
16. S. Amrani *et al.*, Characterization of Nanoscale Loaded Liposomes Produced by 2D Hydrodynamic Flow Focusing. *ACS Biomaterials Science & Engineering* **4**, 502 (2018).
17. A. Jahn *et al.*, Microfluidic Mixing and the Formation of Nanoscale Lipid Vesicles. *ACS Nano* **4**, 2077 (2010).
18. M. Weiss *et al.*, Sequential bottom-up assembly of mechanically stabilized synthetic cells by microfluidics. *Nature Materials* **17**, 89 (2018).
19. A. R. Abate *et al.*, High-throughput injection with microfluidics using picoinjectors. *Proc Natl Acad Sci U S A* **107**, 19163 (2010).
20. A. Jahn *et al.*, Controlled Vesicle Self-Assembly in Microfluidic Channels with Hydrodynamic Focusing. *Journal of the American Chemical Society* **126**, 2674 (2004).
21. D. Carugo *et al.*, Liposome production by microfluidics: potential and limiting factors. *Scientific Reports* **6**, 25876 (2016).
22. E. Rideau *et al.*, Liposomes and polymersomes: a comparative review towards cell mimicking. *Chemical Society Reviews* **47**, 8572 (2018).
23. H. Che *et al.*, Stimuli-responsive polymersomes and nanoreactors. *Journal of Materials Chemistry B* **4**, 4632 (2016).
24. H. Aranda-Espinoza *et al.*, Electromechanical Limits of Polymersomes. *Physical Review Letters* **87**, 208301 (2001).
25. P. V. Pawar *et al.*, Functionalized polymersomes for biomedical applications. *Polymer Chemistry* **4**, 3160 (2013).

26. J. Liao *et al.*, Recent advances in formation, properties, and applications of polymersomes. *Current pharmaceutical design* **18**, 3432 (2012).

27. X. Hu *et al.*, Stimuli-Responsive Polymersomes for Biomedical Applications. *Biomacromolecules* **18**, 649 (2017).

28. V. Balasubramanian *et al.*, Multifaceted polymersome platforms: Spanning from self-assembly to drug delivery and protocells. *Progress in Polymer Science* **60**, 51 (2016).

29. S. S. Klara *et al.*, Magnetically Directed Two-Dimensional Crystallization of OmpF Membrane Proteins in Block Copolymers. *Journal of the American Chemical Society* **138**, 28 (2016).

30. C. De Vocht *et al.*, Assessment of stability, toxicity and immunogenicity of new polymeric nanoreactors for use in enzyme replacement therapy of MNGIE. *Journal of Controlled Release* **137**, 246 (2009).

31. R. Stoenescu *et al.*, Asymmetric ABC-Triblock Copolymer Membranes Induce a Directed Insertion of Membrane Proteins. *Macromolecular Bioscience* **4**, 930 (2004).

32. M. Kumar *et al.*, Highly permeable polymeric membranes based on the incorporation of the functional water channel protein Aquaporin Z. *Proceedings of the National Academy of Sciences* **104**, 20719 (2007).

33. H.-J. Choi *et al.*, Artificial Organelle: ATP Synthesis from Cellular Mimetic Polymersomes. *Nano Letters* **5**, 2538 (2005).

34. S. Khan *et al.*, Durable proteo-hybrid vesicles for the extended functional lifetime of membrane proteins in bionanotechnology. *Chemical Communications* **52**, 11020 (2016).

35. A. Carlsen *et al.*, Block Copolymer Vesicle Permeability Measured by Osmotic Swelling and Shrinking. *Langmuir* **27**, 4884 (2011).

36. Z. Lin *et al.*, Cryo transmission electron microscopy study of vesicles and micelles in siloxane surfactant aqueous solutions. *Langmuir* **10**, 1008 (1994).

37. Jacek T. Mika *et al.*, Measuring the Viscosity of the Escherichia coli Plasma Membrane Using Molecular Rotors. *Biophys J* **111**, 1528 (2016).

38. M. Chemin *et al.*, Hybrid polymer/lipid vesicles: fine control of the lipid and polymer distribution in the binary membrane. *Soft Matter* **8**, 2867 (2012).

39. M. Lynch *et al.*, Membranes, energetics, and evolution across the prokaryote-eukaryote divide. *eLife* **6**, e20437 (2017).

40. K. Y. Lee *et al.*, Photosynthetic artificial organelles sustain and control ATP-dependent reactions in a protocellular system. *Nature Biotechnology* **36**, 530 (2018).

41. S. Berhanu *et al.*, Artificial photosynthetic cell producing energy for protein synthesis. *Nature Communications* **10**, 1325 (2019).

42. J. N. Andexer *et al.*, Emerging Enzymes for ATP Regeneration in Biocatalytic Processes. *ChemBioChem* **16**, 380 (2015).

43. K. A. Calhoun *et al.*, in *In Vitro Transcription and Translation Protocols,* G. Grandi, Ed. (Humana Press, Totowa, NJ, 2007), pp. 3-17.

44. C. von Ballmoos *et al.*, Mimicking respiratory phosphorylation using purified enzymes. *Biochimica et Biophysica Acta (BBA) - Bioenergetics* **1857**, 321 (2016).

45. J. Abramson *et al.*, The structure of the ubiquinol oxidase from Escherichia coli and its ubiquinone binding site. *Nature Structural Biology* **7**, 910 (2000).

46. B. Pitard *et al.*, ATP Synthesis by the F0F1 ATP Synthase from Thermophilic Bacillus PS3 Reconstituted into Liposomes with Bacteriorhodopsin. *European Journal of Biochemistry* **235**, 769 (1996).

47. K. Faxén *et al.*, A mechanistic principle for proton pumping by cytochrome c oxidase. *Nature* **437**, 286 (2005).

48. B. E. Krenn *et al.*, Co-reconstitution of the H^{+}-ATP synthase and cytochrome b-563c-554 complex from a thermophilic cyanobacterium: High ATP yield and mutual effects on the enzymatic activities. *Biochimica et Biophysica Acta (BBA) - Bioenergetics* **1140**, 271 (1993).

49. O. Biner *et al.*, Towards a Synthetic Mitochondrion. *CHIMIA International Journal for Chemistry* **72**, 291 (2018).

50. T. Nilsson *et al.*, Lipid-mediated Protein-protein Interactions Modulate Respiration-driven ATP Synthesis. *Scientific Reports* **6**, 24113 (2016).

51. A. C. Gemperli *et al.*, Sodium ion cycling mediates energy coupling between complex I and ATP synthase. *Proceedings of the National Academy of Sciences* **100**, 839 (2003).

52. O. Biner *et al.*, Bottom-Up Construction of a Minimal System for Cellular Respiration and Energy Regeneration. *ACS Synthetic Biology* **9**, 1450 (2020).

53. M. Denis, Structure and function of cytochrome-c oxidase. *Biochimie* **68**, 459 (1986).

54. G. Nordlund *et al.*, SNARE-fusion mediated insertion of membrane proteins into native and artificial membranes. *Nature Communications* **5**, 4303 (2014).

55. M. Radermacher *et al.*, The three-dimensional structure of complex I from Yarrowia lipolytica: A highly dynamic enzyme. *Journal of Structural Biology* **154**, 269 (2006).

56. H. Leif *et al.*, Isolation and characterization of the proton-translocating NADH: ubiquinone oxidoreductase from Escherichia coli. *Eur J Biochem* **230**, 538 (1995).

57. S. Chen *et al.*, Structure-function studies of DT-diaphorase (NQO1) and NRH: quinone oxidoreductase (NQO2). *Free radical biology & medicine* **29**, 276 (2000).

58. T. Schwander *et al.*, A synthetic pathway for the fixation of carbon dioxide in vitro. *Science* **354**, 900 (2016).

59. T. Beneyton *et al.*, Out-of-equilibrium microcompartments for the bottom-up integration of metabolic functions. *Nat Commun* **9**, 2391 (2018).

60. T. E. Miller *et al.*, Light-powered CO_2 fixation in a chloroplast mimic with natural and synthetic parts. *Science* **368**, 649 (2020).

61. D. Lévy *et al.*, A systematic study of liposome and proteoliposome reconstitution involving Bio-Bead-mediated Triton X-100 removal. *Biochimica et Biophysica Acta (BBA) - Biomembranes* **1025**, 179 (1990).

62. J. L. Rigaud *et al.*, Mechanisms of membrane protein insertion into liposomes during reconstitution procedures involving the use of detergents. 2. Incorporation of the light-driven proton pump bacteriorhodopsin. *Biochemistry* **27**, 2677 (1988).

63. J.-L. Rigaud *et al.*, Reconstitution of membrane proteins into liposomes. *Methods Enzymol* **372**, 65 (2003).

64. J.-L. Rigaud *et al.*, Reconstitution of membrane proteins into liposomes: application to energy-transducing membrane proteins. *Biochimica et Biophysica Acta (BBA) - Bioenergetics* **1231**, 223 (1995).

65. M. T. Paternostre *et al.*, Mechanisms of membrane protein insertion into liposomes during reconstitution procedures involving the use of detergents. 1. Solubilization of large unilamellar liposomes (prepared by reverse-phase evaporation) by Triton X-100, octyl glucoside, and sodium cholate. *Biochemistry* **27**, 2668 (1988).

66. J. Knol *et al.*, Detergent-Mediated Reconstitution of Membrane Proteins. *Biochemistry* **37**, 16410 (1998).

67. D. Lichtenberg, Characterization of the solubilization of lipid bilayers by surfactants. *Biochimica et Biophysica Acta (BBA) - Biomembranes* **821**, 470 (1985).

68. D. Lichtenberg *et al.*, The mechanism of detergent solubilization of lipid bilayers. *Biophys J* **105**, 289 (2013).

69. J. R. Silvius, Solubilization and Functional Reconstitution of Biomembrane Components. *Annual Review of Biophysics and Biomolecular Structure* **21**, 323 (1992).

70. V. Pata *et al.*, Membrane Solubilization by Detergent: Resistance Conferred by Thickness. *Langmuir* **20**, 3888 (2004).
71. S. Rottet *et al.*, Characterisation of Hybrid Polymersome Vesicles Containing the Efflux Pumps NaAtm1 or P-Glycoprotein. *Polymers* **12**, (2020).
72. C. Kleineberg *et al.*, Light-Driven ATP Regeneration in Diblock/Grafted Hybrid Vesicles. *ChemBioChem* **21**, 2149 (2020).
73. M. L. Verkhovskaya *et al.*, Glutamic acid 286 in subunit I of cytochrome bo_3 is involved in proton translocation. *Proceedings of the National Academy of Sciences* **94**, 10128 (1997).
74. S. Dröse *et al.*, Proton pumping by complex I (NADH:ubiquinone oxidoreductase) from Yarrowia lipolytica reconstituted into proteoliposomes. *Biochimica et Biophysica Acta (BBA) - Bioenergetics* **1710**, 87 (2005).
75. L. V. Chernomordik *et al.*, Biomembrane fusion: a new concept derived from model studies using two interacting planar lipid bilayers. *Biochimica et biophysica acta* **906**, 309 (1987).
76. S. Mondal Roy *et al.*, Membrane fusion induced by small molecules and ions. *J Lipids* **2011**, 528784 (2011).
77. M. J. Strohman *et al.*, Local membrane charge regulates β2 adrenergic receptor coupling to Gi3. *Nature Communications* **10**, 2234 (2019).
78. S. D. Nguyen *et al.*, Preferential inhibition of paraoxonase activity of human paraoxonase 1 by negatively charged lipids. *Journal of Lipid Research* **45**, 2211 (2004).
79. J. Serth *et al.*, The inhibition of the GTPase activating protein-Ha-ras interaction by acidic lipids is due to physical association of the C-terminal domain of the GTPase activating protein with micellar structures. *The EMBO Journal* **10**, 1325 (1991).
80. O. Biner *et al.*, Delivery of membrane proteins into small and giant unilamellar vesicles by charge-mediated fusion. *FEBS Letters* **590**, 2051 (2016).
81. T. H. Kloepper *et al.*, An elaborate classification of SNARE proteins sheds light on the conservation of the eukaryotic endomembrane system. *Mol Biol Cell* **18**, 3463 (2007).
82. D. Fasshauer *et al.*, Mixed and non-cognate SNARE complexes. Characterization of assembly and biophysical properties. *The Journal of biological chemistry* **274**, 15440 (1999).
83. T. Söllner *et al.*, A protein assembly-disassembly pathway in vitro that may correspond to sequential steps of synaptic vesicle docking, activation, and fusion. *Cell* **75**, 409 (1993).
84. T. Söllner *et al.*, SNAP receptors implicated in vesicle targeting and fusion. *Nature* **362**, 318 (1993).
85. A. V. Pobbati *et al.*, N- to C-Terminal SNARE Complex Assembly Promotes Rapid Membrane Fusion. *Science* **313**, 673 (2006).
86. J. M. Hernandez *et al.*, Membrane fusion intermediates via directional and full assembly of the SNARE complex. *Science* **336**, 1581 (2012).
87. R. P. Rand, Interacting phospholipid bilayers: measured forces and induced structural changes. *Annual review of biophysics and bioengineering* **10**, 277 (1981).
88. M. M. Kozlov *et al.*, [Possible mechanism of membrane fusion]. *Biofizika* **28**, 242 (1983).
89. M. T. Palfreyman *et al.*, in *Molecular Mechanisms of Neurotransmitter Release,* Z.-W. Wang, Ed. (Humana Press, Totowa, NJ, 2008), pp. 35-59.
90. S. Varlas *et al.*, Polymerization-Induced Polymersome Fusion. *Journal of the American Chemical Society* **141**, 20234 (2019).
91. Y.-L. Lin *et al.*, The fusion mechanism of small polymersomes formed by rod–coil diblock copolymers. *Soft Matter* **10**, 1500 (2014).

92.   I. M. Henderson *et al.*, Lights on: Dye dequenching reveals polymersome fusion with polymer, lipid and stealth lipid vesicles. *Polymer* **83**, 239 (2016).

93.   I. M. Henderson *et al.*, Salt, Shake, Fuse—Giant Hybrid Polymer/Lipid Vesicles through Mechanically Activated Fusion. *Angewandte Chemie International Edition* **53**, 3372 (2014).

94.   C. K. Wong *et al.*, Formation of non-spherical polymersomes driven by hydrophobic directional aromatic perylene interactions. *Nature Communications* **8**, 1240 (2017).

95.   Y. Zhou *et al.*, Real-Time Membrane Fusion of Giant Polymer Vesicles. *Journal of the American Chemical Society* **127**, 10468 (2005).

96.   L. Otrin *et al.*, En route to dynamic life processes by SNARE-mediated fusion of polymer and hybrid membranes. *Nature Communications* **12**, 4972 (2021).

97.   N. Marušič *et al.*, Constructing artificial respiratory chain in polymer compartments: Insights into the interplay between *bo₃* oxidase and the membrane. *Proceedings of the National Academy of Sciences* **117**, 15006 (2020).

98.   R. R. Ishmukhametov *et al.*, Ultrafast purification and reconstitution of His-tagged cysteine-less Escherichia coli F1Fo ATP synthase. *Biochimica et biophysica acta* **1706**, 110 (2005).

99.   V. C. Rombach-Riegraf, Untersuchung des Fo-Motors der H+-ATP synthase aus *Echerichia coli* mit Einzelmolekul-Fluoreszenzspektroskopie. *Dissertation*, Universität Freiburg (2009).

100.   H. L. Frericks *et al.*, Magic-angle spinning solid-state NMR of a 144 kDa membrane protein complex: E. coli cytochrome *bo₃* oxidase. *Journal of biomolecular NMR* **36**, 55 (2006).

101.   E. A. Berry *et al.*, Simultaneous determination of hemes a, b, and c from pyridine hemochrome spectra. *Anal Biochem* **161**, 1 (Feb 15, 1987).

102.   A. Puustinen *et al.*, The heme groups of cytochrome o from Escherichia coli. *Proceedings of the National Academy of Sciences of the United States of America* **88**, 6122 (1991).

103.   K. Hoelsch *et al.*, Engineering of formate dehydrogenase: synergistic effect of mutations affecting cofactor specificity and chemical stability. *Applied Microbiology and Biotechnology* **97**, 2473 (2013/03/01, 2013).

104.   K. Hölsch *et al.*, Enantioselective reduction of prochiral ketones by engineered bifunctional fusion proteins. *Biotechnology and Applied Biochemistry* **56**, 131 (2010).

105.   C. G. Schuette *et al.*, Determinants of liposome fusion mediated by synaptic SNARE proteins. *Proceedings of the National Academy of Sciences of the United States of America* **101**, 2858 (2004).

106.   A. Stein *et al.*, Helical extension of the neuronal SNARE complex into the membrane. *Nature* **460**, 525 (2009).

107.   H. Yavuz *et al.*, Arrest of trans-SNARE zippering uncovers loosely and tightly docked intermediates in membrane fusion. *The Journal of biological chemistry* **293**, 8645 (2018).

108.   A. Witkowska *et al.*, A convenient protocol for generating giant unilamellar vesicles containing SNARE proteins using electroformation. *Scientific Reports* **8**, 9422 (2018).

109.   M. A. Tocilescu *et al.*, Exploring the Ubiquinone Binding Cavity of Respiratory Complex I. *Journal of Biological Chemistry* **282**, 29514 (2007).

110.   N. Kashani-Poor *et al.*, Efficient large scale purification of his-tagged proton translocating NADH:ubiquinone oxidoreductase (complex I) from the strictly aerobic yeast Yarrowia lipolytica. *Biochimica et Biophysica Acta (BBA) - Bioenergetics* **1504**, 363 (2001).

111. M. I. Angelova *et al.*, Liposome electroformation. *Faraday Discussions of the Chemical Society* **81**, 303 (1986).

112. L. S. Khailova *et al.*, Cations SkQ1 and MitoQ accumulated in mitochondria delay opening of ascorbate/FeSO4-induced nonspecific pore in the inner mitochondrial membrane. *Biochemistry (Moscow)* **73**, 1121 (2008).

113. S. R. Schaffazick *et al.*, Protective properties of melatonin-loaded nanoparticles against lipid peroxidation. *International Journal of Pharmaceutics* **289**, 209 (2005).

114. S. V. Albers *et al.*, in *Methods in Microbiology*. (Academic Press, 2006), vol. 35, pp. 161-171.

115. A. Scarpa *et al.*, Cation permeability of liposomes as a function of the chemical composition of the lipid bilayers. *Biochimica et Biophysica Acta (BBA) - Biomembranes* **241**, 789 (1971).

116. J. W. Nichols *et al.*, Net proton-hydroxyl permeability of large unilamellar liposomes measured by an acid-base titration technique. *Proceedings of the National Academy of Sciences of the United States of America* **77**, 2038 (1980).

117. T. P. T. Dao *et al.*, Mixing Block Copolymers with Phospholipids at the Nanoscale: From Hybrid Polymer/Lipid Wormlike Micelles to Vesicles Presenting Lipid Nanodomains. *Langmuir* **33**, 1705 (2017).

118. S. Grzesiek *et al.*, Dependency of delta pH-relaxation across vesicular membranes on the buffering power of bulk solutions and lipids. *Biophys J* **50**, 265 (1986).

119. C. L. Kuyper *et al.*, Proton Permeation into Single Vesicles Occurs via a Sequential Two-Step Mechanism and Is Heterogeneous. *Journal of the American Chemical Society* **128**, 3233 (2006).

120. A. Olżyńska *et al.*, Mixed DPPC/POPC Monolayers: All-atom Molecular Dynamics Simulations and Langmuir Monolayer Experiments. *Biochimica et biophysica acta* **1858**, 3120 (2016).

121. U. Kragh-Hansen *et al.*, The mechanism of detergent solubilization of liposomes and protein-containing membranes. *Biophys J* **75**, 2932 (1998).

122. H. Schägger *et al.*, Tricine-sodium dodecyl sulfate-polyacrylamide gel electrophoresis for the separation of proteins in the range from 1 to 100 kDa. *Analytical Biochemistry* **166**, 368 (1987).

123. T. Portet *et al.*, A New Method for Measuring Edge Tensions and Stability of Lipid Bilayers: Effect of Membrane Composition. *Biophys J* **99**, 3264 (2010).

124. F. Brochard-Wyart *et al.*, Transient pores in stretched vesicles: role of leak-out. *Physica A: Statistical Mechanics and its Applications* **278**, 32 (2000).

125. R. B. Lira *et al.*, Giant unilamellar vesicles formed by hybrid films of agarose and lipids display altered mechanical properties. *Biophys J* **107**, 1609 (2014).

126. J. Zivanov *et al.*, New tools for automated high-resolution cryo-EM structure determination in RELION-3. *eLife* **7**, (2018).

127. S. Q. Zheng *et al.*, MotionCor2: anisotropic correction of beam-induced motion for improved cryo-electron microscopy. *Nature methods* **14**, 331 (2017).

128. A. Wiedenmann *et al.*, Deltapsi and DeltapH are equivalent driving forces for proton transport through isolated F(0) complexes of ATP synthases. *Biochimica et biophysica acta* **1777**, 1301 (Oct, 2008).

129. W. Laubinger *et al.*, Characterization of the ATP synthase of Propionigenium modestum as a primary sodium pump. *Biochemistry* **27**, 7531 (1988).

130. A. Jussupow *et al.*, How cardiolipin modulates the dynamics of respiratory complex I. *Science Advances* **5**, eaav1850 (2019).

131. N. C. Robinson, Functional binding of cardiolipin to cytochromec oxidase. *Journal of Bioenergetics and Biomembranes* **25**, 153 (1993).

132. M. Fry *et al.*, Cardiolipin requirement for electron transfer in complex I and III of the mitochondrial respiratory chain. *Journal of Biological Chemistry* **256**, 1874 (1981).

133. G. Petrosillo *et al.*, Decreased complex III activity in mitochondria isolated from rat heart subjected to ischemia and reperfusion: role of reactive oxygen species and cardiolipin. *The FASEB Journal* **17**, 714 (2003).

134. L. Kalvodova *et al.*, Lipids as Modulators of Proteolytic Activity of BACE: INVOLVEMENT OF CHOLESTEROL, GLYCOSPHINGOLIPIDS, AND ANIONIC PHOSPHOLIPIDS IN VITRO. *Journal of Biological Chemistry* **280**, 36815 (November 4, 2005, 2005).

135. S. J. Slater *et al.*, The modulation of protein kinase C activity by membrane lipid bilayer structure. *Journal of Biological Chemistry* **269**, 4866 (1994).

136. C. Hunte *et al.*, Lipids and membrane protein structures. *Current Opinion in Structural Biology* **18**, 406 (2008).

137. A. Carruthers *et al.*, How bilayer lipids affect membrane protein activity. *Trends in Biochemical Sciences* **11**, 331 (1986).

138. S. Dröse *et al.*, Full recovery of the NADH:ubiquinone activity of complex I (NADH:ubiquinone oxidoreductase) from Yarrowia lipolytica by the addition of phospholipids. *Biochimica et Biophysica Acta (BBA) - Bioenergetics* **1556**, 65 (2002).

139. T. Wenz *et al.*, Role of phospholipids in respiratory cytochrome bc1 complex catalysis and supercomplex formation. *Biochimica et Biophysica Acta (BBA) - Bioenergetics* **1787**, 609 (2009/06/01/, 2009).

140. L. D. Mayer *et al.*, Vesicles of variable sizes produced by a rapid extrusion procedure. *Biochimica et biophysica acta* **858**, 161 (1986).

141. A. Magarkar *et al.*, Molecular Dynamics Simulation of PEGylated Bilayer Interacting with Salt Ions: A Model of the Liposome Surface in the Bloodstream. *The Journal of Physical Chemistry B* **116**, 4212 (2012).

142. J. F. Le Meins *et al.*, Hybrid polymer/lipid vesicles: state of the art and future perspectives. *Materials Today* **16**, 397 (2013).

143. H. A. Lucero *et al.*, Lipid rafts–protein association and the regulation of protein activity. *Archives of Biochemistry and Biophysics* **426**, 208 (2004).

144. J.-L. Rigaud *et al.*, in *Methods Enzymol.* (Academic Press, 2003), vol. 372, pp. 65-86.

145. C. v. Ballmoos *et al.*, Essentials for ATP Synthesis by F1F0 ATP Synthases. *Annual Review of Biochemistry* **78**, 649 (2009).

146. F. Meng *et al.*, Biodegradable polymersomes as a basis for artificial cells: encapsulation, release and targeting. *Journal of Controlled Release* **101**, 187 (2005).

147. J. P. Jain *et al.*, Development of amphotericin B loaded polymersomes based on (PEG)3-PLA co-polymers: Factors affecting size and in vitro evaluation. *European Journal of Pharmaceutical Sciences* **40**, 456 (2010).

148. H.-J. Choi *et al.*, Effects of different reconstitution procedures on membrane protein activities in proteopolymersomes. *Nanotechnology* **17**, 1825 (2006).

149. S. Khan *et al.*, Durable proteo-hybrid vesicles for the extended functional lifetime of membrane proteins in bionanotechnology. *Chem Commun (Camb)* **52**, 11020 (2016).

150. J. Berg *et al.*, Single Proteoliposomes with E. coli Quinol Oxidase: Proton Pumping without Transmembrane Leaks. *Israel Journal of Chemistry* **57**, 437 (2017).

151. M. Ueno, Partition behavior of a nonionic detergent, octyl glucoside, between membrane and water phases, and its effect on membrane permeability. *Biochemistry* **28**, 5631 (1989).

152. S. Vaidyanathan *et al.*, Detergent Induction of HEK 293A Cell Membrane Permeability Measured under Quiescent and Superfusion Conditions Using Whole Cell Patch Clamp. *The Journal of Physical Chemistry B* **118**, 2112 (2014).

153. A. V. Ushakova *et al.*, Triton X-100 as a specific inhibitor of the mammalian NADH-ubiquinone oxidoreductase (Complex I). *Biochimica et Biophysica Acta (BBA) - Bioenergetics* **1409**, 143 (1999/01/05/, 1999).

154. A. Lundin *et al.*, Continuous monitoring of ATP-converting reactions by purified firefly luciferase. *Analytical Biochemistry* **75**, 611 (1976).

155. F. Itel *et al.*, Dynamics of Membrane Proteins within Synthetic Polymer Membranes with Large Hydrophobic Mismatch. *Nano Letters* **15**, 3871 (2015).

156. A. G. Lee, How lipids affect the activities of integral membrane proteins. *Biochimica et biophysica acta* **1666**, 62 (2004).

157. J. Nam *et al.*, Giant Phospholipid/Block Copolymer Hybrid Vesicles: Mixing Behavior and Domain Formation. *Langmuir* **27**, 1 (2011).

158. F. Heinemann *et al.*, Quantifying Lipid Diffusion by Fluorescence Correlation Spectroscopy: A Critical Treatise. *Langmuir* **28**, 13395 (2012).

159. D. W. Deamer *et al.*, Proton-hydroxide permeability of liposomes. *Proceedings of the National Academy of Sciences of the United States of America* **80**, 165 (1983).

160. W. F. Paxton *et al.*, Monitoring and modulating ion traffic in hybrid lipid/polymer vesicles. *Colloids and Surfaces B: Biointerfaces* **159**, 268 (2017).

161. M. G. Elferink *et al.*, Stability and proton-permeability of liposomes composed of archaeal tetraether lipids. *Biochimica et biophysica acta* **1193**, 247 (1994).

162. R. H. Gensure *et al.*, Lipid raft components cholesterol and sphingomyelin increase H+/OH- permeability of phosphatidylcholine membranes. *Biochem J* **398**, 485 (2006).

163. T. P. T. Dao *et al.*, Phase Separation and Nanodomain Formation in Hybrid Polymer/Lipid Vesicles. *ACS Macro Letters* **4**, 182 (2015).

164. M. Seigneuret *et al.*, Analysis of passive and light-driven ion movements in large bacteriorhodopsin liposomes reconstituted by reverse-phase evaporation. 1. Factors governing the passive proton permeability of the membrane. *Biochemistry* **25**, 6716 (1986).

165. B. Kadenbach, Intrinsic and extrinsic uncoupling of oxidative phosphorylation. *Biochimica et biophysica acta* **1604**, 77 (2003).

166. M. P. Murphy, How mitochondria produce reactive oxygen species. *Biochem J* **417**, 1 (2009).

167. A. W. Girotti, Mechanisms of lipid peroxidation. *Journal of free radicals in biology & medicine* **1**, 87 (1985).

168. E. Schnitzer *et al.*, Peroxidation of liposomal lipids. *European biophysics journal : EBJ* **36**, 499 (2007).

169. L. Mrówczyńska *et al.*, Curvature factor and membrane solubilization, with particular reference to membrane rafts. *Cell biology international* **35**, 991 (2011).

170. M. M. Elsayed *et al.*, The vesicle-to-micelle transformation of phospholipid-cholate mixed aggregates: a state of the art analysis including membrane curvature effects. *Biochimica et biophysica acta* **1808**, 140 (2011).

171. M. C. A. Stuart *et al.*, Two distinct mechanisms of vesicle-to-micelle and micelle-to-vesicle transition are mediated by the packing parameter of phospholipid–detergent systems. *Biochimica et Biophysica Acta (BBA) - Biomembranes* **1768**, 2681 (2007).

172. H. Ahyayauch *et al.*, Detergent Effects on Membranes at Subsolubilizing Concentrations: Transmembrane Lipid Motion, Bilayer Permeabilization, and Vesicle Lysis/Reassembly Are Independent Phenomena. *Langmuir* **26**, 7307 (2010).

173. M. Paternostre *et al.*, Partition coefficient of a surfactant between aggregates and solution: application to the micelle-vesicle transition of egg phosphatidylcholine and octyl beta-D-glucopyranoside. *Biophys J* **69 6**, 2476 (1995).

174. A. H. Thomas *et al.*, Soybean phosphatidylcholine liposomes as model membranes to study lipid peroxidation photoinduced by pterin. *Biochimica et Biophysica Acta (BBA) - Biomembranes* **1858**, 139 (2016).

175. A. de la Maza *et al.*, Solubilizing effects caused by the nonionic surfactant dodecylmaltoside in phosphatidylcholine liposomes. *Biophys J* **72**, 1668 (1997).

176. H. R. Lötscher *et al.*, Interconversion of high and low adenosinetriphosphatase activity forms of Escherichia coli F1 by the detergent lauryldimethylamine oxide. *Biochemistry* **23**, 4140 (1984).

177. X. Chen *et al.*, SNARE-Mediated Lipid Mixing Depends on the Physical State of the Vesicles. *Biophys J* **90**, 2062 (2006).

178. A. A. Gurtovenko *et al.*, Effect of NaCl and KCl on Phosphatidylcholine and Phosphatidylethanolamine Lipid Membranes: Insight from Atomic-Scale Simulations for Understanding Salt-Induced Effects in the Plasma Membrane. *The Journal of Physical Chemistry B* **112**, 1953 (2008).

179. R. Dimova, Recent developments in the field of bending rigidity measurements on membranes. *Advances in Colloid and Interface Science* **208**, 225 (2014).

180. H. A. Faizi *et al.*, Bending rigidity of charged lipid bilayer membranes. *Soft Matter* **15**, 6006 (2019).

181. H. Bouvrais *et al.*, Impact of membrane-anchored fluorescent probes on the mechanical properties of lipid bilayers. *Biochimica et Biophysica Acta (BBA) - Biomembranes* **1798**, 1333 (2010).

182. V. G. Almendro-Vedia *et al.*, Nonequilibrium fluctuations of lipid membranes by the rotating motor protein F1F0-ATP synthase. *Proceedings of the National Academy of Sciences of the United States of America* **114**, 11291 (2017).

183. P. Girard *et al.*, Passive or Active Fluctuations in Membranes Containing Proteins. *Physical Review Letters* **94**, 088102 (2005).

184. L. V. Chernomordik *et al.*, Bending membranes to the task: structural intermediates in bilayer fusion. *Current Opinion in Structural Biology* **5**, 541 (1995).

185. R. S. Gracià *et al.*, Effect of cholesterol on the rigidity of saturated and unsaturated membranes: fluctuation and electrodeformation analysis of giant vesicles. *Soft Matter* **6**, 1472 (2010).

186. V. Nikolov *et al.*, Behavior of giant vesicles with anchored DNA molecules. *Biophys J* **92**, 4356 (2007).

187. A. Grafmüller *et al.*, Pathway of Membrane Fusion with Two Tension-Dependent Energy Barriers. *Physical Review Letters* **98**, 218101 (2007).

188. J. C. Shillcock *et al.*, Tension-induced fusion of bilayer membranes and vesicles. *Nature Materials* **4**, 225 (2005).

189. P. Gipson *et al.*, Morphologies of synaptic protein membrane fusion interfaces. *Proceedings of the National Academy of Sciences* **114**, 9110 (2017).

190. J. B. Stock *et al.*, Periplasmic space in Salmonella typhimurium and Escherichia coli. *The Journal of biological chemistry* **252**, 7850 (1977).

191. S. Hupfeld *et al.*, Liposome fractionation and size analysis by asymmetrical flow field-flow fractionation/multi-angle light scattering: influence of ionic strength and osmotic pressure of the carrier liquid. *Chemistry and Physics of Lipids* **163**, 141 (2010).

192. E. Nagamachi *et al.*, Studies on osmotic stability of liposomes prepared with bacterial membrane lipids by carboxyfluorescein release. *Microbiology and immunology* **36**, 231 (1992).

193. D. Hanahan, Studies on transformation of Escherichia coli with plasmids. *Journal of molecular biology* **166**, 557 (1983).

194. J. G. Moloughney *et al.*, Poloxamer 188 (p188) as a membrane resealing reagent in biomedical applications. *Recent patents on biotechnology* **6**, 200 (2012).

195. C. F. Spurney *et al.*, Membrane Sealant Poloxamer P188 Protects Against Isoproterenol Induced Cardiomyopathy in Dystrophin Deficient Mice. *BMC Cardiovascular Disorders* **11**, 20 (2011).

196. S. A. Maskarinec *et al.*, Direct Observation of Poloxamer 188 Insertion into Lipid Monolayers. *Biophys J* **82**, 1453 (2002).

197. W. Zhang *et al.*, Post-insertion of poloxamer 188 strengthened liposomal membrane and reduced drug irritancy and in vivo precipitation, superior to PEGylation. *Journal of controlled release : official journal of the Controlled Release Society* **203**, 161 (2015).

198. D. Smith *et al.*, Human DT-diaphorase, a potential cancer protecting enzyme. Its purification from abdominal adipose tissue. *Cancer letters* **42**, 103 (1988).

199. J. Weber *et al.*, ATP synthase: what we know about ATP hydrolysis and what we do not know about ATP synthesis. *Biochimica et biophysica acta* **1458**, 300 (2000).

200. M. Gholipourmalekabadi *et al.*, Oxygen-Generating Biomaterials: A New, Viable Paradigm for Tissue Engineering? *Trends in Biotechnology* **34**, 1010 (2016).

201. N. Ashammakhi *et al.*, Advances in Controlled Oxygen Generating Biomaterials for Tissue Engineering and Regenerative Therapy. *Biomacromolecules* **21**, 56 (2020).

202. W. Hongpo *et al.*, in *2015 6th International Conference on Manufacturing Science and Engineering*. (Atlantis Press, 2015), pp. 1698-1701.

203. G. Camci-Unal *et al.*, Oxygen-releasing biomaterials for tissue engineering. *Polymer International* **62**, 843 (2013).

204. H. Wang *et al.*, Properties of calcium peroxide for release of hydrogen peroxide and oxygen: A kinetics study. *Chemical Engineering Journal* **303**, 450 (2016).

205. W. Xing *et al.*, in *Rotating Electrode Methods and Oxygen Reduction Electrocatalysts,* W. Xing, G. Yin, J. Zhang, Eds. (Elsevier, Amsterdam, 2014), pp. 1-31.

206. M. A. Joslyn *et al.*, Solubility of Oxygen in Solutions of Various Sugars. *Journal of Food Science* **14**, 209 (1949).

207. S. A. M. van Stroe-Biezen *et al.*, Solubility of oxygen in glucose solutions. *Analytica Chimica Acta* **280**, 217 (1993).

208. S. H. Oh *et al.*, Oxygen generating scaffolds for enhancing engineered tissue survival. *Biomaterials* **30**, 757 (2009).

209. Z. Li *et al.*, An oxygen release system to augment cardiac progenitor cell survival and differentiation under hypoxic condition. *Biomaterials* **33**, 5914 (2012).

210. D.-w. Chung *et al.*, Study on the effect of structure of polydimethylsiloxane grafted with polyethyleneoxide on surface activities. *Colloids and Surfaces A: Physicochemical and Engineering Aspects* **336**, 35 (2009).

211. R. J. Ryham *et al.*, Calculating Transition Energy Barriers and Characterizing Activation States for Steps of Fusion. *Biophys J* **110**, 1110 (2016).

212. F. Manca *et al.*, SNARE machinery is optimized for ultrafast fusion. *Proceedings of the National Academy of Sciences* **116**, 2435 (2019).
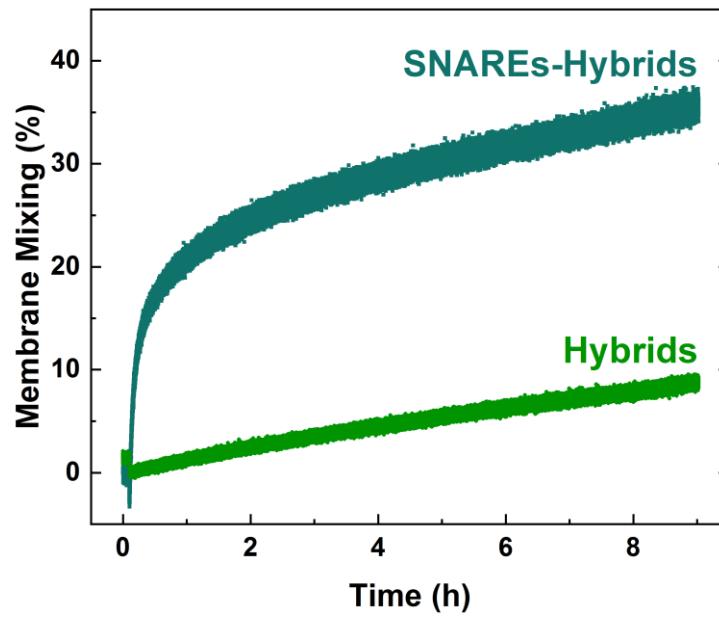
Appx. Fig. 55. SNARE-mediated membrane mixing in hybrid vesicles over the course of several hours. In comparison with proteoliposomes, the plateau in SNARE-induced membrane mixing in hybrids was reached after considerably longer period of time (approx. 11.5 h). Proportionally higher total membrane mixing was observed in said time period. Adapted from (*96*), licensed under CC BY 4.0.
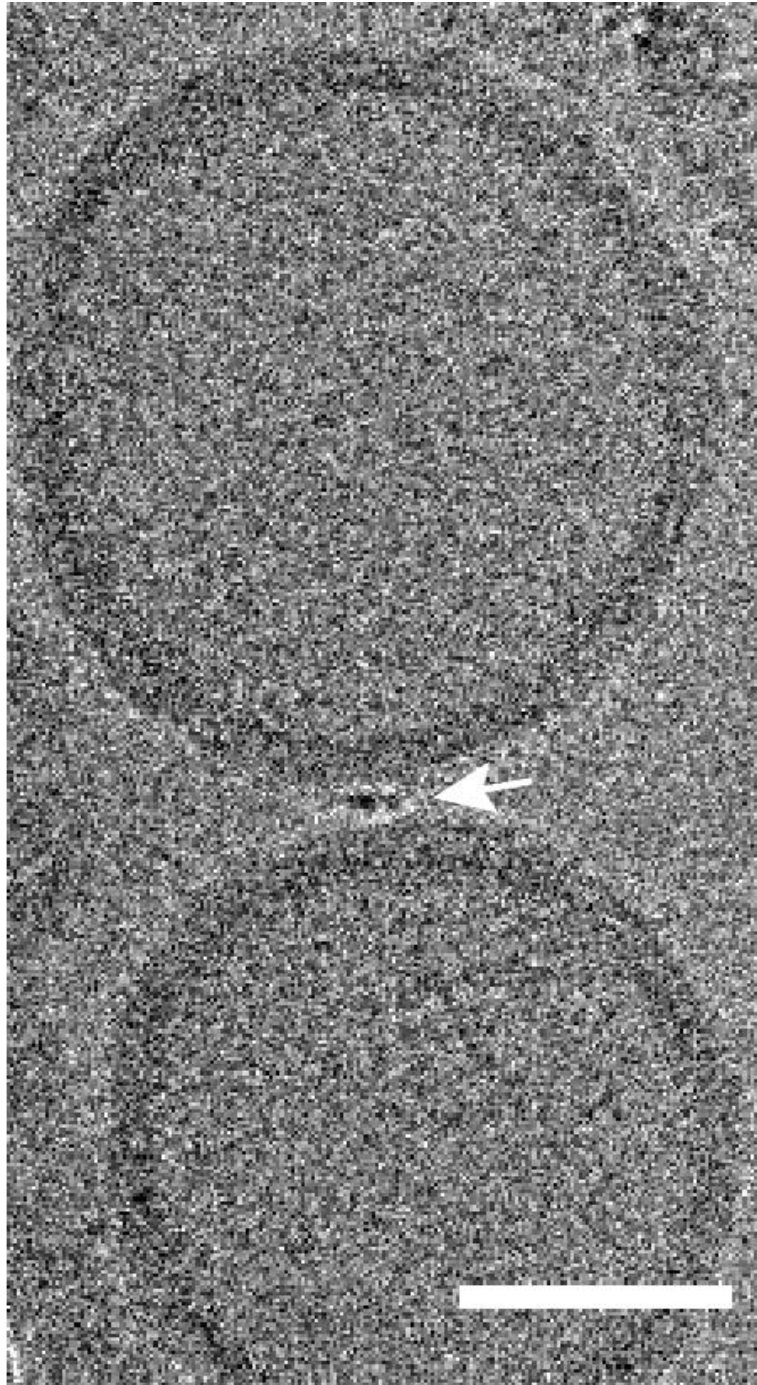
Appx. Fig. 56. Docking between SNARE-inserted polymersomes. Vesicles are drawn into close proximity due to the zippering action between synaptobrevin and ΔN complex, reconstituted in separate vesicles. The fully assembled SNAREs fusion complex is indicated with white arrow. Scale bar = 30 nm. Adapted from (*96*), licensed under CC BY 4.0.
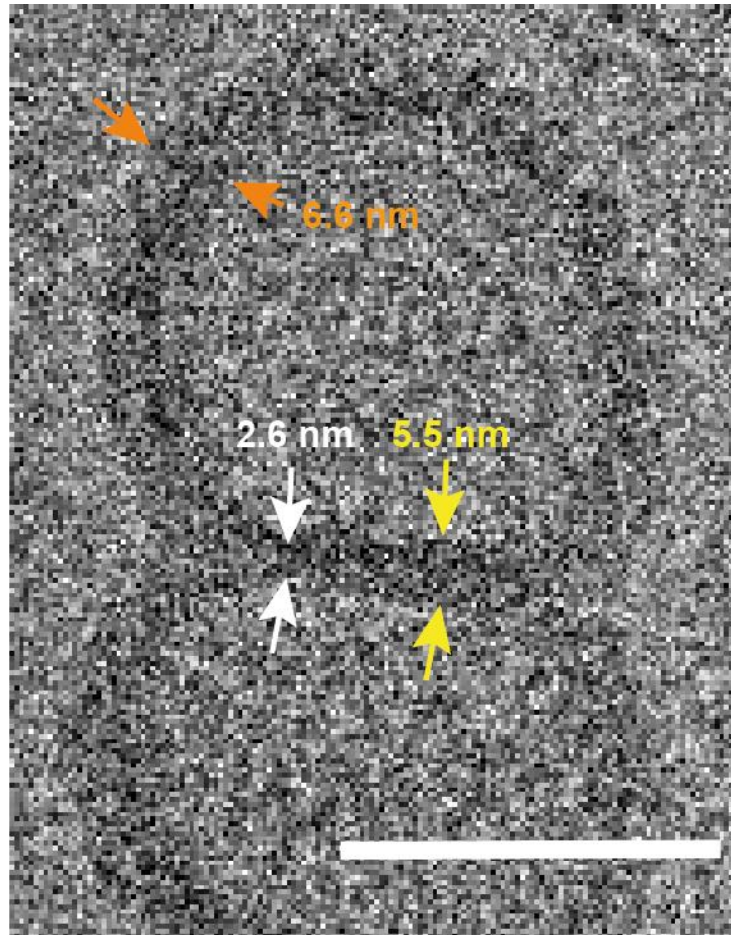
Appx. Fig. 57. Diaphragm thinning in fusing polymersomes. Membrane thinning (shown with white arrows) can be observed at the juncture, indicating the location of eventual pore opening. For a comparison, the average diaphragm thickness (yellow) and the average polymer membrane thickness (orange) are also indicated. Scale bar = 30 nm. Adapted from (*96*), licensed under CC BY 4.0.
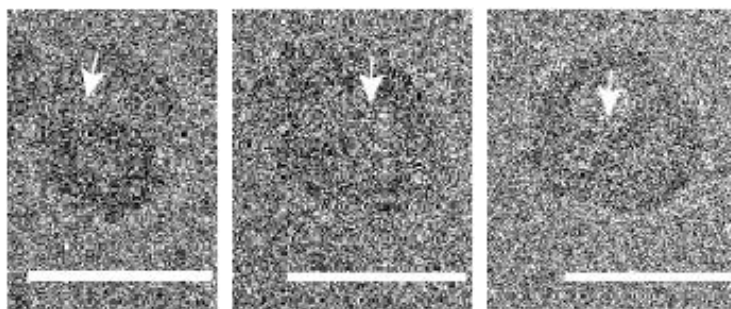
Appx. Fig. 58. Unilateral pore opening in polymersomes. Pores are opened at the diaphragm junctures, indicated with white arrows. Scale bar = 30 nm. Adapted from (*96*), licensed under CC BY 4.0.
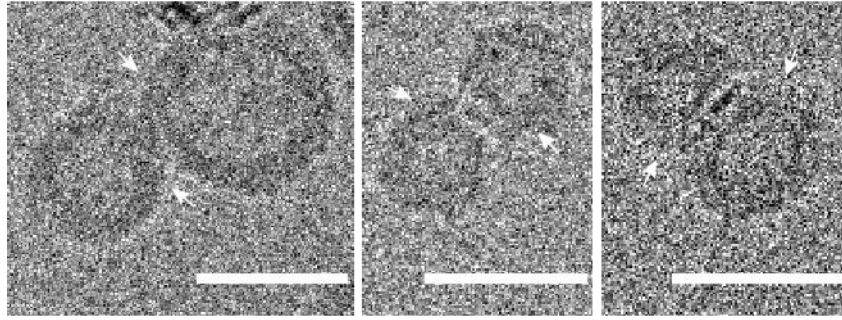
Appx. Fig. 59. Hybrid membrane zippering. Point of contact is initially established at one juncture of fusing vesicles and the membrane mixing is propagated diagonally toward the opposite juncture (marked with white arrows). Scale bar = 30 nm. Adapted from (*96*), licensed under CC BY 4.0.

Acknowledgements

Publications and abstracts

Journal articles

Otrin, L., Marušič, N., Bednarz, C., Vidaković-Koch, T., Lieberwirth, I., Landfester, K., Sundmacher, K. 2017. "Toward Artificial Mitochondrion: Mimicking Oxidative Phosphorylation in Polymer and Hybrid Membranes." *Nano Lett*. 17, 11: 6816–6821.

Conceptualization, methodology, validation, analysis, investigation, writing and editing, visualization.

Wang, M., Wölfer, C., Otrin, L., Ivanov, I., Vidaković-Koch, T., Sundmacher, K. 2018. "Transmembrane NADH Oxidation with Tetracyanoquinodimethane." *Langmuir* 34, 19: 5435–5443.

Conceptualization, methodology.

Otrin, L., Kleineberg, C., da Silva, L. C., Landfester, K., Ivanov, I., Wang, M., Bednarz, C., Sundmacher, K., Vidaković-Koch, T. 2019. "Artificial Organelles for Energy Regeneration." *Adv. Biosyst*. 3: 1800323.

Writing and editing, visualization.

Marušič, N., Otrin, L., Zhao, Z., Lira, R. B, Kyrilis, F. L., Hamdi, F., Kastritis, P. L, Vidaković-Koch, T., Ivanov, I., Sundmacher, K., Dimova, R. 2020. "Constructing artificial respiratory chain in polymer compartments: Insights into the interplay between bo_3 oxidase and the membrane." *PNAS* 117 (26): 15006-15017.

Conceptualization, methodology, validation, analysis, investigation, writing and editing, visualization.

Wohlfromm, F., Richter, M., <u>Otrin, L.</u>, Seyrek, K., Vidaković-Koch, T., Kuligina, E., Richter, V., Koval, O., Lavrik, I. N. 2021. "Interplay Between Mitophagy and Apoptosis Defines a Cell Fate Upon Co-treatment of Breast Cancer Cells with a Recombinant Fragment of Human κ-Casein and Tumor Necrosis Factor-Related Apoptosis-Inducing Ligand." *Front. Cell Dev. Biol.* 8: 617762.

Methodology, validation, investigation, analysis, editing.

<u>Otrin, L.</u>, Witkowska, A., Marušič, N., Zhao, Z., Lira, R. B, Kyrilis, F. L., Hamdi, F., Ivanov, I., Lipowsky, R., Kastritis, P. L, Dimova, R., Sundmacher, K., Jahn, R., Vidaković-Koch, T. 2021. "En Route to Dynamic Life Processes by SNARE-Mediated Fusion of Polymer and Hybrid Membranes." *Nat. Commun.* 12: 4972 (https://doi.org/10.1038/s41467-021-25294-z).

Conceptualization, methodology, validation, analysis, investigation, writing and editing, visualization.

Ivanov, I., Castellanos, S. L., Balasbas III, S., <u>Otrin, L.</u>, Marušič, N., Vidaković-Koch, T., Sundmacher, K. 2021. "Bottom-up Synthesis of Artificial Cells: Recent Highlights and Future Challenges." *Annu. Rev. Chem. Biomol. Eng.* 12:1, 287-308.

Writing and editing, visualization.

Marušič, N., Bednarz, C., Lira, R. B, Zhao, Z., <u>Otrin, L.</u>, Vidaković-Koch, T., Dimova, R., Ivanov, I., Sundmacher, K. 2021. "Fusion/electroformation for functional co-reconstitution of respiratory enzymes in biomimetic hybrid and polymer giant unilamellar vesicles." *ACS Synth. Biol.* (Submitted).

Conceptualization, methodology, analysis, editing.

Conference Papers

Sundmacher, K., Ivanov, I., Mangold, M., <u>Otrin, L.</u>, Vidaković-Koch, T. 2016. "Nachahmung essenzieller Lebensprozesse in minimalen synthetischen Systemen." 18. Heiligenstädter Kolloquium. Heiligenstadt. http://hdl.handle.net/11858/00-001M-0000-002C-3200-4

Marušič, N., <u>Otrin, L.</u>, Zhao, Z., Lira, R. B, Vidaković-Koch, T., Ivanov, I., Dimova, R., Sundmacher, K. 2020. "Reconstitution of Respiratory Enzymes in PDMS-g-PEO Polymer and Polymer/Lipid Hybrid Vesicles." *Biophys. J*. 118 (3): 131a.

<u>Otrin, L.</u>, Diehl, C., Erb, T., Sundmacher, K., Vidaković-Koch, T. 2020. "Mitochondrion Reimagined - Fueling Synthetic Life." *Biophys. J*. 118 (3): 450a.

Curriculum Vitae